INELASTIC WEB CRUSHING PERFORMANCE LIMITS OF HIGH-STRENGTH-CONCRETE STRUCTURAL WALLS

By

Xuejian Liu

A DISSERTATION

Submitted to
Michigan State University
in partial fulfillment of the requirements
for the degree of

DOCTOR OF PHILOSOPHY

CIVIL ENGINEERING

2010

ABSTRACT

INELASTIC WEB CRUSHING PERFORMANCE LIMITS OF HIGH-STRENGTH-CONCRETE STRUCTURAL WALLS

By

Xuejian Liu

The construction of the three new toll bridges in California has highlighted the application of the hollow rectangular bridge piers with highly-reinforced boundary elements and the connecting walls. However, current conservative design approaches result in massive cross sections that can lead to increased construction cost. This study investigates the feasibility of defining new limits for a seldomly considered failure mode that could lead to more slender cross sections with the use of high-strength-concrete (HSC).

The possibility of web crushing failure in shear dominated reinforced concrete element rises when the dimensions of the boundary elements become larger and the webs becomes thinner. Web crushing, or diagonal compression failure, manifests itself as compression failure of concrete struts formed by diagonal tension cracking in the wall web. The failure is brittle in nature and therefore, it is mandated to be suppressed for design in seismic regions. However, it is hypothesized in this study that web crushing failures may occur after significant and stable ductile response by using HSC by increasing the capacity to crushing capacity proportionally to the concrete's compressive strength. To verify the hypothesis, eight 1/5-scale cantilevered structural walls with highly confined boundary elements were tested with design concrete compressive strengths of 34, 69, 103, and 138 MPa (5, 10, 15 and 20 ksi) under cyclic and monotonic loading protocols. The experimental results revealed that HSC can effectively delay web-crushing failures and increase the displacement ductility levels of structural walls.

To evaluate the seismic performance of HSC hollow bridge piers, two 1/4-scale hollow pier units, consisting of an assembly of four walls with heavily confined corner elements, were subjected to simulated seismic demands in diagonal and multi-directional directions with design concrete strengths of 34 and 138 MPa (5 and 20 ksi), respectively. Both test units exhibited stable ductile behavior until web crushing at moderate ductility levels. The comparable ductility capacities of the pier test units indicate that the advantageous effect of HSC in improving web crushing capacity is compromised by concrete damage and strength degradation under multi-directional loading.

Comprehensive nonlinear finite element (FE) modeling was conducted through 3D FE analyses with plasticity-based constitutive models and 2D FE analyses with phenomenological constitutive models to enhance understanding of web crushing capacity in structural walls. The results were compared with test data at the global and local levels to evaluate the performance of analytical methods in predicting flexural and shear behavior. The analytical models revealed that the concrete stress demand at web crushing is only a small portion of the cylinder concrete compressive strength due to the complex stress state in the web crushing region. The results also confirmed that web crushing, in the form of an inelastic shear failure, is caused by flexure-shear interaction effects in the wall web.

In view of the complexity and enormous efforts entailed in finite element modeling as well as the inability of the modeling approaches in capturing failure, simplified analytical method based on truss models extracted from observations of the inelastic shear cracking and failure mechanisms were implemented. This was done by modifying an existing comprehensive inelastic strut-and-tie model for assessment of web crushing capacity. Calibration of the model with experimental results showed that the modifications led to improved predictions of web crushing capacity of high-strength-concrete structural walls.

To my wife Tingyao and my son Cephas.

ACKNOWLEDGEMENTS

I would like to express my sincere gratitude to my advisor, Dr. Rigoberto Burgueño for his continuous support and encouragement. His enthusiasm and devotion to educate students on how to become a researcher impressed me a lot. I am very thankful to him for his understanding, trust and for never giving up on me, which forged me through the enduring PhD study. It has been a challenging and fruitful experience to work under his supervision.

I wish to thank the members of PhD committee, Dr. Ronald S. Harichandran, Dr. Eric M. Hines, Dr. Jung-Wuk Hong, and Dr. Dahsin Liu for their expertise and precious time. Special thanks are due to Dr. Eric M. Hines for his encouragement. He sets an example to me on what an excellent structural engineer should be. His research publications have been textbooks for my study.

I would like to thank Mr. Siavosh Ravanbaksh for his help at the Civil Infrastructure Laboratory. His warm welcome and detailed tutorship made my time at the lab enjoyable.

Lastly, and most importantly, I would like to thank my family. To my wife Tingyao, I cannot image what my life will be without you. To my son, Dad learns gradually on how to be a Dad on your behalf. I am grateful to all of our family members. I know I am not alone when I think about you.

This study was mainly funded by the National Science Foundation under grant NSF-CMS-0530634. Additionally, financial support in the form of assistantships and fellowship awards obtained from the Department of Civil and Environmental Engineering, and the Graduate School at Michigan State University are gratefully acknowledged. Special thanks are addressed to late Dr. Delia Koo for the scholarship granted by the International Studies and Programs at Michigan State University.

TABLE OF CONTENTS

LIST OF TABLES

LIST OF FIGURES

Images in this dissertation are presented in color.

Chapter 1. **Introduction**

1.1 Motivation

The construction of the three new toll bridges in California, the Benicia-Martinez Bridge, the Carquinez Bridge and the San Francisco-Oakland Bay Bridge (SFOBB), has highlighted the relevance of hollow rectangular bridge piers with highly-reinforced boundary elements and connecting walls for the piers of high-profile bridges. The proof-of-concept test of the 1/4-scale SFOBB piers showed that the pier design can exhibit excellent ductile flexural behavior when subjected to severe loading protocols [1][2]. However, the conservative design results in a massive cross section which can make the construction even more expensive. The modification of the design into a more slender cross section by making use of high-strength-concrete and new concepts for shear capacity was recently hypothesized by Hines [3] at the conclusion of the SFOBB proof-of-concept testing. Figure 1.1 shows the cross sections of SFOBB pier test unit with the current design compared to a potentially more slender design as hypothesized by Hines. However, the noted hypothesis lacked experimental verification on the seismic performance of such a slender pier. Especially needing validation is the fact that the potentially slender design hypothesis is rooted in the assumption that increased shear capacity can be obtained from the walls by making use of high-strength-concrete without compromising ductility capacity.

The in-plane behavior of the hollow bridge piers can be well characterized through the study of individual structural walls. The behavior and failure mode varies with aspect ratio. section geometry and reinforcement configuration. For slender shear walls of multistory buildings, the high flexural demand tends to result in flexural failures in the form of the fracture of the tensile reinforcement or crushing of the concrete in the compression zone. For low-rise, or squat, shear walls the possible failure modes include diagonal tension and compression failures, instability, and sliding shear failures. Web crushing, or diagonal compression failure, manifests itself as compression failure of concrete struts formed by diagonal tension cracking in the wall web. The failure is brittle in nature and therefore, it is mandated to be suppressed during design.

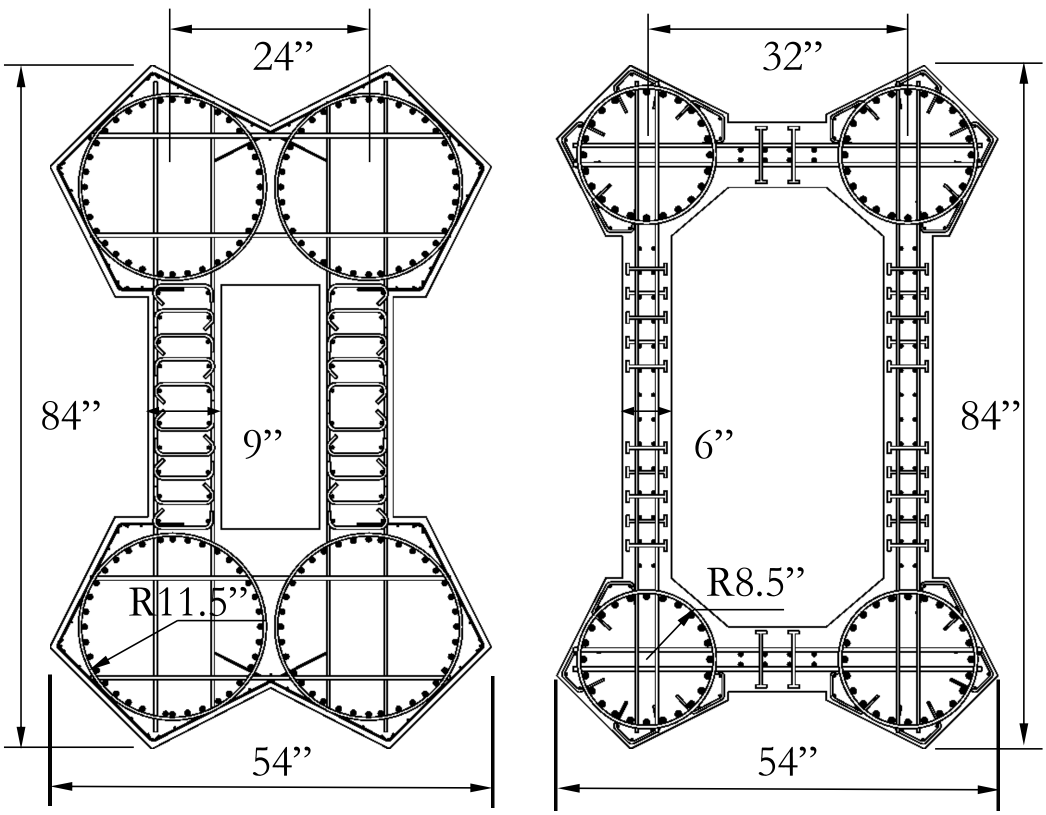

Figure 1.1 SFOBB pier test unit: Present design (Left), Potential design (Right).

Among the structural walls with different cross sections, flanged and barbell shaped walls have been found to be more susceptible to web crushing [4][5]. It has been realized the shear distortion behavior needs to be well investigated in order to study the web crushing behavior of the structural walls. Inelastic shear behavior, exhibited in common structural walls, is characterized by rapid strength and stiffness degradation and hence limited energy-dissipating capacity. In earthquake resistant design, such behavior is undesirable and the corresponding failure modes should be avoided. However, in structural walls with well-confined boundary elements, web crushing failures can take place after adequate ductile response is attained. The key to obtain higher ductility level is that the load-transfer mechanism formed within the structural component should be maintained, that is, the diagonal truss effectively carrying the shear force should be efficient in transferring the load from the tension boundary element to the compression boundary element. It can thus by hypothesized that high-strength-concrete (HSC) can forestall the web crushing failure and increase the displacement capacity of the structural walls since HSC struts should be able to keep the load-transfer mechanism at higher demands.

The response of reinforced concrete elements limited by shear failure but displaying stable inelastic response with adequate energy dissipation characteristics can give rise to a new genre of ductile failure mechanism that may be termed as "ductile shear failure" with a two-fold meaning. First, like ductile flexural failures, a ductile shear failure conforms to the design philosophy appropriate for seismic regions that require a stable hysteretic response able to dissipate energy up to large levels of inelastic deformation before failure. Experimental studies since the mid-seventies of last century [5][6] have demonstrated that structural walls with well-confined boundary elements or flanged sections could exhibit adequate ductile behavior before web crushing failure in the plastic hinge region at displacement ductility levels of four or greater [7]. By establishing reasonable performance limits, ductile shear failures may control the strength and ductility of the structural components for design purposes. Second, failure to consider the shear stiffness degradation of the inelastic flexure-shear region under load reversals could result in an unsafe design according to capacity design procedures. The possibility that flexure controlled structures failing in shear thus arises. Unfortunately, the shear strength and stiffness degradation mechanism of structural walls under coupled inelastic flexure-shear demands is not well understood.

High-strength-concrete (HSC) offers the potential in optimizing structural design and reducing material cost. The potential benefits of HSC bring about new possibilities for the hypothesized more slender designs. First, HSC can provide enough capacity for the compression zone of the boundary element under moment demand. The confinement provided by the spiral will further enhance the strength and ductility of the confined concrete. It should be noted that the fracture failure of the longitudinal reinforcement in the tension boundary element is not considered. Otherwise, the design needs to be modified with higher longitudinal reinforcement ratio. This can be easily checked with sectional moment-curvature analysis. Thus, a more slender design with comparable moment capacity can be obtained by using the same global dimensions of the cross sections and the capacity of the compression zone. Second, the disadvantage of the potential design is that the shear capacity is decreased due to the more slender connecting walls. Thus, possible shear failure modes could happen. Even though the diagonal tension capacity can be satisfied with the configuration of the wall transverse steel, the possibilities of the web crushing could still exists.

The seismic performance of structural walls or wall assemblies is highly dependent on the ductile behavior and energy dissipating capacity of the plastic hinge regions. According to capacity design principles, inelastic shear damage mechanisms should not be relied upon due to their rapid shear stiffness degradation and their inferior energy dissipating capacities. However, recent research [8] has demonstrated that pier walls under shear demands considerably above current design limits can exhibit stable ductile behavior before experiencing web crushing failures, and that their inelastic deformation capacity can be further improved by using high-strength-concrete (HSC). Such facts thus lead to the suggestion that inelastic flexure-shear behavior with subsequent inelastic shear failure can satisfy seismic performance requirements on bridge piers. It also has to be recognized that the use of HSC entails careful damage assessment to meet serviceability objectives and explicit criteria on performance limits to ensure meeting safety.

The vulnerability of structures subjected to earthquake motions along random directions makes the performance evaluation of wall assemblies under multi-directional loading necessary. It is simple to understand that the damage on the web concrete will accumulate with loading in different directions. Some research has been conducted to study the behavior of the three-dimensional shear walls in T, L or I shape [9][10]. However, the demand and capacity of the walls in non-principal directions has not been fully investigated. The dispersion of the tensile forces from the boundary elements or flanges makes it difficult to decide the effective dimension of the web, which plays an important role in the load-transfer mechanism. Characterization of the three-dimensional web crushing behavior is therefore essential in order to evaluate the web crushing capacity of piers along non-principal directions of the cross section.

1.2 High-strength-concrete in seismic regions

Modern concrete manufacturing technology has made the industrial production of high-strength-concrete (HSC) up to 138 MPa (20 ksi) available with the evolution of the silicon fume and chemicals of retarders, superplasticizers, etc. There is no doubt that the use of HSC will continue to increase. However, the lack of the design provisions, especially for the use of HSC in seismic design prompts the need for research in this area.

On one hand, the application of HSC could make the designed structural components be more slender by reducing the cross-section dimensions and by consequence reduce seismic mass and reduce the size and cost of substructure units. The compactness and low creep and shrinkage of HSC would improve the durability of the structures under various weather conditions. On the other hand, HSC could jeopardize the ductility level of the structures in seismic regions due to the rapid strength degradation within a small strain range. Therefore, careful evaluation is needed in order to satisfy functional and safety seismic design criteria. Moreover, premature cracking of HSC elements needs appropriate evaluation to satisfy performance-based requirements.

1.3 In-plane Web Crushing Behavior

A membrane panel under uniform shear stresses along all sides will exhibit parallel shear cracking in the diagonal direction. With the occurrence of axial compression stresses, the cracking angle tends to be less than 45º from the vertical. Web crushing will happen when the compression capacity of the strut is reached. This mechanism, consisting of web crushing failure with parallel shear cracking can be referred to as an "elastic web crushing failure." Structural walls that fail in such kind of mechanism have very limited deformation capacity. Thus, current shear design provisions restrict elastic web crushing failures by providing specifications on the configuration of the transverse steel and thus limit the shear strength of the walls by a diagonal tension failure, which can be seen reviewing the ACI-318 shear design provisions.

Recent research has revealed that structural walls with flanges or boundary elements develop a fanning crack pattern in the plastic hinge region under moderate or large inelastic deformations. It has also been noticed that with the increase of the deformation demand, the diagonal cracks realign in the region of the web next to the compression boundary element. When walls experience large rotations the lower struts become less effective in their load transfer efficiency. Consequently, the realignment of crack results in the formation of a small region with high compressive stresses where web crushing tends to happen. In this study, the web crushing failure mechanism with realigned fanning crack pattern is referred to as an "inelastic web crushing failure".

The just described elastic and inelastic shear cracking patterns can observed in Figure 1.2, which shows a cantilever structural wall test unit that failed by web crushing. The realigned fanning cracks in the plastic hinge region are highlighted, while a strut formed by elastic shear cracking in the web above the plastic hinge region is also highlighted. It can be seen that the flexural cracking on the tension boundary element appears to be flat. In the inelastic shear cracking region of the web, the change of the crack angle can be observed by comparing the inclination of the bottom and top edges. It is reasonable to assume that the smaller the crack angle from the vertical is, the more efficient the strut work to transfer the load from the tension boundary element to the compression boundary element. However, with inelastic deformation and the development of the plastic hinge length the cracking close to the base realigns due to the evolution of the flexural cracking into the web. Thus, the inelastic shear cracking develops due to the combination of the flexure and shear effect. The term of "flexure-shear effect" is thus used in this study to refer to such behavior. This effect makes the struts near the wall base less effective in load transfer since the crack angle (about the vertical) is increasing. Hence, the top-most strut in the inelastic shear region next to the elastic shear cracking region is the most efficient but critical strut for limiting web crushing, as is shown in Figure 1.2 (c).

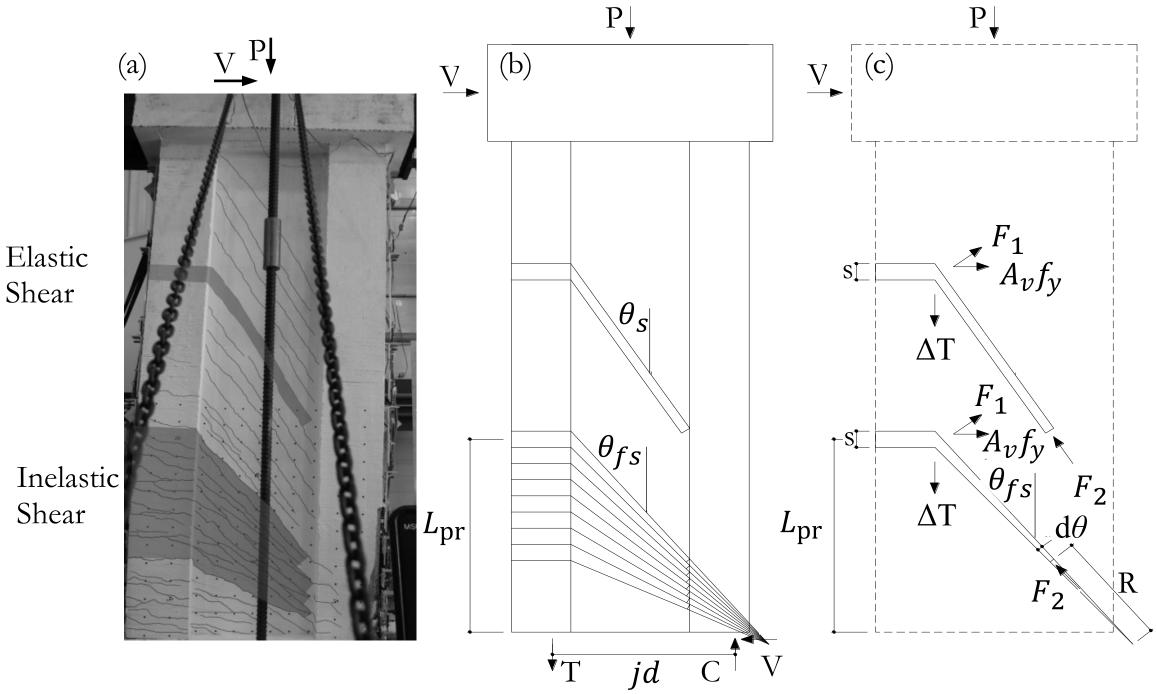

Figure 1.2 Flexure-shear and elastic shear mechanisms: (a) In test wall, (b) Sketch of the regions, (c) Truss models.

However, it has been observed that actual critical region limiting web crushing under cyclic loading may be different. For cyclic loading the failure tends to happen at the height level of the bottom strut in the fanning pattern. It is hypothesized that this is due to the criss-crossed cracking induced by the cyclic loading. For HSC structural walls, the web experiences more densely-distributed cracking due to the brittle nature of concrete. Thus, the concept of well-defined critical struts is more of an ideal assumption than an experimental observation.

1.4 Diagonal Web Crushing Behavior

The web crushing capacity of wall assemblies is complicated due to the spatial distribution of boundary elements and connecting walls. In addition to the response along the principal directions (along the sides), the web crushing capacity along non-principal, or diagonal, directions is of interest in order to characterize the three-dimensional failure behavior. Under loading in the diagonal direction, extreme and intermediate boundary elements with respect to a non-principal axis of bending will be in tension while as little as one element may be in compression. The existence of intermediate boundary elements with respect to the line of bending will disturb and separate the wall shear cracking. In this study, the evaluation of web crushing for wall assemblies was evaluated within the context of a square hollow pier with corner boundary elements. It has been observed the response of such pier units under diagonal loading will cause the crack angle of the tension wall to have a bigger cracking angle from the vertical; while in the compression side the cracking angle is smaller. The coexistence of large tensile stresses due to flexure with the shear demands is the reason for the cracking being relatively flat. The determination of the distribution of the shear stress on the walls between the tension boundary elements (back walls) and the walls between intermediate and compression boundary elements (front walls) is the main issue. It is reasonable to assume that the front walls carry more shear stress than the back walls. Nonetheless, further investigation is needed in order to analyze the diagonal, or non-principal, web crushing capacity of wall assemblies.

1.5 In-plane Cyclic Loading Effect

It seems straightforward to assume that web concrete in structural walls will degrade more under cyclic loading than monotonic loading. Some research has been conducted to study the damage of concrete under complicated stress states with loading history considered. However, further investigation is needed on the degradation of HSC under cyclic loading.

1.6 Multi-directional Loading Effect

The vulnerability of structures subjected to earthquake motions along random directions makes the performance evaluation of wall assemblies under multi-directional loading necessary. Although noteworthy research has been done on the behavior of rectangular hollow bridge piers under biaxial loading, most of it was focused on assessing biaxial flexural behavior and slenderness limits [11]. Mo et al. [12] studied the seismic performance of hollow bridge columns under uni-directional cyclic loading. Takizawa et al. [13] and Bousias et al. [14] studied the biaxial flexural behavior of pier columns under various loading patterns with the aim of establishing the interaction, or coupling, effects between the two perpendicular directions. Hines et al. [1][2] conducted two proof-of-concept tests on a typical hollow rectangular skyway pier of the new San Francisco-Oakland Bay Bridge (SFOBB), which focused on evaluating a pier design with highly-reinforced boundary elements and connecting walls subjected to uni-directional and bi-directional cyclic loading. All of the noted efforts were related to the flexural behavior of the hollow rectangular piers, which can be seen as a closed assembly of walls with corner boundary elements, and none of them considered shear demands and shear failure modes under multi-directional loading. A related investigation related to shear behavior is the work by Wong et al. [15] who studied the ductility level and different failure modes of circular columns with an aspect ratio of 2. Test results revealed that biaxial displacement patterns led to severe strength and stiffness degradation compared to uniaxial displacement and that shear failures with moderate ductility could be achieved. Thus, even though the mechanisms behind inelastic plane shear web crushing have been reported for some time [5][6][7][16][17], as is described in Section 3.4, the three-dimensional shear resistance and failure mechanisms of wall assemblies and hollow rectangular bridge piers is still not fully investigated.

1.7 Objectives

The objective of the study on the in-plane web crushing capacity of the structural walls is to examine the use of high-strength-concrete (HSC) to obtain ductile shear failure behavior and evaluate the hypothesis that web crushing capacity is related to concrete compressive strength f_c' instead of the $\sqrt{f_c'}$. The approach is non-intuitive as web crushing is a brittle failure and it is well known that concrete becomes more brittle as its compressive strength increases. The effect of cyclic loading on concrete damage, structural strength/stiffness degradation, and web crushing capacity is to be evaluated. The appropriate performance evaluation on HSC structural walls exhibiting ductile shear failure is expected to contribute to the groundwork of the next stage in earthquake resistant design of thin-webbed elements and systems. Moreover, the study of web crushing as a fundamental shear failure mechanism can have potential impact on present shear design provisions.

The objective of the study on wall assemblies is to examine the application of HSC to achieve ductile shear failure behavior, evaluate the diagonal web crushing capacity and the concrete degradation under multi-directional effect in order to fully evaluate seismic performance. The behavior of wall assemblies is to be studied within the context of hollow square bridge piers, which are composed of a closed arrangement of walls with corner boundary elements. The study is aimed at corroborating that HSC can increase the web crushing capacity of wall assemblies, to determine the three-dimensional shear demands on wall webs, and to assess the effect of multi-directional loading on the degradation of the shear web crushing resisting mechanism. The diagonal web crushing capacity will be evaluated and analyzed, which can be further applied on the analysis of the three-dimensional walls with cross sections in other shapes.

1.8 Approach

1.8.1 Experimental studies on single structural walls

The in-plane seismic performance of single HSC structural walls featuring highly-reinforced boundary elements and a thin constrained web was evaluated through experiments on eight 1/5-scale single walls designed with concrete compressive strengths of 34, 69, 103, and 138 MPa (5, 10, 15 and 20 ksi) and tested under cyclic and monotonic loading protocols. The objective of this study was to evaluate the effect of concrete strength on the web crushing performance limits of HSC structural walls. The web crushing behavior of the structural walls with the same design concrete compressive strength but under different loading protocols: monotonic and cyclic loading, was compared to identify the seismic effect on the ductility level of the walls. The experimental results demonstrated that high-strength-concrete can effectively delay web-crushing failures and increase the displacement ductility levels of the structural walls. However, web crushing capacity was significantly curtailed due to the rapid shear strength and stiffness degradation under cyclic loading. Nonetheless, ductile shear failures were still attained for HSC structural walls up to intermediate displacement ductility levels.

1.8.2 Experimental studies on wall assemblies

To address the knowledge gap on the shear response of wall assemblies and evaluate the potential of HSC to allow for ductile shear failures as an acceptable inelastic failure mechanism on such systems, two 1/4-scale hollow square bridge piers subjected to multi-directional cyclic loading with design concrete compressive strengths of 34 and 138 MPa (5 and 20 ksi) were tested. The three-dimensional inelastic web crushing behavior was evaluated from observations and measured hysteretic force-displacement behavior. Loading path effects on web crushing capacity and the degradation of shear stiffness and energy dissipating capacity were quantified. Test results support that HSC can delay web crushing shear failures, thus allowing for the dependable inelastic response of hollow bridge piers. However, the mixed flexure-shear cracking under multi-directional loading causes rapid shear stiffness degradation, an effect that is amplified for HSC due to its lower fracture toughness, which curtails the web crushing resistance capacity of the wall assembly.

1.8.3 Nonlinear finite element modeling

Nonlinear finite element modeling (NLFEM) was conducted to assist in the understanding the web crushing behavior of the structural walls and bridge piers. This study gave an appropriate evaluation on the capacity and limits of present finite element tools in evaluating the flexure and shear force-displacement behavior and capacity of reinforced concrete walls. The study provided quantitative data on the stress and strain state of the web crushing region and assisted the development of simplified analytical models.

1.8.4 Simplified analytical modeling

A simplified analytical method based on test observations and a truss analogy approach was developed to study the web crushing capacity of the HSC structural walls and hollow bridge piers. The inelastic web crushing model by Hines and Seible formed the basis for this task. However, the model was modified based on the learned response of HSC walls. The test results from prior tasks in this study were be used to calibrate the model.

1.9 Scope

This study focuses on the web crushing behavior and assessment of HSC structural walls and the potential to define ductile shear failure as a viable failure mechanism for seismic design. As such, the work aims to demonstrate that the traditional opinion that shear failure mechanisms are inferior in seismic performance is not always true and that a dependable ductile failure mechanism ultimately limited by shear (web crushing) is possible. To evaluate and analyze the web crushing capacity of the in-plane structural walls and wall assemblies, the scope of this study was divided into four tasks: First, the in-plane web crushing behavior of the HSC structural walls was investigated through experiment to corroborate that ductile web crushing behavior can be achieved. Second, to evaluate the seismic performance of the HSC wall assemblies, the diagonal web crushing behavior and accumulation of concrete damage under multi-directional loading effect was investigated through hollow pier tests. Third, nonlinear finite element modeling was conducted to assist in the understanding the test observations and results both phenomenologically and quantitatively. Finally, a simplified analytical method is proposed to the engineering field for design purposes.

1.10 Organization

The dissertation has been organized into eight chapters. Chapter 1 provides the motivation of this study, and then highlights the key research aspects of high-strength-concrete in seismic regions, in-plane web crushing behavior, diagonal web crushing behavior, in-plane cyclic loading effects and multi-directional loading effects. The objective of the study is addressed followed by the research approach, with the combination of the experimental methods on structural walls and hollow bridge piers, nonlinear finite element modeling and the simplified analytical method for design.

Chapter 2 reviews general shear strength models and the shear design provisions of US codes. The web crushing capacity models of Oesterle et al., Paulay and Priestley and Hines et al. are reviewed and discussed. The theories and implementation of the finite element approaches used in the work are presented. Finally, the research hypothesis of this study is introduced.

Chapter 3 reports on the experimental studies of web crushing performance of in-plane loaded HSC structural walls. The experimental investigation on single wall test units is described, including details of materials, instrumentation, and loading protocols. Experimental observations and results are described followed by discussion and conclusions.

Chapter 4 reports on the experimental studies of HSC hollow bridge piers. The wall-assembly test units, materials, test setup, instrumentation and loading protocol are described. Experimental results are provided, followed by discussion and conclusions.

Chapter 5 presents the study on nonlinear finite element modeling of HSC structural walls. A general commercial nonlinear finite element program (ABAQUS) and a research nonlinear finite element analysis for reinforced concrete membrane structures (VecTor2) were used to model the web crushing behavior of the structural walls under monotonic loading and cyclic loading. The analyses are described in the sequence of geometrical modeling, definition of material properties, solution controls and results. Discussions and conclusions on the results and the applicability and limitations of the noted numerical tools to capture the inelastic response of reinforced concrete walls are provided.

Chapter 6 reports on a simplified analytical method to assess the web crushing capacity of structural walls based on the inelastic web crushing model by Hines and Seible. A modification to the approach by Hines and Seible is proposed to calculate the softening of web concrete. The modified model is assessed by comparing its prediction to the experimental response of the HSC structural walls tested in this study. A discussion and conclusions are provided at the end.

Chapter 7 describes a simplified analytical method to assess the diagonal web crushing capacity of HSC hollow bridge piers. An equivalent single wall in the diagonal direction was exacted and analyzed. The modified Hines model presented in Chapter 6 was implemented for the three-dimensional web crushing capacity analysis.

Finally, Chapter 8 provides a summary of the research findings, the original contributions and research impact of the study, and the future research needs.

Chapter 2. **Literature Review and State-of-the-art**

2.1 Summary

In this chapter, an approach for estimating the force-displacement behavior of reinforced concrete structural walls is described first. Then, a historical review of shear strength models is provided. The shear design provisions of US codes are reviewed with the maximum allowable design shear stress being emphasized. The web crushing capacity analytical methods of Oesterle et al., Paulay and Priestley and Hines and Seible are reviewed and discussed. With respect to the nonlinear finite element modeling (NLFEM) effort, the Modified Compression Field Theory (MCFT) and the implementation of NLFEM in the program VecTor2; and the continuum damage plasticity theory for concrete implemented in the program ABAQUS are described. Finally, the research hypothesis of this study is presented.

2.2 Force-Displacement Behavior of Structural Walls

The deflection of a cantilever member can be calculated by integrating the curvatures along the height of the member [18] by:

$$\Delta = \int_0^L x\varphi dx \tag{2-1}$$

where L is the height of the cantilever member; and x is the distance of to an infinitesimal segment of length dx from the free end. The tip deflection of an element can thus be calculated based on the moment-curvature relationship of its cross-section. Equation (2-1) is usually simplified based on the idealization of a linear curvature distribution in the elastic and inelastic regions. For this simplification, the inelastic, or plastic, curvatures are taken to be linearly distributed over an equivalent plastic hinge length, L_p. The estimate of plastic rotations and plastic deformations of a member is highly relied upon for the definition of the plastic hinge length L_p.

In this study, the approach proposed by Hines et al. [19] was used to calculate the plastic hinge length and the force-displacement behavior of structural walls. Three distinct phenomena affecting the spread of plasticity in reinforced concrete members are considered: moment gradient, tension shift, and strain penetration. Assuming that plastic rotation occurs about the column base, L_p is evaluated as

$$L_p = \frac{L_{pr}}{2} + L_{sp} \tag{2-2}$$

where L_{pr} is the length of the plastic hinge region (or extent of plasticity); and L_{sp} is the length of the strain penetration (or bond slip region). L_{pr} is calculated as:

$$L_{pr} = \sqrt{\frac{2(T - T_{yav})jd}{\left(\frac{A_v f_v}{s} + f_1 t_w\right)}} \tag{2-3}$$

The displacement of the wall up to the first yield is calculated as:

$$\Delta = \phi L\left(\frac{L}{3} + 2L_{sp}\right)\left(1 + \frac{\Delta_s}{\Delta_f}\right) \tag{2-4}$$

After first yield, the displacement is calculated as:

$$\Delta = \Delta'_{\mathrm{y}}\frac{M}{M'_y} + \left(\phi - \phi'_y\frac{M}{M'_y}\right)L_p L\left(1 + \frac{\Delta_s}{\Delta_f}\right) \tag{2-5}$$

where L_{sp} is equal to $0.15 d_b f_y$, d_b and f_y are the diameter and yield strength of the longitudinal steel. The ratio of the flexural to shear deformations was taken as 0.24 based on the single wall tests by Hines et al. [17] and this study described in Chapter 3 [8]. The values for Δ'_y, M'_y and ϕ'_y are the corresponding values of displacement, moment and curvature at first yield, defined as the first occurrence of yield in the extreme steel bar in tension.

2.3 Historical Overview of Shear Strength Models

The equivalent truss model was been widely used since the 1900's to understand the shear behavior of reinforced concrete beams with transverse reinforcement. The 45º truss model was developed by Ritter in 1899 [20] and refined by Mörsch in the 1920's [21][22]. In 1907, Withey introduced the 45º truss model to the US and reported that compared to experimental results, the model is conservative [23]. In the late 1950's, the 45º truss model was also applied to prestressed concrete structures.

In 1962, the ACI-ASCE Joint Committee 326 on shear and diagonal tension recommended an empirical equation for the shear strength contributed by concrete [24], which is still used in ACI-318-08 [25].

$$v_C = \left(1.9\sqrt{f_C'} + 2500\rho_W \frac{V_u d}{M_u}\right) \tag{2-6}$$

In 1974, Collins and Mitchell developed the compression field theory (CFT) where equilibrium equations, compatibility for averaged concrete and reinforcement strains, and a constitutive relationship for cracked concrete and reinforcement are considered [26][27]. Since CFT is still a truss model, no shear stress transfer at the crack interface is considered and the concrete tensile constitutive relationship is neglected.

In 1986, the modified version of CFT, the modified compression field theory (MCFT) is proposed by Vecchio and Collins [28]. In this refined model, shear stresses at cracks are estimated and concrete tension stiffening effects are included. After parametric calibration with a series of membrane tests, MCFT represents a robust model to predict the shear force-displacement behavior of reinforced concrete members.

Similar to the concept of MCFT, in the 1990's, Hsu et al. developed the rotating-angle softened-truss model (RA-STM) [29][30] and the fixed-angle softened truss model (FA-STM) [31]. The development of these approaches deviates from the MCFT in that no assumption is made with regards to the principal stress and strain directions of stress in the concrete. However, the models are similar in considering a bi-axial state of plane stress on a reinforced concrete element and enforcing equilibrium and compatibility requirements for the cracked reinforced concrete. In this study, the general framework of the MCFT is used.

2.4 US Code Provisions for Shear

2.4.1 ACI-318-08 Shear Provisions

In ACI-318-08 [25], except for prestressed members and members designed based on strut-and-tie models, the nominal shear strength, V_n, is computed as the sum of the contributions from concrete V_c and shear reinforcement V_s, that is,

$$V_n = V_c + V_s \tag{2-7}$$

For normal weight concrete walls subject to axial compression

$$V_c \leq 2\sqrt{f_c'}hd \tag{2-8}$$

unless a more detailed calculation is made. Because of the lack of test data and practical experience on high-strength-concrete (HSC), mainly with compressive strength over 10,000 psi, a maximum value of 100 psi has been placed on $\sqrt{f_c'}$ since the 1989 edition of the code.

The shear strength provided by steel is calculated based on the 45° truss model and is expressed by:

$$V_s = \frac{A_v f_y d}{s} \tag{2-9}$$

Even though there is no explicit limit of $8\sqrt{f_c'}$ on V_S as in ACI-318-02, the same limit on V_n is maintained, that is,

$$V_n \leq 10\sqrt{f_c'}hd \tag{2-10}$$

However, it is admitted in the commentary of the corresponding provision that shear stresses in excess of $10\sqrt{f_c'}$ can be obtained.

2.4.2 AASHTO Standard Specifications for Highway Bridges

The AASHTO Standard specifications [32] follow essentially the same shear design provisions of ACI-318 on reinforced concrete members. The maximum allowable limits on shear stresses from ACI-318 are maintained.

2.4.3 AASHTO LRFD Bridge Design Specifications

Since 1994, the Sectional Design Model based on the Modified Compression Field Theory (MCFT) has been introduced into US bridge design practice [33]. When using the model, the axial strain in the member at mid-height is evaluated under the effect of axial load, moment, prestressing, and shear. The strain and the shear design stress level are used to select values of the coefficients β and θ from tables. These values, obtained by calculations from the CSA method [34], control the contributions of concrete and steel to the shear resistance. The sectional design model is more complicated than the shear design provisions in AASHTO's Standard Specifications, which often requires an iterative solution.

Equation (2-7) is still valid for non-prestressed members. The concrete contribution of shear forces is calculated as:

$$V_C = 0.0316\beta\sqrt{f_c'}b_v d_v \tag{2-11}$$

The contribution from the shear reinforcement is calculated based on the parallel chord truss model with the cracking angle θ being a variable,

$$V_s = \frac{A_v f_y d_v cot\theta}{s} \tag{2-12}$$

With the shear design stress ratio (v/f_c') and the longitudinal strain ε_x at mid-height of the cross section, the values of β and θ can be obtained from a table.

The nominal shear resistance V_n has an upper limit, defined by

$$V_n = 0.25 f_c' b_v d_v \ . \tag{2-13}$$

2.4.4 Discussion

Historically, the 45° truss model for the analysis of cracked reinforced concrete members was been widely used since the early 1900's. The corresponding ACI shear strength provision of Equation (2-6) came into shape in 1960's, and shortly after the 45° truss model was re-examined since it is overly conservative. It is thought-provoking to notice that the same model is still in use in the up-to-date design provisions in the twenty-first century.

There are two types of shear cracking that may take place in reinforced concrete beams, which are described in ACI-318, and can be referred to for the cracking response of reinforced concrete walls. One is web-shear cracking and the other is flexure-shear cracking. Web-shear cracking begins from an interior point in the web when the principal tensile stresses exceed the tensile strength of the concrete. Flexure-shear cracking is initiated by flexural cracking. When flexural cracking occurs, the shear stresses in the concrete above the crack are increased. Flexure-shear crack develops when the combined shear and tensile stresses exceed the tensile strength of the concrete. For the structural walls in this study, web-shear cracking happened at half the load required to produce flexural yielding in the extreme tensile reinforcement. With increasing displacement demand flexure-shear cracks develop and crack-realignment was observed.

It can be seen that ACI-318 shear provisions are oriented and aimed at diagonal tensile cracking and failure. The possibility of the web crushing failure is not considered when diagonal tension failure is well resisted in a conservative design. Since the code does not reflect the direct dependence of web crushing capacity on f_c', but rather limits shear demand based on $\sqrt{f_c'}$, the application of the shear provisions on evaluating the web crushing capacity of the walls is problematic. Moreover, the lack of experience and experimental data on the application of HSC hinders the possible efficient design of reinforced concrete elements limited by web crushing failure.

In AASHTO LRFD, a maximum allowable shear stress of $0.25f_c'$ is prescribed, which is very different from the recommendations in ACI-318-08 and the AASHTO Standard Specifications. This difference is more significant with the increase of concrete compressive strength. As is the case in the ACI-318 recommendations, the upper limit is intended to avoid web crushing failure such that diagonal tension failure occurs first. It is also specified in the AASHTO LRFD Specifications that for concrete strengths over 10.0 ksi, physical tests or specific articles are needed to establish the relationships between the concrete strength and other properties.

Figure 2.1 shows the analytical force-displacement responses [19] of the test units, with varied nominal concrete strengths from 5 ksi to 20 ksi and the corresponding lines for the ACI-318 shear stress limits. The description of the test unit is included in Section 3.2. The values of the lines are calculated purely according to $10\sqrt{f_c'}$ and the limit of 100 psi on $\sqrt{f_c'}$ is not applied. It may be deceiving to see that the ACI-318 limit gives a conservative estimate to the ideal capacity of the walls. However, two aspects need to be pointed out. First, that the force-displacement response is an analytical prediction of the inelastic flexural response of the wall and does not consider shear failure. Second, the estimate will be considerably in error if the limit of 100 psi on $\sqrt{f_c'}$ is applied. It should be further noted that the force-displacement responses are essentially unchanged as the flexural response is dictated by the longitudinal reinforcement in the boundary elements and not the concrete compressive strength. This follows from the heavy reinforcement in the boundary elements in the test units in this study. The heavily reinforced boundary elements are necessary to develop the necessary shear stress in the wall web and properly anchor the diagonal shear struts in the compression toe of the wall. The increase of the moment capacity with HSC is thus not significant.

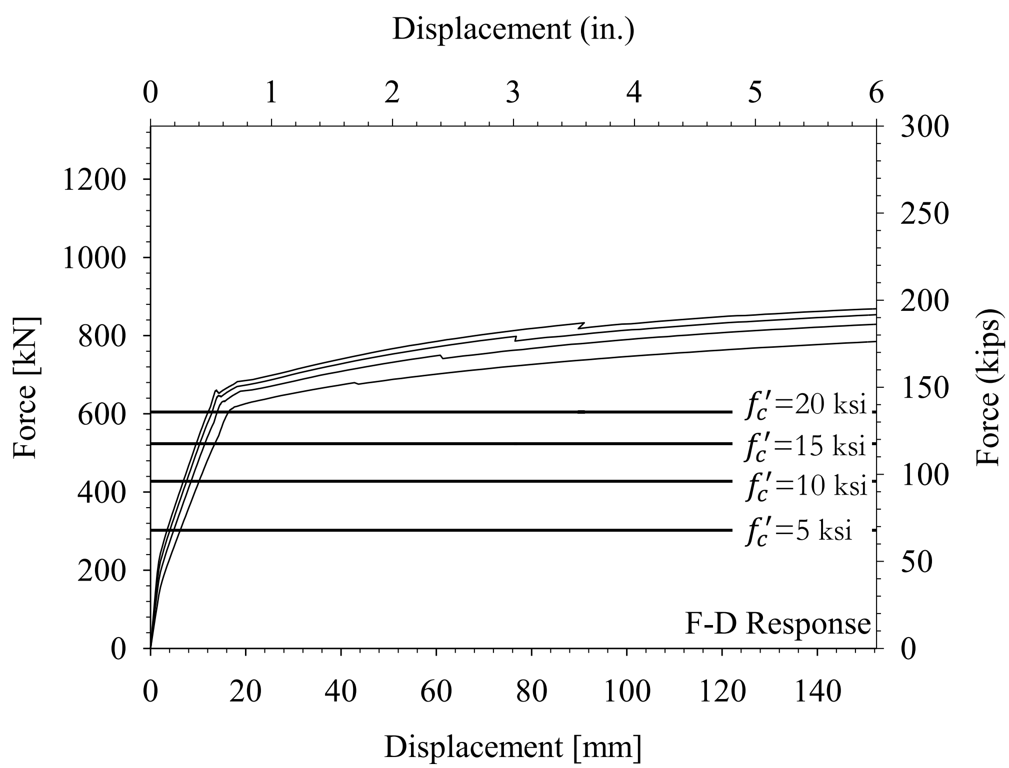

Figure 2.1 Analytical force-displacement responses of the single walls with ACI-318 shear stress limits.

2.5 *Web Crushing Capacity Models*

2.5.1 Oesterle et al.

The research results by Oesterle et al. based on the experiments conducted by Portland Cement Association (PCA) on structural walls [4][5] failing in web crushing are summarized in this section.

Among the tested walls with flanged, barbell and rectangular cross sections, only flanged and barbell walls were found to exhibit web crushing. From this observation, it can be seen that the concentration of the resultant tension and compression forces is necessary to form the load-transfer mechanism of the strut-and-tie model with the web demanded in diagonal compression.

A fanning crack pattern in the plastic hinge region was observed on the walls. It was also noticed that with the increase of the deformation demand, the diagonal cracks realigned in the region of the web next to the compression boundary element. When specimen experienced large rotations, the lower struts become less effective in load transfer. The realignment of cracks resulted in the formation of a small region with high compressive stresses where web crushing tended to happen.

An average effective compressive strut strength of 0.16~0.49f_c' was obtained based on the PCA wall tests. This value is deemed to be too low since a truss analogy with parallel cracking and no realigned cracking was considered in its development. In view of this, the calculation of the concrete softening parameter κ proposed by Collins [27],

$$k = \frac{3.6}{1+2\gamma_m/\varepsilon_0}, \tag{2-14}$$

is not applicable for the inclined struts with realigned cracking geometry being considered.

The web crushing model by Oesterle et al. relate the shear strength $v_{\omega c}$ to the drift ratio within the plastic hinge region, δ, by:

$$v_{\omega c} = \frac{1.8f'_c}{1+420\delta} \text{ when } \frac{N}{A_g f'_c} > 0.09 \qquad \text{(2-15a)}$$

$$v_{\omega c} = \frac{1.8f'_c}{1+\left(600-2000\frac{N}{A_g f'_c}\right)\delta} \text{ when } 0 > \frac{N}{A_g f'_c} > 0.09 \qquad \text{(2-15b)}$$

where $v_{\omega c}$ is the nominal shear stress at web crushing, $v_{\omega c} \leq 0.18f'_c$, f'_c is the concrete compressive strength, N is the applied axial load, and A_g is the gross cross sectional area. $\delta = \Delta/L_p$, where Δ is the total deformation at the top of the plastic hinge region, L_p is the length of the plastic hinge region.

Discussion

Figure 2.2 shows the analytical force-displacement responses [19] of the test units, with varied nominal concrete compressive strengths from 5 ksi to 20 ksi and the corresponding web crushing capacity curves as predicted by the model of Oesterle et al. The description of the test unit is included in Section 3.2. It can be seen that the failure models provide a more realistic dependence of web crushing capacity with inelastic deformation, where as deformations increase, the web crushing capacity decreases. The shift of the capacity curves with increasing concrete compressive strength is also obvious. It should be noted, however, that the plotted curves have not implemented the limit proposed by Oesterle et al., for the compressive struts of 0.16~0.49f'_c, which would lead to dramatically conservative capacity estimates.

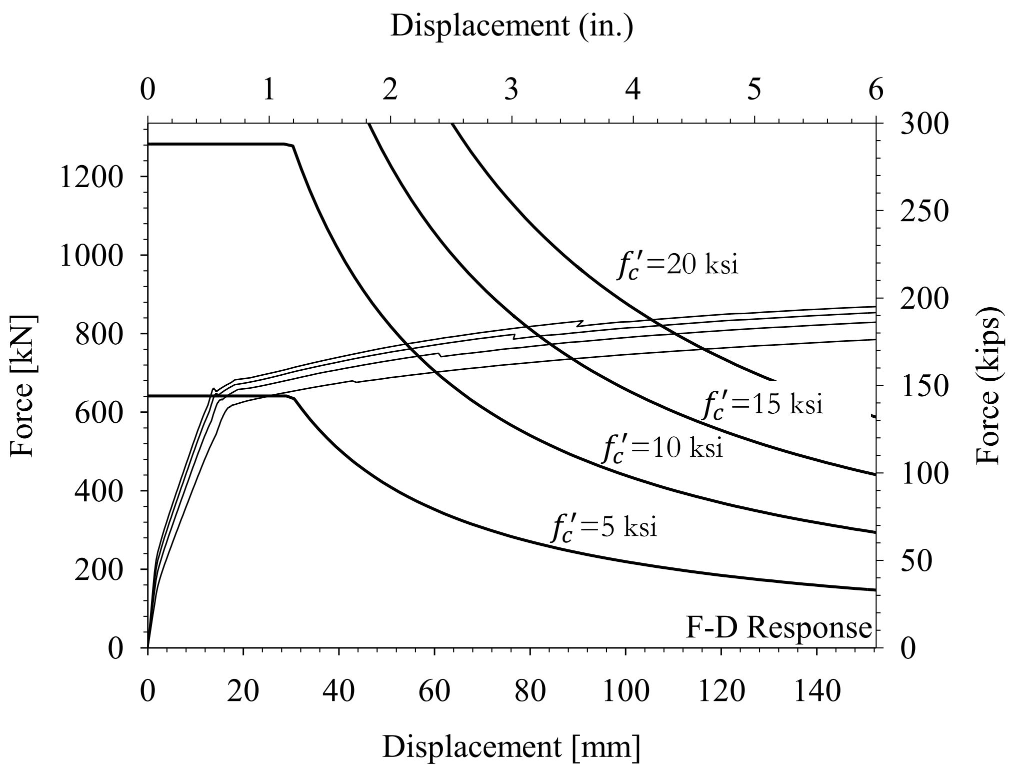

Figure 2.2 Analytical force-displacement responses of the single walls with web crushing capacity curves of Oesterle et al.

2.5.2 Paulay and Priestley

To prevent premature diagonal web crushing failure from occurring before the yielding of the shear reinforcement, a nominal shear stress is limited of $v_i \leq 0.16f_c'$ in the plastic hinge regions of beams, columns, and walls was proposed by Paulay and Priestley [7]. It was realized from tests at PCA [5] and at the University of California, Berkeley [6], that web crushing in the plastic hinge region could happen at displacement ductility levels of 4 or more. When displacement ductility is equal to or less than 3, a shear stress over $0.16f_c'$ could be achieved. Paulay and Priestley [7], thus proposed a shear design equation that indicates that web crushing capacity is directly proportional to concrete strength but degrades with increased ductility:

$$v_{\omega c} = \left(\frac{0.22}{\mu_{\Delta}} + 0.03\right) f_c' \leq 0.16 f_c' \tag{2-16}$$

where μ_{Δ} is the displacement ductility ratio and f_c' is the concrete compressive strength.

Discussion

Figure 2.3 shows the analytical force-displacement responses [19] of the single wall test units from this research, with varied nominal concrete compressive strengths from 5 ksi to 20 ksi and the corresponding web crushing capacity curves from the model of Paulay and Priestley. The description of the test unit is included in Section 3.2. As discussed for the Oesterle et al. model, the Paulay and Priestley model appropriately capture an increasing web crushing shear strength with increasing concrete compressive strength and a degradation of this capacity with increasing inelastic deformations. However, the plotted curves were also removed from the proposed stress limit by Paulay and Priestly, which, if plotted would lead to highly conservative estimates of shear strength. Compared to the mode by Oesterle et al, the model by Paulay and Priestley is more conservative. The reason is that the Paulay and Priestley model was intended mainly for design purposes while the model by Oesterle was calibrated for assessment based on the test data from the PCA wall tests.

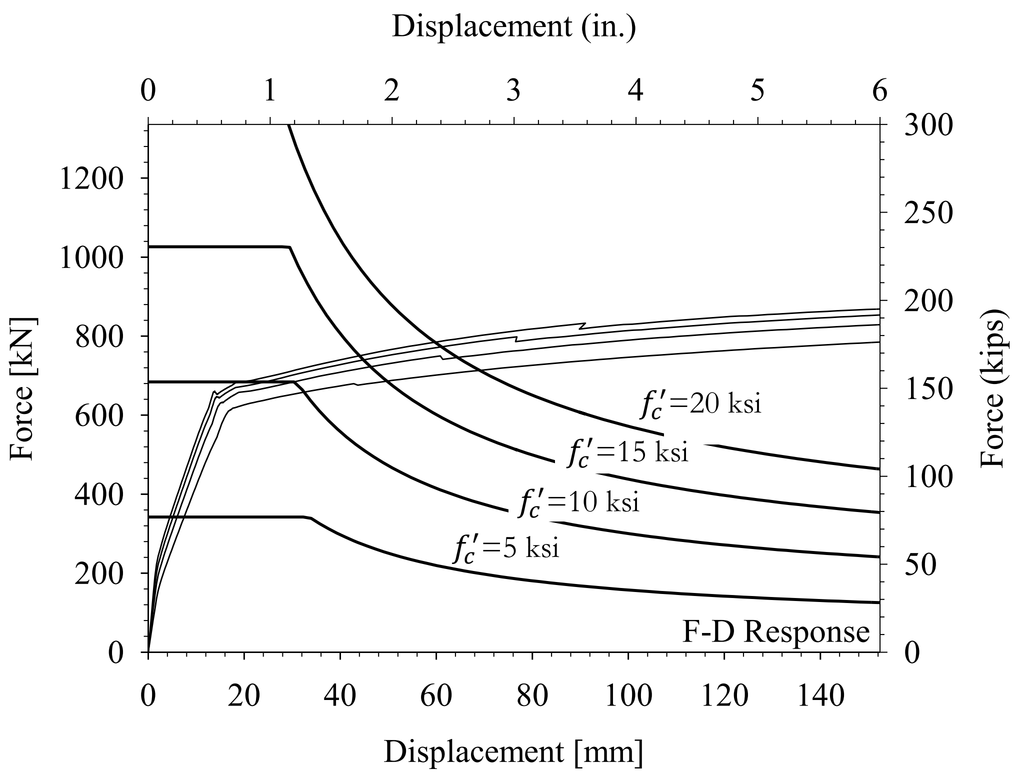

Figure 2.3 Analytical force-displacement responses of the single walls with web crushing capacity curves of Paulay et al.

2.5.3 Hines and Seible

The recent study by Hines and Seible [16] recognized a clear distinction in assessing the capacities of elastic and inelastic web crushing based on the mechanisms noted in Figure 1.2. A flexure-shear model based on a truss analogy and the observed fanning crack pattern inside the plastic hinge region was proposed, compared to an elastic and parallel shear cracking pattern outside the hinge region. The demand of the critical strut in flexure-shear (N_{Dfs}) as well as the strut in elastic shear (N_{Ds}) was assessed based on equilibrium consideration of the shown free body diagrams. The capacity of the critical flexure-shear struts (N_{Cfs}) was derived based on an appropriately formulated length of the plastic hinge region (L_{pr}), a concrete compression softening factor (κ) calculated based on the modified compression field theory (MCFT) [28] and the estimated radius (R) for the critical compression strut fan.

The dimension of the strut in the elastic shear region is determined based on the vertical width of the strut generated from flexure cracks at a spacing equaling the transverse steel (s). The dimension of the critical strut in the inelastic shear region is determined based on the spacing of the transverse steel on the tension boundary element with its width at the tension side defined through the calculation of the angle between the edges of the strut ($d\theta$). The derivation of the demand and the capacity of the strut in the elastic shear region are shown in below.

The resultant tensile force on the strut (ΔT) is calculated through by moment equilibrium of the strut,

$$\Delta T = scot\theta_{fs}\left(\frac{A_v f_v}{s} + f_1 t_w\right) \tag{2-17}$$

The demand on the strut, N_{Dfs} can be calculated by considering force equilibrium in the vertical direction,

$$N_{Dfs} = \frac{\Delta T}{cos\theta_{fs}} - f_1 s t_w sin\theta_{fs} \tag{2-18}$$

The inelastic shear crack angle θ_{fs} is calculated based on the estimate of the length of the plastic hinge region (L_{pr})

$$cot\theta_{fs} = \frac{L_{pr}}{jd} \tag{2-19}$$

where L_{pr} is calculated as [19]

$$L_{pr} = \sqrt{\frac{2(T - T_{yav})}{\frac{A_v f_v}{s} + f_1 t_w}} \tag{2-20}$$

To calculate the capacity of the strut N_{Cfs}, the width of the strut next to the compression boundary element ($Rd\theta$) and the concrete softening parameter κ due to the coexistence of the tensile are evaluated:

$$N_{Cfs} = \kappa t_w R d\theta \tag{2-21}$$

where $d\theta$ and R are estimated based on the development of the fanning crack pattern along the height of the plastic hinge region,

$$d\theta = cot^{-1}\left(\frac{L_{pr} - s}{jd}\right) - \theta_{fs} \tag{2-22}$$

$$R = \frac{(x + D_b - \frac{t_w}{2})}{sin\theta_{fs}} \tag{2-23}$$

The influence of the concrete softening parameter, which controls the decay of the capacity curve with inelastic deformations, is discussed further in Chapter 6.

<u>Discussion</u>

Figure 2.4 shows the analytical force-displacement responses [19] of the test units, with varied nominal concrete compressive strengths from 5 ksi to 20 ksi and the corresponding web crushing capacity curves of Hines and Seible. The description of the test unit is included in Section 3.2. It can be seen that the web crushing capacity is predicted to increase dramatically with an increase of concrete strength and the capacity is properly predicted to decay with inelastic deformations. It should be noted that the maximum stress limit of $0.3f_c'$ has been applied on the capacity curves. This threshold is much less conservative than that proposed by Oesterle et al. and Paulay and Priestley.

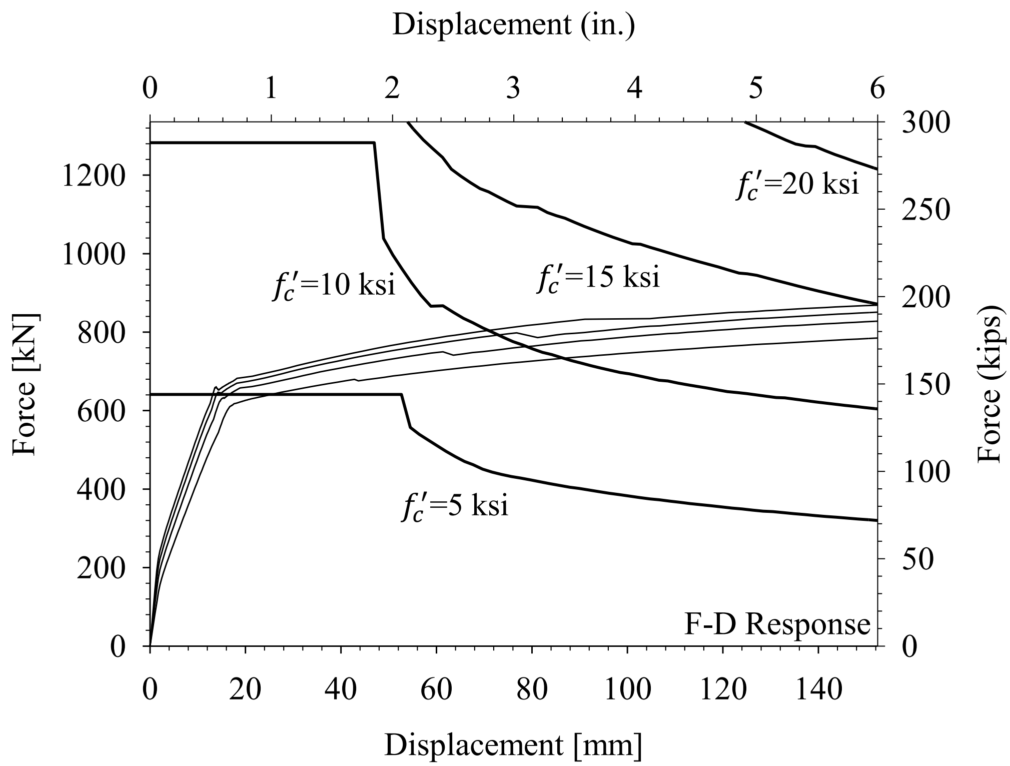

Figure 2.4 Analytical force-displacement responses of the single walls with web crushing capacity curves of Hines and Seible

2.5.4 Discussion on Truss Models

The truss analogy is a simple in concept and seems easy to be implemented. However, the evaluation of compressive strength of the critical strut entails the evaluation of the strength of the damaged concrete material. This requirement is quite complicated when considering the cyclic loading effects since the diagonal struts will experience cracking in two directions upon load reversal. Thus, the evaluation of the compressive strength of the struts cannot be appropriate until the effect of cyclic loading and crack width are fully considered. In view of these difficulties, ACI 318-08 considers the shear strength of structures to be related to the square root of the f'_c with an upper-bound limit. However, the degradation of f'_c under complicated stress demands and load reversals is essential to evaluate the web crushing capacity of HSC structural walls.

2.6 Nonlinear Finite Element Modeling Method

2.6.1 Continuum Damage Plasticity model in ABAQUS

The general purpose finite element program ABAQUS [35] was chosen in this study for conducting three-dimensional (3D) modeling due to its robustness to simulate nonlinear mechanics problems and its distinctive concrete material models. There are two main concrete models in the material library of ABAQUS, one is the concrete smeared cracking model; the other is the concrete damaged plasticity (CDP) model. The concrete smeared cracking model is mainly designed for monotonic loading and may not be applied for the walls tested under cyclic loading. In contrast, the CDP model is regarded to be able to better represent the behavior of concrete since it is well founded on plasticity theory with cracking being regarded as a limit state of plastic yielding and various types of loading can be applied, including cyclic loading. With the introduction of concepts on damage mechanics, stiffness degradation can be considered through the definition of damage indices.

The features of the CDP model are described in the following. Damage is introduced in the definition of the elastic modulus, and the tensile and compressive plastic strains to represent the inelastic behavior of concrete. Two different damage indices are required to define cracking in tension and compression separately. The CDP model can be used for cyclic loading with the unilateral effect being explicitly considered, i.e., the compressive stiffness is recovered upon crack closure as load changes from tension to compression. A non-associated flow rule is used to derive the plastic strain rate since the associative flow rule could result in the problem in the control of dilatancy.

Overview of the CDP model

The framework of the CDP model is described briefly in the following. For a rate-independent model, the total strain rate $\dot{\varepsilon}$ can be decomposed into an elastic part $\dot{\varepsilon}^{el}$ and a plastic part $\dot{\varepsilon}^{pl}$

$$\dot{\varepsilon} = \dot{\varepsilon}^{el} + \dot{\varepsilon}^{pl} \tag{2-24}$$

The constitutive equation of the material with scalar isotropic damage is expressed as

$$\sigma = (1-d)D_0^{el}:\left(\varepsilon - \varepsilon^{pl}\right) = D^{el}:\left(\varepsilon - \varepsilon^{pl}\right) \tag{2-25}$$

where σ is the Cauchy stress tensor, d is the corresponding scalar stiffness degradation variable, ε is the strain tensor, D_0^{el} is the initial (undamaged) elastic stiffness, and $D^{el} = (1-d)D_0^{el}$ is the degraded elastic stiffness tensor.

Based on the concepts of continuum damage mechanics, the effective stress tensor is defined as

$$\bar{\sigma} := D_0^{el}:\left(\varepsilon - \varepsilon^{pl}\right) \tag{2-26}$$

where ε^{pl} is the plastic strain tensor. The Cauchy stress is related to the effective stress through a scalar damage index, d, by:

$$\sigma = (1-d)\bar{\sigma} \tag{2-27}$$

Hardening variables

Damage states in tension and compression are characterized independently by two hardening variables $\widetilde{\varepsilon_t}^{pl}$ and $\widetilde{\varepsilon_c}^{pl}$, which are referred to as the equivalent plastic strains in tension and compression, respectively. The evolution of the hardening variables is expressed as

$$\tilde{\varepsilon}^{pl} = \left[\tilde{\varepsilon}_t^{pl} \quad \tilde{\varepsilon}_c^{pl}\right]^T \tag{2-28}$$

$$\dot{\tilde{\varepsilon}}^{pl} = h(\bar{\sigma}, \tilde{\varepsilon}^{pl}) \cdot \dot{\varepsilon}^{pl} \tag{2-29}$$

Yield function

The yield function, $F\left(\bar{\sigma}, \tilde{\varepsilon}^{pl}\right)$, represents a surface in the effective stress space, which determines the states of failure and damage. For the inviscid plastic-damage model

$$F\left(\bar{\sigma}, \tilde{\varepsilon}^{pl}\right) \leq 0 \tag{2-30}$$

The CDP model in ABAQUS uses the yield function proposed by Lubliner et al. [36] and incorporates the modifications proposed by Lee and Fenves [37] to account for different evolution of strength under tension and compression. In terms of effective stress, the yield function takes the form

$$F = \frac{1}{1-\alpha}\left(\bar{q} - 3\alpha\bar{p} + \beta\left(\tilde{\varepsilon}^{pl}\right)\langle\hat{\bar{\sigma}}_{max}\rangle - \gamma\langle-\hat{\bar{\sigma}}_{max}\rangle\right) \tag{2-31}$$

where $\bar{p} = -\frac{1}{3}\text{trace}(\bar{\sigma})$, is the effective hydrostatic pressure; $\bar{q} = \sqrt{\frac{3}{2}(\bar{\mathrm{S}} : \bar{\mathrm{S}})}$, is the Mises equivalent effective stress; $\bar{\mathrm{S}} = \bar{\sigma} + \bar{p}\mathbf{I}$, is the deviatoric part of the effective stress tensor $\bar{\sigma}$; and $\hat{\bar{\sigma}}_{max}$ is the maximum eigenvalue of $\bar{\sigma}$. The coefficients of α, β, and γ are defined by:

$$\alpha = \frac{(\sigma_{b0}/\sigma_{c0}) - 1}{2(\sigma_{b0}/\sigma_{c0}) - 1} \tag{2-32}$$

$$\beta = \frac{\bar{\sigma}_c\left(\tilde{\varepsilon}_c^{pl}\right)}{\bar{\sigma}_t\left(\tilde{\varepsilon}_t^{pl}\right)}(1-\alpha) - (1+\alpha) \tag{2-33}$$

$$\gamma = \frac{3(1-K_c)}{2K_c - 1} \tag{2-34}$$

where σ_{b0}/σ_{c0} is the ratio of initial equibiaxial compressive yield stress to uniaxial compressive yield stress; K_c is the ratio of the second stress invariant on the tensile meridian to that on the compressive meridian; $\bar{\sigma}_t\left(\tilde{\epsilon}_t^{pl}\right)$ is the effective tensile stress; and $\bar{\sigma}_c\left(\tilde{\epsilon}_c^{pl}\right)$ is the effective compressive stress.

<u>Flow rule</u>

Plastic flow is governed by a flow potential G according to the flow rule

$$\dot{\varepsilon}^{pl} = \dot{\lambda}\frac{\partial G(\bar{\sigma})}{\partial \bar{\sigma}} \tag{2-35}$$

where $\dot{\lambda}$ is the nonnegative plastic multiplier. $\dot{\lambda}$ and F obey the Kuhn-Tucker conditions: $\dot{\lambda}F = 0$; $\dot{\lambda} \geq 0$; $F \leq 0$. The plastic potential is defined in the effective stress space.

A non-associated plastic flow is used in the CDP model. The flow potential G is the Druckder-Prager hyperbolic function

$$G = \sqrt{\left(\epsilon\sigma_{t0}\tan\psi\right)^2 + \bar{q}^2} - \bar{p}\tan\psi \tag{2-36}$$

where ψ is the dilation angle measured in the $\bar{p} - \bar{q}$ plane at high confining pressure; σ_{t0} is the uniaxial tensile stress at failure; and ϵ is the flow potential eccentricity. A result of introducing a non-associated flow rule is that the stiffness matrix will be asymmetric. In ABAQUS, an asymmetric matrix storage and solution scheme can be used to improve computational efficiency.

<u>Damage and stiffness degradation</u>

The evolution equations of the hardening variables $\widetilde{\varepsilon_t}^{pl}$ and $\widetilde{\varepsilon_c}^{pl}$ are conveniently formulated by considering uniaxial loading conditions first and then extended to multi-axial conditions.

<u>Uniaxial conditions</u>

As shown in Figure 2.5 and Figure 2.6, when a concrete specimen is unloaded from any point on the strain softening branch, the unloading stiffness degrades. The degraded response of concrete is characterized by two independent uniaxial damage variables, d_t and d_c, which are assumed to be functions of the plastic strains by neglecting the factors of temperature or other field variables

$$d_t = d_t\left(\tilde{\varepsilon}_t^{pl}\right) \quad (0 \leq d_t \leq 1)$$
$$d_c = d_c\left(\tilde{\varepsilon}_c^{pl}\right) \quad (0 \leq d_t \leq 1) \tag{2-37}$$

The uniaxial degradation variables are increasing functions of the equivalent plastic strains which ranges from zero for undamaged material to one for fully damaged material.

The effective uniaxial cohesion stresses, $\bar{\sigma}_t$ and $\bar{\sigma}_c$, are expressed as

$$\bar{\sigma}_t = \frac{\sigma_t}{(1-d_t)} = E_0\left(\varepsilon_t - \tilde{\varepsilon}_t^{pl}\right)$$
$$\bar{\sigma}_c = \frac{\sigma_c}{(1-d_c)} = E_0\left(\varepsilon_c - \tilde{\varepsilon}_c^{pl}\right) \tag{2-38}$$

Under uniaxial cyclic loading conditions, the degradation mechanisms are quite complex, involving the opening and closing of the previously formed micro-cracks, as well as their interaction. It has been observed through experiments that there is some stiffness recovery under load reversal. This effect is more pronounced when tensile cracks close and concrete is in compression. For uniaxial cyclic conditions, ABAQUS assumes that

$$(1-d) = (1-s_t d_c)(1-s_c d_t) \tag{2-39}$$

where s_t and s_c are functions of stress state introduced to represent stiffness recovery effects

$$s_t = 1 - \omega_t r^*(\bar{\sigma}_{11}) \quad 0 \leq \omega_t \leq 1$$
$$s_c = 1 - \omega_c\big(1 - r^*(\bar{\sigma}_{11})\big) \quad 0 \leq \omega_c \leq 1 \tag{2-40}$$

where

$$r^*(\bar{\sigma}_{11}) = H(\bar{\sigma}_{11}) = \begin{cases} 1 & \text{if } \bar{\sigma}_{11} > 0 \\ 0 & \text{if } \bar{\sigma}_{11} < 0 \end{cases} \tag{2-41}$$

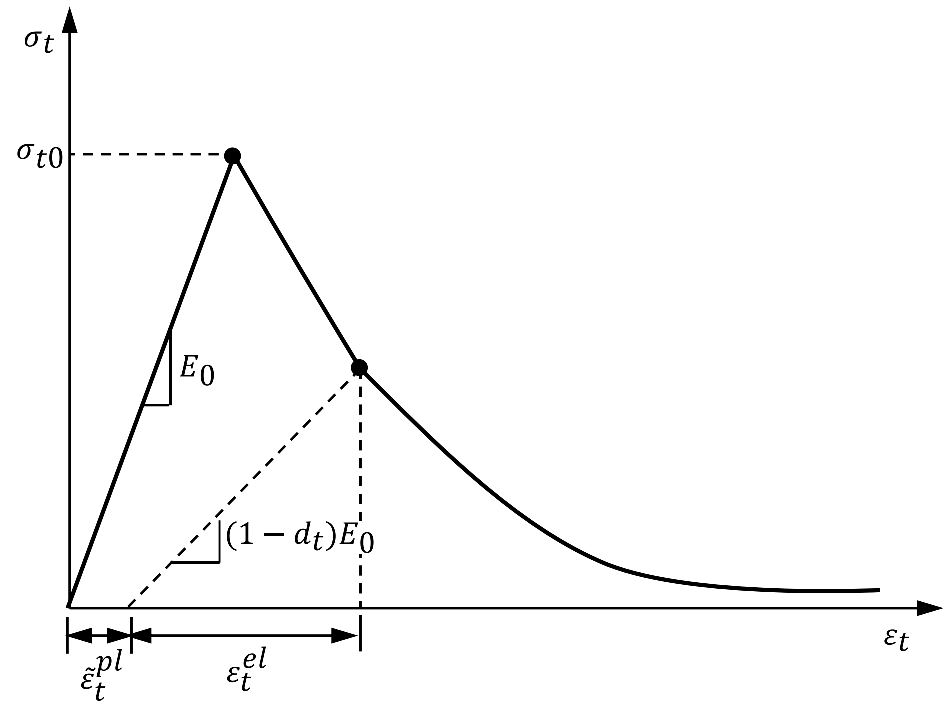

Figure 2.5 Concrete stress-strain curve under uniaxial tension

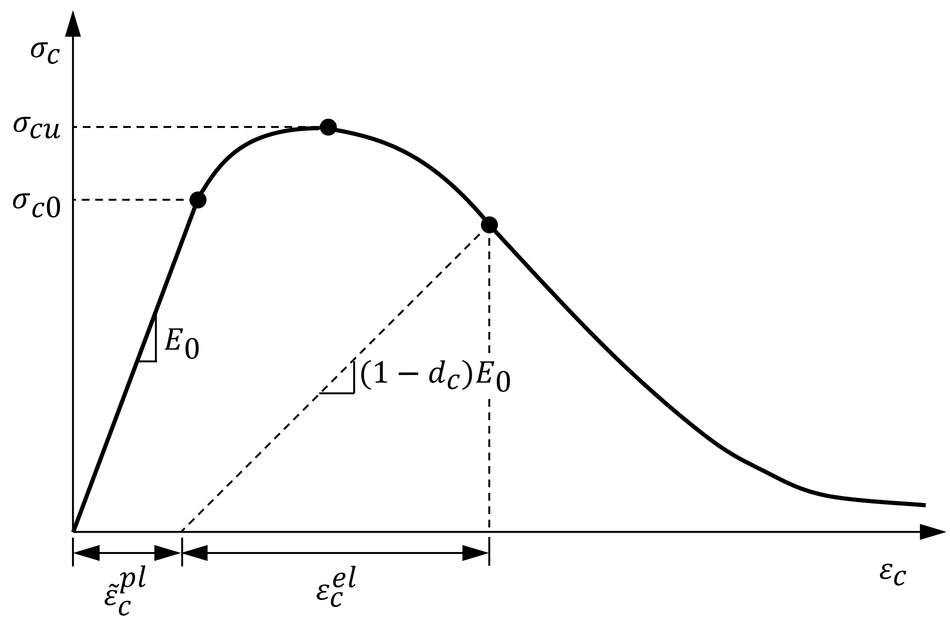

Figure 2.6 Concrete stress-strain curve under uniaxial compression

The weight factors ω_t and ω_c control the recovery of the tensile and compressive stiffness upon load reversal. Figure 2.7 illustrates the effect of the compression stiffness recovery parameter ω_c.

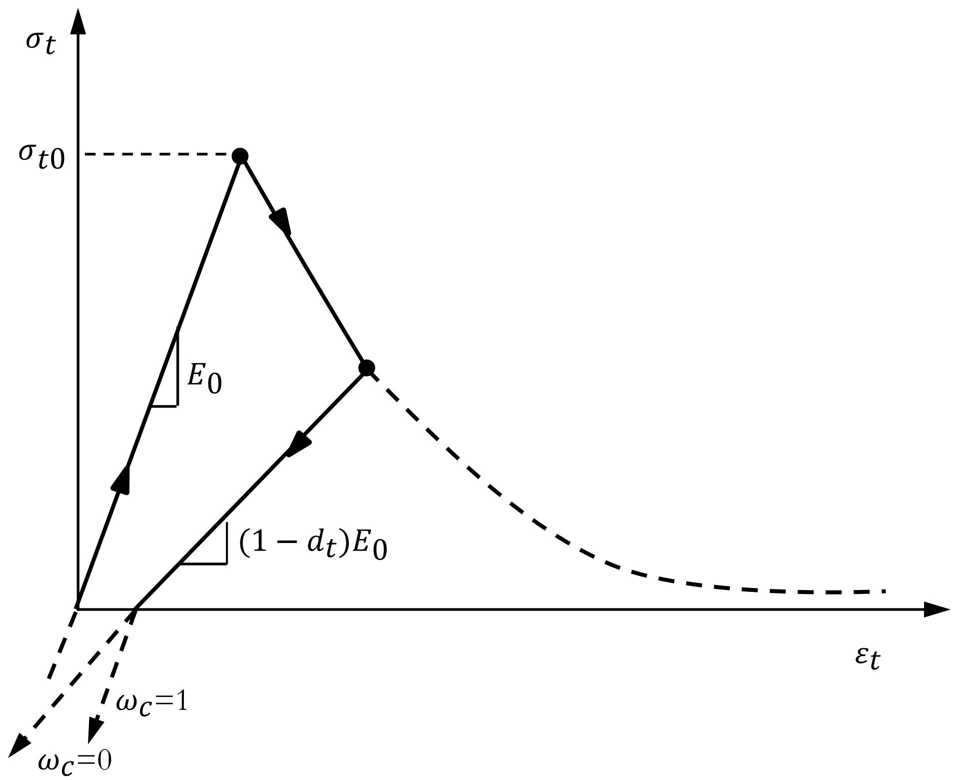

Figure 2.7 Illustration of the effect of the compression stiffness recovery parameter ω_c.

<u>Multiaxial conditions</u>

Based on the work of Lee and Fenves [37], the equivalent plastic strain rates are evaluated according to

$$\dot{\tilde{\varepsilon}}_t^{pl} := r(\hat{\bar{\sigma}})\hat{\dot{\varepsilon}}_{max}^{pl}$$
$$\dot{\tilde{\varepsilon}}_c^{pl} := -\left(1 - r(\hat{\bar{\sigma}})\right)\hat{\dot{\varepsilon}}_{min}^{pl} \tag{2-42}$$

where $\hat{\dot{\varepsilon}}_{max}^{pl}$ and $\hat{\dot{\varepsilon}}_{min}^{pl}$ are the maximum and minimum eigenvalues of the plastic strain rate tensor $\dot{\varepsilon}^{el}$ and

$$r(\hat{\bar{\sigma}}) := \frac{\sum_{i=1}^{3}\langle\hat{\bar{\sigma}}_i\rangle}{\sum_{i=1}^{3}|\hat{\bar{\sigma}}_i|} \quad 0 \leq r(\hat{\bar{\sigma}}) \leq 1 \tag{2-43}$$

is a stress weight factor that is equal to one (1.0) if all principal stresses $\hat{\bar{\sigma}}_i$, $(i = 1, 2, 3)$ are positive and equal to zero (0.0) if they are negative. The Macauley bracket $\langle\cdot\rangle$ is defined by $\langle x\rangle = 1/2(|x| + x)$.

The evolution equation for general multiaxial stress conditions can be expressed in matrix form as

$$\dot{\varepsilon}^{pl} = \begin{bmatrix}\dot{\tilde{\varepsilon}}_t^{pl} & \dot{\tilde{\varepsilon}}_c^{pl}\end{bmatrix}^T = \hat{h}\left(\hat{\bar{\sigma}}, \tilde{\varepsilon}^{pl}\right) \cdot \dot{\hat{\varepsilon}}^{pl} \tag{2-44}$$

where

$$\hat{h}\left(\hat{\bar{\sigma}}, \tilde{\varepsilon}^{pl}\right) = \begin{bmatrix} r(\hat{\bar{\sigma}}) & 0 & 0 \\ 0 & 0 & -\left(1 - r(\hat{\bar{\sigma}})\right) \end{bmatrix} \tag{2-45}$$

and

$$\dot{\hat{\varepsilon}}^{pl} = \begin{bmatrix}\dot{\hat{\varepsilon}}_1 & \dot{\hat{\varepsilon}}_2 & \dot{\hat{\varepsilon}}_3\end{bmatrix}^T \quad \dot{\hat{\varepsilon}}_1 \geq \dot{\hat{\varepsilon}}_2 \geq \dot{\hat{\varepsilon}}_3 \tag{2-46}$$

The definition of the scalar degradation variable d is consistent with the uniaxial conditions with equations shown in Equation (2-39) and (2-40).

Viscoplastic regularization

The softening behavior of concrete under both tension and compression leads to severe convergence difficulties. The availability of a viscoplastic regularization in ABAQUS Standard permits overcoming these difficulties. ABAQUS uses a generalization of the Duvaut-Lions regularization method, according to which the viscoplastic strain rate tensor, $\dot{\varepsilon}_v^{pl}$, is defined as

$$\dot{\varepsilon}_v^{pl} = \frac{1}{\mu}\left(\varepsilon^{pl} - \varepsilon_v^{pl}\right) \tag{2-47}$$

where μ is the viscosity parameter representing the relaxation time of the viscoplastic system. Similarly, a viscous stiffness degradation variable, d_v, is defined as

$$\dot{d}_v = \frac{1}{\mu}(d - d_v) \tag{2-48}$$

where d is the degradation variable evaluated in the inviscid backbond model. The stress-strain relation of the viscoplastic model is given as

$$\sigma = (1 - d_v)D_0^{el}:\left(\varepsilon - \varepsilon_v^{pl}\right) \tag{2-49}$$

Integration of the CDP model

The model is integrated using the backward Euler method generally used with the plasticity models in ABAQUS [35][38]. A material Jacobian consistent with this integration operator is used for the equilibrium iterations.

The description of damage and the definition of damage evolution curve for the material input of the model parameter is presented in Chapter 5.

2.6.2 MCFT based FE modeling – VecTor2

Overview

2D plane stress finite element analysis can be implemented at a lower computational cost to simulate the response of reinforced concrete beams and shear walls under in-plane loading. VecTor2 is a program based on the Modified Compression Field Theory (MCFT) [28] for nonlinear finite element analysis of reinforced concrete membrane structures [39]. It incorporates a variety of phenomenological nonlinear material models into the framework of the finite element method to represent the realistic features of the behavior of reinforced concrete structures observed from experiments, e.g., compression softening, tension stiffening and tension softening, etc.

Theories of VecTor2 – MCFT and DSFM

Two theories/models form the theoretical core of VecTor2, the modified compression field theory (MCFT) and the disturbed stress filed model (DSFM). MCFT was proposed based on tests of reinforced concrete membrane elements subjected to shear and normal stresses. The outline of MCFT is shown in Figure 2.8 [40]. The theory is composed of three sets of relationships: equilibrium equations with average stresses in concrete and reinforcement; geometrical compatibility conditions; and the average stress-average strain constitutive relationships of cracked concrete and reinforcement. The first two relationships are derived based on Mohr's circle of stress and strain. MCFT is based on the smeared rotational crack concept, which was verified through membrane tests.

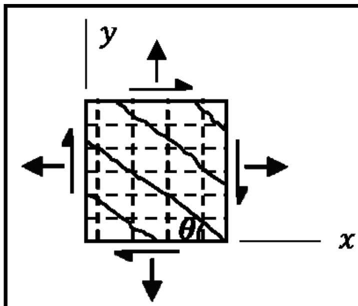

Equilibrium:

Average Stresses:

$$\rho_x f_{sx} = f_x + v\cot\theta - f_1$$

$$\rho_y f_{sy} = f_y + v\tan\theta - f_1$$

$$f_2 = v(\tan\theta + \cot\theta) - f_1$$

Stresses at Cracks:

$$\rho_x f_{sxcr} = f_x + v\cot\theta + v_{ci}\cot\theta$$

$$\rho_y f_{sycr} = f_y + v\tan\theta - v_{ci}\cot\theta$$

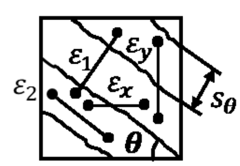

Geometric Conditions:

Average Strains:

$$\varepsilon_x = \frac{(\varepsilon_1 \tan^2\theta + \varepsilon_2)}{(1 + \tan^2\theta)}$$

$$\varepsilon_y = \frac{(\varepsilon_1 + \varepsilon_2 \tan^2\theta)}{(1 + \tan^2\theta)}$$

$$\tan^2\theta = \frac{(\varepsilon_x - \varepsilon_2)}{(\varepsilon_y - \varepsilon_2)}$$

$$\gamma_{xy} = \frac{2(\varepsilon_x - \varepsilon_2)}{\tan\theta}$$

Crack Widths:

$$w = s_\theta \varepsilon_1$$

$$s_\theta = 1/\left(\frac{\sin\theta}{s_x} + \frac{\cos\theta}{s_y}\right)$$

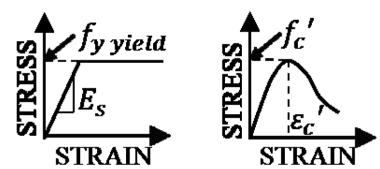

Average Stress-Average Strain Relationships:

Reinforcement:

$$f_{sx} = E_s \varepsilon_x \leq f_{x\,yield}$$

$$f_{sy} = E_s \varepsilon_y \leq f_{y\,yield}$$

Concrete:

$$f_2 = \frac{f_c'}{0.8 + 170\varepsilon_1}\left[2\frac{\varepsilon_2}{\varepsilon_c'} - \left(\frac{\varepsilon_2}{\varepsilon_c'}\right)^2\right]$$

$$f_1 = \frac{f_{cr}}{1 + \sqrt{500\varepsilon_1}}$$

Allowable Shear Stress on Crack

$$v_{ci} \leq \frac{0.18\sqrt{f_c'}}{0.31 + \frac{24w}{a + 16}}$$

Figure 2.8 The modified compression field theory (MCFT) [40].

The DSFM [39] addresses the deficiencies of the MCFT in predicting the response of certain structures and loading scenarios. The DSFM is conceptually similar to the MCFT, but extends it in several aspects. Most importantly, the DSFM augments the compatibility relationships of the MCFT to include crack shear slip deformations. The strains due to the slip deformations are distinguished from the strains of the concrete continuum due to stress. Therefore, the DSFM decouples the orientation of the principal stress field from that of the principal strain field, resulting in a smeared delayed rotating-crack model.

Analysis features

Some other features of VecTor2 include a comprehensive set of so-called phenomenological constitutive models to consider both major and secondary effects in the response of reinforced concrete structures. An important feature, which is essential for the single wall analyses in this study, is the concrete strength increase due to the lateral confinement provided by transverse stirrups, which can be adequately captured by VecTor2.

Modeling of triaxial stresses

Although the MCFT is formulated for a state of plane stress, VecTor2 accounts for out-of-plane stresses (z-direction) due to the confinement of lateral concrete expansion by out-of-plane reinforcement. A triaxial stress state is then utilized in computing the strength enhancement due to confinement. The out-of-plane concrete strain is computed as follows.

$$\varepsilon_{cz} = \frac{E_c}{E_c + \rho_z \cdot E_{sz}} \left(-v_{12} \frac{f_{c2}}{\bar{E}_{c2}} - v_{21} \frac{f_{c1}}{\bar{E}_{c1}} \right) \tag{2-50}$$

where ρ_Z is the reinforcement ratio of the out-of-plane reinforcement. If the out-of-plane reinforcement has yielded, the out-of-plane concrete strain is computed as follows

$$\varepsilon_{cz} = -\frac{\rho_z \cdot f_{z,yield}}{E_c} - v_{12} \frac{f_{c2}}{\bar{E}_{c2}} - v_{21} \frac{f_{c1}}{\bar{E}_{c1}} \tag{2-51}$$

The stress, f_{SZ}, in the out-of-plane reinforcement is determined as follows.

$$f_{sz} = E_s \varepsilon_{cz} \leq f_{z,yield} \quad (2\text{-}52)$$

The resulting out-of-plane concrete compressive stress, f_{cz}, is determined from equilibrium as follows.

$$f_{cz} = -\rho_z \cdot f_{sz} \quad (2\text{-}53)$$

Finite element implementation

Regarding the finite element implementation in VecTor2, reinforced concrete is dealt as an orthotropic material in the principal stress directions. The material secant stiffness matrix of concrete is expresses as follows by ignoring the Poisson's effect,

$$[D_c]' = \begin{bmatrix} \bar{E}_{c1} & 0 & 0 \\ 0 & \bar{E}_{c2} & 0 \\ 0 & 0 & \bar{G}_c \end{bmatrix} \quad (2\text{-}54)$$

The secant moduli, $\bar{E}_{c1}$, $\bar{E}_{c2}$, and $\bar{G}_c$ are calculated as follows,

$$\bar{E}_{c1} = \frac{f_{c1}}{\varepsilon_{c1}}; \bar{E}_{c2} = \frac{f_{c2}}{\varepsilon_{c2}}; \bar{G}_c = \frac{\bar{E}_{c1} \cdot \bar{E}_{c2}}{\bar{E}_{c1} + \bar{E}_{c2}} \quad (2\text{-}55)$$

The material secant stiffness matrix of *i*-th reinforcement component based on its longitudinal axis is calculated as follows,

$$[D_s]_i = \begin{bmatrix} \rho_i \bar{E}_{si} & 0 & 0 \\ 0 & 0 & 0 \\ 0 & 0 & 0 \end{bmatrix} \quad (2\text{-}56)$$

where ρ_i is the reinforcement ratio of the corresponding component. The secant modulus $\bar{E}_{si}$, is calculated as $\bar{E}_{si} = \frac{f_{si}}{\varepsilon_{si}}$.

The global stiffness matrix is assembled in the global coordinate system as follows,

$$[D] = [D_c] + \sum_{i=1}^{n} [D_s]_i \quad (2\text{-}57)$$

where,

$$[D_c] = [T_c]^T [D_c]' [T_c] \tag{2-58}$$

$$[D_s]_i = [T_s]_i^T [D_s]_i' [T_s]_i \tag{2-59}$$

$$[T] = \begin{bmatrix} cos^2\psi & sin^2\psi & cos\psi sin\psi \\ sin^2\psi & cos^2\psi & -cos\psi sin\psi \\ -scos\psi sin\psi & 2cos\psi sin\psi & cos^2\psi - cos^2\psi \end{bmatrix} \tag{2-60}$$

The constitutive equation of stress and total strain is expressed as

$$[\sigma] = [D][\varepsilon] - [\sigma_0] \tag{2-61}$$

$[\sigma_0]$ is a pseudo-stress produced due to strain offsets in concrete and reinforcement, defined as

$$[\sigma_0] = [D_c]\left\{[\varepsilon^s] + \left[\varepsilon_c^0\right] + \left[\varepsilon_c^p\right]\right\} + \sum_{i=1}^{n}[D_s]_i\left\{\left[\varepsilon_s^0\right]_i + \left[\varepsilon_s^p\right]_i\right\} \tag{2-62}$$

where $\left[\varepsilon_c^0\right]$ are the elastic strain offsets in concrete, $\left[\varepsilon_c^p\right]$ are the plastic strain offsets in concrete, and $[\varepsilon^s]$ are the strain due to crack shear slip. $\left[\varepsilon_s^0\right]_i$ are the elastic strain offsets in concrete and $\left[\varepsilon_s^p\right]_i$ are the plastic strain offsets in concrete.

2.7 Research Hypothesis of This Study

Evidence supporting the hypothesis that HSC increases the web crushing capacity of structural walls has been available for some time. Intuitively, web crushing strength should be proportional to the concrete compressive strength in view of the fact that the struts fracture under compression. Research by the Portland Cement Association (PCA) in the 1970's on walls with boundary elements [5] noted that specimen B6 with a concrete compressive strength of 22 MPa (3,165 psi) failed in web crushing at significantly lower deformation capacity than specimen B7 with a concrete compressive strength of 49 MPa (7,155 psi). However, no further HSC structural walls were tested.

All the reviewed models in Section 2.5 show that web crushing strength is linearly related to concrete compressive strength, indicative of new possibilities for increasing the web crushing capacity of slender structural members with increased concrete compressive strength. However, this potential is currently impaired by outdated design provisions and lack of experience. The lack of experimental data has been dealt with by setting an upper-bound limit as noted in Equation (2-15) and Equation (2-16). However, without careful calibrations with experimental data from structural wall tests with various concrete strengths, the specified values are questionable. While there is no explicit upper-bound limit in the model by Hines and Seible [16], its reliability to predict capacities for HSC structural walls is expected to deteriorate since the model was calibrated with data from tests of normal-strength-concrete walls. The ACI 318-08 [25] code does not reflect the direct dependence of web crushing capacity on f_c', but rather limits shear demand based on $\sqrt{f_c'}$, a quantity commonly related to concrete tensile strength and diagonal tension failure of structural walls. It should be noted that a maximum value of 100 psi [0.69 MPa] has been applied by the code because of the lack of test data and practical experience with concrete strength over 10,000 psi (69 MPa).

The research summarized in this dissertation was thus developed with the intention of testing the following hypotheses:

1. Web crushing strength increases in proportion to f'_c as long as the struts are not damaged. Hence, transformation from an elastic web crushing failure to an inelastic web crushing failure can be achieved simply by increasing the concrete strength.
2. Damage to struts caused by multi-directional loading, cyclic loading and inelastic deformations can limit web strength independently of f'_c. Hence, increases in f'_c may not lead to proportional increases in ductility capacity.

3. The contribution of cyclic loading to strut degradation can be observed by comparing test units loaded cyclically to similar test units loaded monotonically.
4. Three-dimensional shear demands on wall assemblies curtail web crushing capacity by virtue of a reduced strut geometry and combined flexure/shear stress demand. Nonetheless, acceptable predictions for three-dimensional wall assemblies may be obtained by resolving the flexure and shear demands into a two-dimensional model.
5. Inelastic web crushing capacity can be predicted with sufficient accuracy to support the design of thin webbed elements that experience "ductile shear failures" which may be easier to repair than ductile flexural failures. Inelastic shear behavior and failure can thus be an acceptable and reliable failure mode for seismic performance design.
6. Concrete strengths for high-strength-concrete can be reliably obtained to facilitate such designs.
7. High-strength-concrete can transform the design of pier walls and other slender reinforced concrete elements under seismic loads.

Chapter 3. **Experimental Studies on HSC Structural Walls**

3.1 Summary

A common preconceived notion is that use of high-strength-concrete (HSC) can jeopardize the ductility level of the structures in seismic regions. However, a well-designed structure with appropriate detailing may take full advantage of the benefits of HSC with adequate ductility being achieved. In this study, the seismic performance of HSC structural walls with highly-reinforced boundary elements and thin constrained web was experimentally evaluated. Eight 1/5-scale single walls were tested with design concrete compressive strengths of 34, 69, 103, and 138 MPa (5, 10, 15 and 20 ksi) under cyclic and monotonic loading protocols. Among the possibilities of various shear failure mechanisms, web crushing is the only failure mode designed to happen. The objective of this study was to evaluate the effect of concrete strength on the web crushing performance limits of HSC structural walls. The web crushing behavior of the structural walls with same design concrete compressive strength but under different loading protocols, monotonic and cyclic loading, was compared to assess the effect of loading protocol and damage accumulation on web crushing capacity. A new concept of "ductile shear failure" is introduced in contrast to the conventional and inferior inelastic shear failure mechanism. The experimental results revealed that high-strength-concrete can effectively delay web crushing failures and increase the displacement ductility capacity of structural walls. However, web crushing capacity can be significantly curtailed under cyclic loading, particularly as the concrete compressive strength increases. This is attributed to the rapid shear strength and stiffness degradation under cyclic loading. Nonetheless, ductile shear failures were still obtained for HSC structural walls up to moderate displacement ductility levels.

3.2 Experimental Investigation

The structural walls featured highly-reinforced boundary elements and a thin constrained wall web. An aspect ratio of 2.5 was maintained, which falls at the interface of slender and squat walls. The cross section of the walls resembles a dumbbell shape with two highly-reinforced boundary elements at the ends of the thin wall web. The boundary elements are designed to ensure that the moment capacity of the walls is above the shear capacity. The walls were designed such that the shear failure mechanism was web crushing. Thus, diagonal tension failure of the wall under shear was avoided by the configuration of the wall transverse reinforcement. It should be noted that researchers have reported that the introduction of diagonal reinforcement can dramatically increase the diagonal tension capacity in walls. Further research on this detailing aspect is out of the scope of this study [41] and thus not considered. The constraint provided by the boundary elements along the edge of the web prevents instability of the walls. The extension of the boundary element steel cages into the footing provides enough anchorage to prevent sliding failure of the walls. The concrete in the boundary elements is thus expected to display enhanced strength and ductile behavior due to the confinement provided by the stirrups and the footing. The well-designed structure will ensure the development of a plastic region under flexure. At the same time, flexural deformations are introduced into the wall web. The mixed flexure and shear demand and its effect on the web crushing capacity and ductility level is the foci of this study.

This research examines the use of high-strength-concrete (HSC) to obtain ductile shear failure behavior and to improve the seismic performance of structural walls. The effect of concrete strength on web crushing failure mechanism, strength, and ductility has been studied. The approach is non-intuitive as web crushing is a brittle failure and it is well known that concrete becomes more brittle as its compressive strength increases. Comparative results have been obtained to assess the cyclic loading effect on concrete damage, structural strength/stiffness degradation, and web crushing capacity. The appropriate performance evaluation on HSC structural walls exhibiting ductile shear failures is expected to contribute to the groundwork of the next stage in earthquake resistant design of thin-webbed elements and systems.

3.2.1 Single Wall Test Units

To verify the above-noted hypothesis and establish rational performance levels on the inelastic web crushing limits for HSC structural walls, eight 1/5-scale cantilever structural walls with design concrete compressive strengths of 34, 69, 103, and 138 MPa (5, 10, 15 and 20 ksi) were tested under cyclic and monotonic loading [8]. The walls consisted of highly-reinforced boundary elements with constrained thin web which were designed to induce the desired web crushing failure mode and were not intent to represent a component from a prototype structure. The test unit cross sections with reinforcement details are shown in Figure 3.1. The identification name for the test units starts with 'M' followed by two digits denoting the design concrete compressive strength in kips/in^2 (1 kip/in^2 (ksi) = 6.895 MPa) and then by a letter describing loading protocol: 'C' for cyclic and 'M' for monotonic loading. The structural walls have a height of 2540 mm (100 in.) from the base up to the mid-height of the loading block, which results in an aspect ratio of 2.5. As is shown in Figure 3.1, the steel reinforcement was essentially the same with a small variation for test unit M15C. The change was made to facilitate specimen construction while a close reinforcement ratio was maintained. The wall transverse steel is spaced at 76 mm (3 in.) vertically for walls

M20M and M20C while the spacing is 102 mm (4 in.) for the rest. The transverse steel was designed to avoid diagonal tension failure.

The walls were loaded monotonically and cyclically according to an, incrementally increasing fully-reversed cyclic pattern with constant axial load. The axial load for all test units was 579 kN (130 kips), corresponding to $0.10f_c'A_g$ for a compressive strength of 34 MPa (5 ksi). The axial load was applied by means of hydraulic jacks and high-strength rods reacting against the wall top load stub through a spandrel beam. The horizontal load was applied with a servo-controlled actuator connected to a load stub at the top of the wall. Lateral stability was provided by means of a pair of parallel inclined tensioned chains on both side of the wall. An overview of the test setup is shown in Figure 3.2.

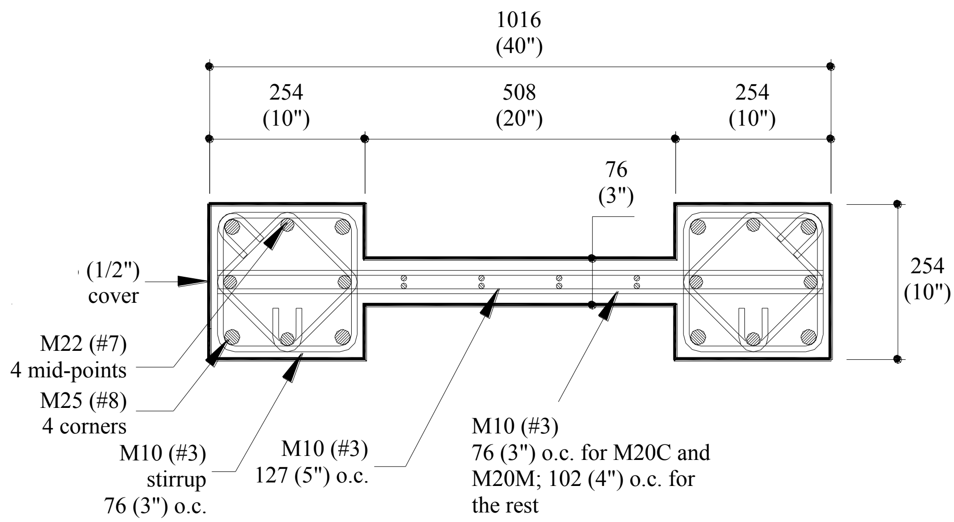

Cross section of the test units M05C, M05M, M10C, M10M, M15M, M20C, and M20M.

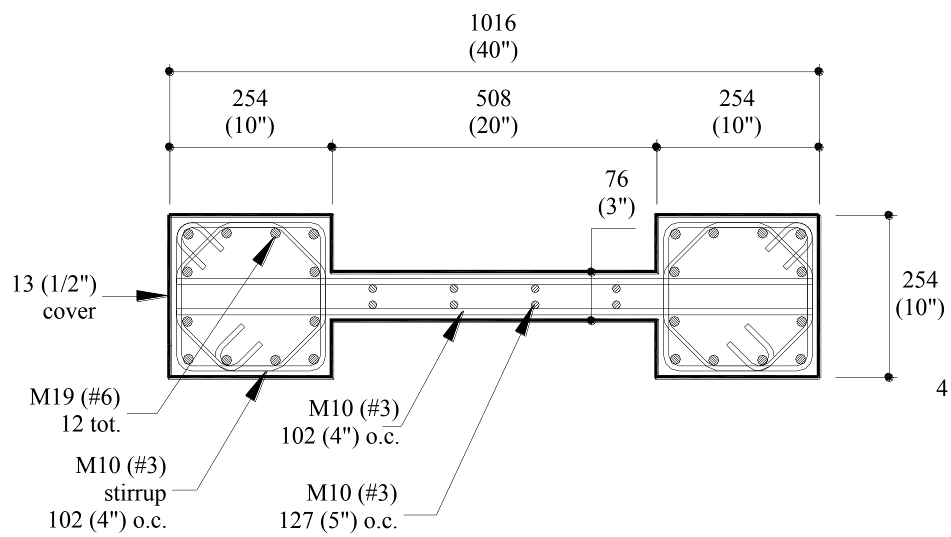

Cross section of the test units M15C.

Figure 3.1 Single wall test unit cross sections with reinforcement details.

Figure 3.2 Single wall test setup overview.

(For interpretation of the references to color in this and all other figures, the reader is referred to the electronic version of this dissertation.)

3.2.2 Material Properties

Modern concrete technology makes it realistic to produce 138 MPa (20,000 psi) or even higher strength of concrete with traditional mixing ingredients and without using any exotic aggregates or special process. The addition of silica fume to obtain HSC is essential because its high fineness property improves the hydration process. Concrete mixture proportions for all the test units are shown in Table 3-1. The concrete compressive strength development was monitored by a series of cylinder tests for each batch of concrete. The corresponding concrete strength development curves are shown in Figure 3.3. The concrete material properties of compressive strength, tensile strength and modulus of rupture were evaluated at day-of-test. The data is shown in Table 3-2.

Table 3-1 Summary of the concrete mixtures for the single wall test units.

Item	M05C M05M	M10C	M10M	M15C M15M	M20C M20M
Cement Type I, kg	167	167	345	393	431
Fly ash, kg	89.4	89.4	–	–	–
Silica fume, kg	–	–	–	32.7	68.1
Fine Aggregate, kg	695	695	619	524	454
Coarse Aggregate, kg	795	795	788	826	840
HRWR, Type F, liter	1.00	1.00	9.47	12.0	6.51
Retarder, Type D, liter	–	–	–	–	1.30
Air, liter	–	–	–	0.622	–
Water, kg	116	116	121	99.4	106
Water-cementitious ratio	0.45	0.45	0.35	0.25	0.21

Note: 1 lb = 0.454 kg; 1 oz = 0.0296 liter.

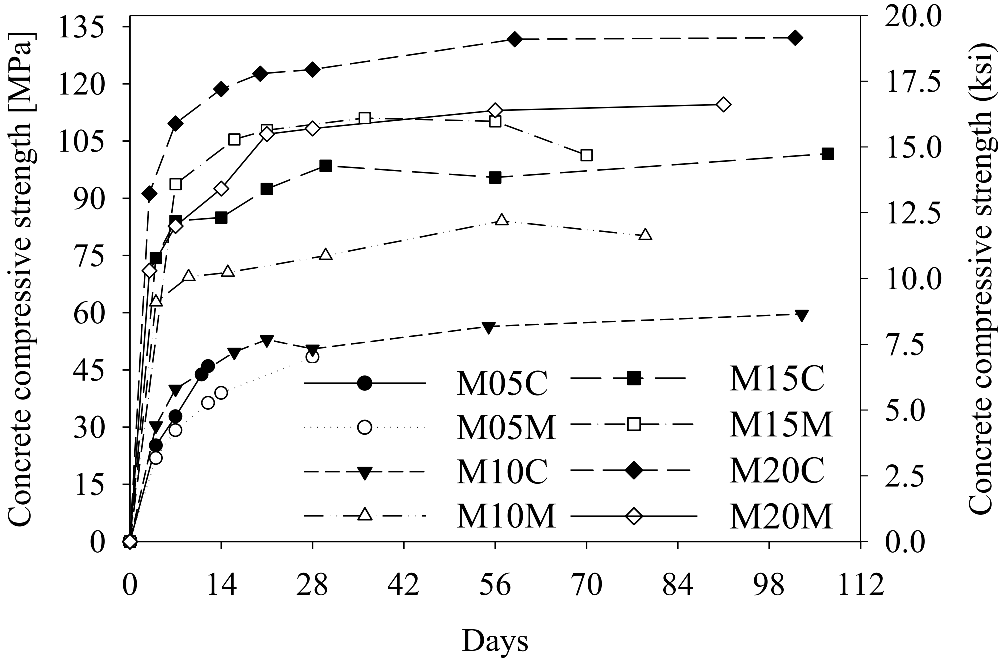

Figure 3.3 Concrete material strength development curves for single wall tests.

Table 3-2 Concrete material properties at day-of-test: Compressive strength, tensile strength and modulus of rupture for the single wall test units.

Strength (MPa)	M05C	M05M	M10C	M10M	M15C	M15M	M20C	M20M
f_c'	46.0	38.9	56.4	84.0	102	111	131	115
dev.	1.37	1.23	1.86	1.37	1.01	4.99	3.01	2.55
f_t'	3.25	3.55	4.50	5.54	5.70	6.17	6.19	5.96
dev.	0.207	0.0966	0.331	0.490	0.441	0.910	0.400	0.172
f_r	5.49	5.37	6.57	7.33	9.01	9.35	11.5	10.2
dev.	0.0897	0.0551	0.221	0.669	0.559	1.08	0.359	0.593

Note: 1 MPa = 0.145 ksi.

Table 3-3 lists the steel reinforcement properties for all the single wall test units and the corresponding modeling parameters. Most of the rebars displayed an obvious yield plateau and were fitted with Mander's model (M) [42], except for two #8 rebars without obvious yielding are fitted with Menegotto-pinto model (MP) [43]. Limited by the capacity of the MTS Grip System used for rebar test, the #8 rebars could be tested until fracture and only a small range of the stress-strain curves was obtained.

Table 3-3 Steel properties and modeling parameters for the single wall test units.

Test Unit	Model	Size	f_y (MPa)	f_u (MPa)	ε_{sh}	E_{sh} (MPa)
M05C M05M	M	M22	448	672	0.0026	11262
		M10	445	692	0.0083	7759
		M10	459	703	0.0075	7759
M10C M10M	M	M25	464	697	0.0096	8966
		M22	448	672	0.0094	8966
		M10	476	746	0.0060	8966
		M10	545	730	0.0050	7586
M15C	M	M19	439	705	0.0078	8966
		M10	481	759	0.0054	9655
		M10	503	756	0.0030	7931
M15M	M	M22	421	630	0.0093	8621
		M10	478	748	0.0060	10690
		M10	510	656	0.0072	5517
M20C M20M	M	M25	451	703	0.0054	9310
		M22	446	699	0.0060	8966
		M10	438	703	0.0043	8793
		M10	443	717	0.0037	8621
Test Unit	Model	Size	f_y (ksi)	–	r	E_h (ksi)
M15M	MP	M25	586	–	2.5	2759
M05C M05M	MP	M25	524	–	6	11034

Note: 1 MPa = 0.145 ksi.

3.2.3 Instrumentation

The test units were instrumented to measure flexural and shear deformations, flexural curvatures, and steel strains at specific locations in the steel reinforcement. Flexural deformations were obtained by the integrating the flexural curvatures at the extreme edges of the boundary elements. Flexure curvatures were calculated from displacement transducer measurements mounted on both tension and compression sides of the boundary elements along the wall height. Shear deformations were determined by using two instrumentation panels featuring two independent displacement transducers arranged diagonally on the south wall face. The global displacement was measured at the center of the west surface of the load stub with a displacement transducer. The contribution to lateral deformations from strain penetration, or bond-slip, effects into the footing block was monitored by measuring deformations of a rigid reference frame (cantilevers anchored on the footing surface to avoid the possible disturbance of the footing concrete cracking) with respect to the footing top over a gage length of 51 mm [2 in.]. Strain gauges were installed at strategic locations of the longitudinal and transverse steel reinforcement to monitor flexural yielding of the longitudinal reinforcement in the boundary elements and yielding of the transverse reinforcement in the wall web. The instrumentation layout for LVDTs and string pots is shown in Figure 3.4.

3.2.4 Loading protocol

Cyclic and monotonic loading was applied on the two test units of equal design concrete strength, separately, to evaluate the effect of loading history on the shear strength/stiffness degradation and displacement limits. Loading was applied by means of a servo-controlled hydraulic actuator mounted on a reaction frame and attached to the test unit through a stiff top block. The cyclic loading protocol is shown in Figure 3.5. Four initial cycles were applied in force control until the theoretical first yield force, F_y', the force at which the extreme steel rebar in tension first yields, was reached. The remainder of the test was conducted in displacement control with two cycles at each displacement ductility levels μ_Δ = 1, 1.5, 2, 3, 4 and 6, or until failure of the test unit. The ideal yield displacement, Δ_y, defined as displacement ductility one, μ_Δ= 1, was derived based on the stiffness at first yield and the theoretical force at which either the extreme confined concrete fibers reached ε_C = 0.004 or the extreme steel fiber in tension reached ε_S = 0.015. The monotonic loading was applied in force control until F_y' and then in displacement control until failure. The values of F_y' and Δ_y which are needed to define the loading protocol are listed in Table 3-4.

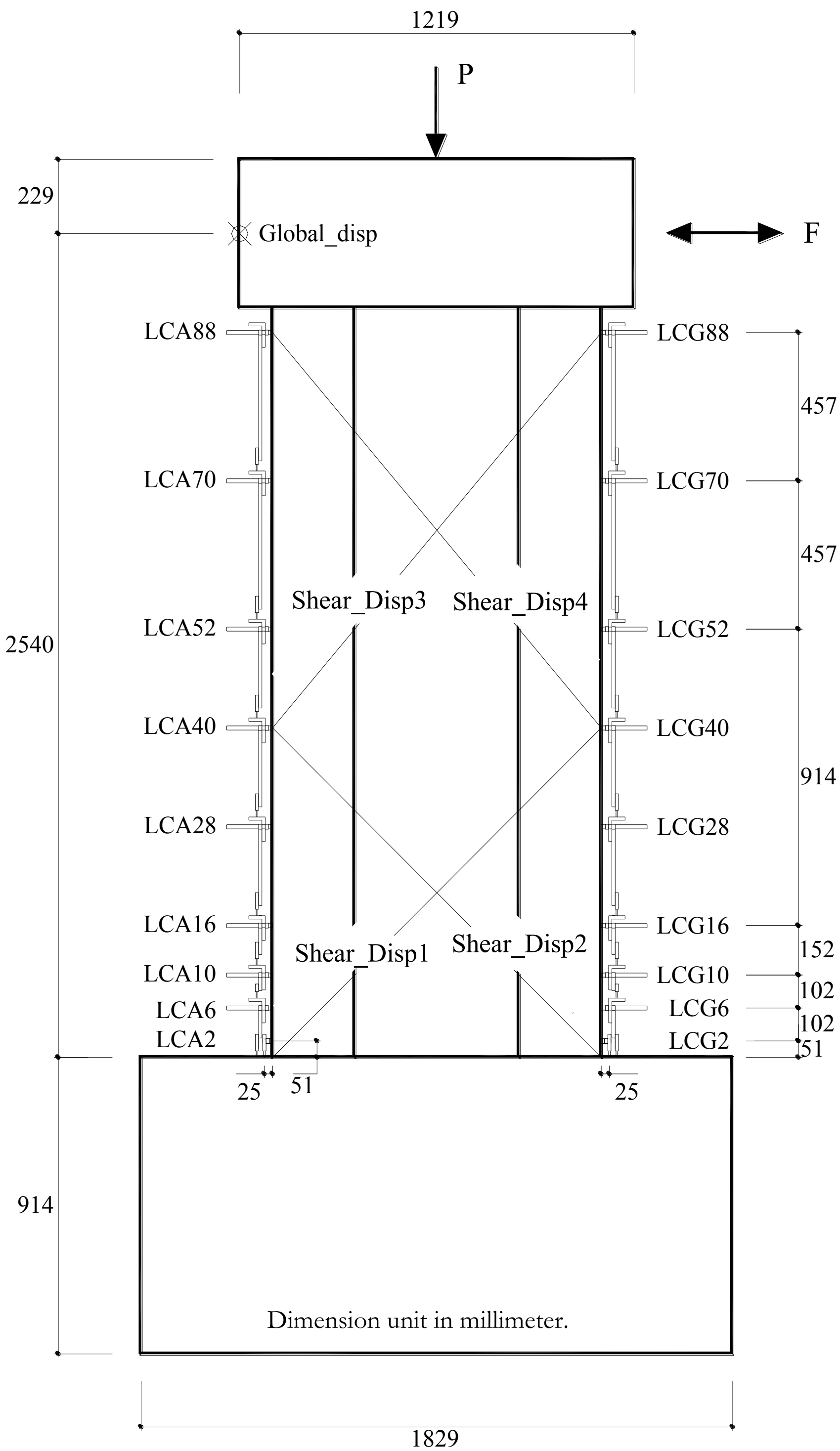

Figure 3.4 Single wall test unit instrumentation layout.

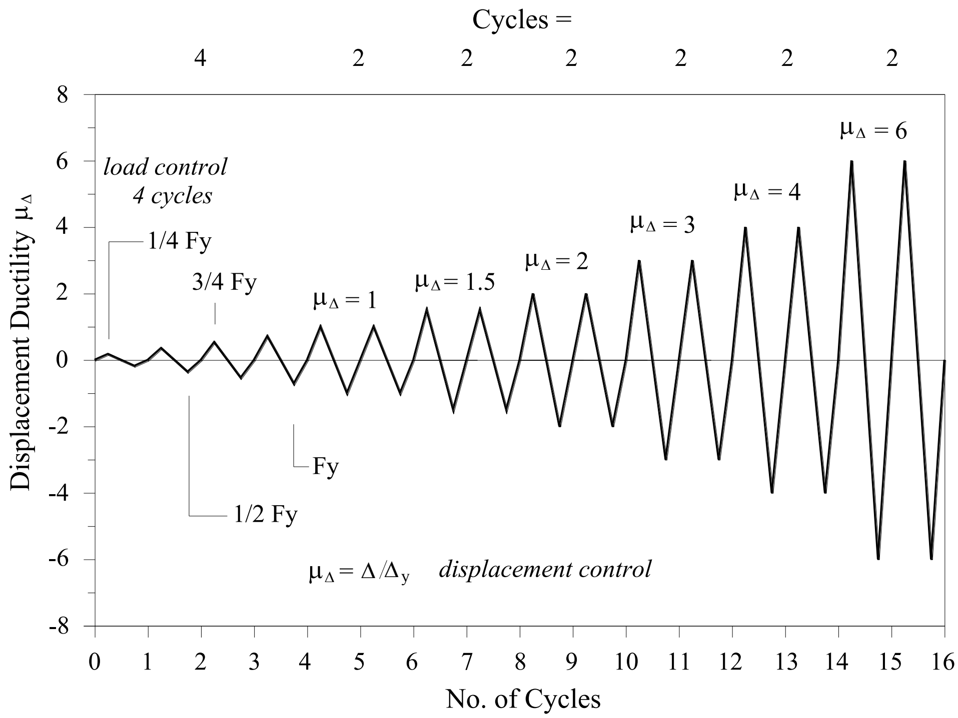

Figure 3.5 Cyclic loading protocol for single wall tests.

Table 3-4 Values of force at first yield and ideal yield displacement for single wall tests.

Test	M05C	M05M	M10C	M10M	M15C	M15M	M20C	M20M
F'_y (kN)	578	576	583	618	586	644	576	572
Δ_y (mm)	25.7	26.9	22.9	19.1	19.6	20.6	19.1	21.3

Note: 1 kip = 4.45 kN; 1 in. = 25.4 mm.

3.3 Experimental Observations

First, the common behavior observed on all test units is described. No cracks were observed through the loading up to $\frac{1}{4}F'_y$. At $\frac{1}{2}F'_y$, flexural cracking in the boundary elements and diagonal shear cracking in the webs appeared. At $\frac{3}{4}F'_y$, shear cracks were observed to spread throughout the entire web. The development of cracking for the single walls under cyclic loading at $\mu_\Delta = 1$ is illustrated through Figure 3.6 and Figure 3.7. It can be seen that HSC walls have relatively denser flexural and shear cracking than the NSC walls, which complies with the brittle nature of HSC. Figure 3.8 shows the cracking of M05M at F'_y. With the increase of displacement ductility, more cracks developed between the existing cracks and the active cracks became wider. Overall, the spacing of shear cracks for the HSC walls was much smaller than for the NSC walls. Even though the diagonal shear cracking under tension does not control the capacity of the walls, it defines the height and width of the struts formed by adjacent cracks and thus affects the struts compressive capacities. Moreover, the width of the cracks affects the shear slip behavior at the crack interface, which affects the compressive capacity of the strut as well. Another common feature in the test units was the spalling of the cover concrete in the compression boundary element. Relatively larger spalling was observed on the HSC wall units. Nonetheless, since the columns are well-confined by the stirrups, the boundary elements had no problem resisting the compression force well.

Second, the peculiarities of the web crushing failures and the displacement ductility reached by the test units are described individually. Test unit M05C failed on the first excursion to μ_Δ = 2. Web crushing was observed to occur at μ_Δ = 1.8. The failure mode is shown in Figure 3.9. Wall M10C failed on the first excursion to μ_Δ = 2. Web crushing was observed to occur at μ_Δ = 1.8. Upon failure, loading dropped approximately 40%, demonstrating a significant loss of flexural strength. The failure mode is shown in Figure 3.10. Test unit M15C performed in a ductile manner up to μ_Δ = 4. Web crushing was observed to occur on the second excursion to ductility 4. The load dropped only approximately 8%, compared with the corresponding load on the first cycle of ductility 4, demonstrating that the flexural strength of the test unit did not deteriorate very much. The failure mode is shown in Figure 3.11. Test unit M20C performed in a ductile manner up to

μ_Δ = 6. Web crushing was observed to occur on the first excursion to μ_Δ = 6. Web crushing started to happen at a displacement of 2.6 in. The strength of the test unit degraded around 40% when the displacement reached the target value for this cycle. The failure mode is shown in Figure 3.12. Wall M05M failed at μ_Δ = 2.3. The failure mode is shown in Figure 3.13. Test unit M10M performed in a ductile manner until web crushing occurred at μ_Δ = 7. The failure mode is shown in Figure 3.14. Wall M15M performed in a ductile manner until web crushing occurred at μ_Δ = 6.5. The failure mode is shown in Figure 3.15. Test unit M20M performed in a ductile manner until web crushing occurred at μ_Δ = 9.2. The failure mode is shown in Figure 3.16.

All walls failed in web crushing according to the experimental aim. Test units with lower concrete compressive strength (M05C, M05M and M10C) failed after only minor levels of inelastic response (μ_Δ). Tensile cracking was minimal and cracks fully closed upon load reversal. No crack realignment was observed and thus these walls were limited by standard, or elastic, web crushing. The failures were sudden and the crushing of the concrete struts occurred along the interface of the wall web and the compression boundary element and propagated along the wall height almost simultaneously.

The rest of the test units exhibited moderate to high ductile behavior before web crushing failure. Cracking was much more extensive and crack spacing was much smaller. The fanning flexure-shear cracking pattern was formed within the plastic hinge region with fairly flat cracks close to the bottom and much steeper cracks at the top. For the walls tested under cyclic loading, the crisscross cracking pattern under cyclic loading broke the concrete in the wall web into small diamond-shaped blocks. Such damage was particularly evident in the wall cover concrete. The excessive stress introduced by crack misalignment, shear friction and distortion caused the web cover concrete to lose its bond to the reinforcement and spall off. The test units gradually lost their load-carrying capacity as a result diminished load transfer efficiency of the concrete struts. Web crushing was observed to expand over a large area within the plastic hinge region of the wall and crushing of the flexure-shear struts initiated in the center of the web and then rapidly extended to the edge of the compression boundary element. Under monotonic loading, the compression struts remained integral, though severely cracked, and therefore the test units were able to sustain larger inelastic deformations, a difference that became more significant for higher values of concrete compressive strength.

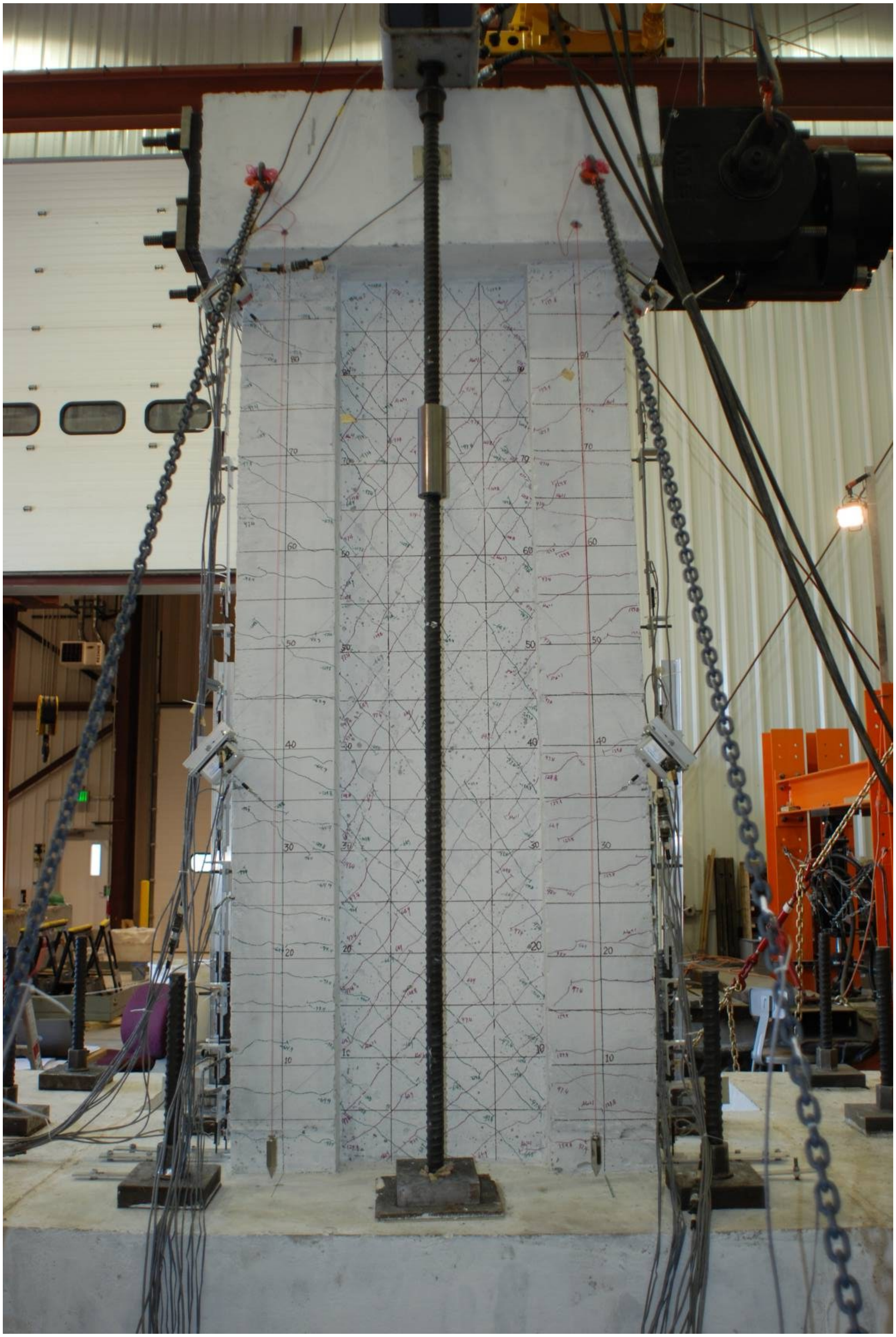

Figure 3.6 Test Unit M05C: south face, $\mu_\Delta = 1 \text{ x } +1$, push (positive) towards west.

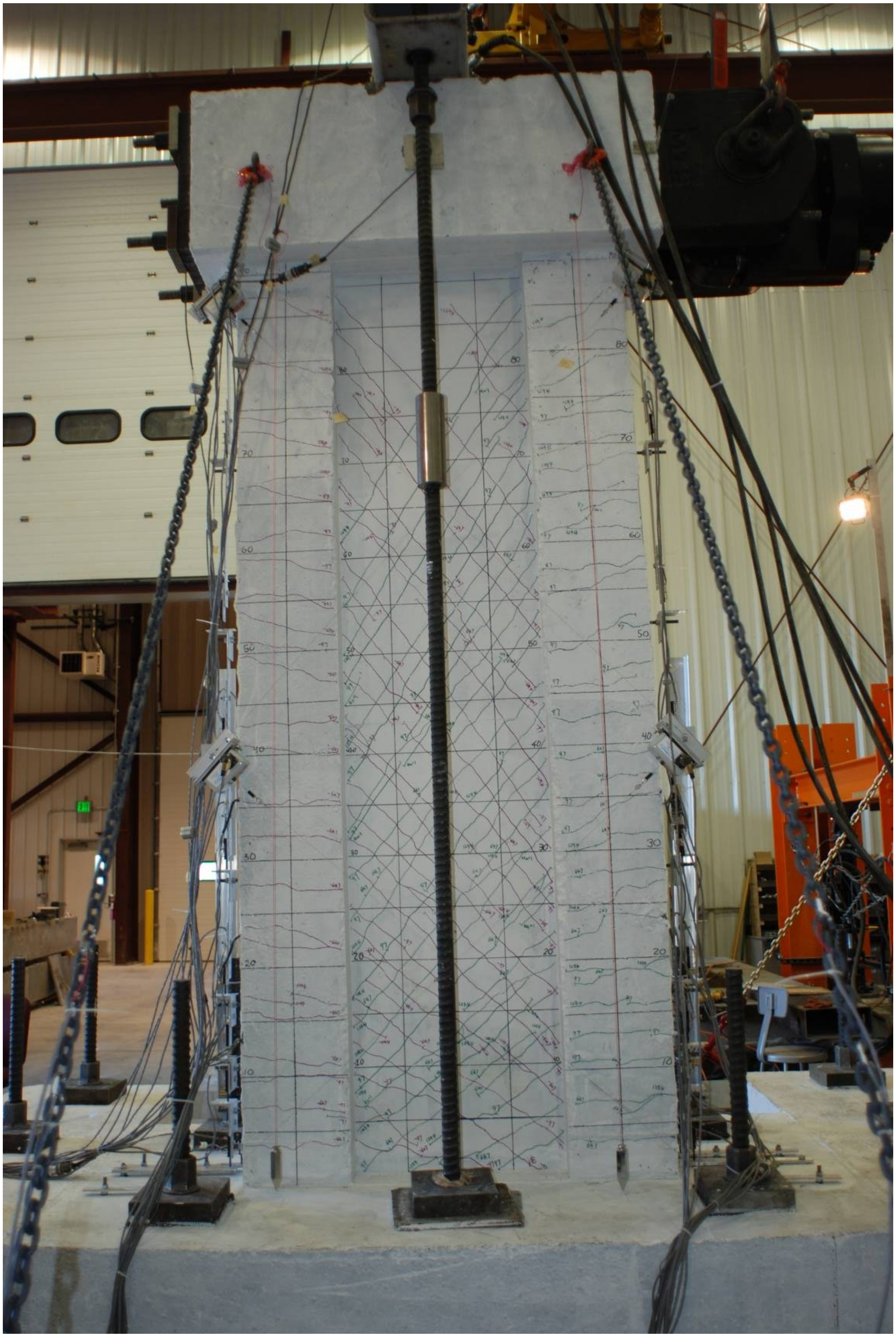

Figure 3.7 Test Unit M20C: south face, μ_Δ= 1 x +1, push (positive) towards west.

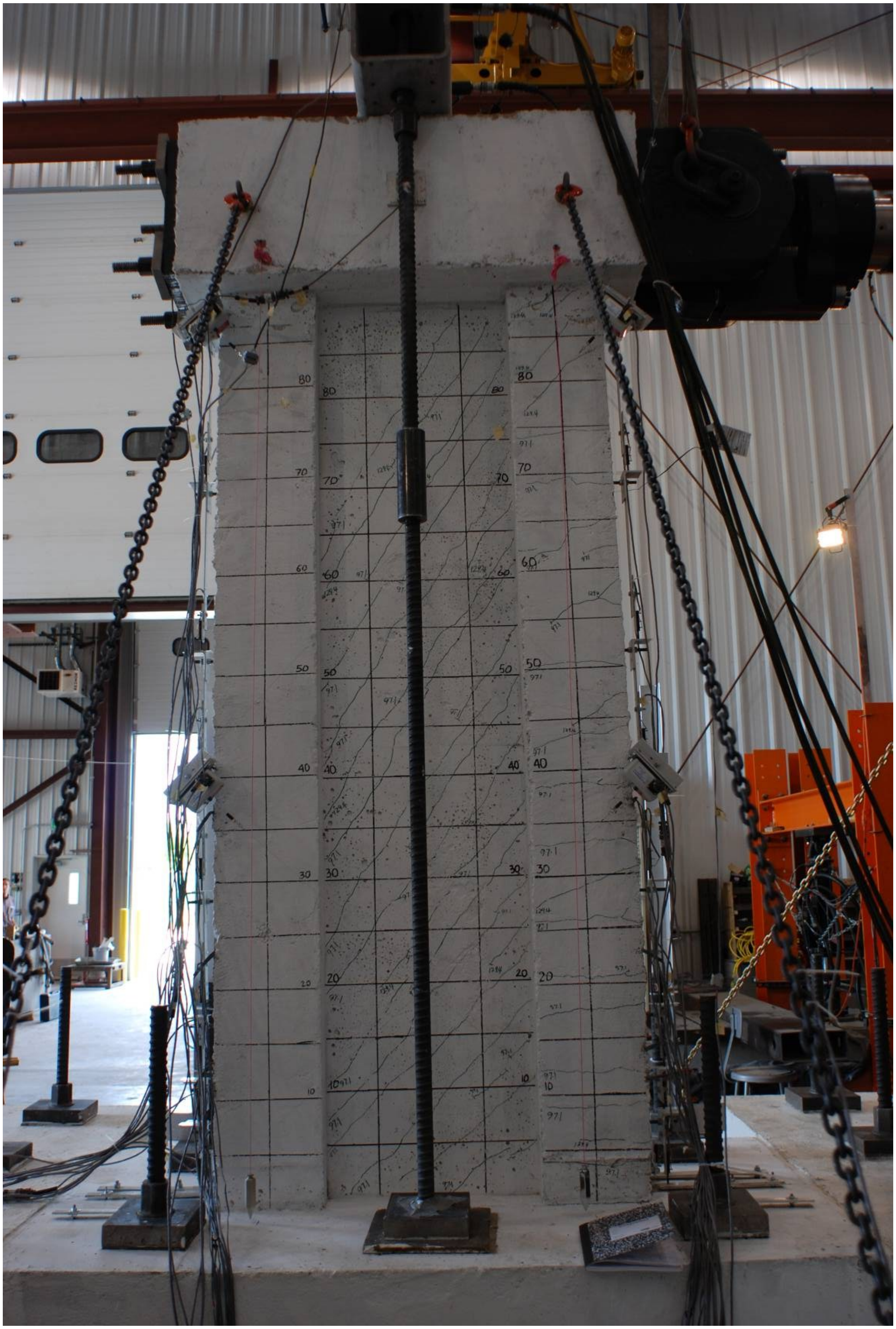

Figure 3.8 Test Unit M05M: south face, force control F'_y, push (positive) towards west.

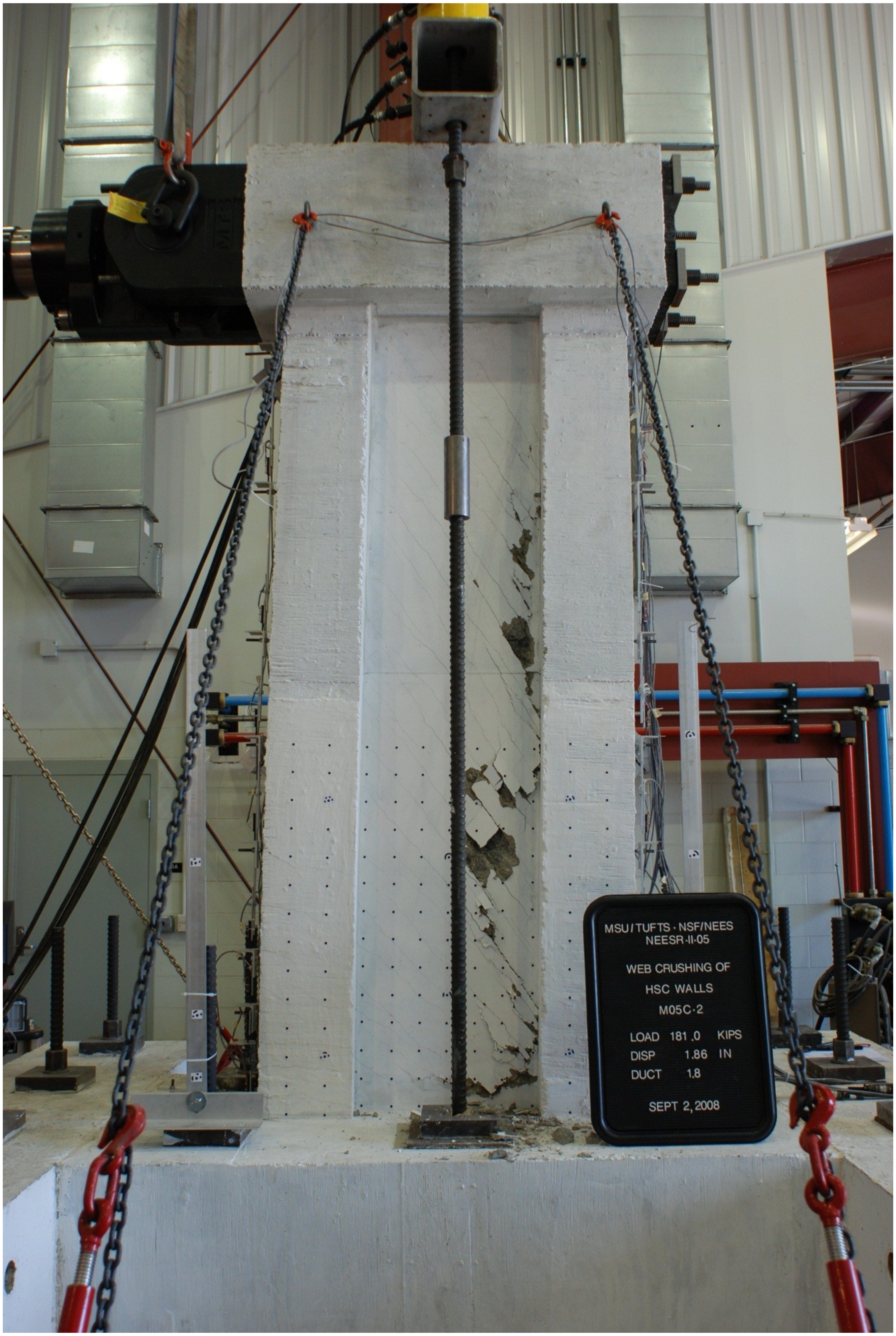

Figure 3.9 Test Unit M05C: north face, μ_{Δ} = 1.8 x +1, push (positive) towards west.

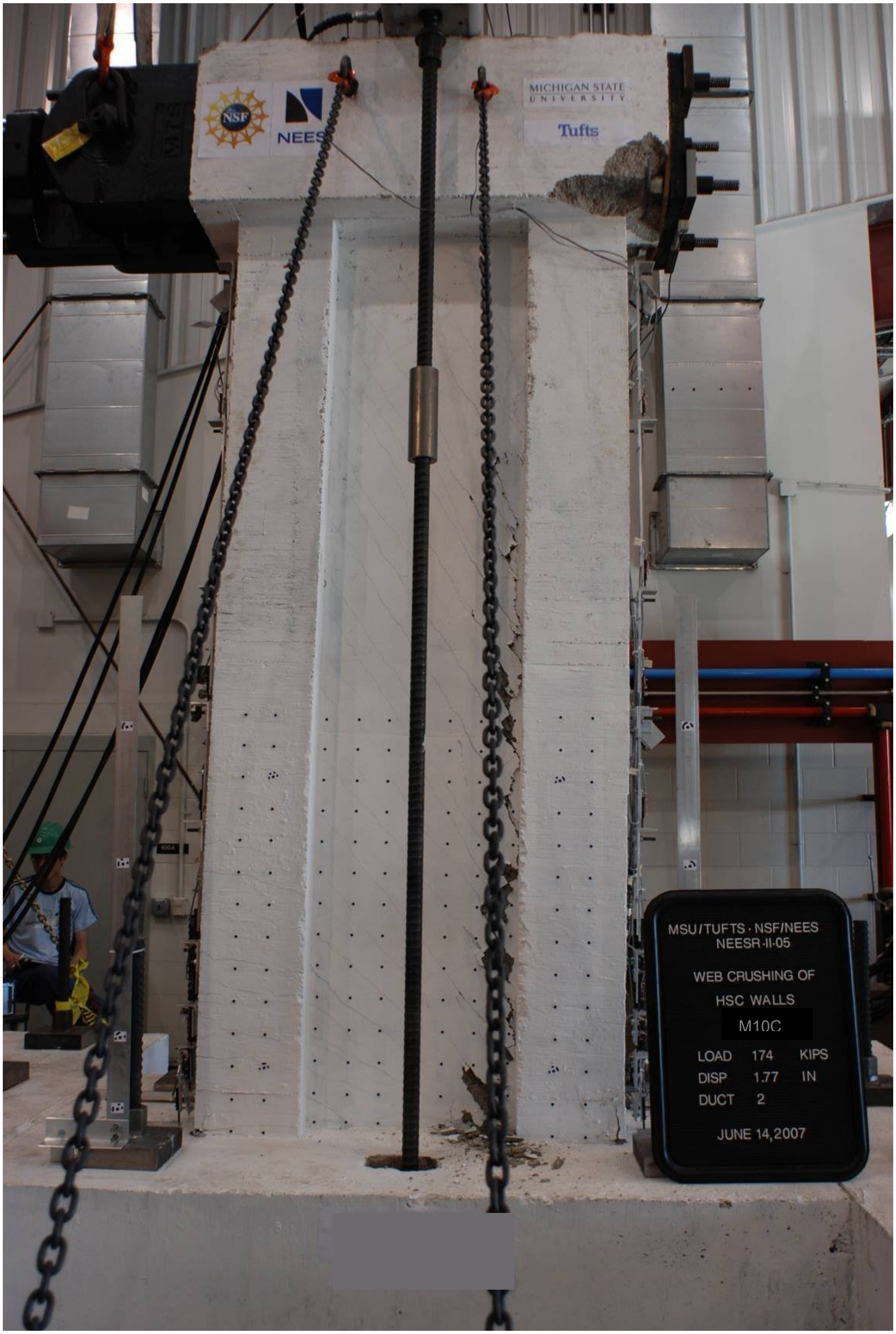

Figure 3.10 Test Unit M10C: north face, μ_Δ = 2 x +1, push (positive) towards west.

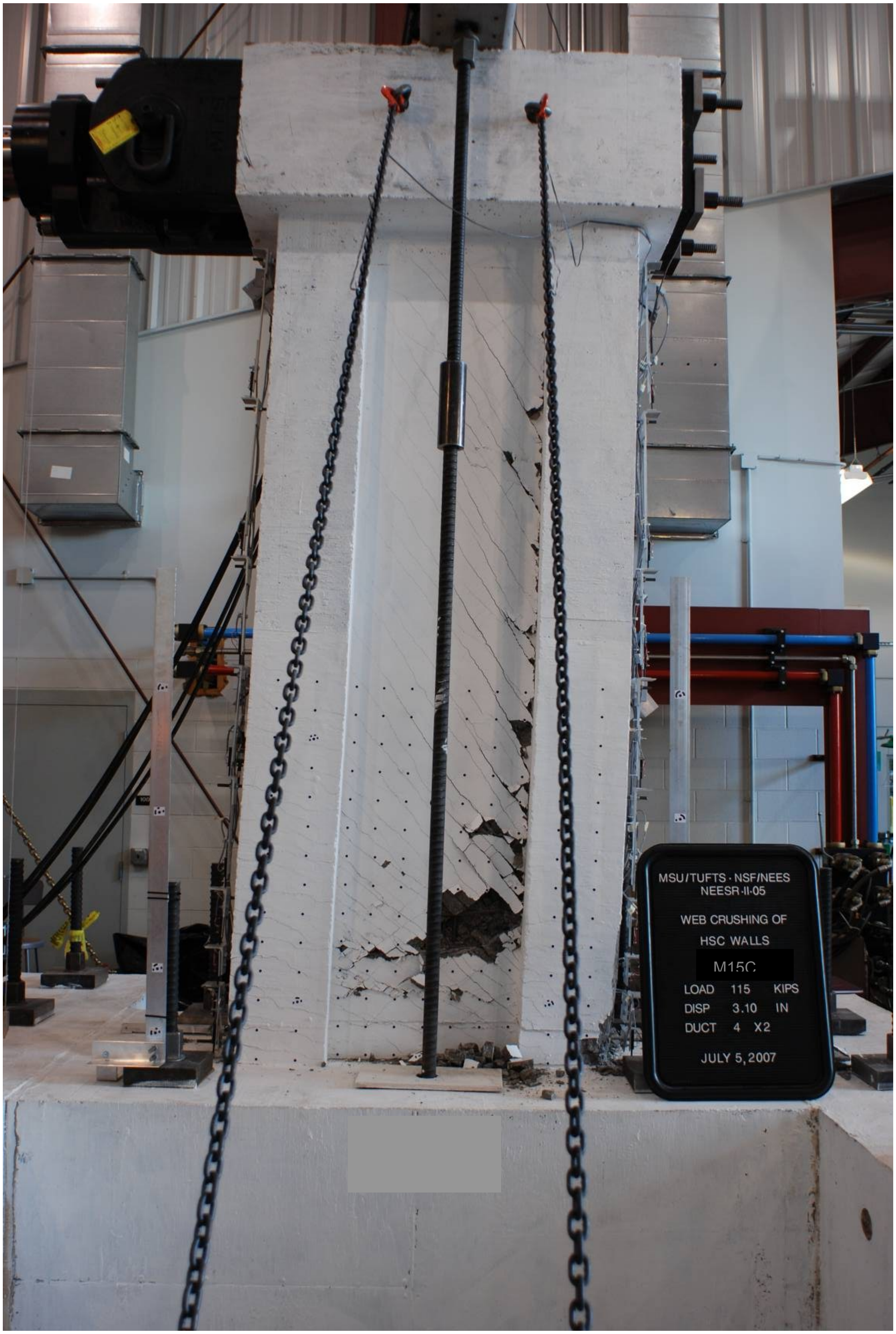

Figure 3.11 Test Unit M15C: north face, μ_{Δ} = 4 x +2, push (positive) towards west.

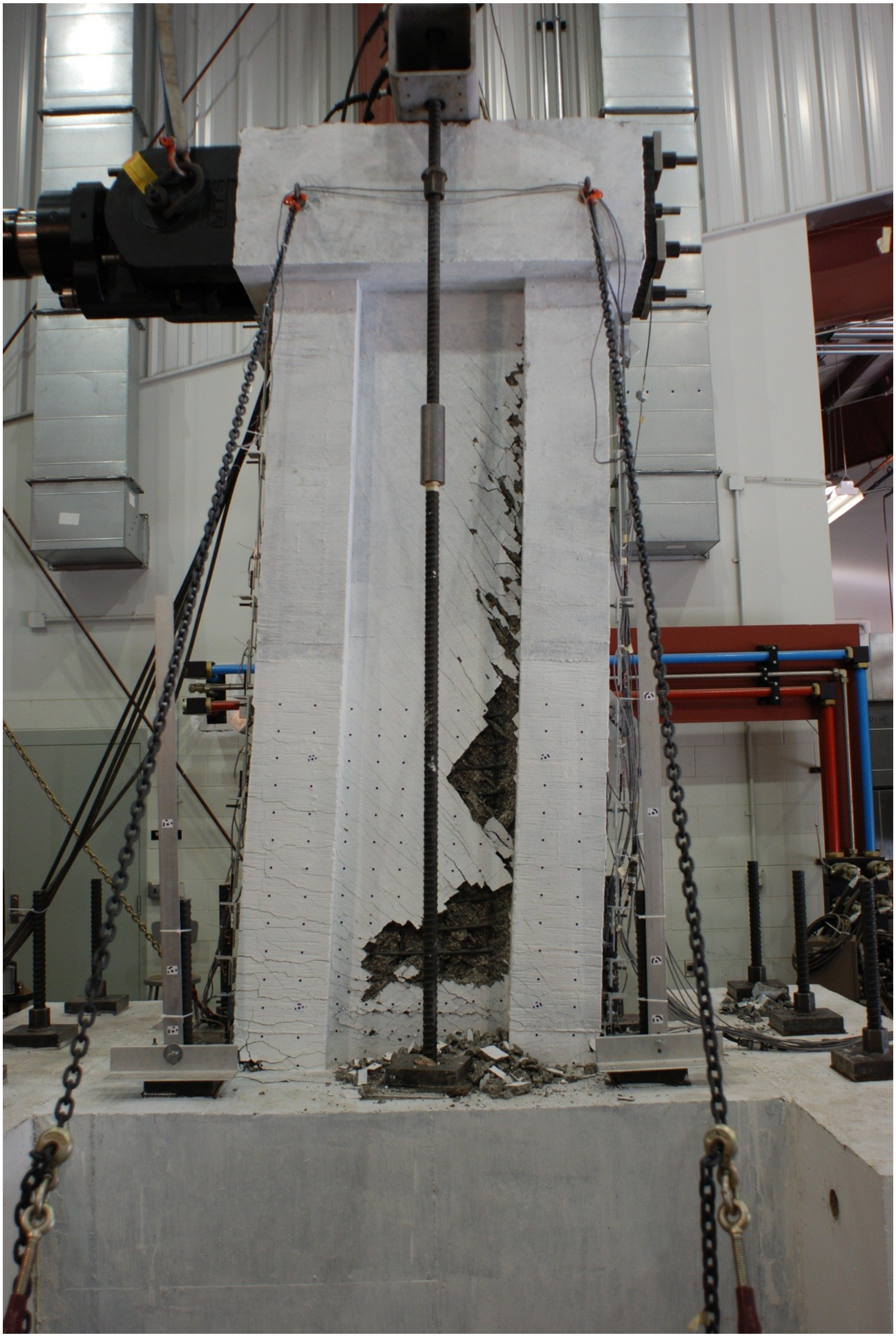

Figure 3.12 Test Unit M20C: north face, μ_{Δ} = 6 x 1, push (positive) towards west.

Figure 3.13 Test Unit M05M: north face, $\mu_\Delta = 2.3$, push (positive) towards west.

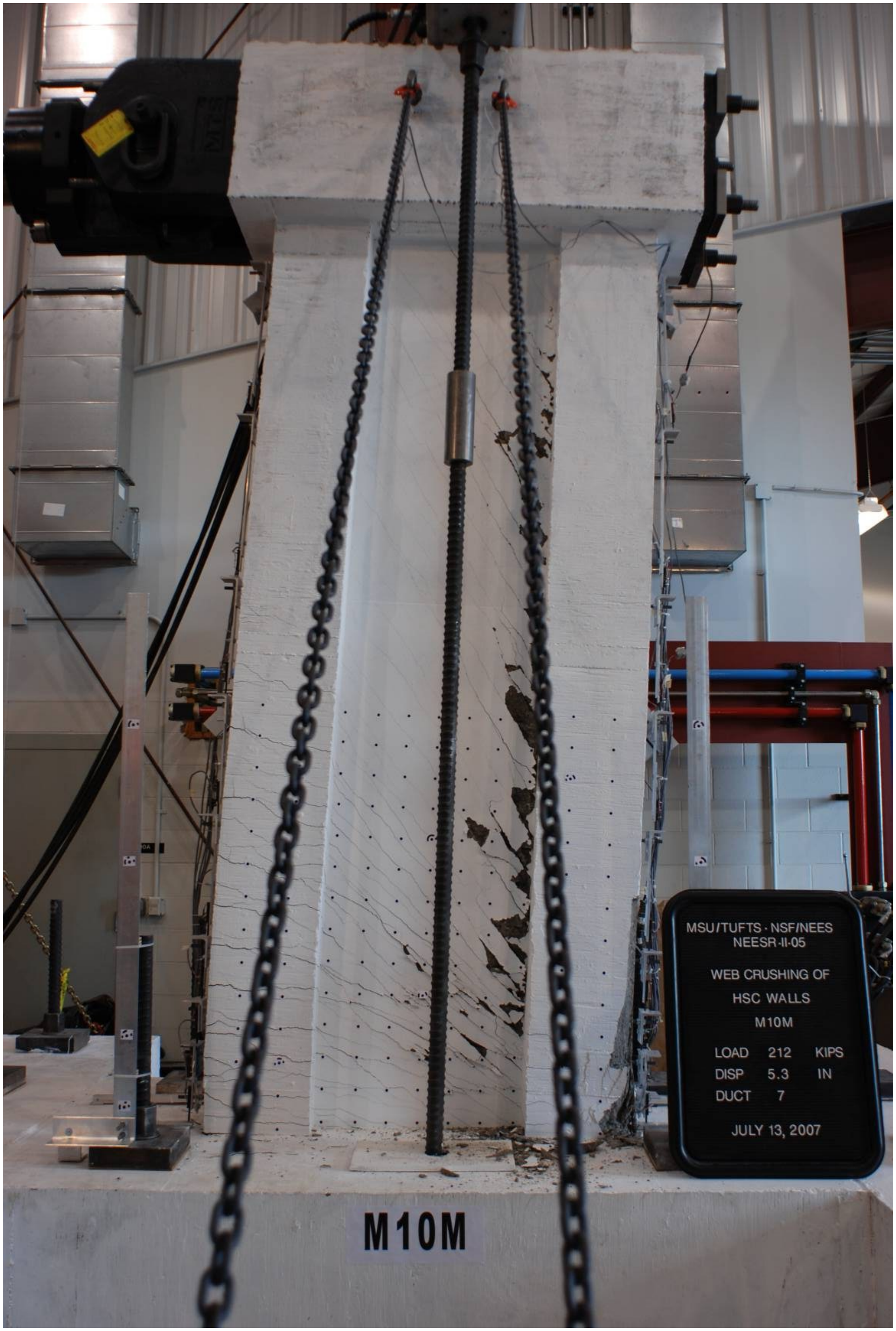

Figure 3.14 Test Unit M10M: north face, $\mu_\Delta = 7$, push towards west.

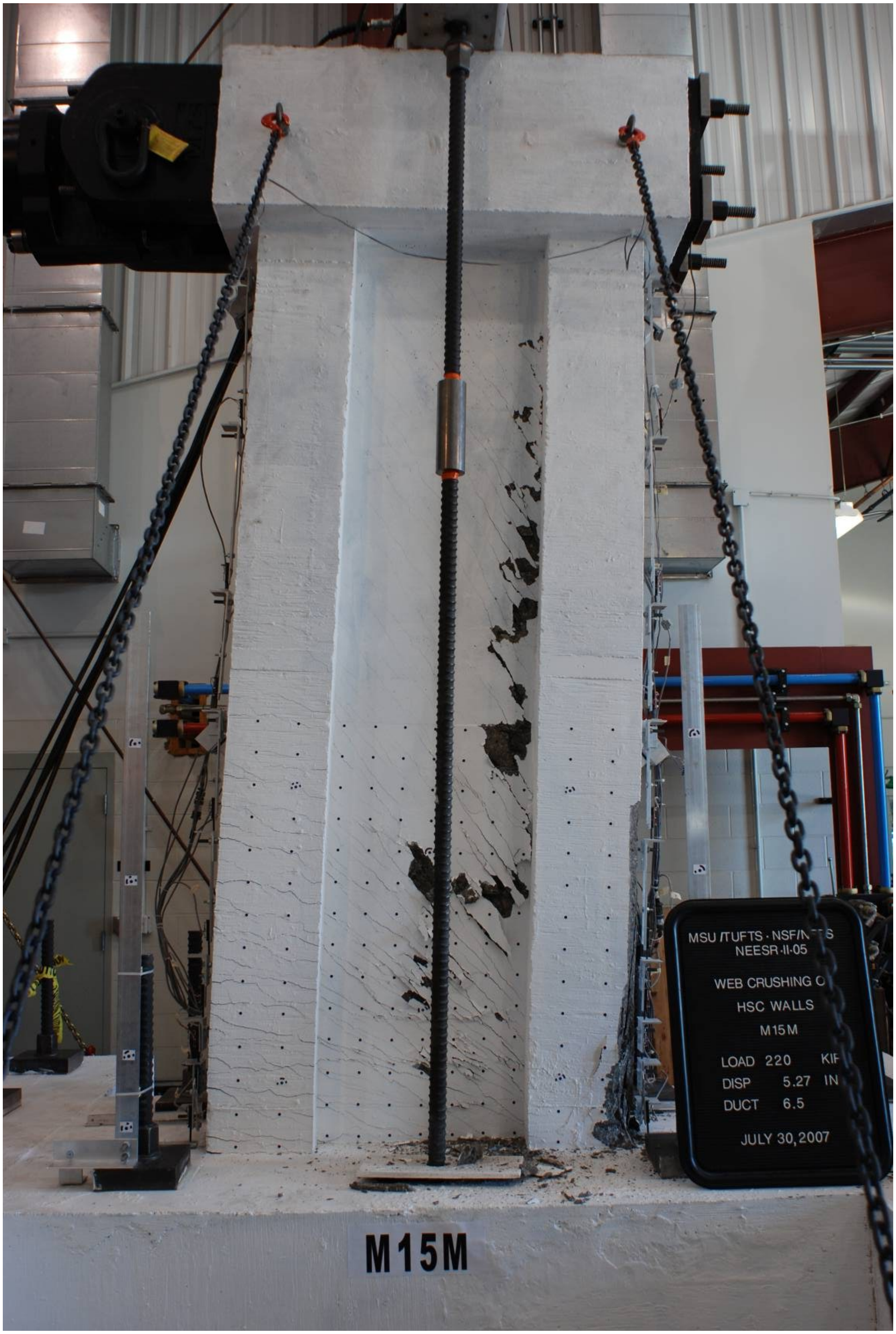

Figure 3.15 Test Unit M15M: north face, μ_{Δ} = 6.5, push towards west.

Figure 3.16 Test Unit M20M: south face, μ_{Δ}= 9.2, push towards west.

3.4 Experimental Results

The hysteretic force-displacement response of the four walls under cyclic loading is shown in Figure 3.17 to Figure 3.20. Test data reduction was conducted to separate the flexure and shear deformations in order to study the strength/stiffness degradation and energy-dissipating capacity of the test units. Table 3-5 shows the calculated flexural and shear deformations, their corresponding ratio and the calculated and measured total deformation versus ductility levels for all walls. A comparison of the sum of the flexure and shear deformations with the measured values verifies the accuracy of the curvature and shear instrumentation. The ratio of the flexural and shear deformation ranges between 18~34% with a mean value of approximately 24%, which was the value used to estimate shear deformations in the force-displacement characterization described in Section 2.2. Furthermore, it can be seen through the comparison of flexural and shear deformations that the single walls exhibited a flexure-dominated behavior, which can also be seen in Figure 3.21 to Figure 3.24 where the hysteretic loops of M05C and M20C in flexure and shear are shown. The hysteretic loops of the flexural deformation versus shear deformation show that a constant ratio of the shear over flexural deformation could represent the relationship well, as is illustrated in Figure 3.25, particularly at moderate to large levels of inelastic response.

Even if shear deformation is only a small portion of the total deformation, it cannot be overlooked considering that web crushing is a shear failure mode. The contribution of the shear deformation from the bottom panel and top panel was thus investigated. The bottom panel mainly covers the plastic hinge region and is the area where web crushing initiates. Refer to Figure 3.4 for the layout of the instrumentation. Figure 3.26 and Figure 3.27 show a comparison of the shear behavior measured from the two panels for M05C and M20C, respectively. It can be seen that comparable shear deformations were obtained from the top and bottom panels for wall M05C. Almost a linear shear force-displacement relationship is observed from the two panels. In contrast, the shear deformation from the bottom panel is much larger than that from the top panel for wall M20C. A ductile shear behavior can be observed on the bottom panel, while an elastic shear response is observed on the top one. Based on the difference of the measured shear force-deformation response between the NSC and HSC structural walls, the web crushing of NSC walls can be defined as an elastic shear failure while that of the HSC walls is better defined as an inelastic shear failure.

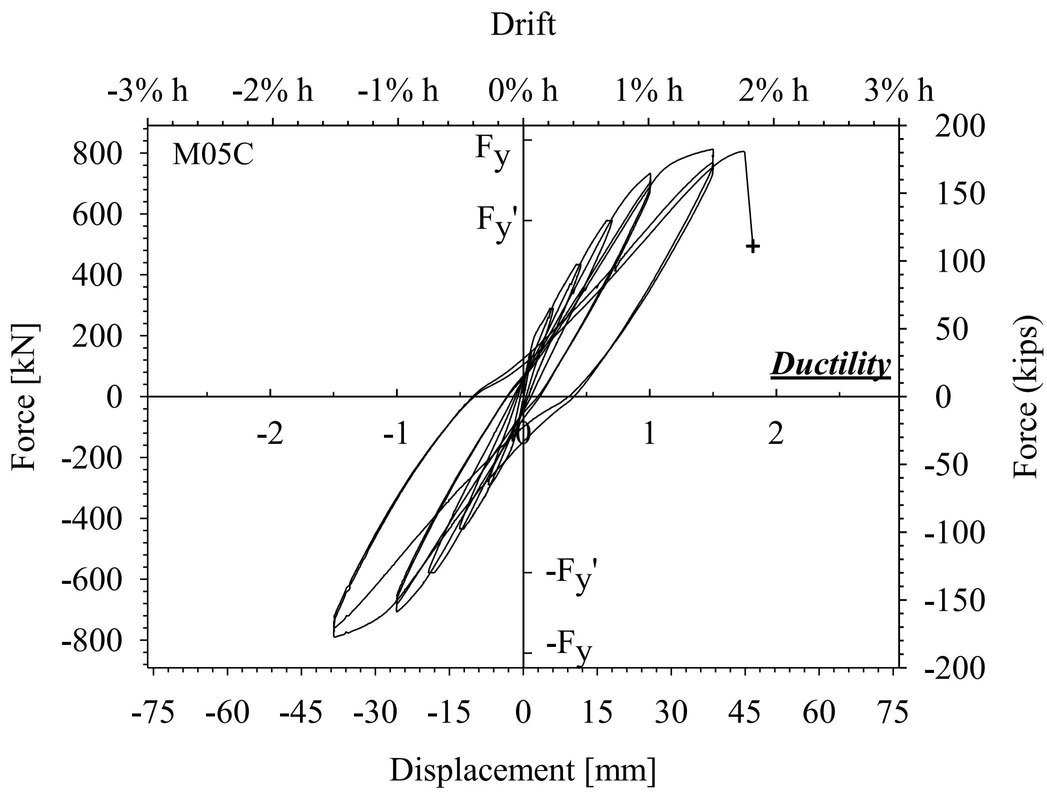

Figure 3.17 Test Unit M05C: Hysteretic loops.

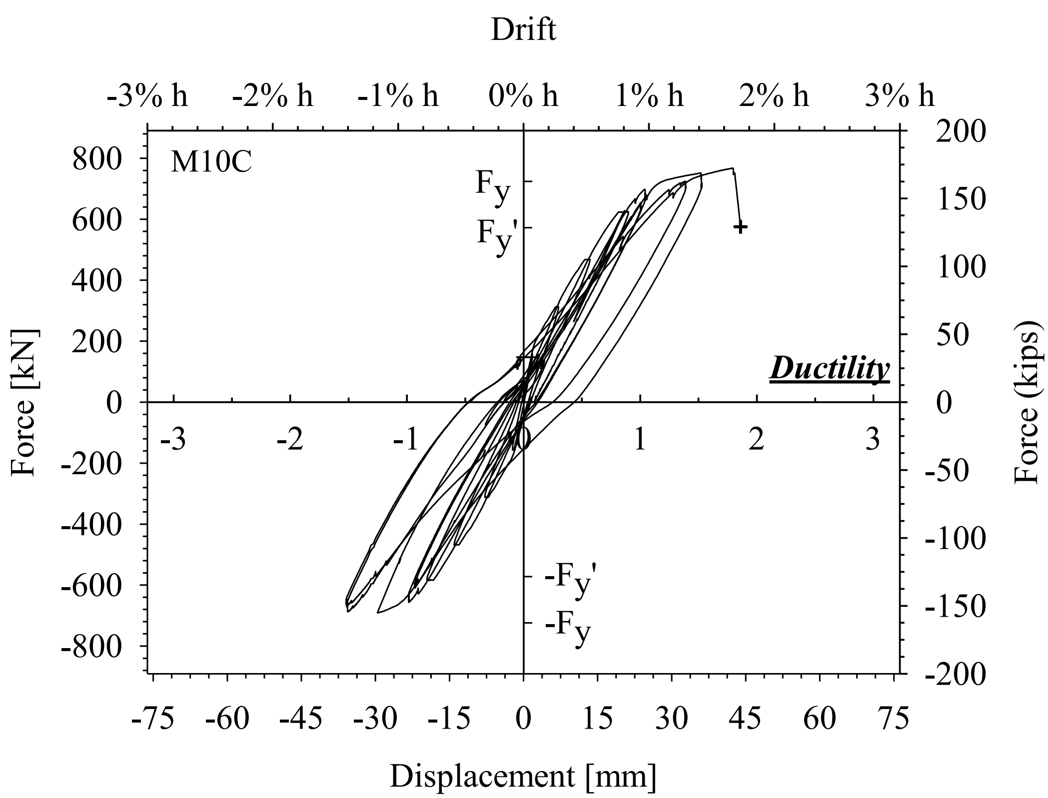

Figure 3.18 Test Unit M10C: Hysteretic loops.

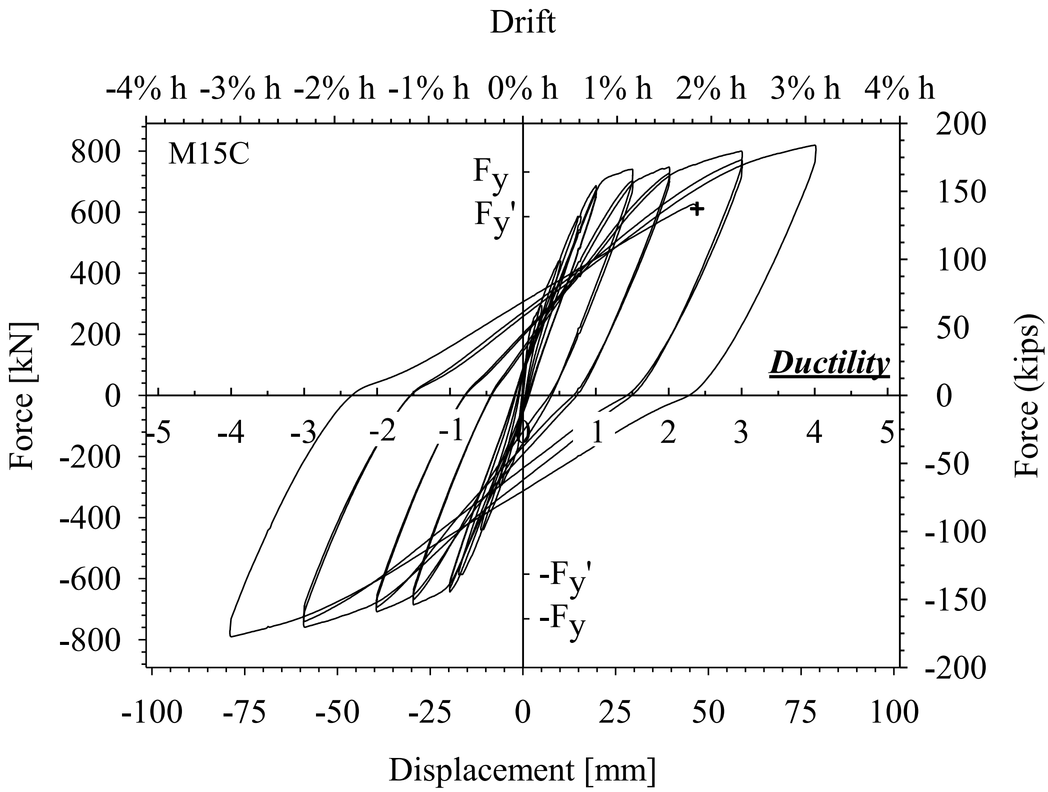

Figure 3.19 Test Unit M15C: Hysteretic loops.

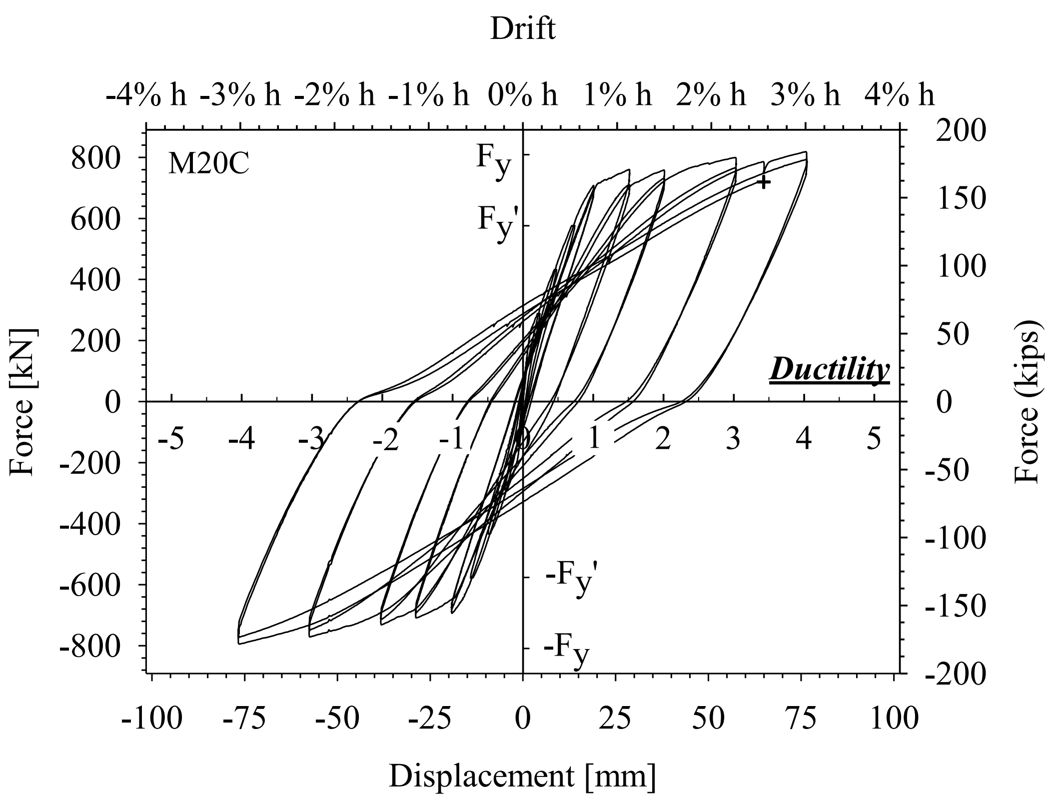

Figure 3.20 Test Unit M20C: Hysteretic loops.

Table 3-5 Single wall tests: flexural and shear deformations versus ductility levels and comparison of the calculated and measured global displacement

Single Wall Test Unit	μ_Δ	Δ_f (mm)	Δ_s (mm)	Δ_s/Δ_f	$\Delta_f + \Delta_s$ (mm)	$\Delta_{t,exp}$ (mm)
M05C	1 x 1	18.5	5.08	0.27	23.6	25.7
	1.5x 1	28.4	7.62	0.27	36.1	38.4
M05M	1	22.6	7.37	0.33	30.0	31.0
	1.5	34.3	10.4	0.30	44.7	45.0
M10C	1 x 1	18.0	6.10	0.34	24.1	24.6
	1.5 x 1	27.7	7.87	0.28	35.6	36.1
M10M	1	13.7	3.81	0.28	17.5	19.1
	1.5	21.6	5.33	0.25	26.9	28.7
	2	30.2	6.60	0.22	36.8	38.4
	3	46.7	9.65	0.21	56.4	57.4
	4	63.0	13.2	0.21	76.2	76.5
	5	79.2	16.8	0.21	96.0	95.5
	6	95.3	20.3	0.21	116	115
M15C	1 x 1	14.5	3.56	0.25	18.0	19.8
	1.5 x 1	22.6	4.83	0.21	27.4	29.5
	2 x 1	30.5	6.60	0.22	37.1	39.4
	3 x 1	47.0	9.40	0.20	56.4	58.9
	4 x 1	62.5	13.2	0.21	75.7	78.7
M15M	1	15.0	4.06	0.27	19.1	20.6
	1.5	23.4	5.59	0.24	29.0	31.0
	2	32.3	6.86	0.21	39.1	41.1
	3	48.5	9.65	0.20	58.2	61.7
	4	65.8	11.7	0.18	77.5	82.3
	5	82.8	15.7	0.19	98.6	103
	6	99.3	19.6	0.20	119	123
M20C	1	14.5	3.30	0.23	17.8	19.1
	1.5	23.1	4.57	0.20	27.7	28.7
	2	30.7	6.60	0.21	37.3	38.1
	3	47.0	9.91	0.21	56.9	57.4
	4	62.0	15.5	0.25	77.5	76.5
M20M	1	15.5	3.81	0.25	19.3	20.1
	1.5	24.6	5.33	0.22	30.0	30.7
	2	33.8	6.86	0.20	40.6	41.4
	3	52.3	9.91	0.19	62.2	62.7
	4	70.4	13.5	0.19	83.8	84.3
	5	87.9	17.3	0.20	105	106
	6	106	21.3	0.20	127	127
	7	125	27.2	0.22	153	151
	8	140	32.3	0.23	172	170

Note: 1 in. = 25.4 mm.

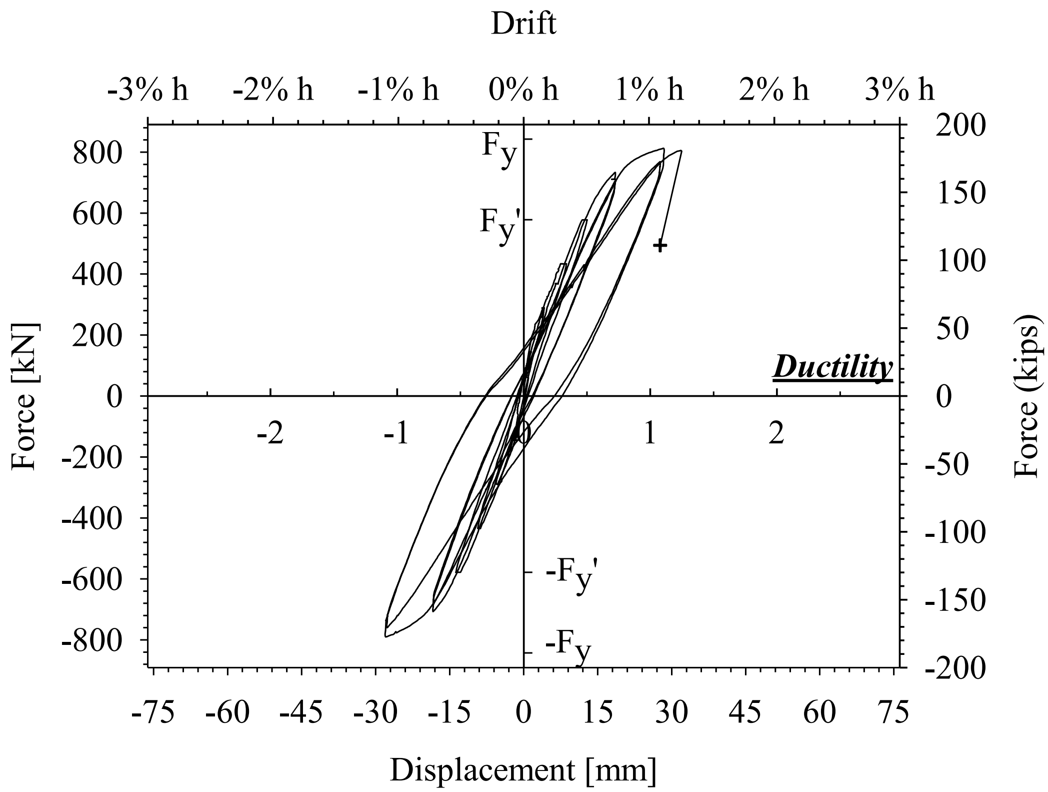

Figure 3.21 Test Unit M05C: Hysteretic loop in flexure.

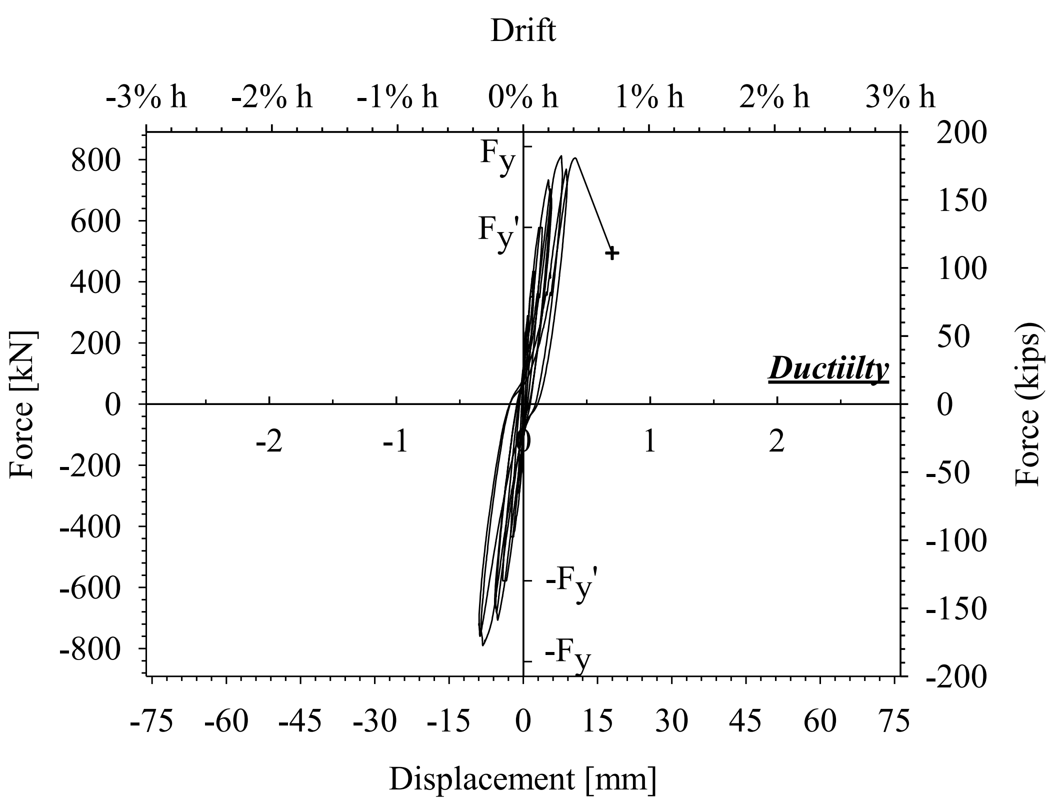

Figure 3.22 Test Unit M05C: Hysteretic loop in shear.

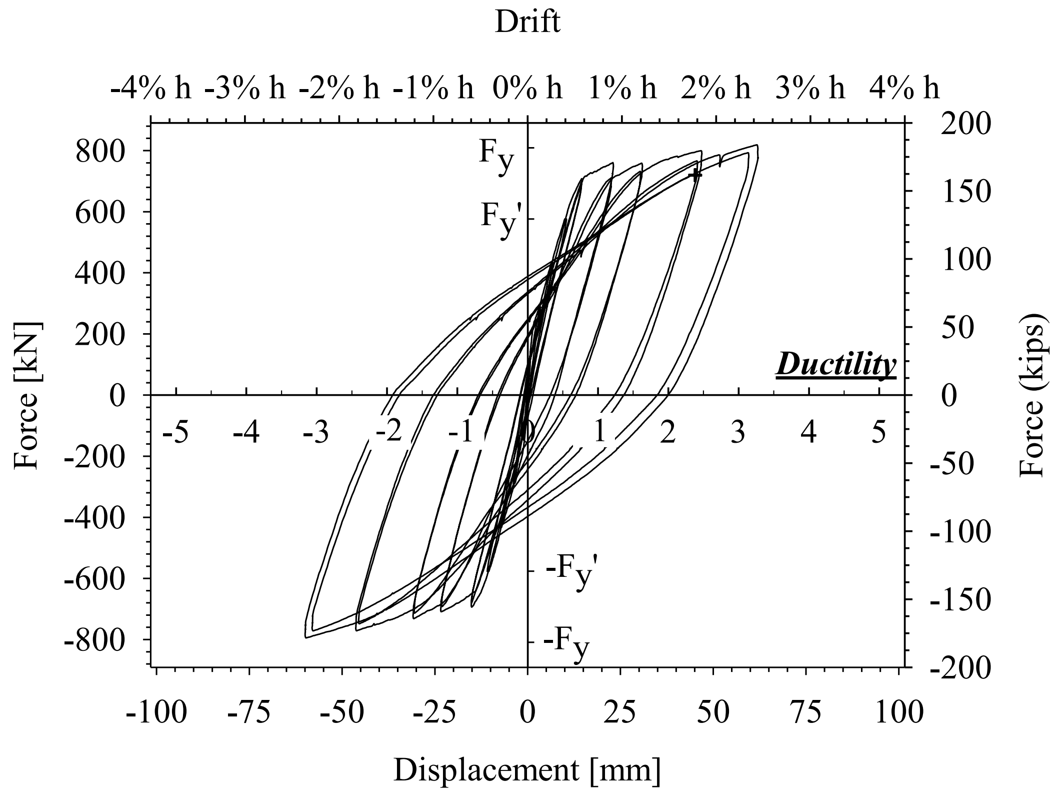

Figure 3.23 Test Unit M20C: Hysteretic loop in flexure.

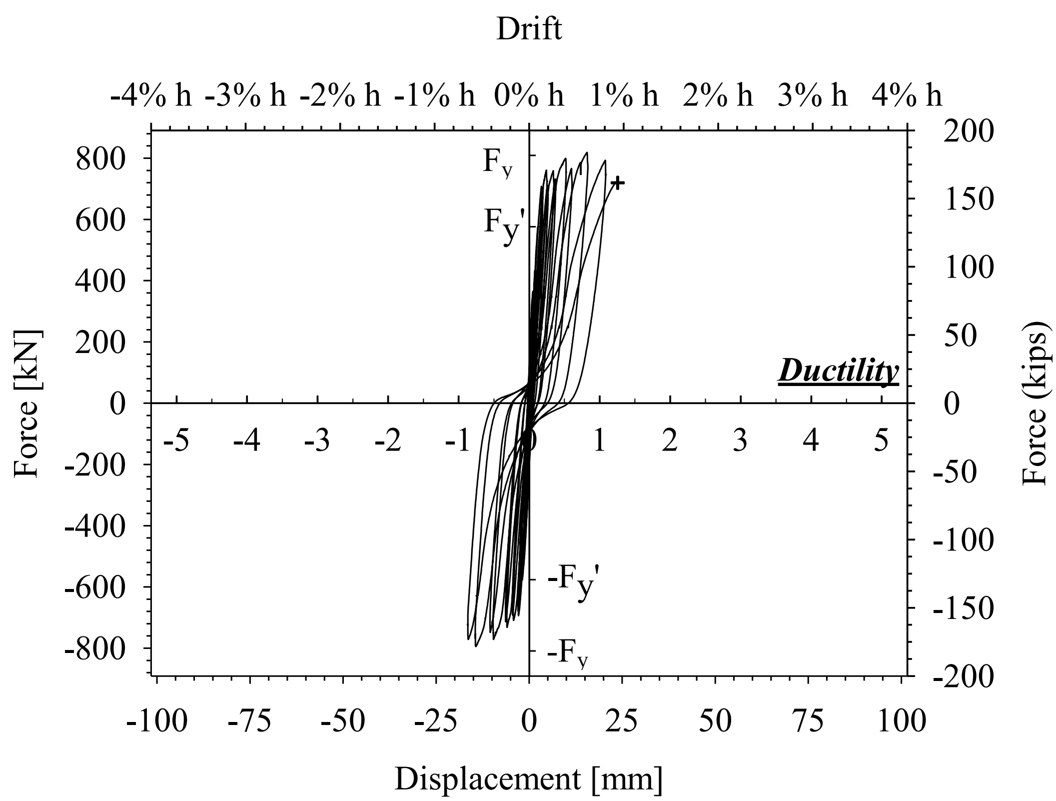

Figure 3.24 Test Unit M20C: Hysteretic loop in shear.

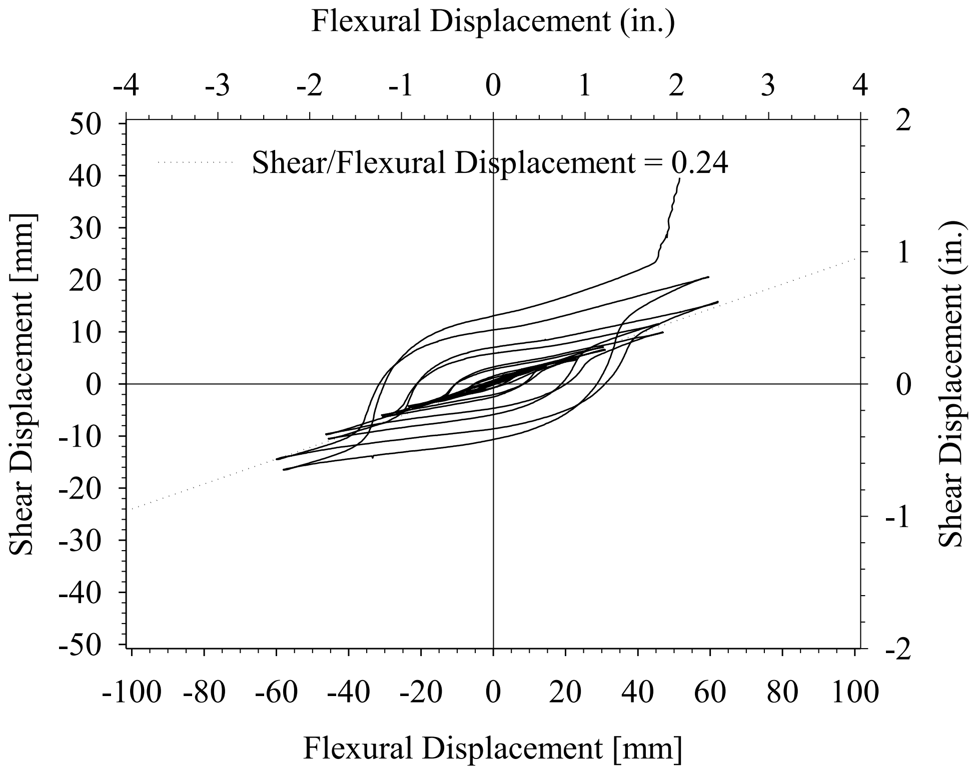

Figure 3.25 Test Unit M20C, shear displacements as a function of the flexural displacements

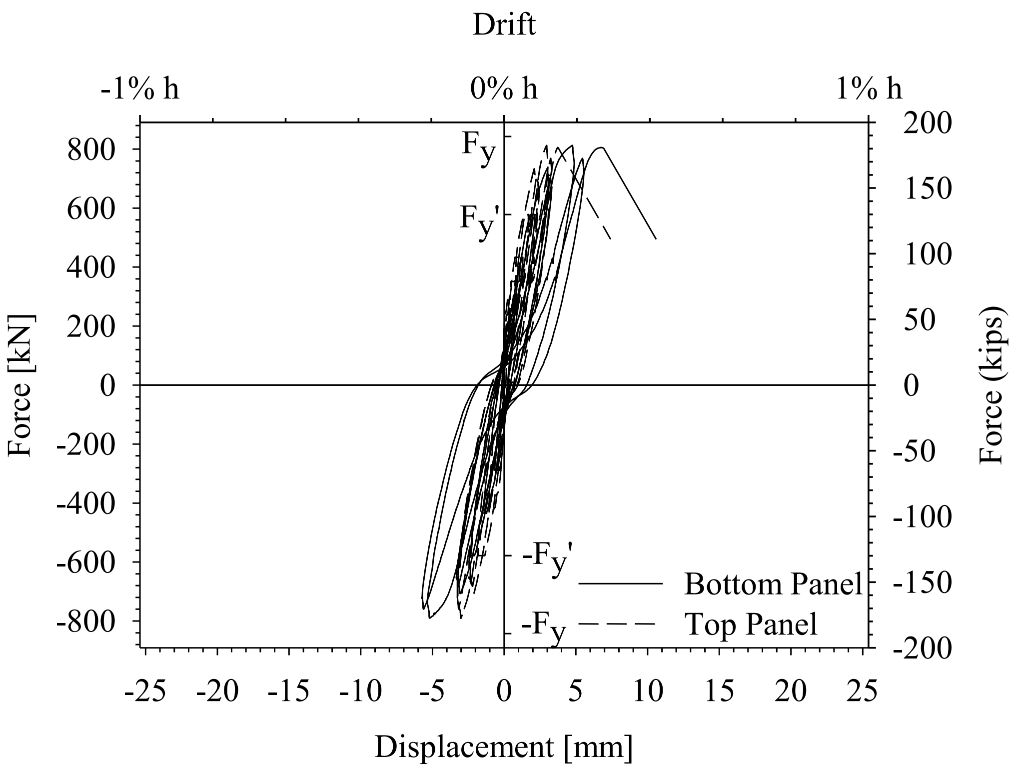

Figure 3.26 Test Unit M05C: Comparison of the shear deformation between the bottom and top panel.

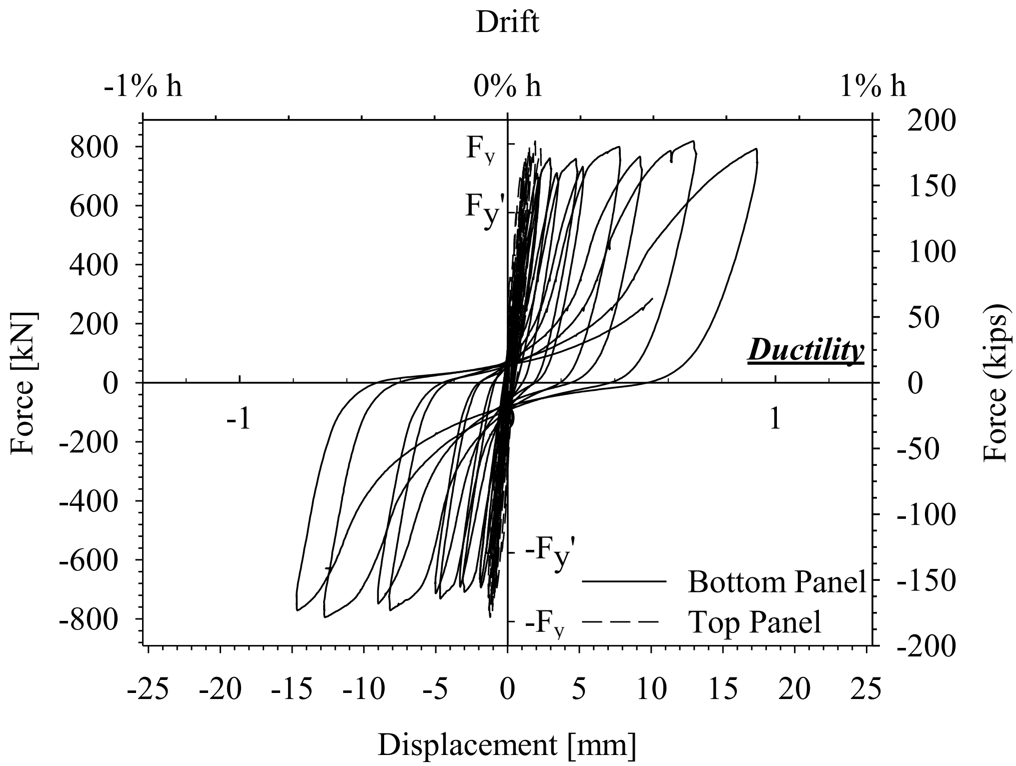

Figure 3.27 Test Unit M20C: Comparison of the shear deformation between the bottom and top panel.

The curvature profiles of walls M10 and M20 are shown in Figure 3.28 and Figure 3.29. It can be seen that the flexural deformation demands from the monotonic and cyclic test units was very similar. For the cyclically loading test units that failed at low to medium ductility levels, the curvature distribution along the height was almost linear until failure. For the monotonic loaded walls that failed at high ductility levels, the plastic rotations were mainly concentrated within 200 mm [8 in.] from the bottom of the wall. Figure 3.30 compares strain profiles on the transverse steel at different height levels for walls M10C and M20C. The wall transverse steel yielded before failure in both tests, which impairs the confining effect onto the web concrete and most importantly, causes the cover concrete of the web spall off easier and thus degrades the compression capacity of the diagonal struts.

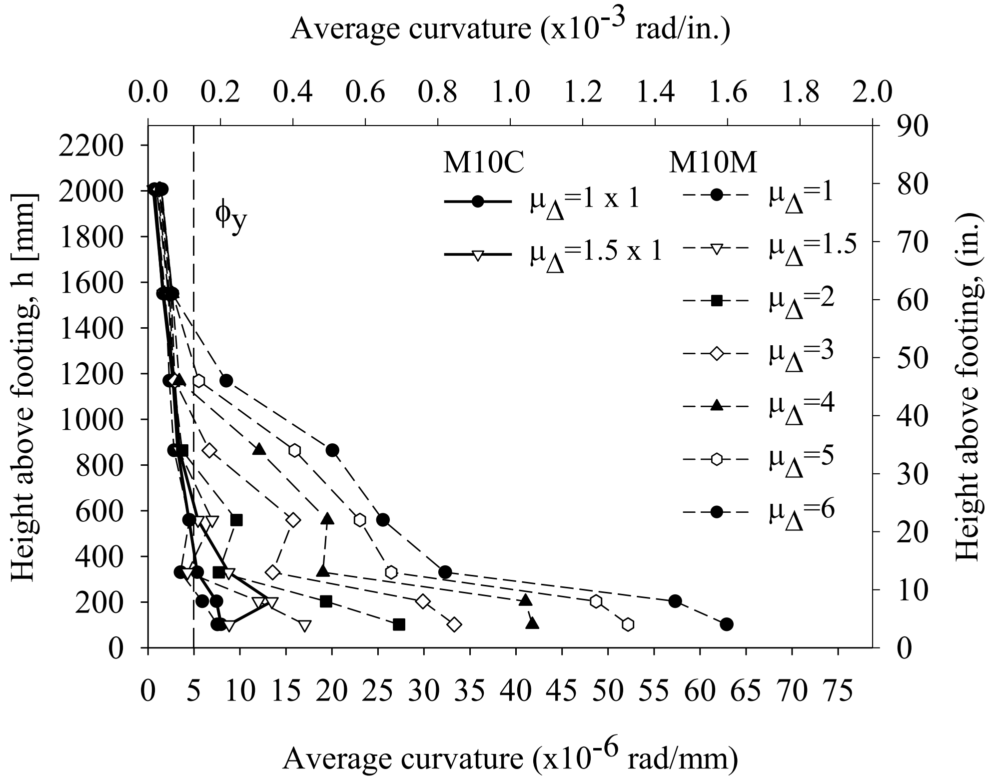

Figure 3.28 Test Units M10: Curvature profiles (average of push and pull maximums).

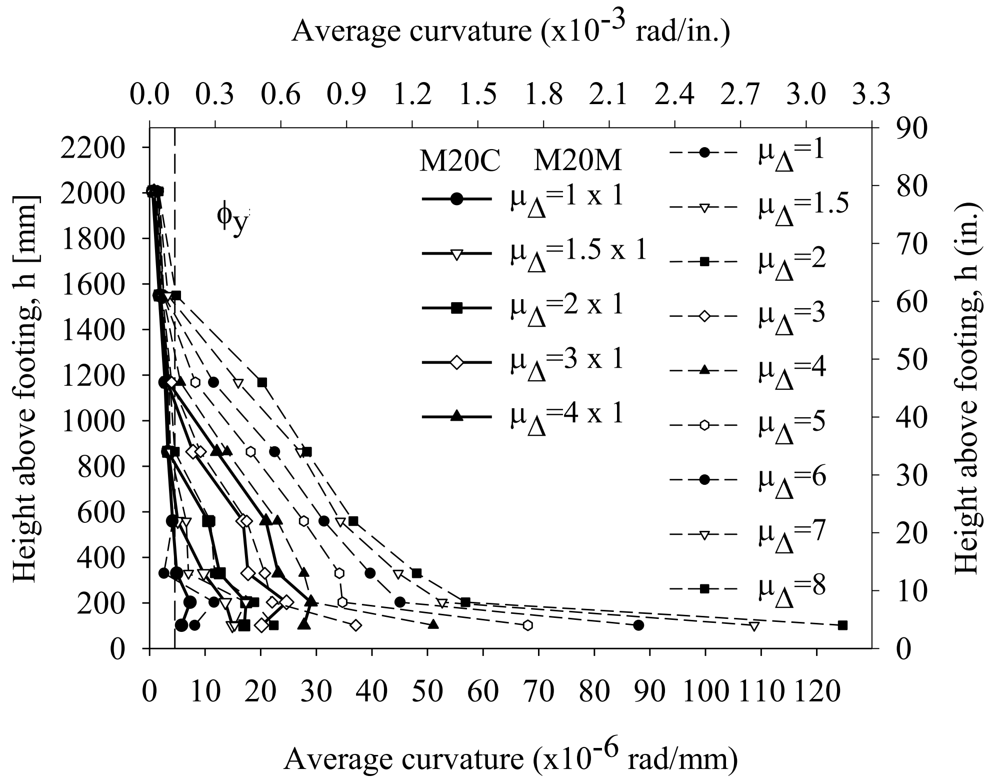

Figure 3.29 Test Units M20: Curvature profiles (average of push and pull maximums).

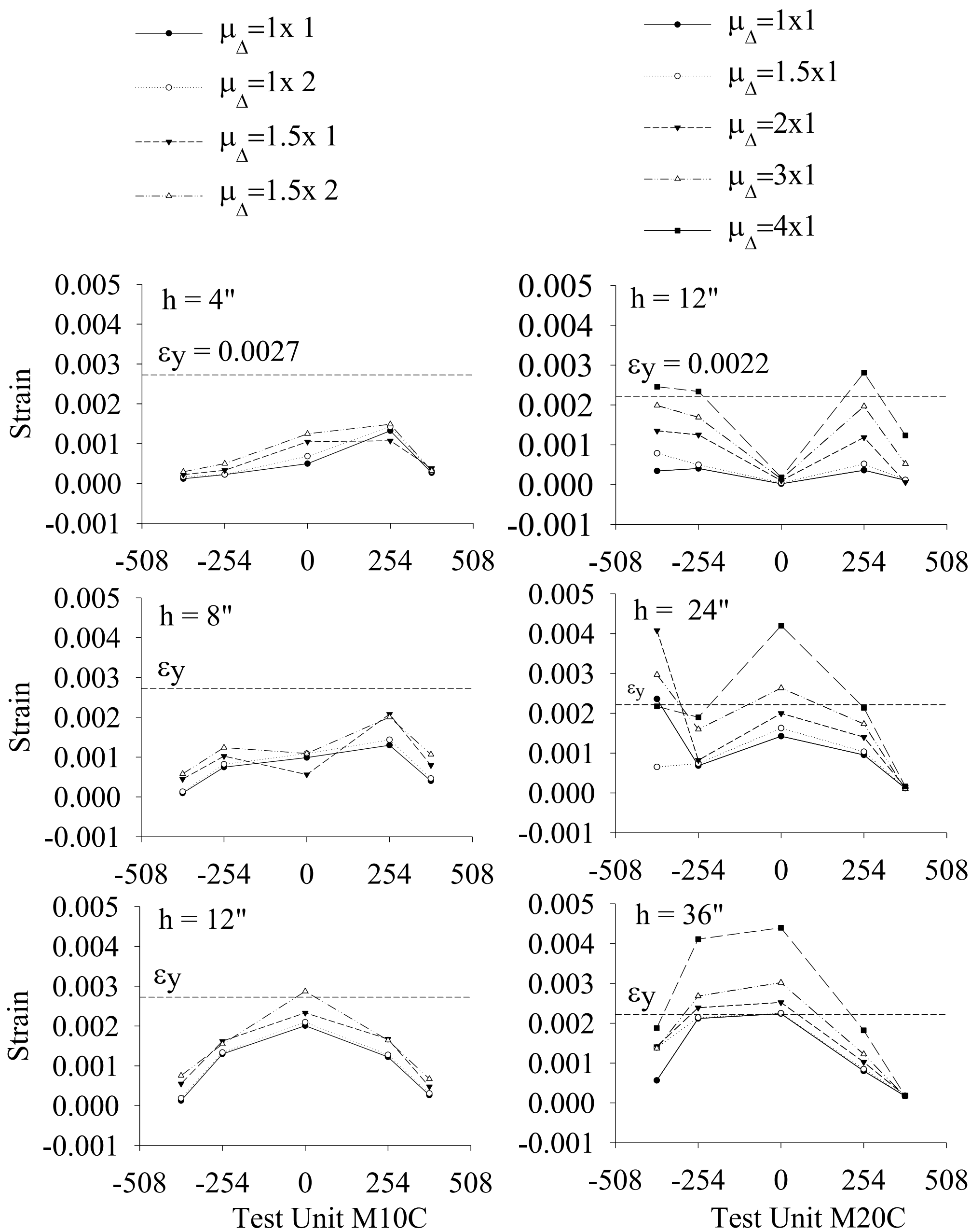

Note: 1 in. = 25.4 mm

Figure 3.30 Test Units M10C and M20C: Strain profiles of transverse steel.

A comparison of the force-displacement envelopes for the cyclic and monotonic tests is shown in Figure 3.31 to Figure 3.34. Walls M05C, M05M and M10C failed at a displacement ductility of about 1.5. The other walls exhibited moderate to high ductility before web crushing. Test units M15C and M20C achieved a displacement ductility of 4 while units M10M, M15M and M20M failed at a displacement ductility of 6~9. The results clearly show that the higher compressive strength allowed the walls to sustain higher inelastic deformation and a stable hysteretic ductile response. It can be seen in Figure 3.31 that cyclic loading had no significant effect on the capacity of the 34 MPa [5 ksi] test unit. However, cyclic loading, and its resulting degradation, had a growing effect on the web crushing limits with increasing concrete compressive strength. Thus, the gains in forestalling web crushing with higher concrete compressive strength were curtailed by the greater susceptibility of higher strength concrete to damage under cyclic loading, as higher concrete compressive strength results in more brittleness and less energy-dissipation capacity from the material. This explains the reasons for the comparable ductility levels achieved by walls M15C and M20C. Thus, the shear stiffness degradation and damage of HSC structural walls under load reversals has to be evaluated appropriately. Nonetheless, comparison of the response of walls M15M and M20M shows that M20M had a larger deformation capacity, which supports the hypothesis that the higher concrete strength can increase the inelastic capacity of structural walls with confined boundary elements.

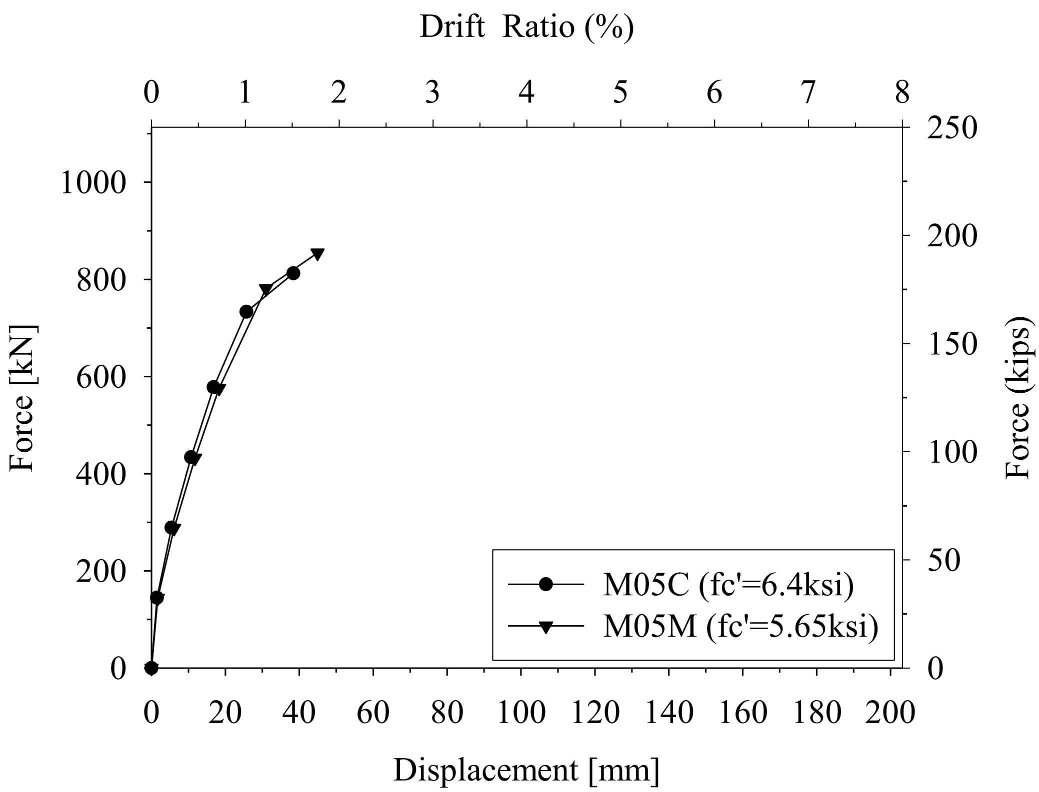

Figure 3.31 Test Units M05: Comparison of the force-displacement envelopes

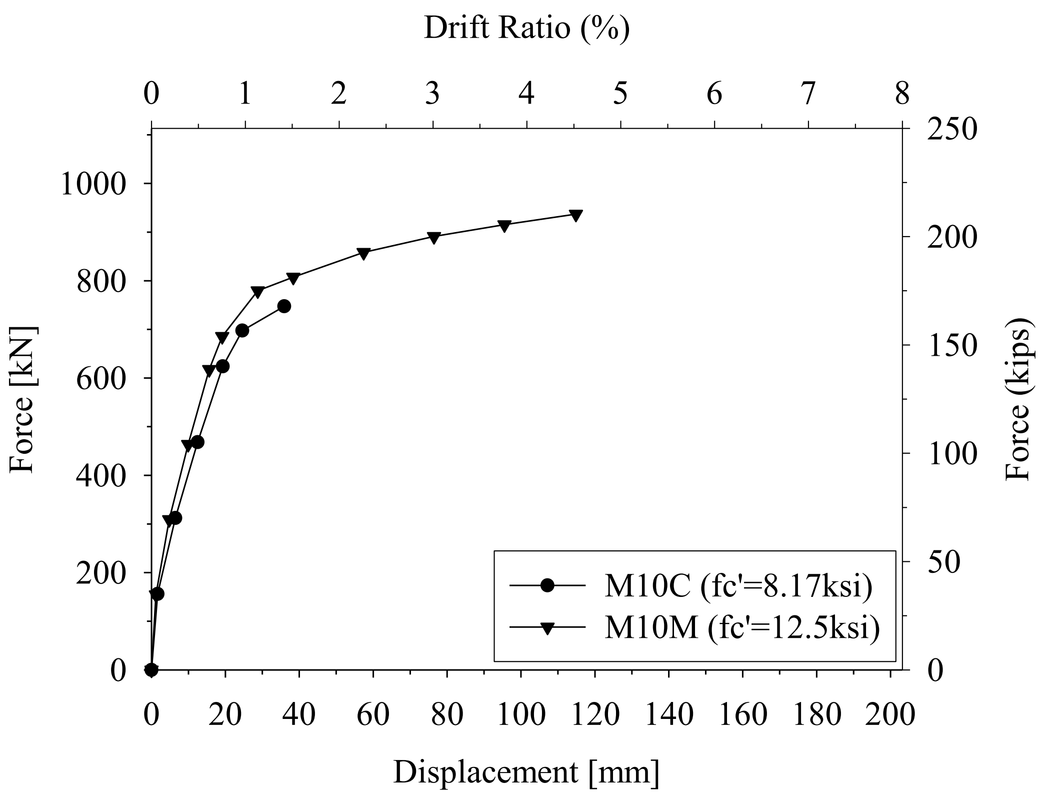

Figure 3.32 Test Units M10: Comparison of the force-displacement envelopes

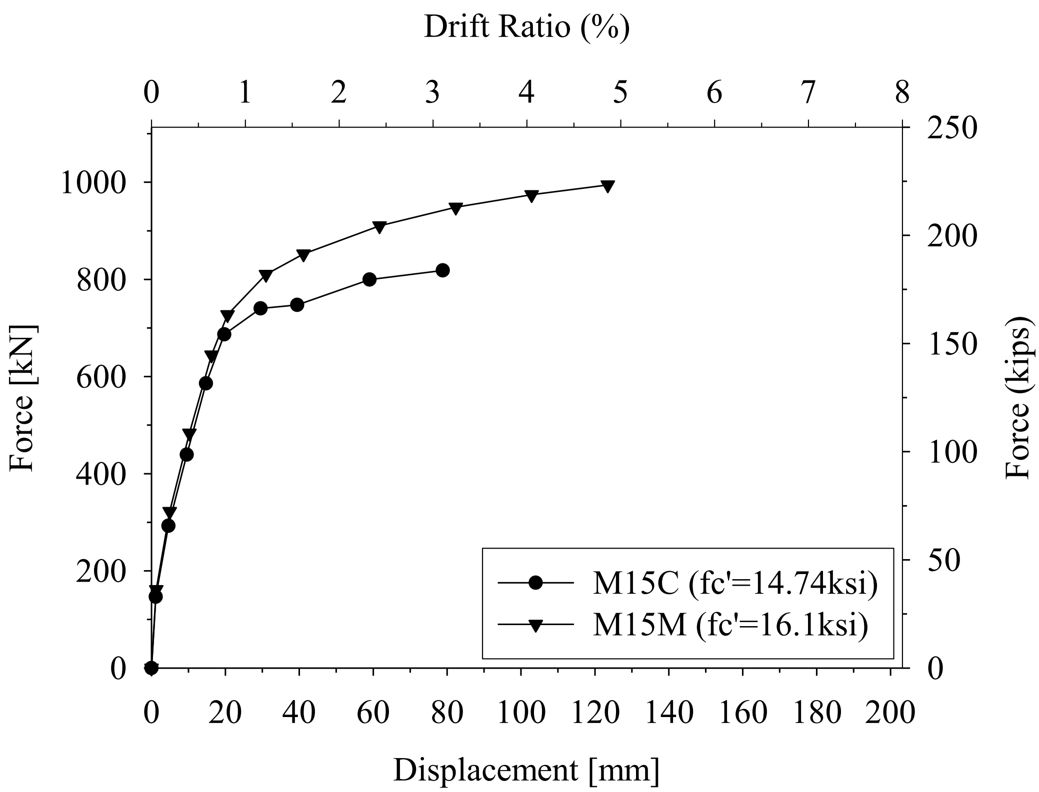

Figure 3.33 Test Units M15: Comparison of the force-displacement envelopes

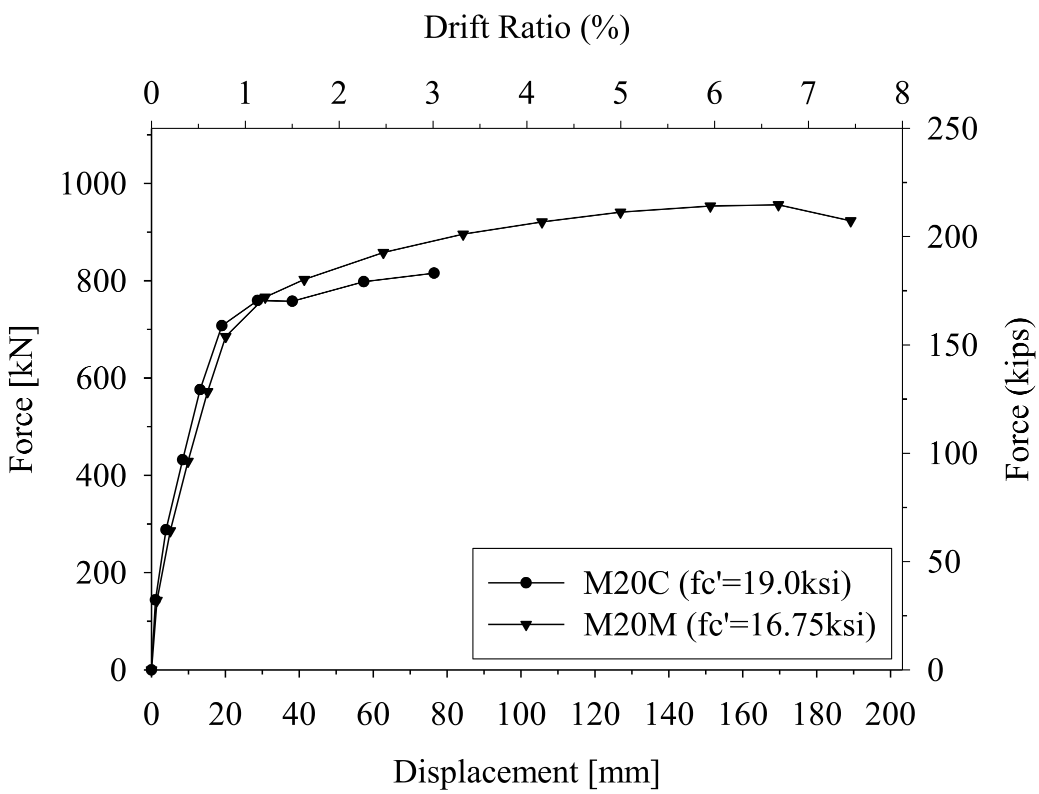

Figure 3.34 Test Units M20: Comparison of the force-displacement envelopes

3.5 Discussion

Table 3-6 compares the web crushing capacities of the eight single walls tested in the program with the capacities predicted by different models. It can be noted that the ACI shear provision considerably underestimates the web crushing strength. At the same time, the prediction quality of the model by Hines and Seible [16] on cyclic tests deteriorates with the increase of concrete compressive strength since the model was calibrated using wall tests with normal-strength-concrete and the strength and stiffness degradation of HSC was not taken into account. Thus, the experimental program revealed that rational web crushing models like the one by Hines and Seible need further considerations to be applicable to HSC structural walls.

The experimental program has clearly proven the hypothesis that HSC can forestall web crushing failures and allow the system to attain larger levels of inelastic deformation, thus obtaining an inelastic flexure-shear response, or a ductile shear failure. It is clear that the shear stress demands on the walls are well in excess of currently prescribed limits. However, the experiments revealed that while HSC enables the shear-carrying compressive struts to be stronger, and thus sustain higher effective wall shear stresses, the effect damage accumulation due to cyclic loading on HSC needs to be carefully evaluated. A preliminary evaluation was done with the model by Park and Ang [44] to assess the damage on the test units due to ultimate deformation and hysteretic energy dissipation. Figure 3.35 illustrates the damage indices of the four cyclic test units. The tendency of the damage indices based on test data can be fitted by an exponential function very well. It can be seen that with the increase of concrete strength, the damage due to ultimate deformation decreases while that due to the energy dissipation increases. Thus, the fact that HSC increases the energy dissipation capacity and ductility of the structural walls has been verified through tests.

However, it can be noted that the damage indices remain relatively unchanged for walls M15C and M20C, indicating that no significant additional inelastic deformation capacity was gained by increasing the concrete strength between these two test units. This effect is attributed to the decrease in fracture toughness of the concrete with compressive strength, which curtails the capacity of the shear-carrying struts. Further studies on this aspect are required and are considered fundamental in establishing quantitative limits to the inelastic web crushing behavior of HSC walls evidenced in this study.

Table 3-6 Comparison of inelastic web-crushing capacities of single walls with shear models.

Test Unit	Experiment		ACI (2008)			Oesterle et al. (1984)			Paulay and Priestley (1992)			Hines and Seible (2004)		
	Δ_u (mm)	F_u (kN	Δ_u (mm)	F_u (kN)	Diff. (%)	Δ_u (mm)	F_u (kN)	Diff. (%)	Δ_u (mm)	F_u (kN)	Diff. (%)	Δ_u (mm)	F_u (kN)	Diff. (%)
M05C	45.0	803	8.64	342	81	32.8	765	27	23.6	714	47	48.5	821	8
M05M	45.0	855	8.13	322	82	26.9	725	40	21.8	685	51	26.9	725	40
M10C	42.7	751	8.38	387	80	46.5	722	9	24.9	677	42	64.3	751	51
M10M	130	900	9.91	478	92	66.3	804	49	36.3	726	74	101	853	22
M15C	78.7	819	10.2	497	87	77.7	818	1	39.4	731	50	128	889	62
M15M	133	934	11.7	542	91	78.5	886	41	53.8	835	60	160	966	20
M20C	76.5	815	14.0	589	82	90.4	917	18	56.6	842	26	Flexure		
M20M	189	923	13.2	553	93	81.8	888	57	50.3	815	73	196	992	3

Note: 1 in. = 25.4 mm; 1 kip = 4.45 kN.

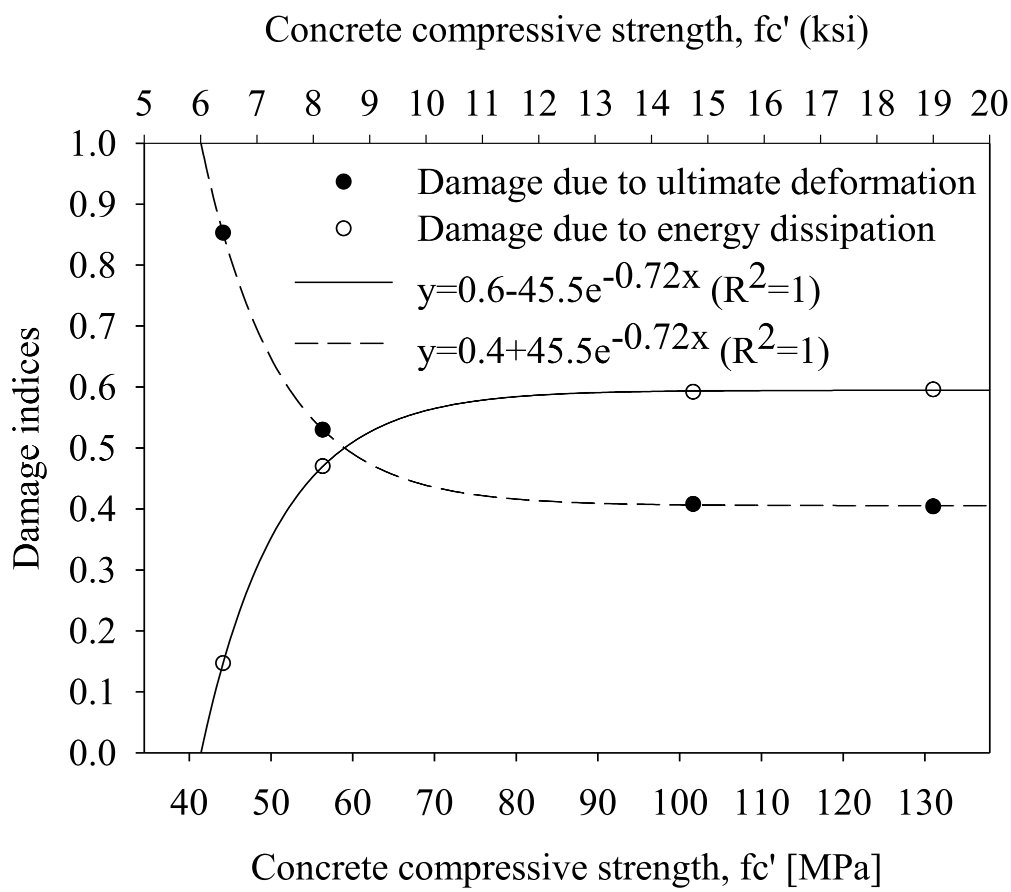

Figure 3.35 Concrete strength effect on damage index due to ultimate deformation and hysteretic energy dissipation.

3.6 Conclusions

Eight cantilever walls were tested with design concrete compressive strengths of 34, 69, 103, and 138 MPa (5, 10, 15 and 20 ksi) under cyclic and monotonic loading to study the effect of high-strength-concrete (HSC) and load reversals on the inelastic web-crushing capacity of structural walls.

Two conclusions are offered based on the experimental study presented in this chapter:

1. High-strength-concrete can effectively delay web-crushing shear failures in structural walls thus allowing the system to attain stable inelastic force-displacement response before failure. This response is possible by the strength gained by the shear-

carrying concrete struts and their anchorage into well-confined boundary elements, which in turn govern the inelastic flexural response of the system. The result is a stable and dependable ductile response, which supports the research hypothesis and the possibility of accepting what can be called 'ductile shear failures' as acceptable inelastic failure mechanisms for seismic design.

2. Second, web crushing at moderate displacement ductilities can be reliably attained for HSC walls under cyclic loading. Comparison of cyclic and monotonic test results reveal that cyclic loading significantly curtails the compression capacity of the inclined shear-resisting struts in HSC walls. Such effect is attributed to the lower fracture toughness of HSC, which leads to rapid shear strength and stiffness degradation. Such behavior was most noticeable for concretes with compressive strength over 103 MPa (15 ksi). This aspect is essential in establishing dependable limits to the inelastic web crushing capacity of HSC structural walls.

Chapter 4. **Experimental Studies on HSC Wall Assemblies under Multi-directional Loading**

4.1 Summary

High-strength-concrete (HSC) offers the potential in optimizing structural design and reduce material costs due to the possibility to satisfy design requirements with more slender elements. However, the use of HSC in seismic regions is not well studied and the corresponding design guidelines are missing. This chapter presents the seismic performance of HSC wall assemblies within the context of hollow square bridge piers through a large-scale experimental investigation. Two 1/4-scale hollow square bridge pier test units featuring highly-reinforced boundary elements at four corners and thin connecting webs, were subjected to diagonal and multi-directional cyclic loading with design concrete strengths of 34 and 138 MPa (5 and 20 ksi), respectively. Both test units exhibited stable ductile behavior until web crushing at moderate ductility levels. The diagonal web crushing performance was evaluated based on the test observations of the crack pattern and failure mode and the hysteretic force-displacement behavior. The degradation of shear stiffness and energy dissipating capacity were quantified by comparing the response of the pier assembly with that of a single wall in-plane test to evaluate the load path effect on web crushing capacity. The ductility levels achieved by the two pier test units confirmed that the effect of HSC in improving web crushing capacity as evaluated in the single wall test program is also true in wall assemblies. Nonetheless, the pier tests indicated that web crushing capacity is significantly compromised by concrete damage and strength degradation under multi-directional loading, an effect that is aggravated due to the three-dimensional load demand.

4.2 Experimental Investigation

4.2.1 Wall-Assembly Test Units

The three-dimensional inelastic web crushing capacity of structural wall assemblies was studied within the context of hollow rectangular piers featuring four connected walls with heavily confined boundary elements. Two pier test units with design concrete compressive strengths of 34 and 138 MPa (5 and 20 ksi) were constructed and tested at NEES MAST laboratory at the University of Minnesota [45]. Based on the difference of loading protocols, the 34 MPa (5 ksi) test unit was named the Diagonal Pier Test (DPT) unit and the 138 MPa (20 ksi) pier was named the Biaxial Pier Test (BPT) unit. Elevation and cross section drawings (with reinforcement details) of the DPT test unit are shown in Figure 4.1. The body (cross-section) of the test units was cast such that it was rotated 45 degrees with respect to the principal directions of the footing and load stub, as shown in Figure 4.1(a). This detail, as well as the overall dimensions of the test units was dictated by laboratory construction and test setup constraints. The test unit featured highly-reinforced and well-confined boundary corner elements with thin connecting walls arranged symmetrically in the form of a hollow square. Confinement to the concrete in the boundary elements was provided by steel spirals with a spacing of 50 mm (2 in.) within the plastic hinge length and 76 mm (3 in.) beyond that. Both test units shared the same cross-section dimensions as well as the longitudinal and confining steel configurations. Other than the concrete compressive strength the only difference between the test units was the vertical spacing of the wall transverse steel. The DPT unit had its wall transverse steel uniformly distributed at 102 mm (4 in.) along the height, while the spacing was 76 mm (3 in.) for the BPT unit in order to provide greater diagonal tension resistance under shear. A 13 mm (0.5 in.) gap was provided along the cover concrete in the octagonal boundary elements, except along the side connecting to the walls, to prevent premature spalling of the cover concrete. A construction photograph in Figure 4.2 shows the reinforcement details of one wall in the BPT pier. An additional change for the BPT unit, was the provision of 6 #3 secondary longitudinal steel reinforcement bars were added in each wall panel to help control the excessive cracking. These bars did not continue into the footing or load block to avoid adding flexural resistance to the section. Anchorage for these bars was achieved by providing them with 180-deg. Hooks at their ends.

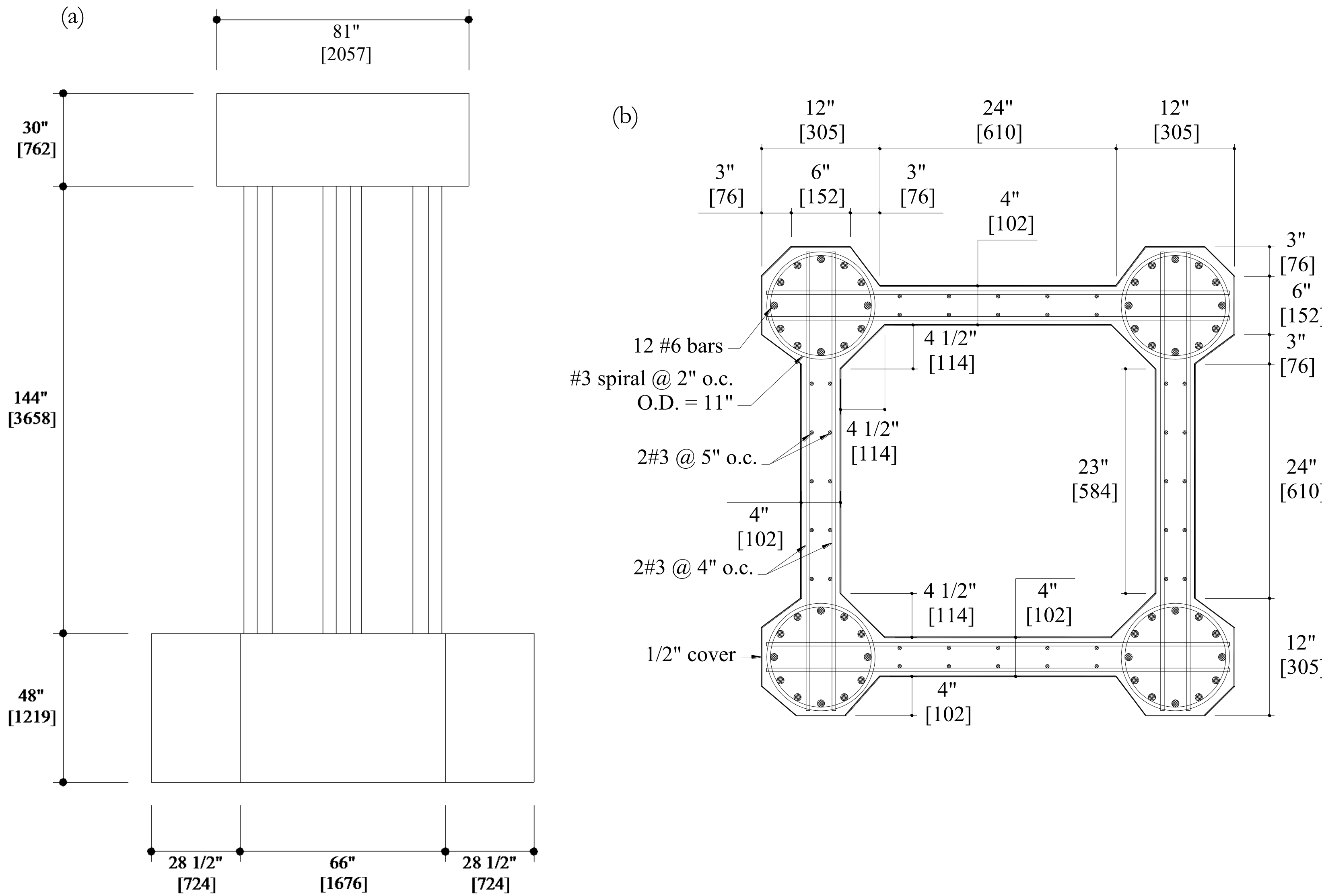

Figure 4.1 (a) Elevation of the pier test units; (b) Cross section of DPT unit with reinforcement details.

Figure 4.2 Reinforcement at BPT column base with foam at the base of the boundary elements and secondary longitudinal steel in the wall.

4.2.2 Materials

The cast of two similar test units with 34 MPa (5 ksi) normal-strength-concrete and 138 MPa (20 ksi) high-strength-concrete allowed comparison of test results in terms of structural displacement ductility, concrete damage and shear stiffness degradation. Mix proportions of the concrete for both test units are given in Table 4-1. The concrete compressive strength development was monitored by a series of cylinder tests for each batch of concrete. The corresponding concrete strength development curves for both test units are shown in Figure 4.3. Tension tests were conducted on each bar type used in the pier units. Properties of the reinforcement are provided in Table 4-2 with parameters corresponding to Mander's uniaxial steel model [42].

Table 4-1 Concrete mixtures for pier test units.

Item	BPT	DPT
Cement Type I, kg (lb)	393 (865)	161 (355)
Fly Ash, kg (lb)	–	51 (112)
Silica Fume, kg (lb)	45 (100)	–
Fine Aggregate, kg (lb)	561 (1236)	740 (1629)
Coarse Aggregate, kg(lb)	817 (1800)	795 (1750)
HRWR Type F, liter (oz)	–	1.1 (37)
Retarder Type D, liter (oz)	1.3 (44)	–
Water, kg (lb)	96 (211)	112 (246)
Water Cementitious Ratio	0.22	53

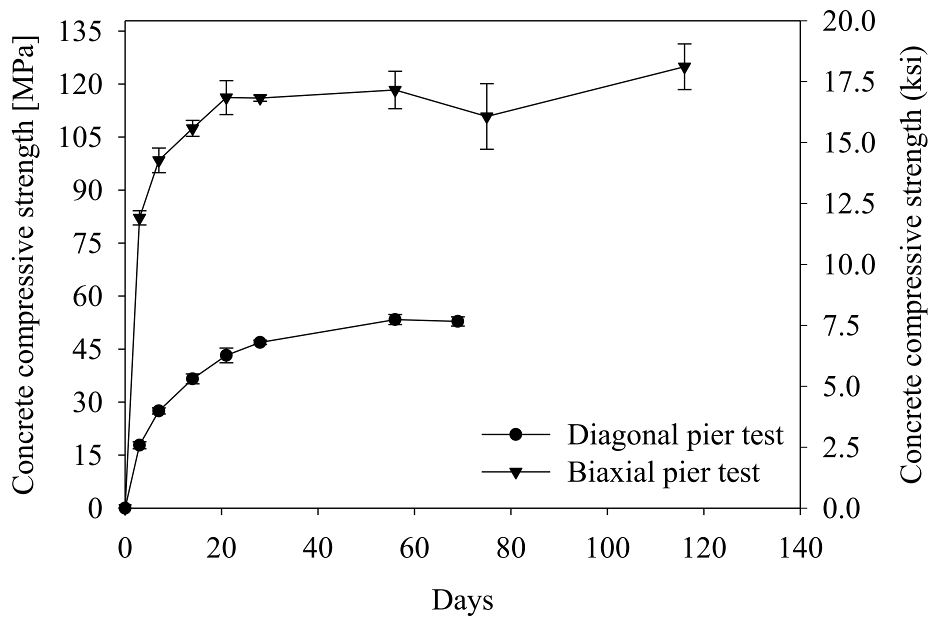

Figure 4.3 Concrete material strength development curves.

Table 4-2 Steel properties and modeling parameters for pier test units.

Test Unit	Bar Name	Size	f_y (ksi)	f_u (ksi)	ε_{sh}	E_{sh} (ksi)
BPT/DPT	Longitudinal	#6	64.3	100.7	0.0084	1267
	Longitudinal	#3	71.8	112.2	0.0061	1400
	Spiral	#3	61.5	99.7	0.0053	1150
BPT	Transverse	#3	72.4	114.9	0.0045	1517
DPT	Transverse	#3	64.9	100.6	0.0064	1142

Note: 1 MPa = 0.145 ksi.

4.2.3 Test setup

Figure 4.4 shows an overview of BPT setup at the MAST laboratory at the University of Minnesota. The MAST facility has the unique feature of being able to apply loading to structural test units by controlling the six degrees of freedom of a stiff loading crossbeam through eight servo-controlled actuators, two horizontally in each principal direction and four vertically at the ends of the crossbeam. A flexure/shear aspect ratio of 2.5 was maintained by controlling the loading such as to create an inflection point 3.05 m (120 in.) above the top of the footing or 1.37 m (54 in.) down from the top of the load stub where the crossbeam was attached. The loading components and moment diagram during tests are shown in Figure 4.5. A moment, the magnitude of which equals the shear force component times the distance l, which is the vertical length from the desired point of inflection to the bottom of the loading crossbeam, was applied to keep the inflection point at the desired location during testing. During the displacement control phase of loading, the feedback signal from the displacement transducer at the inflection point in the corresponding direction was used to control the test. All displacement related results and parameters (e.g., displacement ductility) in the pier tests are with respect to the measured lateral deformations at the induced inflection point. The active and constrained degrees of freedom at the top of the pier column during testing are shown in Figure 4.5 are expressed in Equation (4-1). Both units were tested under a constant axial load of 434 kips, corresponding to $0.10 f_c' A_g$ for 34 MPa (5 ksi) concrete.

$$Q = \begin{Bmatrix} F_{x'}(u') & F_{y'}(v') & -F_Z & M_{Z'} = F_{y'} \cdot h & -M_{y'} = F_{x'} \cdot h & \theta_{Z'} \\ F(D) & F(D) & F & F & F & D \end{Bmatrix} \qquad (4\text{-}1)$$

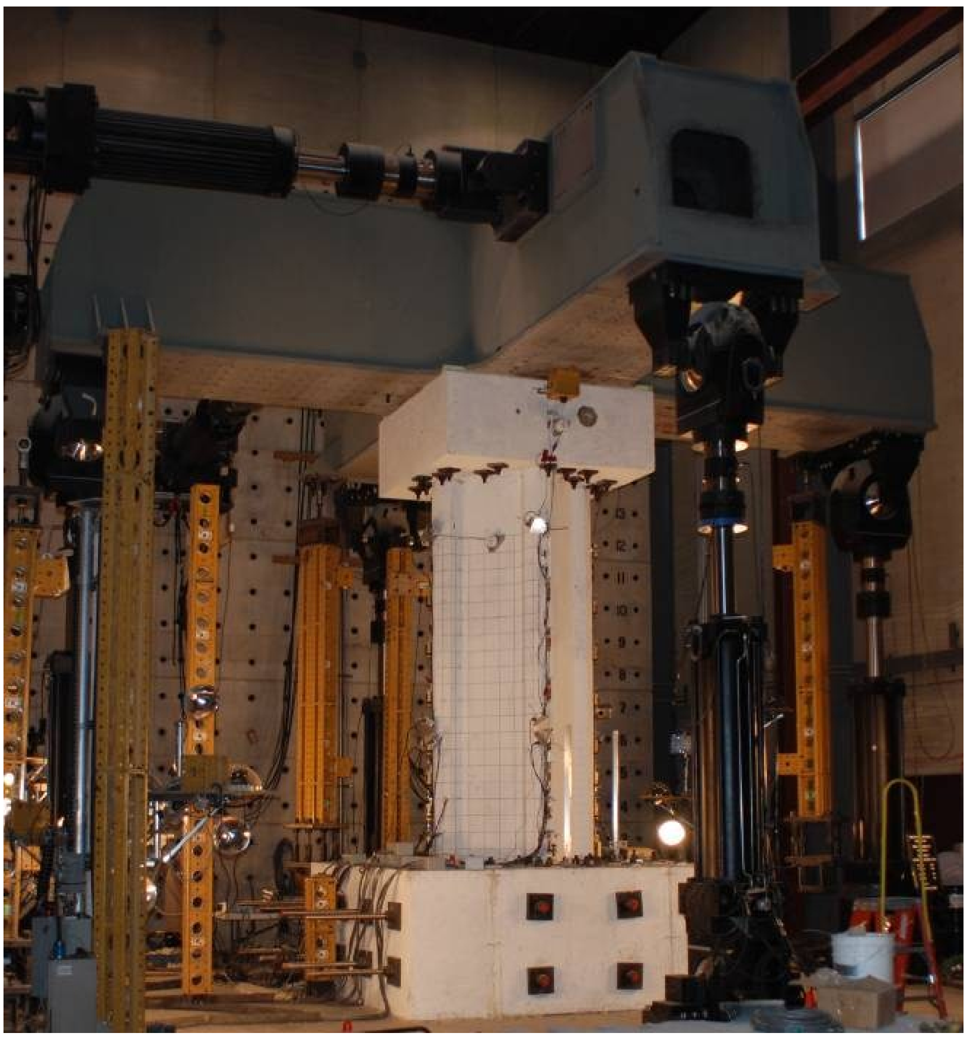

Figure 4.4 BPT Test setup at the NEES Multiaxial subassemblage Testing (MAST) laboratory.

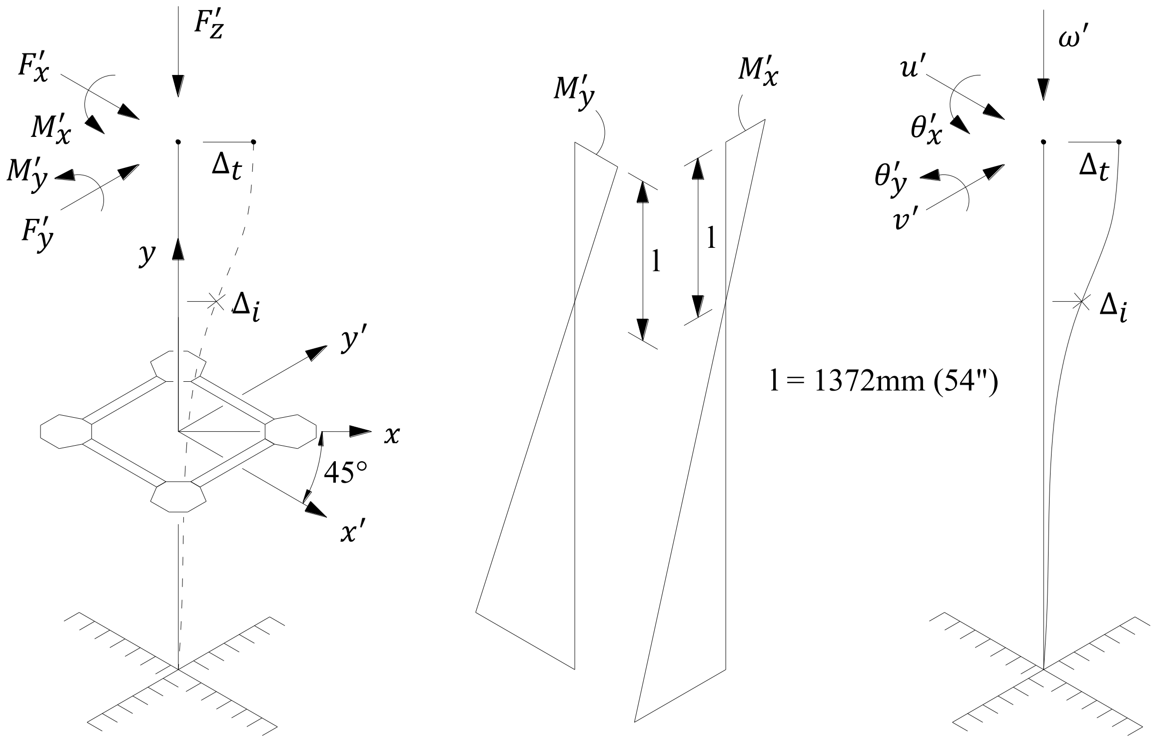

Figure 4.5 Loading components and moment diagram.

4.2.4 Instrumentation

The test units were instrumented to measure flexural deformations, shear deformations, flexure curvatures, and steel reinforcement strains. Curvature was determined by measuring the vertical deformations at the edges of the boundary elements along the test unit height. Global flexural deformation were integrated and averaged based on the curvature values along the height of the pier. Shear deformations were measured by placing shear measuring panels on two adjacent sides of the test unit featuring two independent displacement transducers arranged diagonally at each height level. The displacements at the inflection point were measured with displacement transducers along the corresponding directions. The flexural deformation contribution from strain penetration, or bond-slip, was calculated from vertical displacement measurements at the section base. This was achieved by 2 in. displacement transducers sitting on the cantilevers mounted on the footing surface away from the strain penetration influence. Strain gauges were used to measure strains in the transverse reinforcement at target locations in the walls. The curvature and shear deformation instrumentation on the north-east elevation for both test units is shown in Figure 4.6(a) and (b).

In addition to the conventional instrumentation noted above, the Metris K600 Dynamic Measuring Machine (DMM) was used to measure the spatial deformation of the north-west wall of the test unit by tracing the movement of the LED target points mounted on the wall during test, shown in Figure 4.6(b). Also, the South East wall of the test unit was placed with high-contrast photogrammetry targets so as to evaluate in-plane deformation fields by digital photogrammetry using photographs taken by DDC camera at the peak of each loading pattern, as shown in Figure 4.6(b).

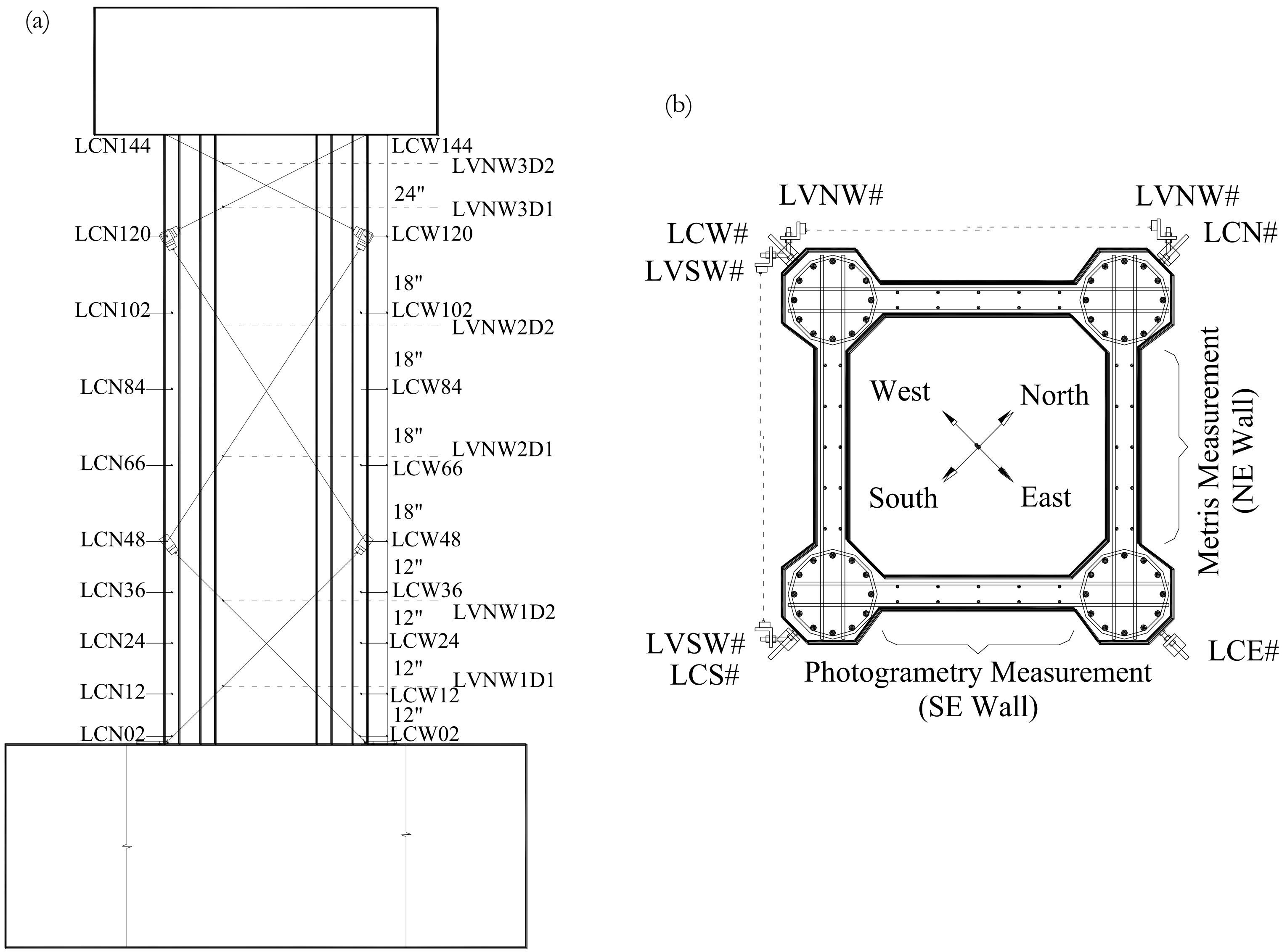

Figure 4.6 (a) Curvature and shear deformation instrumentation, North-East elevation; (b) Cross section with instrumentation on each side.

4.2.5 Loading Protocol

Both piers were tested quasi-statically according to incrementally increasing, fully reversed cyclic loading patterns. The 34 MPa (5 ksi) pier, identified as the diagonal pier test (DPT) unit, was loaded about the section's diagonal axis (an axis 45^{o} with respect to wall principal directions) with the loading sequence shown in Figure 4.7(a). Four initial loading excursions in load control were applied diagonally along the South-North direction to $\frac{1}{4}F'_{yD}$, $\frac{1}{2}F'_{yD}$, $\frac{3}{4}F'_{yD}$ and F'_{yD}, where F'_{yD} is the lateral force to first yield in the diagonal direction. Loading was then switched to displacement control at the inflection point with the loading sequence from O→A→B→O, where O represents the origin or zero deformation. Loading continued by imposing two cycles at each of the ductility level increments of μ_{Δ} = 1, 1.5, 2, 3, 4, and 6 or until failure.

The 138 MPa (20 ksi) pier, identified as biaxial pier test (BPT) unit, was loaded with a biaxial loading protocol with the loading sequence shown in Figure 4.7(b). Four initial load cycles in load control were applied diagonally along East-West direction to $\frac{1}{4}F'_{yD}$, $\frac{1}{2}F'_{yD}$, $\frac{3}{4}F'_{yD}$ and F'_{yD}. Then three cycles at F'_{yL}, F'_{yT}, and F'_{yD} were applied along the longitudinal direction (SE-NW), the transverse direction (NE-SW) and the other diagonal direction (North-South), respectively; where F'_{yL} and F'_{yT} are the first yield forces in the principal longitudinal and transverse directions. The test was switched to displacement control at the inflection point following the loading sequence described by the incremental letter sequence shown in Figure 4.7(b), that is from O→A→…→H→O. One full bi-axial loading cycle was applied at the displacement ductility levels of μ_{Δ}= 1, 1.5, 2, 3, 4, and 6 until failure of the test unit.

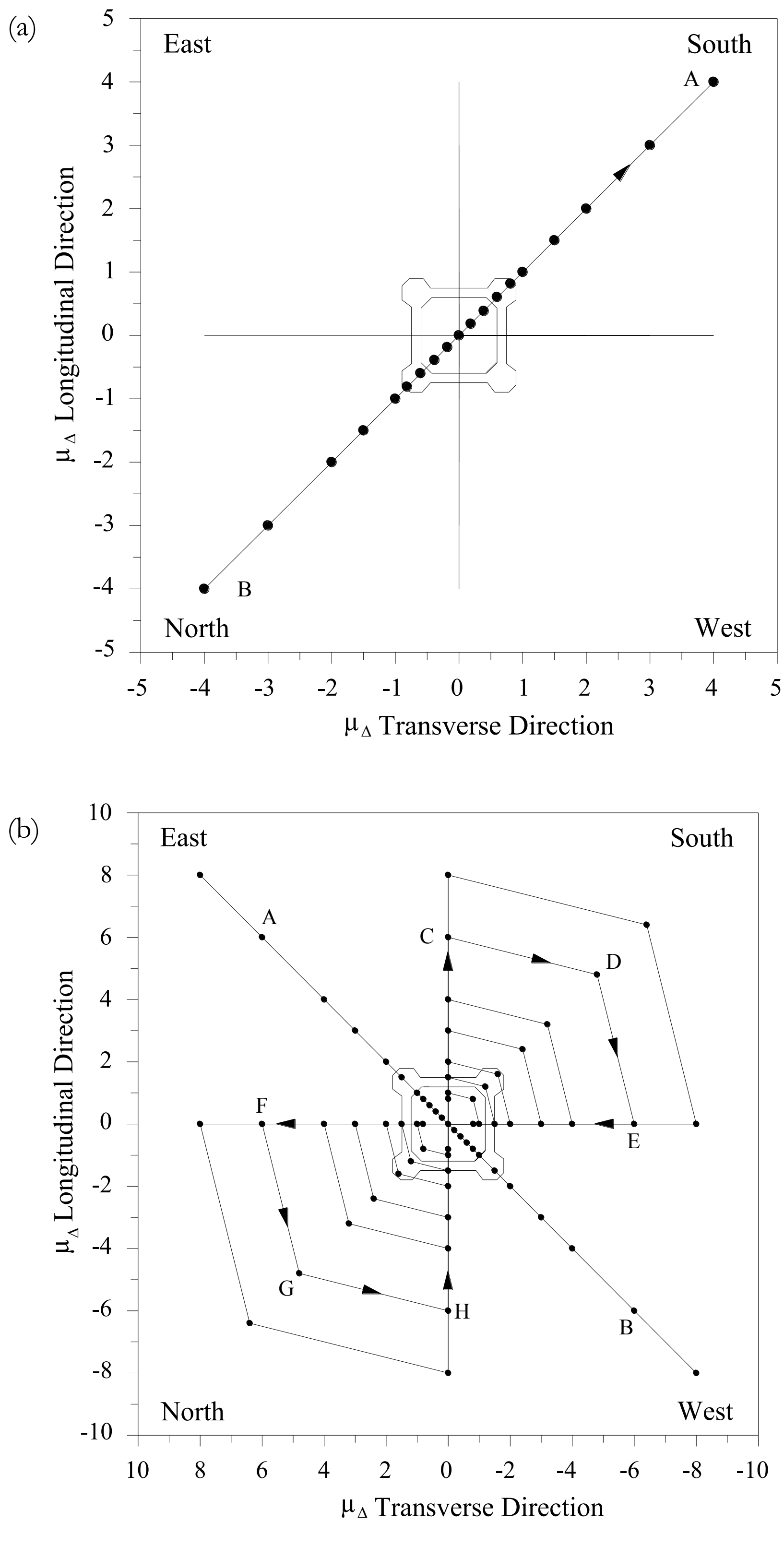

Figure 4.7 (a) DPT diagonal loading protocol and (b) BPT biaxial loading protocol.

The values of first yield forces F'_y and ideal yield displacements Δ_y, which are needed to define the described loading protocols are listed in Table 4-3. A detailed explanation on the assumptions and methods to determine these quantities can be found in reference [17].

Table 4-3 Values of force at first yield and ideal yield displacement.

Test Unit	Direction	F'_y kN (kips)	Δ_y mm (in.)
DPT	L	823 (185.0)	13.7 (0.54)
DPT	T	823 (185.0)	13.7 (0.54)
DPT	D	1164 (261.6)	19.6 (0.77)
BPT	L	1384 (310.9)	17.3 (0.68)
BPT	T	1384 (310.9)	17.3 (0.68)
BPT	DL	1028 (231.1)	13.0 (0.51)
BPT	DT	1028 (231.1)	13.0 (0.51)
BPT	D	1454 (326.8)	18.3 (0.72)

4.3 Experimental Results

Both pier test units behaved in a ductile manner before web crushing failure, which was accompanied by spalling of wall concrete and gradual loss of the load-carrying capacity. The DPT unit failed on the second excursion to point A at displacement ductility μ_Δ = 4 when the load-carrying capacity dropped 17% in Y' direction and the BPT unit failed on the excursion to point B at μ_Δ = 6 (see Figure 4.7) when the load-carrying capacity dropped over 20% in both principal directions. Figure 4.8 shows the cracking pattern and the web crushing failure mode of the DPT unit. The flexural demands on the pier led to concrete spalling on the compression boundary elements and the NE wall, which mainly concentrated at the bottom of the specimen. The inelastic flexure-shear cracking effects were observed on all walls and the critical damage and concrete spalling in the SW wall led to the ultimate failure of the test unit. The gradual loss of the load-carrying capacity demonstrated a ductile web crushing failure.

Figure 4.9 shows the cracking pattern and the web crushing failure mode of BPT unit. Web crushing in this unit initiated at the region next to the compression boundary element, which was severely degraded due to the multi-directional loading demands. The failure, however, was limited to the plastic hinge region of the walls. Spalling of the wall cover concrete was observed on the NW side at the interface of the wall and boundary element. Ultimate failure of the test unit was due to rupture of the transverse spiral reinforcement immediately above the critical section and subsequent longitudinal bar buckling on the West compression boundary element when loading toward A at $\mu_\Delta = 8$ upon completing a full cycle at $\mu_\Delta = 6$.

The hysteretic force-displacement response of the DPT and BPT units along their principal axes is shown in Figure 4.10 and Figure 4.11, respectively. The hysteretic loops of the BPT unit at $\mu_\Delta = 4$ are isolated and shown in Figure 4.12, which shows the distinct feature from unloading effects while transitioning from loading points G to H in the longitudinal direction and D to E in the transverse direction. This phenomenon illustrates the interactions of the flexural behavior of the test unit under biaxial loading, which leads to what are considered important effects of unloading and reloading of the longitudinal steel and the change of the stress state in the compression zone. Table 4-4 and Table 4-5 show the tabulated force and displacements values at peaks of the hysteretic loops.

Representative curvature profiles of the BPT and DPT pier test units in different loading directions at $\mu_\Delta = 4$ are shown in Figure 4.13. It is interesting to see that the curvatures profiles along the height of the test units are very close to each other, which verifies the equivalent nature of the loading protocols and justifies comparing results from both tests at equal ductility levels.

Figure 4.14 shows a contour plot of the in-plane minimum principal strains, E2, as well as the test photograph showing the with LED Krypton targets at $\mu_\Delta = 4 \text{ x } 1$ for the DPT unit. The targets define the mesh for a displacement field analysis of the wall. The three-dimensional coordinates obtained from the Krypton measuring system were used to compute the Green-Lagrange strain within the framework of the finite element method. In the same way, Figure 4.15 shows the E2 contour at $\mu_\Delta = 4 \text{ x A}$ for the BPT unit. The strain contours are not only the result of a quite promising non-contact instrumentation strategy, but provide interesting insight into the behavior of the test unit. It can be noted that the maximum principal strains for the DPT in Figure 4.14 are indeed very close to the expected maximum concrete strain of 0.0025, on average, at the compression zone at the bottom of the wall. The DPT unit failed at this load level but on the SW wall (the Krypton measuring system was installed in the NE wall). Conversely, the strain contour for the BPT unit in Figure 4.15 shows that the strains are quite high at the bottom compression zone of the wall (approximately 0.006). Indeed, attention to the photograph in the same figure shows that the bottom of the wall had begun to crush due to the biaxial loading demands (compression demands from flexural excursions on the NE wall). The BPT unit went on to resist a full cycle of loading at $\mu_{\Delta =}$ 4 and eventually failed upon a diagonal cycle at $\mu_{\Delta =}$ 6. Yet, the noted strain levels are indicative of the type of damage that the biaxial loading pattern has in curtailing the web crushing capacity of the walls in the pier unit.

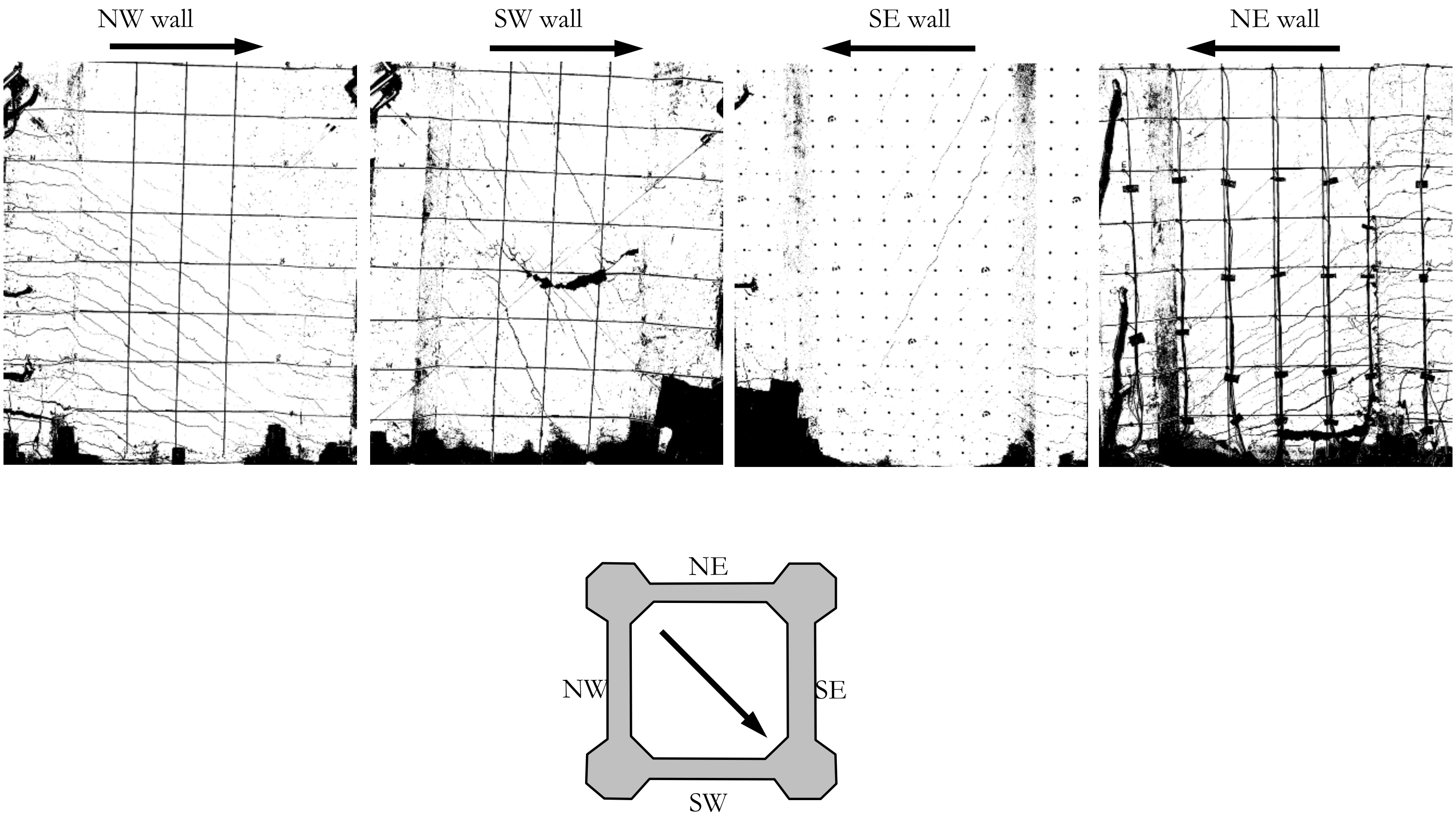

Figure 4.8 DPT web crushing failure at μ_{Δ}=4 x 2 loading toward A.

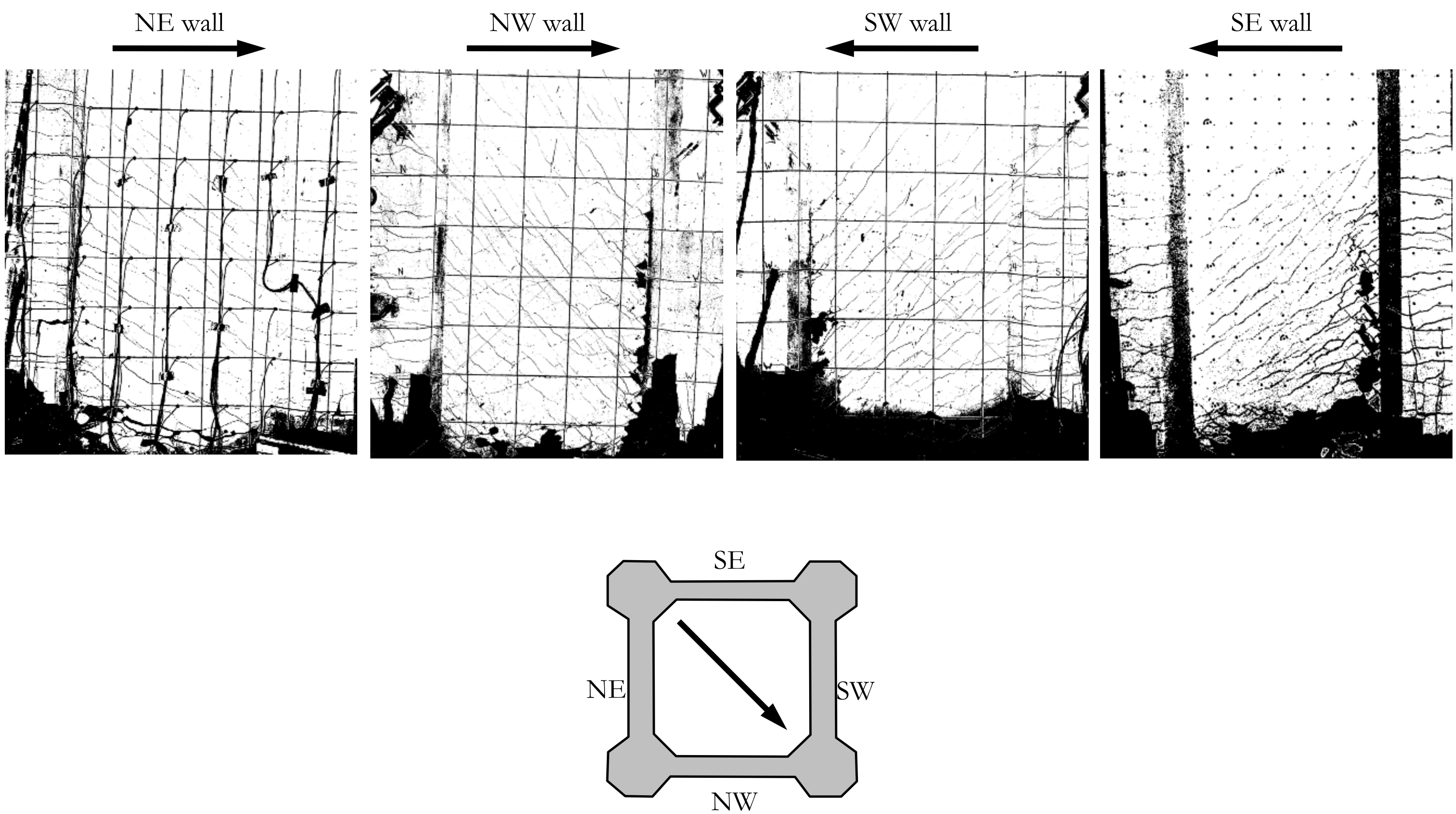

Figure 4.9 BPT web crushing failure at $\mu_{\Delta}=6$ loading toward B.

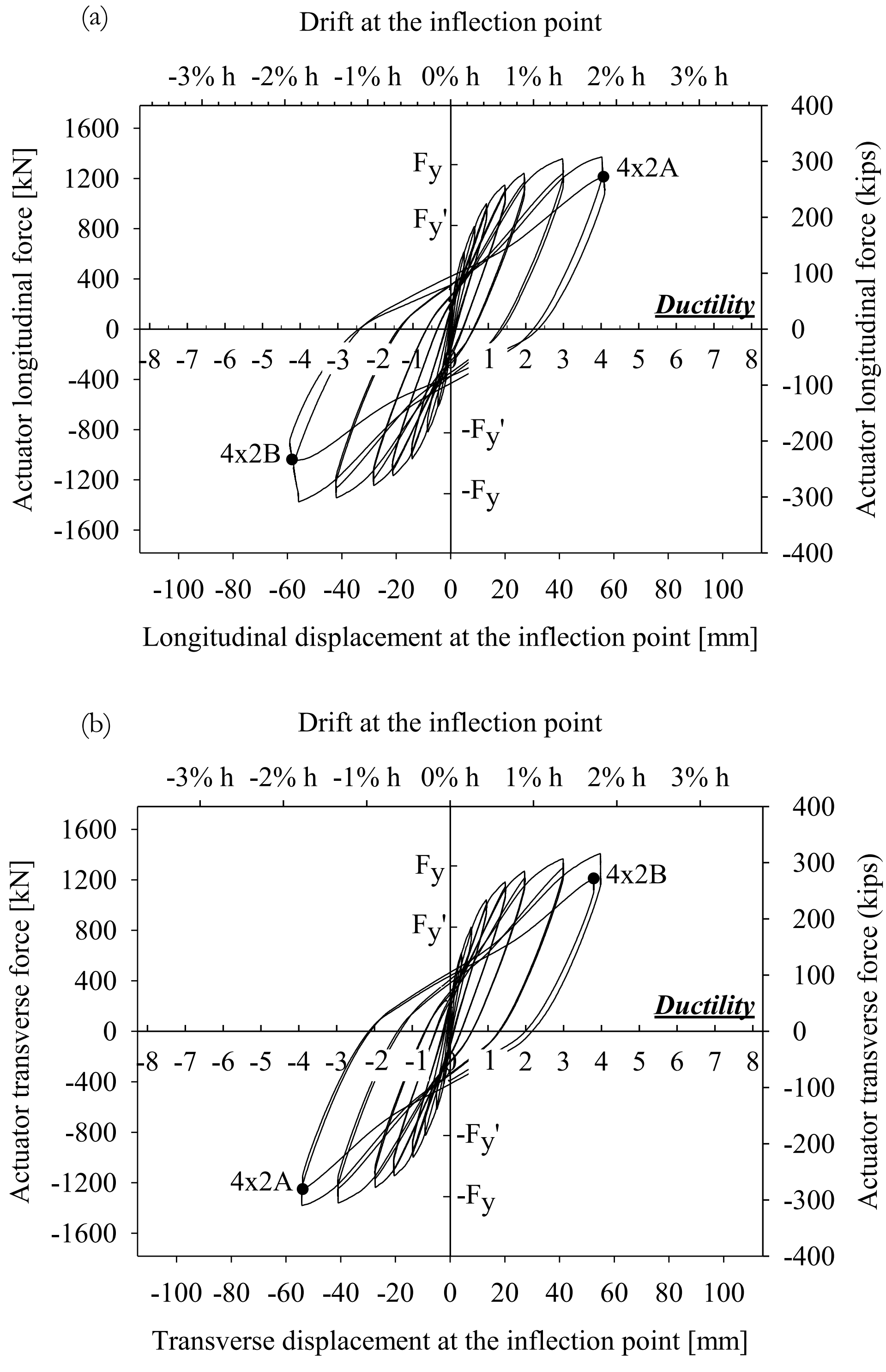

Figure 4.10 Hysteretic loops of DPT: (a) longitudinal axis and (b) transverse axis.

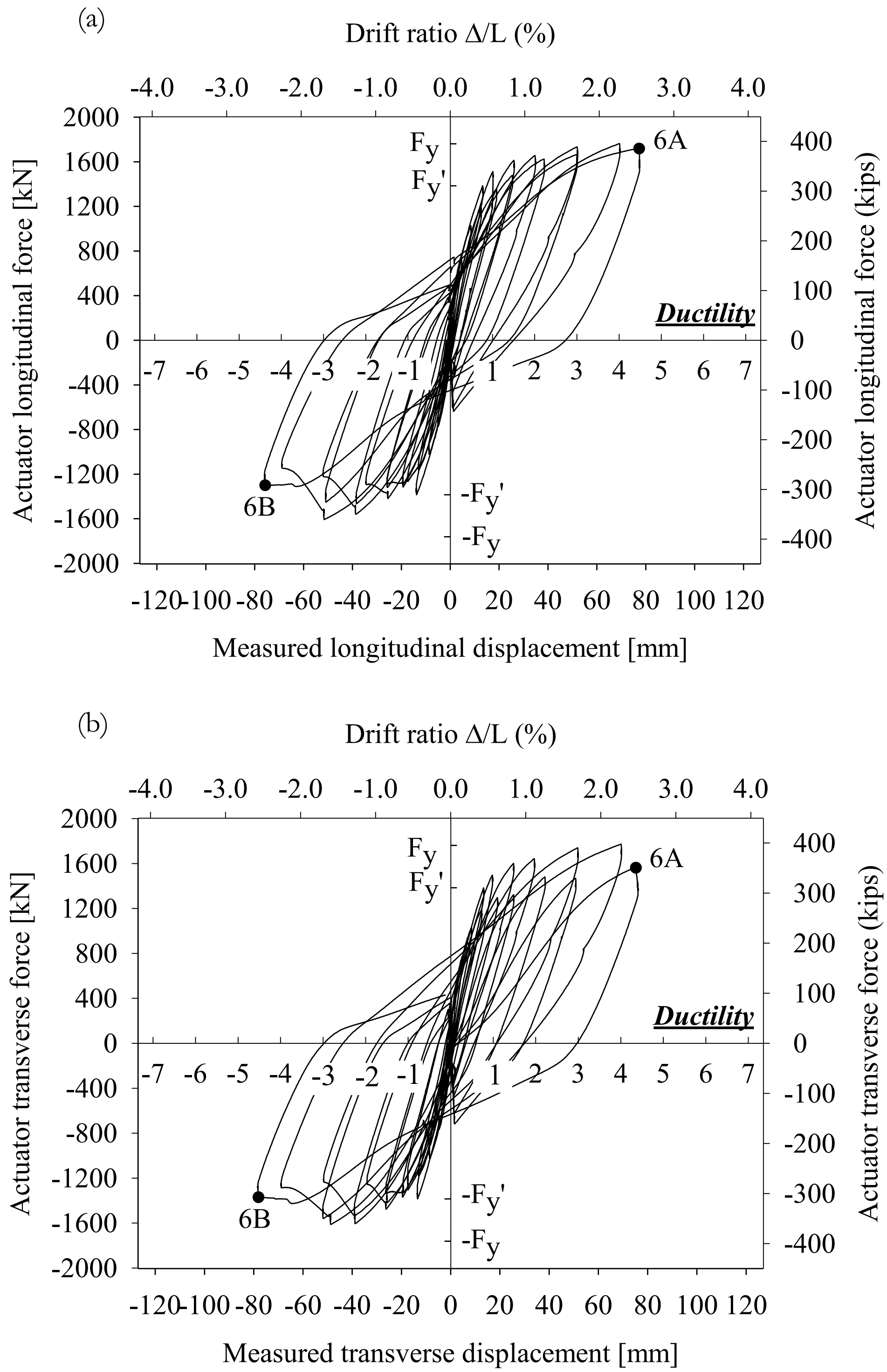

Figure 4.11 Hysteretic loops of BPT: (a) longitudinal axis and (b) transverse axis.

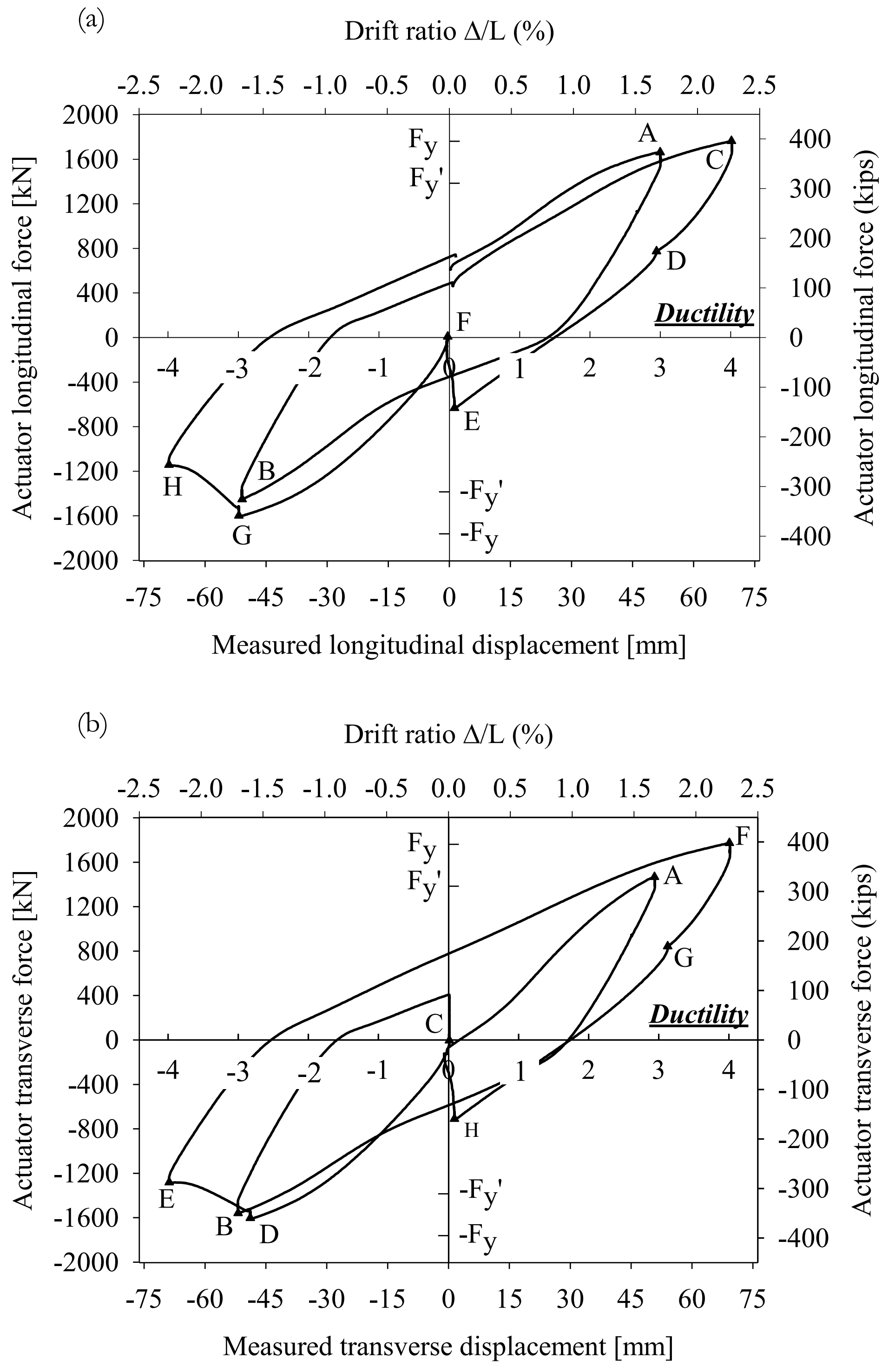

Figure 4.12 Hysteretic loops of BPT at μ_{Δ}=4: (a) longitudinal axis and (b) transverse axis.

Table 4-4 DPT unit: peak force-displacement values.

Level	Δ_L (in.)	F_L (kips)	Δ_T (in.)	F_T (kips)
$+1/4\ F_{yD}'$	0.030	46.2	-0.031	-47.1
$-1/4\ F_{yD}'$	-0.026	-46.9	0.015	45.4
$+1/2\ F_{yD}'$	0.087	92.4	-0.087	-92.5
$-1/2\ F_{yD}'$	-0.074	-92.6	0.062	91.5
$+3/4\ F_{yD}'$	0.192	137.0	-0.192	-138.9
$-3/4\ F_{yD}'$	-0.177	-137.8	0.161	139.0
$+F_{yD}'$	0.342	183.6	-0.355	-185.0
$-F_{yD}'$	-0.327	-183.6	0.300	185.1
$\mu_\Delta = +1 \times 1$	0.518	224.2	-0.534	-223.8
$\mu_\Delta = -1 \times 1$	-0.557	-231.4	0.521	233.5
$\mu_\Delta = +1 \times 2$	0.516	215.5	-0.535	-215.8
$\mu_\Delta = -1 \times 2$	-0.557	-221.3	0.518	224.3
$\mu_\Delta = +1.5 \times 1$	0.783	257.6	-0.805	-257.0
$\mu_\Delta = -1.5 \times 1$	-0.834	-261.5	0.792	265.7
$\mu_\Delta = +1.5 \times 2$	0.788	246.4	-0.810	-246.1
$\mu_\Delta = -1.5 \times 2$	-0.838	-252.0	0.793	256.0
$\mu_\Delta = +2 \times 1$	1.063	278.5	-1.076	-277.7
$\mu_\Delta = -2 \times 1$	-1.113	-279.5	1.069	284.9
$\mu_\Delta = +2 \times 2$	1.063	262.3	-1.078	-262.2
$\mu_\Delta = -2 \times 2$	-1.111	-266.4	1.069	272.2
$\mu_\Delta = +3 \times 1$	1.622	302.6	-1.613	-303.4
$\mu_\Delta = -3 \times 1$	-1.657	-300.8	1.627	306.5
$\mu_\Delta = +3 \times 2$	1.629	277.5	-1.614	-279.5

Table 4-4 (cont'd).

μ_Δ = -3 x 2	-1.661	-283.7	1.627	290.5
μ_Δ = +4 x 1	2.189	307.7	-2.133	-310.1
μ_Δ = -4 x 1	-2.199	-308.8	2.161	316.1
μ_Δ = +4 x 2	2.213	272.3	-2.121	-281.0
μ_Δ = -4 x 2	-2.295	-233.3	2.066	271.9
μ_Δ = +6 x 1	3.591	160.8	-2.909	-336.5
μ_Δ = -6 x 1	-3.606	-113.0	2.836	307.1
μ_Δ = +6 x 2	3.569	106.8	-3.067	-291.9
μ_Δ = -6 x 2	-3.412	-95.3	3.000	174.3

Table 4-5 BPT unit: peak force-displacement values.

Level	Δ_L (in.)	F_L (kips)	Δ_T (in.)	F_T (kips)
+1/4 F_{yD}'	0.026	57.5	0.024	58.6
-1/4 F_{yD}'	-0.033	-58.2	-0.026	-56.7
+1/2 F_{yD}'	0.081	115.4	0.081	115.7
-1/2 F_{yD}'	-0.090	-115.7	-0.083	-114.4
+3/4 F_{yD}'	0.181	172.5	0.181	173.1
-3/4 F_{yD}'	-0.191	-173.3	-0.185	-172.2
+F_{yD}'	0.333	230.4	0.329	231.1
-F_{yD}'	-0.338	-229.9	-0.336	-231.0
+F_{yL}'	0.521	311.2	-0.026	-12.1
+F_{yL}'	-0.543	-311.0	-0.016	19.1
+F_{yT}'	-0.059	-25.0	0.528	310.8
+F_{yT}'	-0.057	-7.9	-0.529	-310.8
μ_Δ = A x 1	0.495	266.3	0.492	266.7
μ_Δ = B x 1	-0.505	-260.8	-0.503	-263.8
μ_Δ = C x 1	0.682	338.7	-0.023	-7.7
μ_Δ = D x 1	0.683	290.4	-0.328	-203.7
μ_Δ = E x 1	0.328	96.6	-0.681	-292.8
μ_Δ = F x 1	0.003	-18.9	0.668	336.2
μ_Δ = G x 1	-0.497	-259.0	0.534	228.1
μ_Δ = H x 1	-0.680	-284.2	0.029	-53.8
μ_Δ = A x 1.5	0.743	304.7	0.746	291.4
μ_Δ = B x 1.5	-0.758	-289.4	-0.755	-298.8
μ_Δ = C x 1.5	1.025	362.1	-0.020	-0.6
μ_Δ = D x 1.5	0.797	227.7	-0.770	-307.4
μ_Δ = E x 1.5	0.027	-82.6	-1.033	-299.4
μ_Δ = F x 1.5	0.001	-10.7	1.006	359.3
μ_Δ = G x 1.5	-0.761	-294.6	0.795	230.2
μ_Δ = H x 1.5	-1.015	-288.6	0.036	-83.3
μ_Δ = A x 2	1.002	331.7	1.007	297.0

Table 4-5 (cont'd).

μ_Δ = B x 2	-1.011	-296.3	-1.014	-318.6
μ_Δ = C x 2	1.363	371.9	-0.022	-0.7
μ_Δ = D x 2	1.072	222.5	-1.034	-330.7
μ_Δ = E x 2	0.034	-106.1	-1.334	-281.4
μ_Δ = F x 2	-0.002	-7.7	1.334	368.9
μ_Δ = G x 2	-1.006	-316.4	1.053	223.0
μ_Δ = H x 2	-1.355	-290.0	0.045	-105.3
μ_Δ = A x 3	1.513	364.8	1.508	332.5
μ_Δ = B x 3	-1.511	-329.2	-1.536	-344.8
μ_Δ = C x 3	2.043	389.4	-0.011	1.6
μ_Δ = D x 3	1.586	208.4	-1.531	-359.3
μ_Δ = E x 3	0.041	-135.8	-2.028	-277.4
μ_Δ = F x 3	-0.014	-4.6	2.031	390.6
μ_Δ = G x 3	-1.525	-350.0	1.600	209.8
μ_Δ = H x 3	-2.042	-274.7	0.058	-140.4
μ_Δ = A x 4	2.038	373.2	1.999	329.6
μ_Δ = B x 4	-2.003	-325.8	-2.041	-350.0
μ_Δ = C x 4	2.727	396.0	0.008	-0.9
μ_Δ = D x 4	2.004	173.9	-1.922	-360.0
μ_Δ = E x 4	0.051	-141.9	-2.710	-287.9
μ_Δ = F x 4	-0.015	1.8	2.725	398.0
μ_Δ = G x 4	-2.035	-358.9	2.127	189.2
μ_Δ = H x 4	-2.711	-256.5	0.058	-159.5
μ_Δ = A x 6	3.043	385.5	2.962	350.5
μ_Δ = B x 6	-2.979	-292.2	-3.073	-307.9
μ_Δ = C x 6	4.082	353.6	0.023	-15.9
μ_Δ = D x 6	3.454	130.2	-2.650	-272.3
μ_Δ = E x 6	0.121	-142.5	-3.977	-216.0
μ_Δ = F x 6	0.043	-2.5	4.088	277.5
μ_Δ = G x 6	-2.786	-235.5	3.119	68.5
μ_Δ = H x 6	-4.030	-197.4	0.181	-122.2

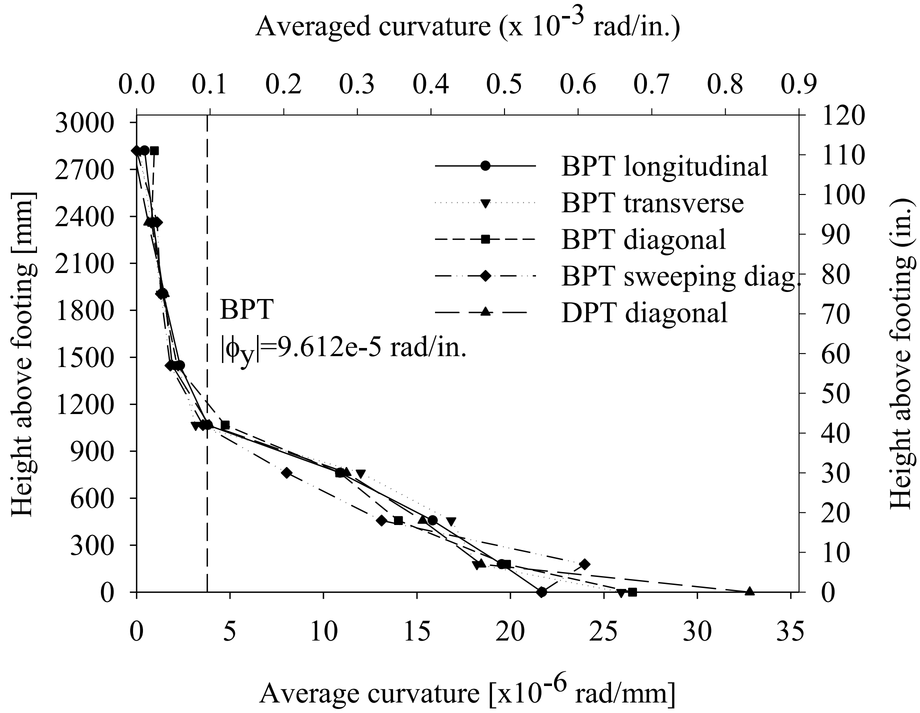

Figure 4.13 Curvature profiles of BPT and DPT in different directions.

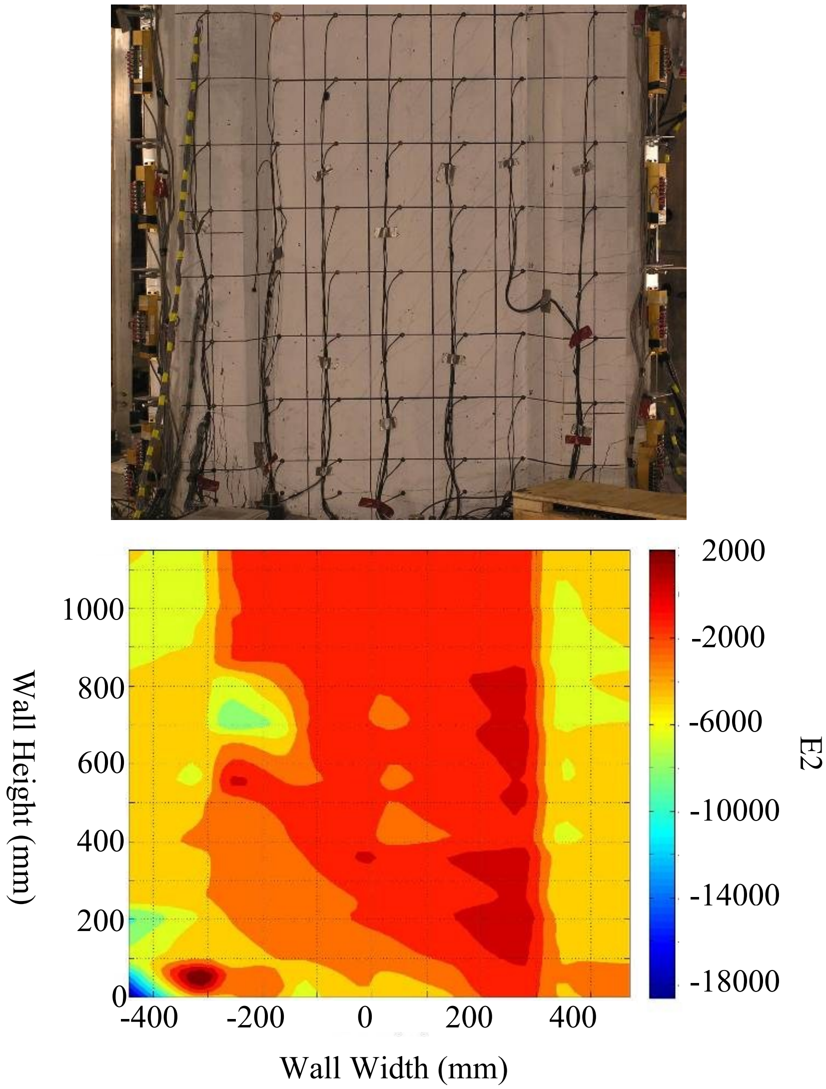

Figure 4.14 DPT in-plane minimum principal strain, E2 at μ_{Δ}=4x1.

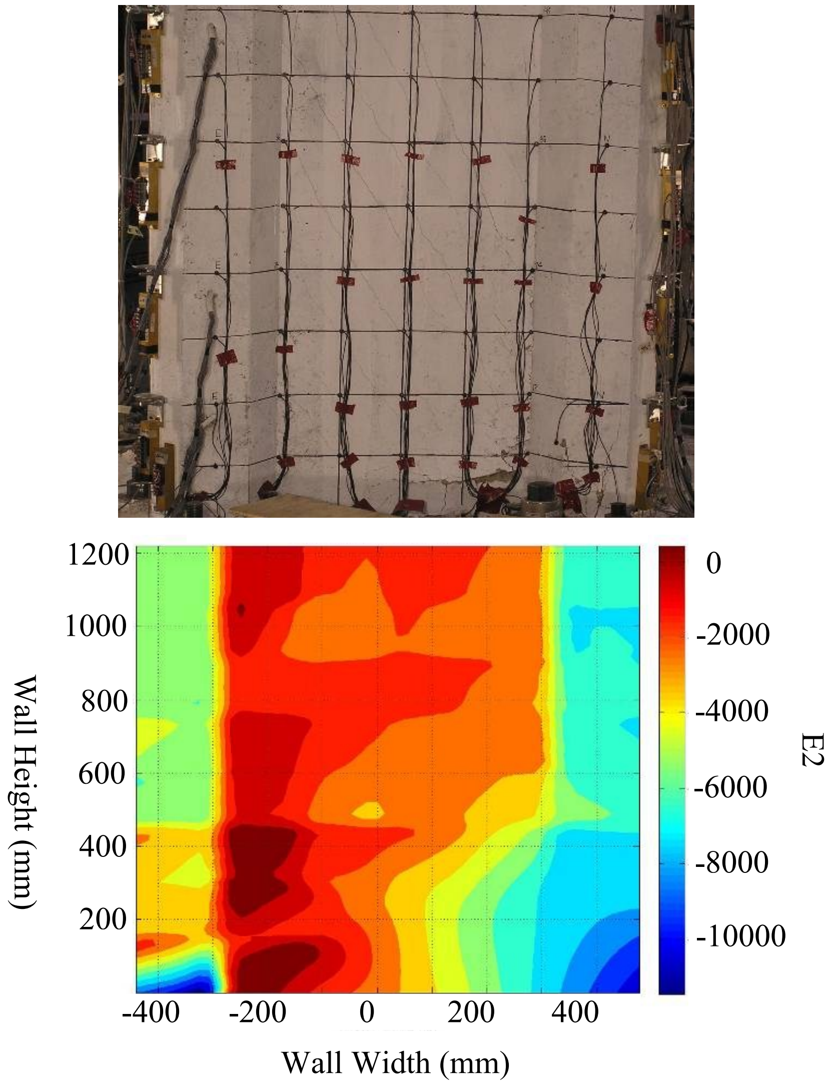

Figure 4.15 BPT in-plane minimum principal strain, E2 at μ_{Δ}=4xA.

4.4 Discussion

Figure 4.16 compares the force-displacement envelopes of the BPT pier unit along different directions. It is interesting to note that the behavior of the test unit in the sweeping diagonal direction is close to that of the principal directions instead of the straight diagonal directions. The coupling between the two orthogonal directions decreases the stiffness in the sweeping diagonal direction. By comparison, loading along the other directions passes through the centroid of the cross section and no coupling exists. Figure 4.17 compares the

DPT hysteretic loop with the BPT envelopes in the diagonal and sweeping diagonal directions. It can be seen that the BPT has higher load-carrying capacity than the DPT in the diagonal direction. In the sweeping diagonal direction, the BPT experienced complicated unloading behavior due to the eccentricity of the loading.

The shear stiffness degradation and the energy dissipating capacity of the inelastic shear mechanism of the test units under various loading patterns are of interest in this study. The displacement ductility limit of the hollow piers before web crushing failure is directly related to those two factors. Figure 4.18 and Figure 4.19 show the hysteretic loops of both test units for flexure and shear deformations, respectively. It can be seen that flexure (Figure 4.18(a) and Figure 4.19(a)) dominates the force-displacement behavior of both test units, while comparison of Figure 4.18(b) and Figure 4.19(b) indicates that the DPT unit exhibited larger inelastic shear deformations and energy dissipating capacity than the BPT unit.

To study the shear stiffness degradation of the DPT, a linear regression analysis was conducted on the unloading curves of the shear hysteretic loops. The unloading stiffness degradation of the DPT against displacement ductility is shown in Figure 4.20(a). It is noteworthy that the damage degradation from the first loading peak (Point A) with respect to the second loading peak (Point B) progressively decreases, indicating overall damage to the structure. For the BPT unit, the "butterfly" loading pattern disturbed the unloading scheme of the test unit and the unloading stiffness is difficult to evaluate. Therefore, the degradation of the secant stiffness was studied since plastic shear deformations were small. The secant stiffness degradation of the BPT test unit is shown in (b). Of interest here is the fact that the degradation follows a quadratic trend, compared to the linear degradation that was seen in structural walls subjected to in-plane shear demands [16][45]. More discussion on this observation follows.

Hines et al. [17] tested a single cantilever wall (Unit 3A) with the same cross section, steel reinforcement, and aspect ratio as one of the sides of the pier units in this program. Figure 4.21 shows the global and the shear hysteretic loops of Unit 3A. A comparison of the shear hysteretic loops indicates that Unit 3A (scaled by a factor of 2 to account for the number of walls in the pier units) exhibited less shear stiffness degradation and better inelastic shear behavior than the piers, which suffered much greater and rapid shear stiffness degradation due to the mixed flexure-shear cracking under multi-directional loading. The shear dissipating energy of both piers along their principal directions is compared with that of Unit 3A in Figure 4.22. It can be seen that BPT had less shear energy dissipating capacity than the DPT and that both pier tests dissipated much less energy compared to twice the single wall test. The linear energy dissipation of the in-plane loaded wall compared to the quadratic degradation of the piers can also be noted.

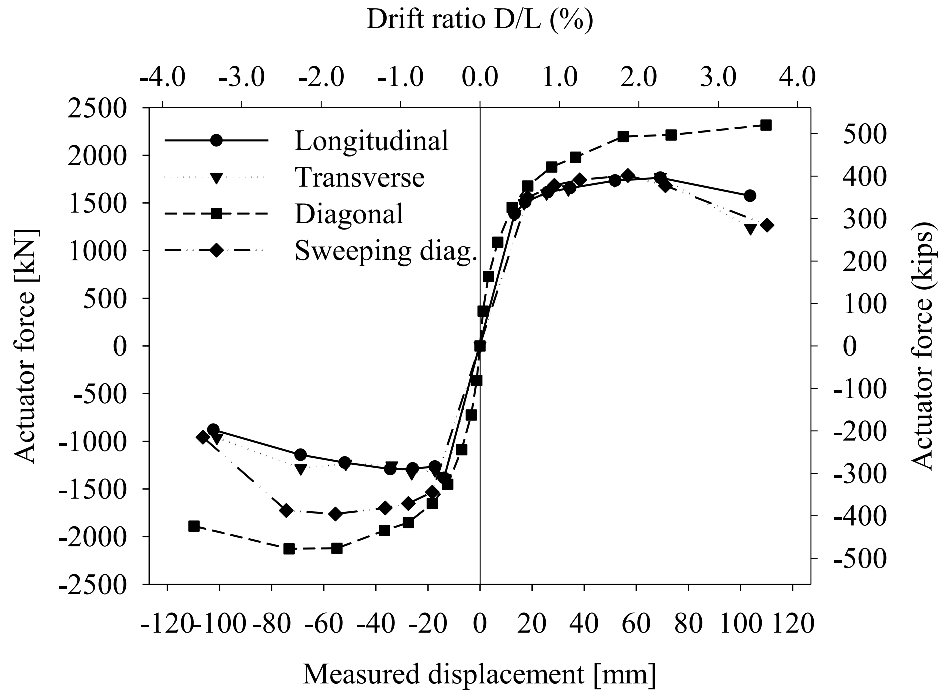

Figure 4.16 Comparison of the BPT force-displacement envelopes in different directions.

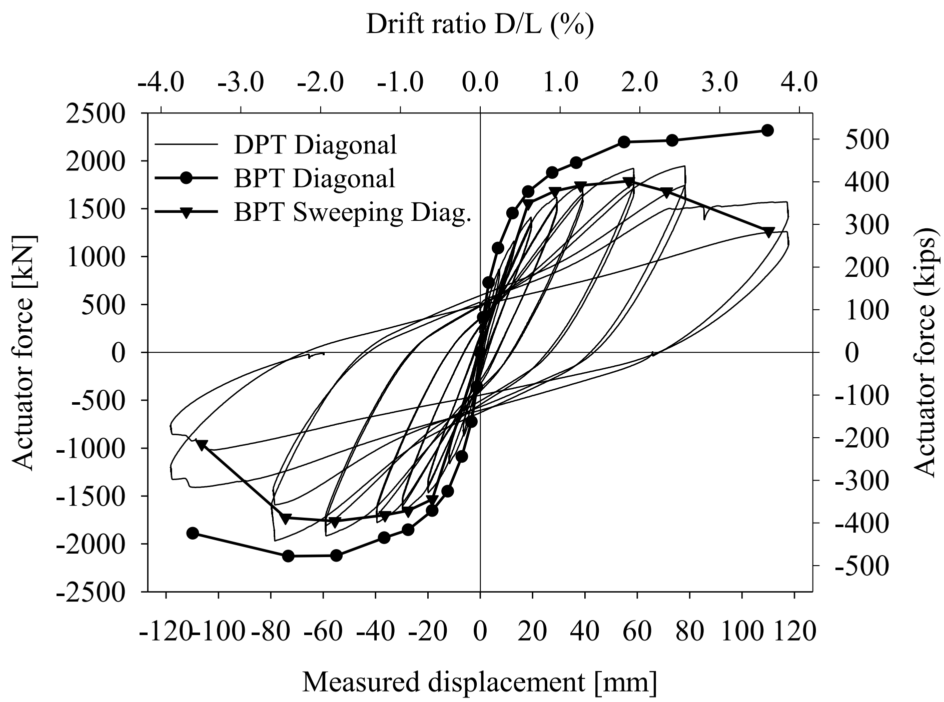

Figure 4.17 DPT hysteretic loop compared to BPT envelopes in diagonal and sweeping diagonal direction.

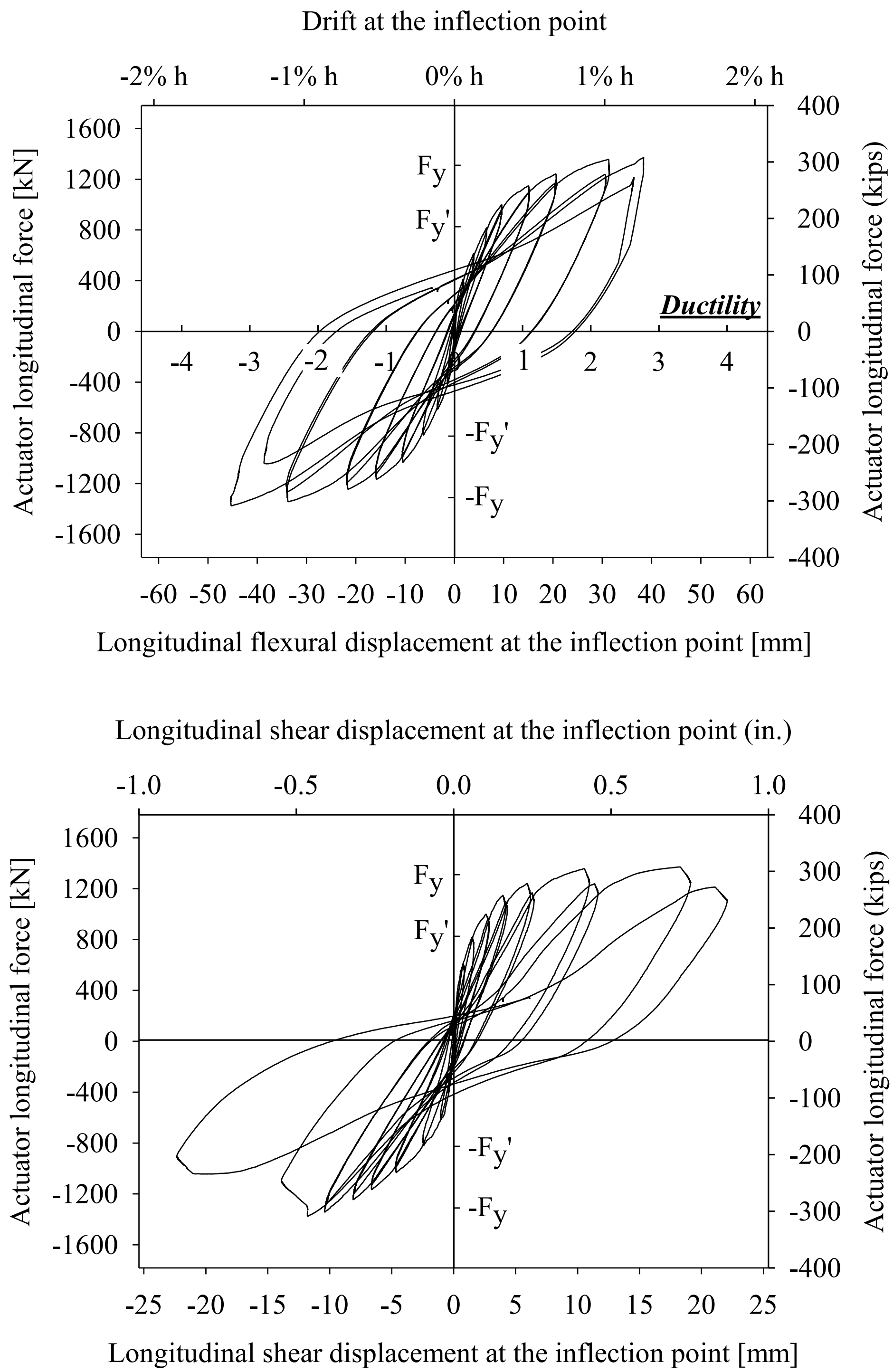

Figure 4.18 Hysteretic loops of DPT in (a) flexure and (b) shear.

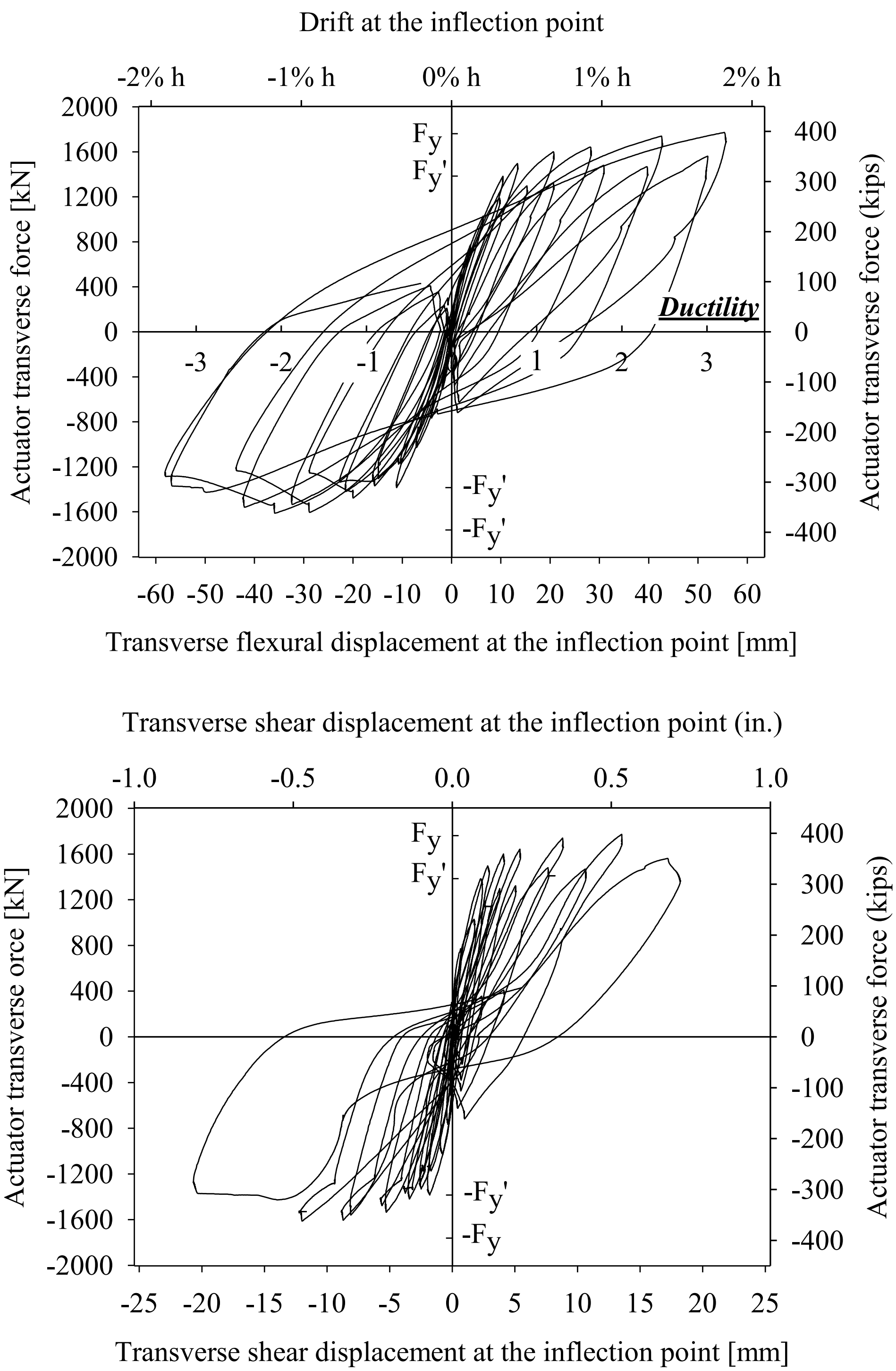

Figure 4.19 Hysteretic loops of BPT in (a) flexure and (b) shear.

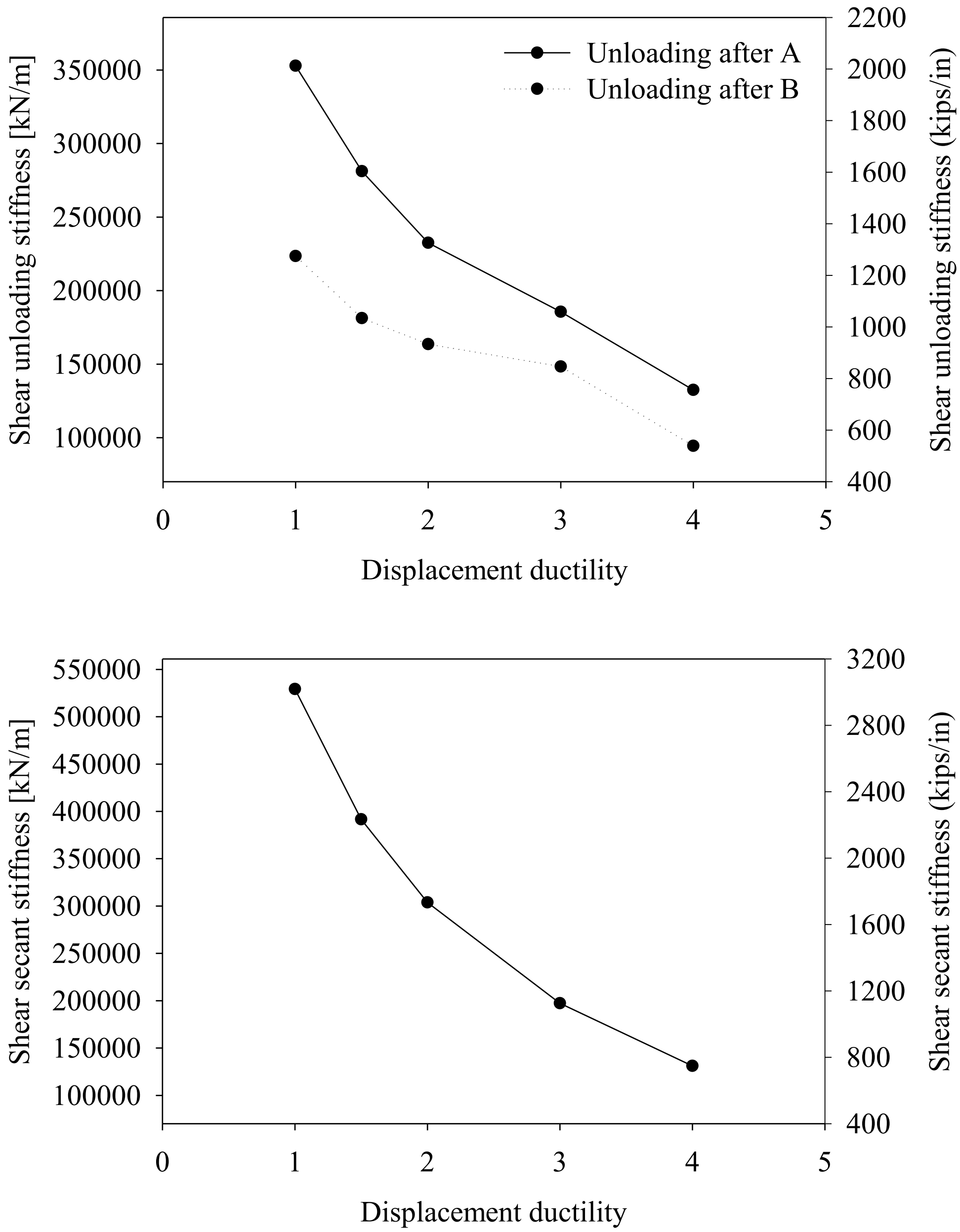

Figure 4.20 Multidirectional loading effects: (a) Shear unloading stiffness degradation of DPT in diagonal direction, and (b) Shear secant stiffness degradation of BPT in transverse direction.

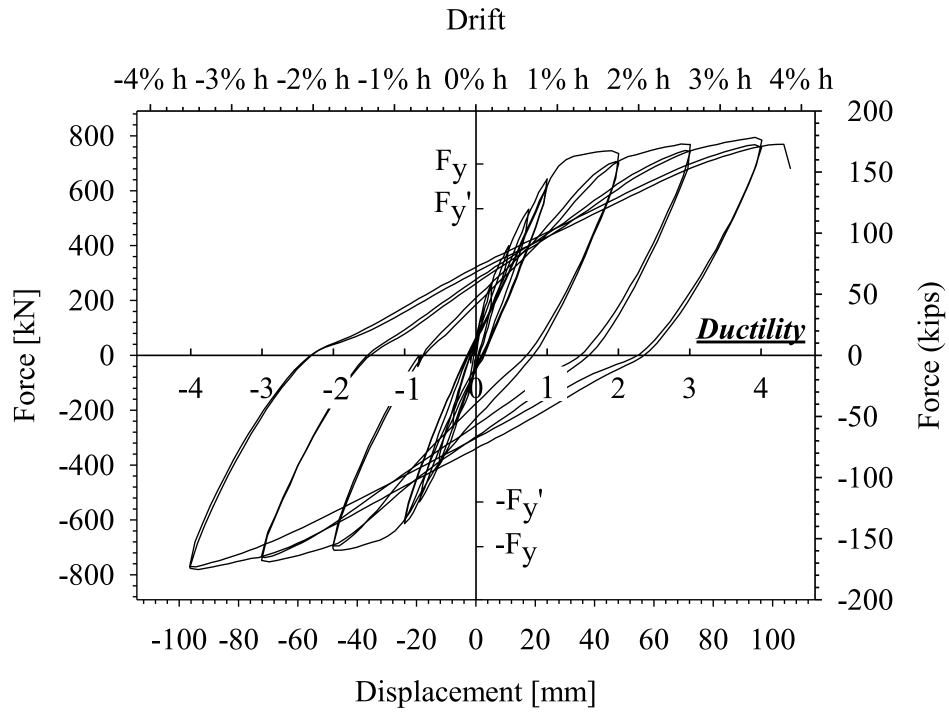

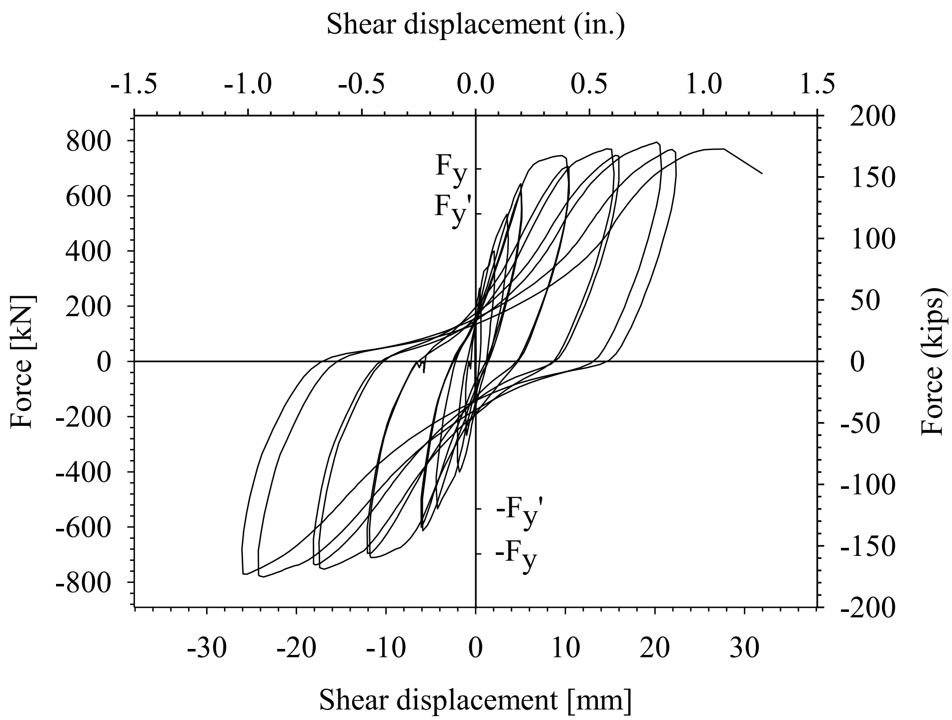

Figure 4.21 Hysteretic loops of Unit 3A (a) Global behavior (b) Shear behavior (Hines 2004).

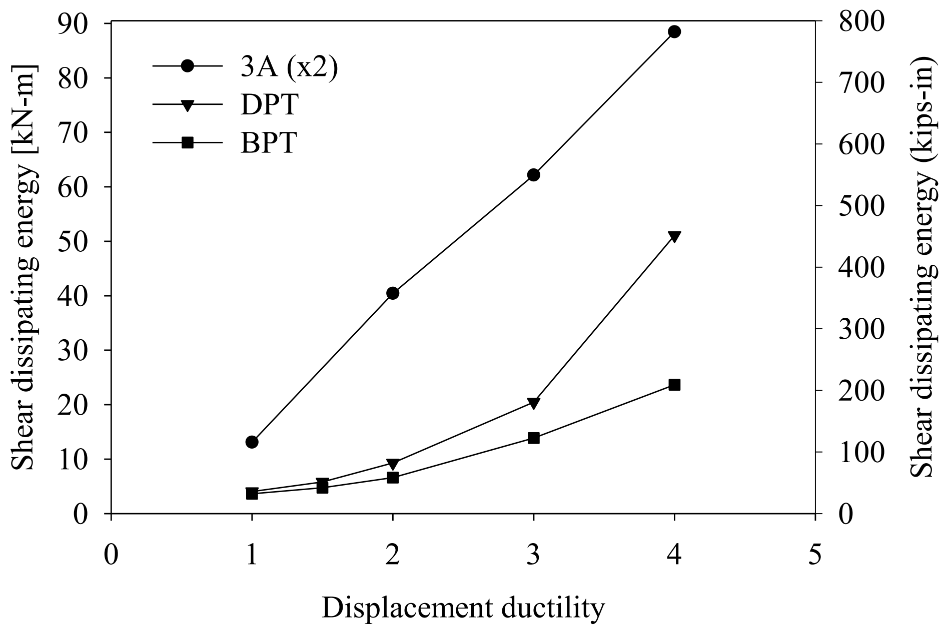

Figure 4.22 Comparison of shear dissipating energy of pier tests and single wall test.

4.5 Conclusions

The effect of multi-directional loading on the inelastic web crushing capacity of HSC wall assemblies was experimentally investigated within the context of hollow square bridge piers through tests on two 1/4-scale units subjected to diagonal and multi-axial cyclic loading. Results have confirmed some of the advantages hypothesized for using HSC but have also brought forth important issues in establishing performance limits to inelastic web crushing in walls under three-dimensional shear demands. The following conclusions are offered based on the noted results and findings to date.

1. Both pier test units exhibited a stable ductile response up to moderate ductility levels before experiencing a web crushing shear failure. The three dimensional force-resisting mechanism provided by the integrated response of the boundary elements to resist flexure and the walls to resist shear was efficient and can be relied upon for new designs.

2. The effect of high-strength-concrete (HSC) in delaying the web-crushing shear failure in the BPT pier compared to the DPT unit was verified even though the BPT wall assembly was loaded under more severe multi-directional demands.

3. The BPT unit exhibited less inelastic shear deformation and more damage due to the application of HSC and the multi-directional loading pattern compared to the DPT unit. Therefore, the use of HSC to increase the ductility level was impaired by the severe biaxial demands and the higher damage susceptibility of HSC.

4. Compared to a prior single wall test by Hines et al. [17], both pier test units exhibited rapid shear stiffness degradation, which is attributed to the damage accumulation under multi-directional loading and the lower fracture toughness of HSC.

Chapter 5. **Nonlinear Finite Element Modeling of HSC Structural Walls**

5.1 Summary

Nonlinear finite element modeling (NLFEM) on the web crushing capacity of high-strength-concrete (HSC) structural walls was conducted and described in this chapter. Two parallel approaches were followed for this task. One is three-dimensional continuum-type finite element modeling with ABAQUS using a concrete damaged plasticity (CDP) model for concrete. The other is in-plane modeling with VecTor2 based on the Modified Compression Field Theory (MCFT). The analyses are described from the aspects of geometrical modeling, material properties, solution controls, and results. The results are compared with test data at the global and local levels to evaluate their performance in predicting flexural and shear behavior of structural walls failing in web crushing. Capabilities and limitations of the methods in evaluating the web crushing failure mechanism and capacity of structures were investigated. The continuum-type plasticity-based 3D models in ABAQUS were able to capture the global behavior of the single walls under monotonic loading well. However, issues related to the numerical technique of viscoplastic regularization and the behavior of the reinforced concrete structures under cyclic loading remain. The need for modifications to the concrete damaged plasticity model in ABAQUS in order to capture the inelastic shear behavior is recommended. On the other hand, VecTor2 analyses could model the behavior of the structural walls under both monotonic and cyclic loading well. Even the inelastic shear behavior in the plastic hinge region was captured. However, the concrete strength degradation under cyclic loading and the web crushing capacity are not considered appropriately and the web crushing capacity of the walls under cyclic loading could not be predicted. Both analytical methods revealed that the concrete

stress at web crushing was only a small portion of the compressive strength of HSC due to the complicated stress state in the web crushing region. The analytical results confirm that web crushing in the form of an inelastic shear failure is caused by the flexure-shear interaction effects induced in the web of the structural walls.

5.2 Introduction

Finite element modeling (FEM) is commonly conducted in order to improve the understanding of observed experimental phenomena or predict the complicated behavior of designed structures. With the rapid growth of computing resources and the use of parallel-computing, the analysis of large-scale reinforced concrete structures is becoming realistic and cost-effective.

The earliest application of FEM to reinforced concrete structures was by Ngo and Scordelis in 1967 [46]. Intensive research has been carried out since the 1970s on the special features of finite element analysis of reinforced concrete structures, including: constitutive relationships, failure theories, multi-axial stress theories, modeling of reinforcement, behavior on the interface between reinforcement and concrete, crack representation, mechanism of shear transfer, cyclic and dynamic loading effects, and the time-dependent effects of creep, shrinkage, and temperature variation.

However, the application of FEM on even traditional reinforced concrete structures has some problems due to the complicated nature of concrete material with crack propagation, slip across cracks, localization of stresses, and blond-slip behavior of the reinforcement. The weakness of concrete in tension leads to early cracking and the homogenous continuum assumption in conventional finite element theory is not valid in a strict sense. Moreover, to study the seismic behavior of the structures, it is essential for the models to be able to consider the effect of cyclic loading on the degrading concrete, which is still a challenge for most analysis models and procedures.

The earliest finite element analyses of reinforced concrete structures introduced the concept of discrete cracks [46]. However, due to the difficulty in updating the mesh with the progress of cracking with realistic computer resources, the application and development of the discrete crack approach is very limited. On the other hand, the smeared crack concept was introduced [47], which is compatible with the framework of the FEM since the mesh topology does not need to be updated during the analysis. Within the framework of smeared crack models, two concepts of cracking have been introduced: the fixed crack and the rotating crack concepts. The fundamental difference between them lies in the orientation of the cracks, which is kept constant in the fixed crack model and it is continuously updated in the rotating crack model. Another difference is related to the consideration of shear effects. In the fixed crack model, shear on the crack surface makes the axes of principal strain and stress non-coincident. This problem is solved by introducing a unique shear term that enforces coaxiality between principal stresses and strains. Nonetheless, use of the smeared rotating crack model is gaining popularity as indicated by the prevalence of the modified compression field theory (MCFT), which will be discussed later.

In the 3D modeling of reinforced concrete structures, a lot of effort has been dedicated in developing constitutive relationships for concrete materials within the framework of plasticity, fracture and damage mechanics. A noteworthy contribution was done by Chen et al. [48] who developed a plastic theory for concrete materials. Generally, 3D modeling has a very high demand on computer resources. Nowadays, the use of high performance parallel computing is common for the nonlinear analysis of large models. Unlike the modeling of plain concrete or very-light reinforced concrete structures like dams, the steel reinforcement in structures like bridge girders or structural walls changes the mechanical properties of the concrete material, which may place the efficiency of 3D concrete model in doubt. For example, the amount of reinforcement can affect the dowel effect on concrete and the tension behavior of concrete. Moreover, the confinement provided by stirrups improves the compressive strength of concrete. The bond and slip behavior of the embedded reinforcement is also paramount in adequately capturing localized stress effects as well as the distribution of inelastic actions. Unfortunately, these effects are very difficult to capture within a strict theoretical mechanics framework and most of the currently available finite element formulations fail to consider these effects.

On the other hand, phenomoenological models based on moment-curvature analyses [19] or relatively complicated beam-column-element [49] can work quite well for predicting the behavior of structures. They do this by capturing macro-scale behavior through experimentally calibrated models. These models have become increasingly valuable due to their ability to reliably predict global response. Further, in many cases, complicated 3D modeling is usually not needed and may not be able to give more accuracy compared to the much simpler, yet not strictly theoretically justified, phenomenological models. However, a common difficulty in analyzing reinforced concrete structural walls with finite element methods is the challenge of capturing inelastic shear behavior. Unlike the response of beams or slender walls, shear deformations contribute significantly, or dominate, the behavior and failure in squat or relatively short walls (aspect rations below 3).

In this chapter, two numerical investigations with different FE programs were conducted in parallel to analyze and model cantilevered structural walls subjected to flexure/shear effects. The case studies consist of the single wall test units evaluated experimentally in the first phase of this study (see Chapter 3). One study was conducted using 3D continuum-type plasticity-based FE modeling; the other consisted in performing 2D plane-stress analysis phenomenological-based FE models. In both cases, large general commercial nonlinear finite element software was used. The program ABAQUS [35] was used for the 3D continuum plasticity-based FE analyses, with particular use of its concrete damaged plasticity (CDP) model. The program VecTor2 [39] was used for the 2D plane-stress phenomenological-based FE analysis, with particular use of its implementation of the MCFT [28][39]. The analyses in this chapter are described from the aspects of geometrical modeling, material properties, solution controls, and results. Results were compared with test data at the global and local levels to evaluate performance of the analytical methods in predicting flexural/shear behavior of structural walls failing in web crushing. Capabilities and limitations of the methods in evaluating the web crushing failure mechanism and capacity in reinforced concrete walls were investigated. Further, the analytical results provided deep insights and promoted the understanding of web crushing behavior and the inelastic shear failure mechanism in structural walls with both qualitative and quantitative information.

5.3 ABAQUS Analysis of Single Walls under Monotonic Loading

5.3.1 Geometrical Modeling

Models for the single wall test units were created through ABAQUS CAE. ABAQUS version 6.9-2 Standard [35] was used to implement all the nonlinear static analyses. Half of the walls were modeled in view of the symmetry along the central vertical plane of the walls. An overview of the model is shown in Figure 5.1(a). Two parts were created, one for the concrete material which included the footing, the column body and the loading block, and the other for the reinforcement where only the column body steel was explicitly modeled. Figure 5.1(b) shows the reinforcement part while the concrete part is as shown Figure 5.1(a).

Each part was meshed separately with the reinforcement being embedded in the concrete solid elements. The meshed model is shown in Figure 5.1(c). Both footing and load block were assigned elastic material properties without reinforcement. The concrete damaged plasticity (CDP) material model in ABAQUS was used for the column body concrete. The element type for the concrete parts was a three-dimensional continuum-type solid element with 8 nodes and reduced integration (C3D8R). The steel reinforcement was modeled with three-dimensional two-node truss elements with full integration.

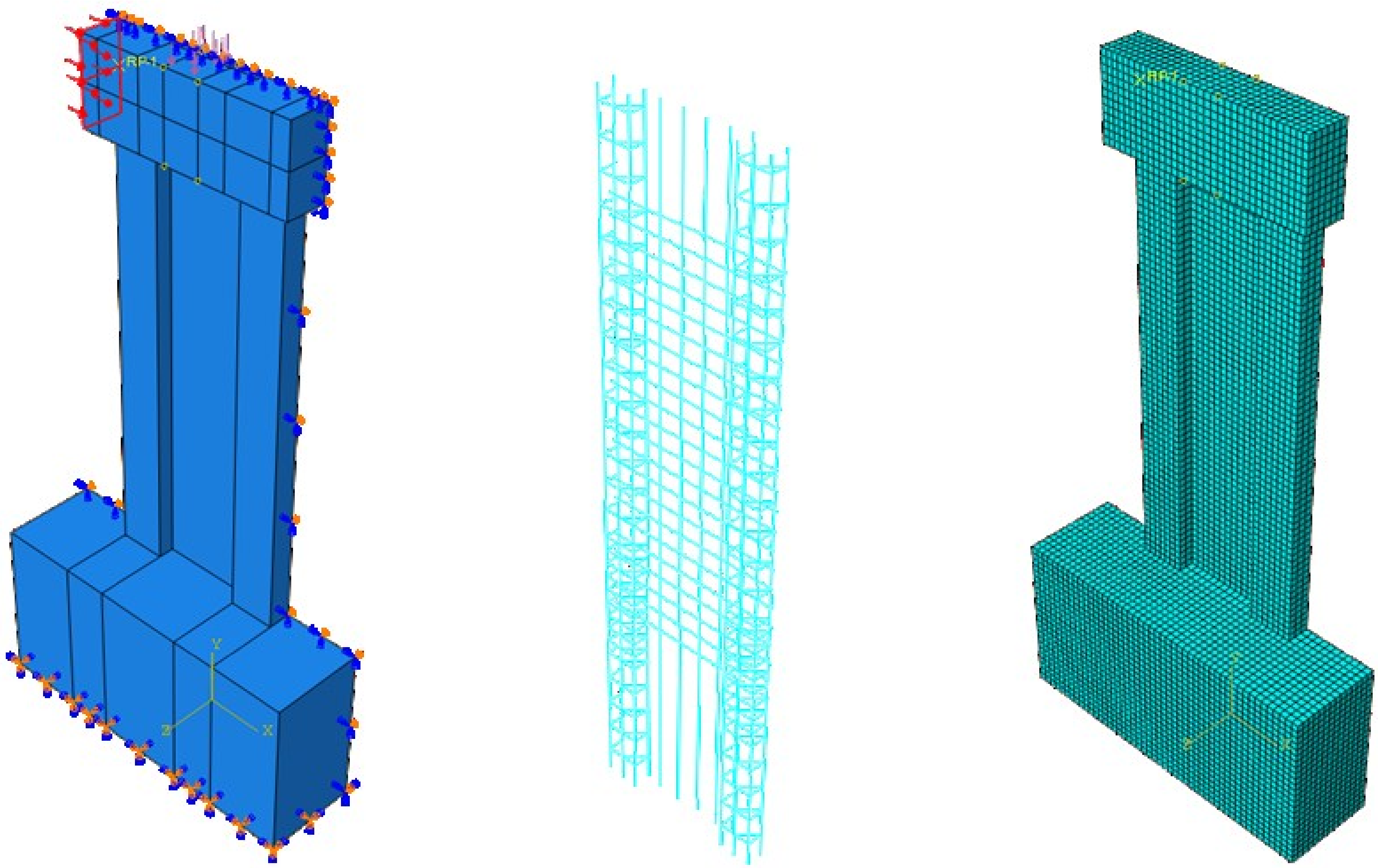

Figure 5.1 Overview of 3D ABAQUS model: (a) Model geometry; (b) Reinforcement part; (c) Mesh of the concrete part

5.3.2 Material Properties

With the use of the CDP model, it is critical to appropriately define the compression softening and tension stiffening behavior of the concrete material. Very high material nonlinearity is expected in reinforced concrete walls failing by web crushing, which normally causes numerical problems and convergence difficulties in ABAQUS Standard. It is almost essential to introduce some viscoplastic damping to achieve convergence; however, the viscosity parameter μ, should be as small as possible so that adequate accuracy of the results can be achieved. Therefore, a trial-and-error on the value of the parameter is usually needed.

The elastic property of the concrete material is defined by the elastic modulus and the Poisson's ratio. To define the CDP model, curves for concrete compression hardening, compression damage, concrete tension stiffening, tension damage and parameters to describing the shape of the flow potential and yield function need to be defined. These parameters include the dilation angle ψ, the flow potential eccentricity ϵ, the ratio of initial equibiaxial compressive yield stress to initial uniaxial compressive yield stress σ_{b0}/σ_{c0}, and the ratio of the second stress invariant on the tensile meridian to that on the compressive meridian K_C. The experimental values for tensile and compressive strengths of concrete were used to generate uniaxial stress-strain curves with the model suggested by Collins et al. for compression [50] and the exponential model for tension [51]. Concrete damage was defined by following the recommendations by Lee and Fenves [37].

The steel reinforcement properties were defined based on experimental data on tension tests of the different bar sizes fitted with uniaxial models. The calibrated parameters were then used to define the input curves for analysis.

The definition of the CDP model is explained in the following. The uniaxial compressive stress-strain constitutive relationship follows the model proposed by Collins et al. [50] with the equations shown below.

$$\frac{f_c}{f'_c} = \frac{\varepsilon_c}{\varepsilon'_c} \cdot \frac{n}{n - 1 + (\varepsilon_c/\varepsilon'_c)^{nk}} \tag{5-1}$$

where

$$k = 0.67 + \frac{f'_c}{9000} \text{ (psi units)} \tag{5-2}$$

$$n = 0.8 + \frac{f'_c}{2500} \quad \text{(psi units)} \tag{5-3}$$

$$\varepsilon'_c = \frac{f'_c}{E_c} \cdot \frac{n}{n - 1} \tag{5-4}$$

$$E_c = 40{,}000\sqrt{f'_c} + 1{,}000{,}000 \text{ (psi units)} \tag{5-5}$$

An exponential law is used to model the tension stiffening of concrete material [51]. The corresponding exponential equation is

$$\sigma = f_t \cdot e^{-b\left(\varepsilon - \frac{f_t}{E}\right)} \tag{5-6}$$

$$b = \frac{f_t}{G_f - \frac{f_t^2}{2E}} \tag{5-7}$$

where G_f is the fracture energy of concrete, which is the energy required to propagate a tensile crack of unit area. The values of G_f for different strengths of concrete were obtained from Table 2.1.4, which is provided by the CEB-FIP Model Code 1990 [52]. Table 5-1 shows the G_f values corresponding to the maximum aggregate size of 8 mm (0.315 in.). A linear fit equation of the data in Table 5-1 was used to calculate the G_f values for the corresponding concrete compressive strengths in the high-strength-concrete wall test units.

Table 5-1 Fracture energy of concrete materials

f_c' (ksi)	20	28	38	48	58	68	78	88
G_f (Nm/m2)	40	50	65	70	85	95	105	115

Another important part of the CDP model definition are the damage properties. Cervera et al. [53] proposed a damage model for concrete dam analysis. However, in this study, the damage evolution rules by Lee and Fenves [37] are referred for the definition of damage curves. The explanation of the definition is shown in the following.

For damage in both tension and compression $\aleph \in \{t,\ c\}$,

$$D_\aleph = 1 - \left[\left(\frac{1}{a_\aleph}\right)\left(1 + a_\aleph - \sqrt{\phi_\aleph(\kappa_\aleph)}\right)\right]^{d_\aleph/b_\aleph} \tag{5-8}$$

$$\phi_\aleph(\kappa_\aleph) = 1 + a_\aleph(2 + a_\aleph)\kappa_\aleph \tag{5-9}$$

$$\kappa_\aleph = \frac{1}{g_\aleph}\int_0^{\varepsilon^p} \sigma_\aleph(\varepsilon^p)d\varepsilon^p \tag{5-10}$$

$$g_\aleph = \int_0^{\varepsilon^p} \sigma_\aleph(\varepsilon^p)d\varepsilon^p \tag{5-11}$$

$$\frac{d_c}{b_c} = \frac{log\left(1 - \widetilde{D}_c\right)}{log\left(\frac{1 + a_c}{2a_c}\right)} \qquad \text{for compression} \tag{5-12a}$$

$$\frac{d_t}{b_t} = \frac{log\left(1 - \widetilde{D}_t\right)}{log\left[(1 + a_t) - \sqrt{1 + a_t^2}\right] - log(2a_t)} \qquad \text{for tension} \tag{5-12b}$$

where $\widetilde{D}_c$ is the damage value at the maximum compressive stress and $\widetilde{D}_t$ is corresponding to $\sigma_t = f_t/2$, a_c can be calculated from $\sqrt{\phi(\kappa_c')} = \frac{1+a_c}{2}$ and a_t can be calculated from

$\sqrt{\phi(\kappa_t')} = \frac{1+a_t+\sqrt{1+a_t^2}}{2}$, where κ_c' is corresponding to the maximum compressive stress and κ_t' is corresponding to $\sigma_t = f_t/2$.

Table 5-2 to Table 5-5 show the parameters of the CDP model for concrete and the steel nonlinear parameters for the four single walls tested under monotonic loading.

Table 5-2 The concrete and steel material parameters for M05M.

M05M		The parameters of CDP model	
		ψ	28°
		ϵ	0.1
Concrete elasticity		σ_{b0}/σ_{c0}	1.16
E(ksi)	4006.7	K_c	0.667
ν	0.2	μ	0.03
Concrete compression hardening		Concrete compression damage	
Stress (ksi)	Crushing strain	DamageC	Crushing strain
4.00	0	0	0
5.12	0.00022	0.05	0.00022
5.65	0.00068	0.15	0.00068
3.45	0.00239	0.43	0.00239
1.88	0.00378	0.59	0.00378
0.83	0.00554	0.74	0.00554
0.39	0.00740	0.89	0.00740
0.32	0.00792	0.89	0.00792
Concrete tension stiffening		Concrete tension damage	
Stress (ksi)	Cracking strain	DamageT	Cracking strain
0.515	0	0	0
0.258	0.00051	0.50	0.00051
0.052	0.00159	0.89	0.00159
0.011	0.00260	0.97	0.00260
0.011	0.00500	0.97	0.00500

Reinforcing Steel Properties					
#8 Steel		#7 Steel		#3 Steel	
E(ksi)	29000	E(ksi)	29000	E(ksi)	29000
ν	0.3	ν	0.3	ν	0.3
Stress (ksi)	Plastic strain	Stress (ksi)	Plastic strain	Stress (ksi)	Plastic strain
76.32	0	65.05	0	66.63	0
88.81	0.00689	86.68	0.01681	66.97	0.00516
97.44	0.01153	93.65	0.02633	80.22	0.01704
106.14	0.01614	98.11	0.03584	88.52	0.02651
114.93	0.02073	100.92	0.04531	95.09	0.03594
123.79	0.02529	102.75	0.05473	100.19	0.04534
132.74	0.02982	104.06	0.06407	104.07	0.05468
141.77	0.03433	105.12	0.07334	106.98	0.06397
150.88	0.03881	106.11	0.08252	109.14	0.0732
160.07	0.04327	107.09	0.09162	110.77	0.08236
				112.05	0.09145

Table 5-3 The concrete and steel material parameters for M10M.

M10M		The parameters of CDP model	
		ψ	34.6°
		ϵ	0.1
Concrete elasticity		σ_{b0}/σ_{c0}	1.16
E(ksi)	5472.1	K_c	0.667
ν	0.2	μ	0.02
Concrete compression hardening		Concrete compression damage	
Stress (ksi)	Crushing strain	DamageC	Crushing strain
9.25	0	0	0
11.58	0.00013	0.048	0.00013
12.5	0.00048	0.16	0.00048
7.21	0.00193	0.509	0.00193
2.26	0.00334	0.773	0.00334
0.19	0.00472	0.929	0.00472
0.19	0.00750	0.929	0.00750
Concrete tension stiffening		Concrete tension damage	
Stress (ksi)	Cracking strain	DamageT	Cracking strain
0.804	0	0	0
0.573	0.0003	0.292	0.0003
0.402	0.00059	0.500	0.00059
0.197	0.00116	0.744	0.00116
0.068	0.00199	0.904	0.00199
0.068	0.00320	0.977	0.00320
0.068	0.00500	0.977	0.00500

Reinforcing Steel Properties					
#8 Steel		#7 Steel		#3 Steel	
E(ksi)	29000	E(ksi)	29000	E(ksi)	29000
ν	0.3	ν	0.3	ν	0.3
Stress (ksi)	Plastic strain	Stress (ksi)	Plastic strain	Stress (ksi)	Plastic strain
68.16	0	65	0	68.76	0
68.68	0.008	65.5	0.008	68.99	0.003
79.43	0.017	75.84	0.017	74.86	0.007
88.21	0.027	83.64	0.027	86.57	0.017
95.22	0.036	89.37	0.036	95.82	0.026
100.65	0.045	93.44	0.046	102.95	0.036
104.72	0.055	96.26	0.055	108.26	0.045
107.66	0.064	98.18	0.064	112.11	0.054
109.7	0.073	99.53	0.074	114.8	0.064
111.12	0.082	100.57	0.083	116.67	0.073
112.2	0.091	101.51	0.092	118.01	0.082
				119.13	0.091

Table 5-4 The concrete and steel material parameters for M15M.

M15M		The parameters of CDP model	
		ψ	25°
		ϵ	0.1
Concrete elasticity		σ_{b0}/σ_{c0}	1.16
E(ksi)	6075.4	K_c	0.667
ν	0.2	μ	0.02
Concrete compression hardening		Concrete compression damage	
Stress (ksi)	Crushing strain	DamageC	Crushing strain
11.99	0	0	0
14.66	8.60E-05	0.026	8.60E-05
16.10	0.00042	0.130	0.00042
13.81	0.00098	0.273	0.00098
8.15	0.00216	0.530	0.00216
3.51	0.00317	0.734	0.00317
0.19	0.00447	0.934	0.00447
0.19	0.00600	0.934	0.00600
Concrete tension stiffening		Concrete tension damage	
Stress (ksi)	Cracking strain	DamageT	Cracking strain
0.898	0	0	0
0.664	0.00029	0.265	0.00029
0.449	0.00065	0.500	0.00065
0.255	0.00116	0.707	0.00116
0.158	0.00157	0.812	0.00157
0.077	0.00219	0.903	0.00219
0.077	0.00300	0.903	0.00300
0.077	0.00380	0.903	0.00380
0.077	0.00500	0.903	0.00500

Reinforcing Steel Properties					
#8 Steel		#7 Steel		#3 Steel	
E(ksi)	29000	E(ksi)	29000	E(ksi)	29000
ν	0.3	ν	0.3	ν	0.3
Stress (ksi)	Plastic strain	Stress (ksi)	Plastic strain	Stress (ksi)	Plastic strain
85.81	0	61.31	0	69.95	0
93.48	0.017	61.78	0.008	70.2	0.004
98.73	0.026	73.45	0.017	76.38	0.007
103.95	0.036	81.97	0.027	89.17	0.017
109.22	0.045	88.18	0.036	98.66	0.026
114.55	0.054	92.57	0.046	105.51	0.036
119.96	0.064	95.57	0.055	110.28	0.045
125.45	0.073	97.59	0.064	113.53	0.054
131.03	0.082	98.98	0.074	115.72	0.064
136.68	0.091	100.03	0.083	117.26	0.073
		100.96	0.092	118.47	0.082
				119.56	0.091

Table 5-5 The concrete and steel material parameters for M20M.

<table>
<tr><td colspan="6" rowspan="3">M20M</td><td colspan="6">The parameters of CDP model</td></tr>
<tr><td colspan="3">ψ</td><td colspan="3">25°</td></tr>
<tr><td colspan="3">ϵ</td><td colspan="3">0.1</td></tr>
<tr><td colspan="6">Concrete elasticity</td><td colspan="3">σ_{b0}/σ_{c0}</td><td colspan="3">1.16</td></tr>
<tr><td colspan="3">E(ksi)</td><td colspan="3">6075.4</td><td colspan="3">K_c</td><td colspan="3">0.667</td></tr>
<tr><td colspan="3">ν</td><td colspan="3">0.2</td><td colspan="3">μ</td><td colspan="3">0.02</td></tr>
<tr><td colspan="6">Concrete compression hardening</td><td colspan="6">Concrete compression damage</td></tr>
<tr><td colspan="3">Stress (ksi)</td><td colspan="3">Crushing strain</td><td colspan="3">DamageC</td><td colspan="3">Crushing strain</td></tr>
<tr><td colspan="3">11.99</td><td colspan="3">0</td><td colspan="3">0</td><td colspan="3">0</td></tr>
<tr><td colspan="3">14.66</td><td colspan="3">8.60E-05</td><td colspan="3">0.026</td><td colspan="3">8.60E-05</td></tr>
<tr><td colspan="3">16.10</td><td colspan="3">0.00042</td><td colspan="3">0.130</td><td colspan="3">0.00042</td></tr>
<tr><td colspan="3">13.81</td><td colspan="3">0.00098</td><td colspan="3">0.273</td><td colspan="3">0.00098</td></tr>
<tr><td colspan="3">8.15</td><td colspan="3">0.00216</td><td colspan="3">0.530</td><td colspan="3">0.00216</td></tr>
<tr><td colspan="3">3.51</td><td colspan="3">0.00317</td><td colspan="3">0.734</td><td colspan="3">0.00317</td></tr>
<tr><td colspan="3">0.19</td><td colspan="3">0.00447</td><td colspan="3">0.934</td><td colspan="3">0.00447</td></tr>
<tr><td colspan="3">0.19</td><td colspan="3">0.00600</td><td colspan="3">0.934</td><td colspan="3">0.00600</td></tr>
<tr><td colspan="6">Concrete tension stiffening</td><td colspan="6">Concrete tension damage</td></tr>
<tr><td colspan="3">Stress (ksi)</td><td colspan="3">Cracking strain</td><td colspan="3">DamageT</td><td colspan="3">Cracking strain</td></tr>
<tr><td colspan="3">0.898</td><td colspan="3">0</td><td colspan="3">0</td><td colspan="3">0</td></tr>
<tr><td colspan="3">0.664</td><td colspan="3">0.00029</td><td colspan="3">0.265</td><td colspan="3">0.00029</td></tr>
<tr><td colspan="3">0.449</td><td colspan="3">0.00065</td><td colspan="3">0.500</td><td colspan="3">0.00065</td></tr>
<tr><td colspan="3">0.255</td><td colspan="3">0.00116</td><td colspan="3">0.707</td><td colspan="3">0.00116</td></tr>
<tr><td colspan="3">0.158</td><td colspan="3">0.00157</td><td colspan="3">0.812</td><td colspan="3">0.00157</td></tr>
<tr><td colspan="3">0.077</td><td colspan="3">0.00219</td><td colspan="3">0.903</td><td colspan="3">0.00219</td></tr>
<tr><td colspan="3">0.077</td><td colspan="3">0.00300</td><td colspan="3">0.903</td><td colspan="3">0.00300</td></tr>
<tr><td colspan="3">0.077</td><td colspan="3">0.00380</td><td colspan="3">0.903</td><td colspan="3">0.00380</td></tr>
<tr><td colspan="3">0.077</td><td colspan="3">0.00500</td><td colspan="3">0.903</td><td colspan="3">0.00500</td></tr>
<tr><td colspan="12">Reinforcing Steel Properties</td></tr>
<tr><td colspan="4">#8 Steel</td><td colspan="4">#7 Steel</td><td colspan="4">#3 Steel</td></tr>
<tr><td colspan="2">E(ksi)</td><td colspan="2">29000</td><td colspan="2">E(ksi)</td><td colspan="2">29000</td><td colspan="2">E(ksi)</td><td colspan="2">29000</td></tr>
<tr><td colspan="2">ν</td><td colspan="2">0.3</td><td colspan="2">ν</td><td colspan="2">0.3</td><td colspan="2">ν</td><td colspan="2">0.3</td></tr>
<tr><td colspan="2">Stress (ksi)</td><td colspan="2">Plastic strain</td><td colspan="2">Stress (ksi)</td><td colspan="2">Plastic strain</td><td colspan="2">Stress (ksi)</td><td colspan="2">Plastic strain</td></tr>
<tr><td colspan="2">65.57</td><td colspan="2">0</td><td colspan="2">64.86</td><td colspan="2">0</td><td colspan="2">63.64</td><td colspan="2">0</td></tr>
<tr><td colspan="2">65.78</td><td colspan="2">0.003</td><td colspan="2">65.1</td><td colspan="2">0.004</td><td colspan="2">63.77</td><td colspan="2">0.002</td></tr>
<tr><td colspan="2">71.98</td><td colspan="2">0.007</td><td colspan="2">70.36</td><td colspan="2">0.008</td><td colspan="2">71.07</td><td colspan="2">0.007</td></tr>
<tr><td colspan="2">83.26</td><td colspan="2">0.017</td><td colspan="2">81.54</td><td colspan="2">0.017</td><td colspan="2">81.82</td><td colspan="2">0.017</td></tr>
<tr><td colspan="2">91.89</td><td colspan="2">0.026</td><td colspan="2">90.25</td><td colspan="2">0.026</td><td colspan="2">90.36</td><td colspan="2">0.026</td></tr>
<tr><td colspan="2">98.3</td><td colspan="2">0.036</td><td colspan="2">96.84</td><td colspan="2">0.036</td><td colspan="2">96.95</td><td colspan="2">0.036</td></tr>
<tr><td colspan="2">102.93</td><td colspan="2">0.045</td><td colspan="2">101.67</td><td colspan="2">0.045</td><td colspan="2">101.91</td><td colspan="2">0.045</td></tr>
<tr><td colspan="2">106.17</td><td colspan="2">0.055</td><td colspan="2">105.11</td><td colspan="2">0.055</td><td colspan="2">105.5</td><td colspan="2">0.055</td></tr>
<tr><td colspan="2">108.39</td><td colspan="2">0.064</td><td colspan="2">107.49</td><td colspan="2">0.064</td><td colspan="2">108.04</td><td colspan="2">0.064</td></tr>
<tr><td colspan="2">109.94</td><td colspan="2">0.073</td><td colspan="2">109.14</td><td colspan="2">0.073</td><td colspan="2">109.8</td><td colspan="2">0.073</td></tr>
<tr><td colspan="2">111.12</td><td colspan="2">0.082</td><td colspan="2">110.35</td><td colspan="2">0.082</td><td colspan="2">111.07</td><td colspan="2">0.082</td></tr>
<tr><td colspan="2">112.16</td><td colspan="2">0.091</td><td colspan="2">111.39</td><td colspan="2">0.091</td><td colspan="2">112.13</td><td colspan="2">0.091</td></tr>
</table>

5.3.3 Solution Controls

An axial load of 130 kips was applied on the top surface of the load stub for all the analyzed test units. The magnitude of the distributed load was 0.9 ksi applied on a bearing area of 8 in. x 18 in. to model the real test setup. A horizontal ramp load was applied on a side surface of the load stub. The magnitude of the distributed load was decided according to the load-carrying capacity of the test unit. The bottom surface of the footing was fixed to the floor. Figure 5.1(a) shows the axial and horizontal loads with the bottom boundary condition and the symmetric constraints.

5.3.4 Results

Figure 5.2 to Figure 5.5 show a comparison of the global force-displacement curves between the experiment and the ABAQUS analyses for test units M05M, M10M, M15M and M20M [54]. It can be seen that the simulated global behavior of the test units matched the experimental response well. However, the models were not able to predict the web crushing failure since no load-carrying capacity drop was observed from the simulation. The comparison was made by plotting the numerical results up to the point same displacement reached in the experiment. Further comparisons were made by investigating the flexure and shear behavior separately. The same data reduction process was conducted on each model with a complete set of numerical simulated data output corresponding to the experimental instrumentation measurements. Figure 5.6 and Figure 5.7 show comparisons of the flexural and shear force-displacement behavior for wall M05M, respectively; while Figure 5.8 and Figure 5.9 show the corresponding comparisons for wall M20M. Although the global behavior was well predicted, distinct discrepancies were observed on the predicted flexural and shear components of behavior. It can be seen that shear deformations were over-predicted. Actually, data reduction shows that the calculated shear deformation from the bottom panel and the top panel was close for the four models, which indicates that the web experienced uniform damage, as is observed on the contour plots for the compressive damage index (DamageC). Figure 5.10 and Figure 5.11 show the contour plots of DamageC for walls M05M and M20M.

On the other hand, the ABAQUS analyses under-estimated flexural deformations. Figure 5.12 and Figure 5.13 show the comparisons of curvature profiles between the tests and analyses. It can be seen that the spread of plasticity along the height of the wall was not as large as in the experiment. Plasticity in the FE models was mainly concentrated in the bottom 2 ft (610 mm) of the wall height. The comparison of curvature profiles for wall M05M is better since the wall failed in elastic shear and the spread of plasticity barely developed.

To evaluate the stress state in the web, especially at the web crushing region, Figure 5.14 and Figure 5.15 show the contour plots of compressive equivalent plastic strain (PEEQ) for walls M05M and M20M. The maximum strain region is located next to the compression boundary element and expands out with increasing displacement demand, which is consistent with the web crushing regions observed in the tests of walls M05M and M20M. However, it is difficult for the contour to reflect the crack pattern observed in the experiment, such as the expansion of the diagonal tensile cracking in the web. This shortcoming may be attributed to the CDP model, which is a continuum based model and has no crack concept in its formulation.

It is of interest to evaluate the stress state of the elements in the web crushing region in order to investigate the degradation of concrete strength under such complicated stress state. Figure 5.16 and Figure 5.17 show traces for the minimum principal stress versus the logarithmic strain of elements in the crushed region for walls M05M and M20M, respectively. It is important to notice that the maximum compressive stress reached before failure is close for both test walls, which indicates that HSC degrades significantly under multi-axial stress state and only 10~20% of the uniaxial concrete compressive strength is left while for the NSC wall, almost 50% of the strength is left at the onset of failure. It should be noted that the curves of minimum principal stress versus logarithmic strain are not similar to the uniaxial compressive stress-strain curves due to the highly localized behavior and complicated loading and unloading that happens in the web-crushing region, even under a monotonic loading process.

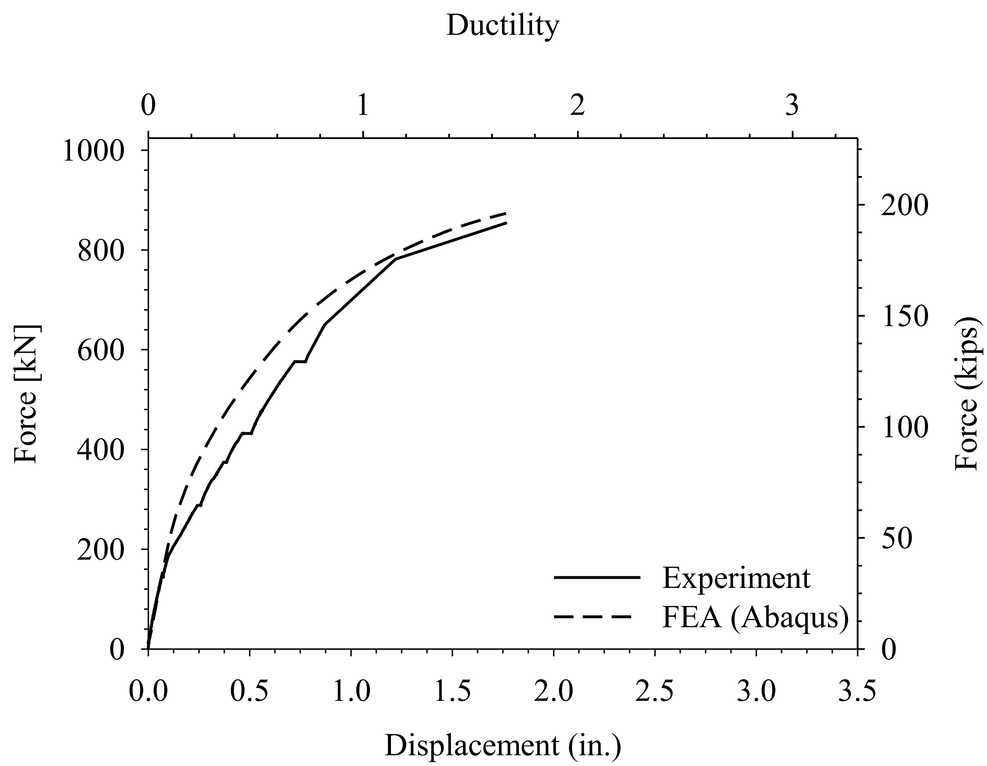

Figure 5.2 M05M global force-displacement behavior comparison between experiment and ABAQUS.

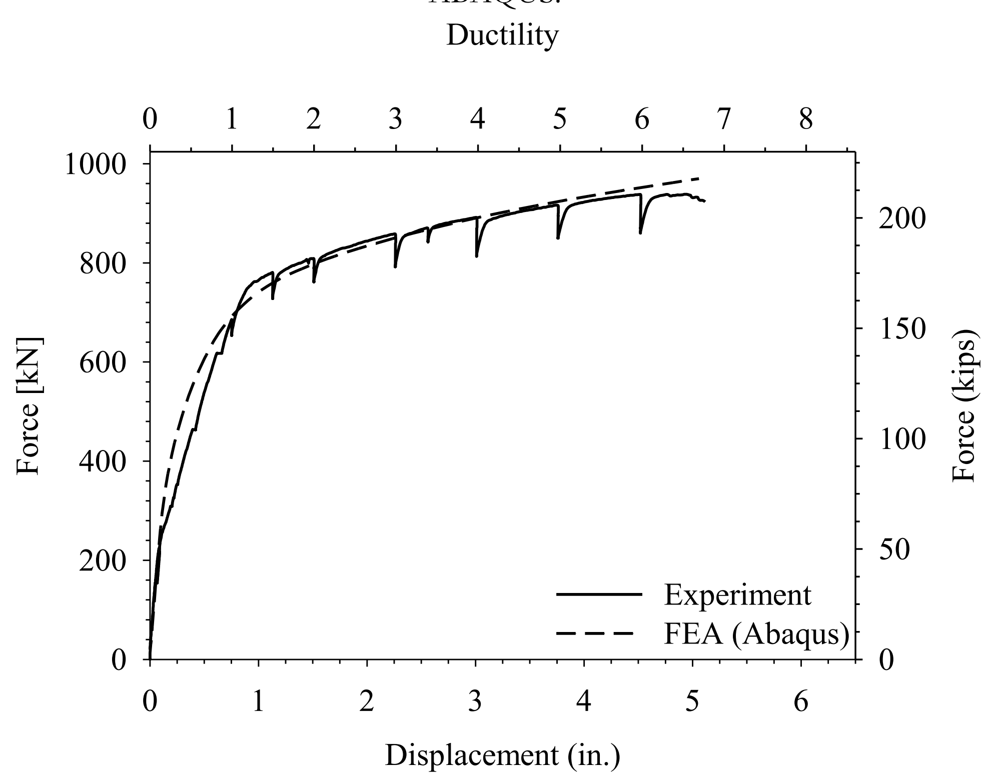

Figure 5.3 M10M global force-displacement behavior comparison between experiment and ABAQUS.

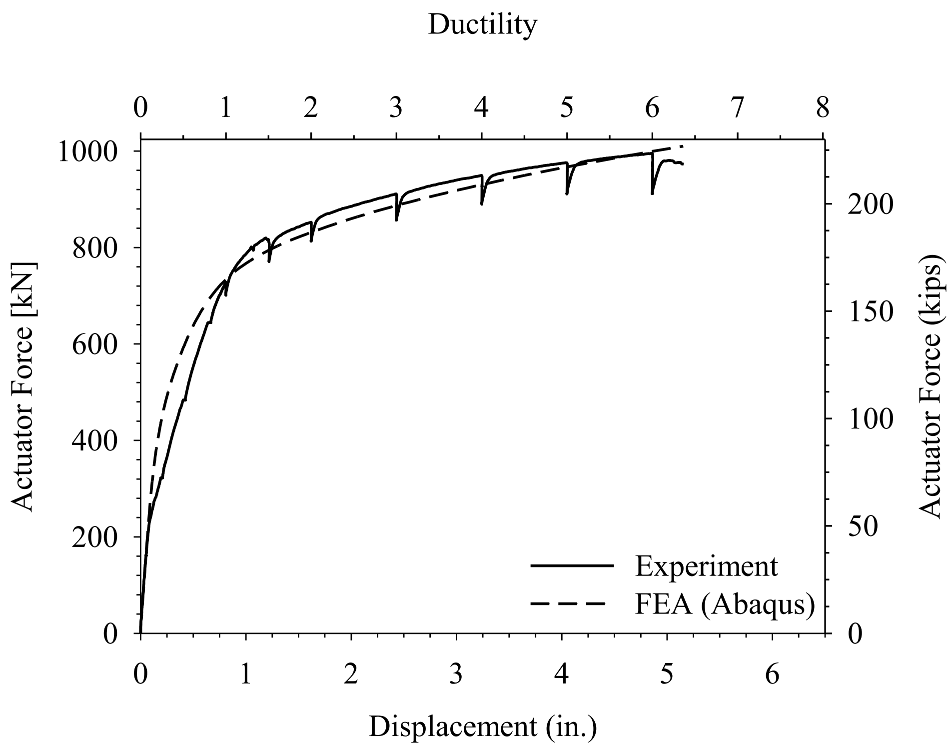

Figure 5.4 M15M global force-displacement behavior comparison between experiment and ABAQUS.

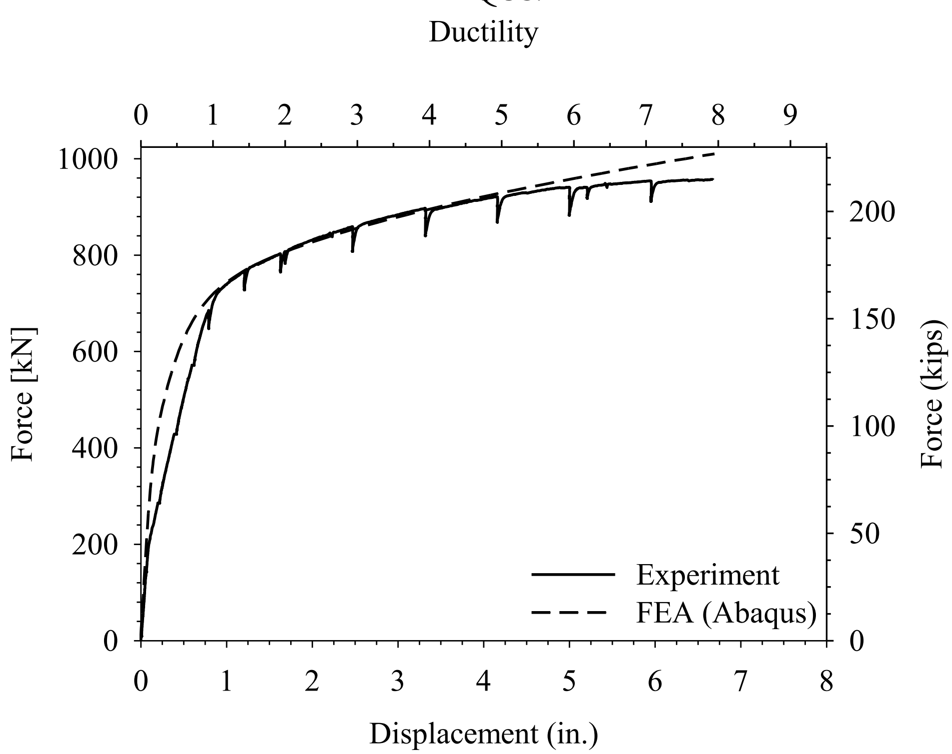

Figure 5.5 M20M global force-displacement behavior comparison between experiment and ABAQUS.

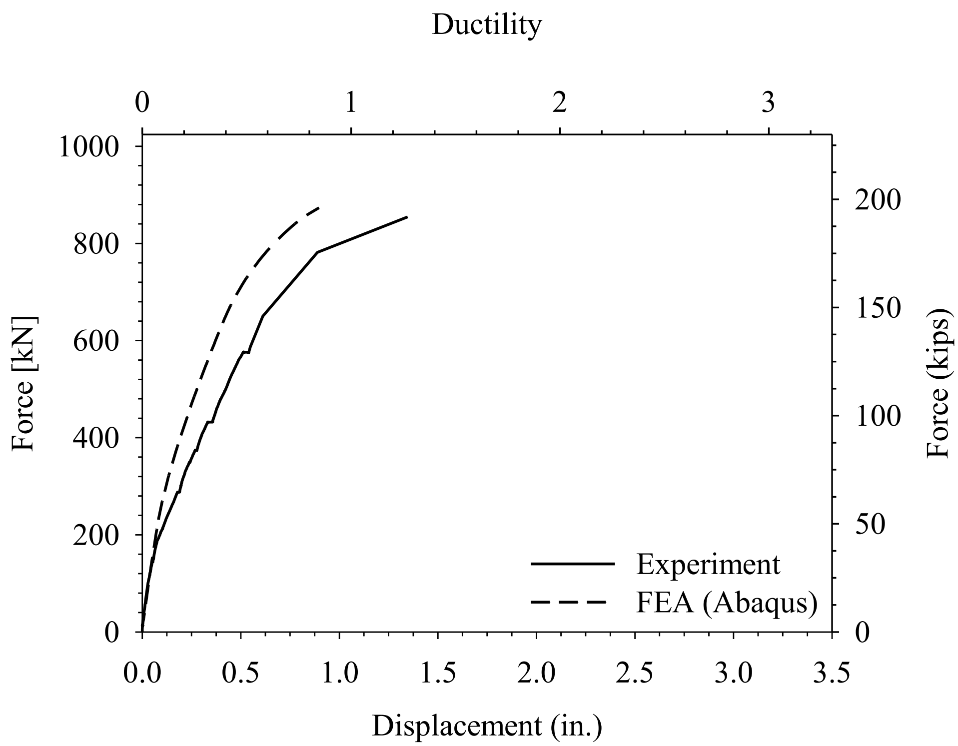

Figure 5.6 M05M flexural force-displacement behavior comparison between experiment and ABAQUS.

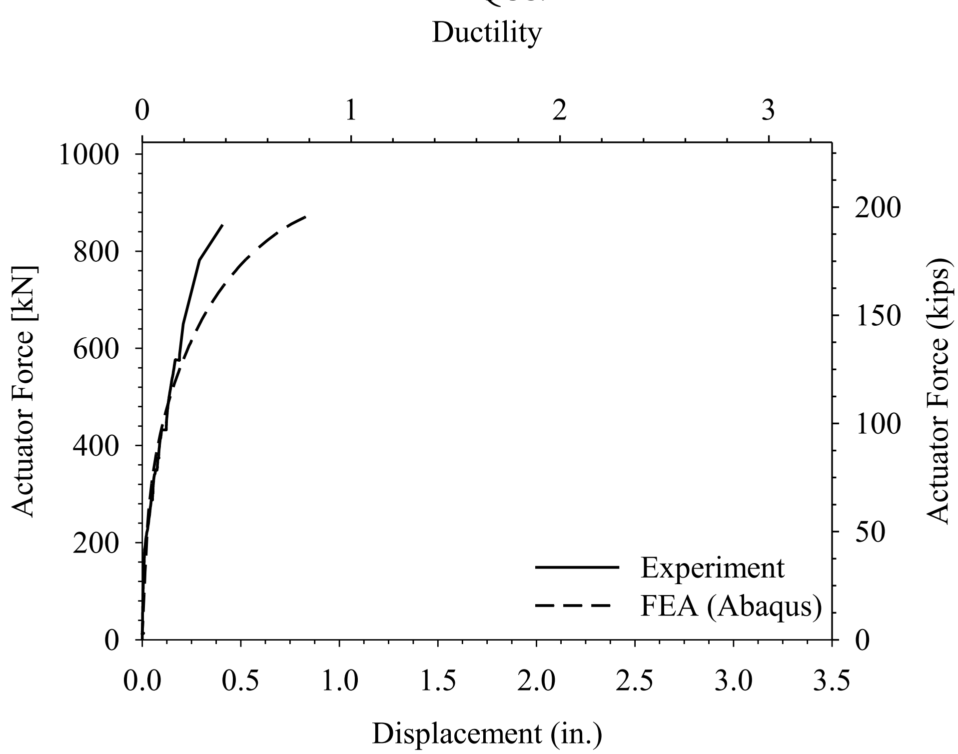

Figure 5.7 M05M shear force-displacement behavior comparison between experiment and ABAQUS.

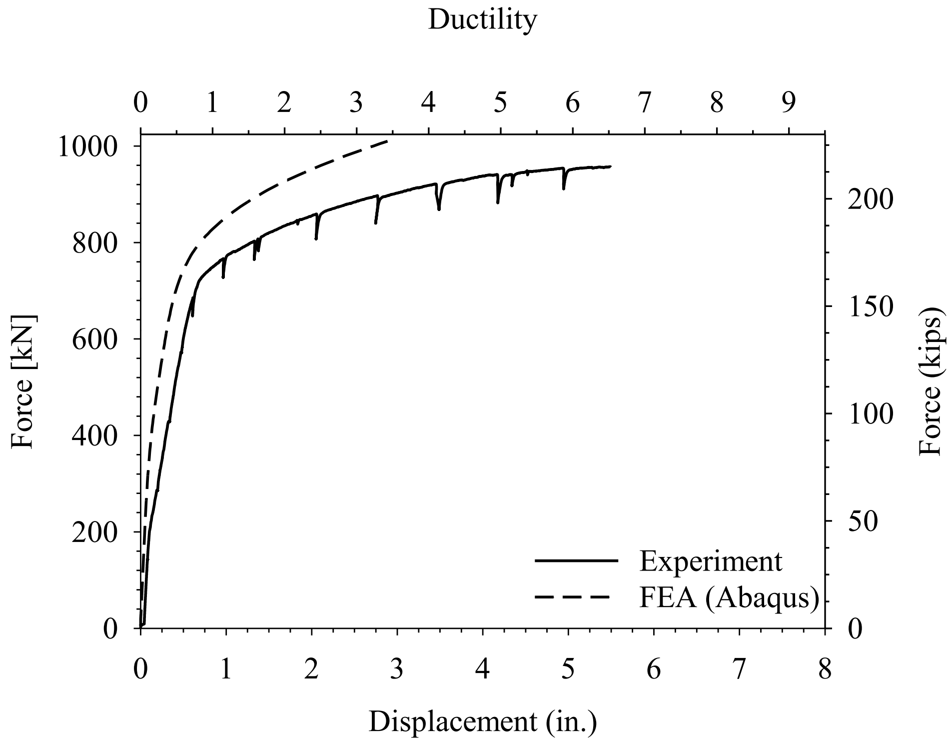

Figure 5.8 M20M flexural force-displacement behavior comparison between experiment and ABAQUS.

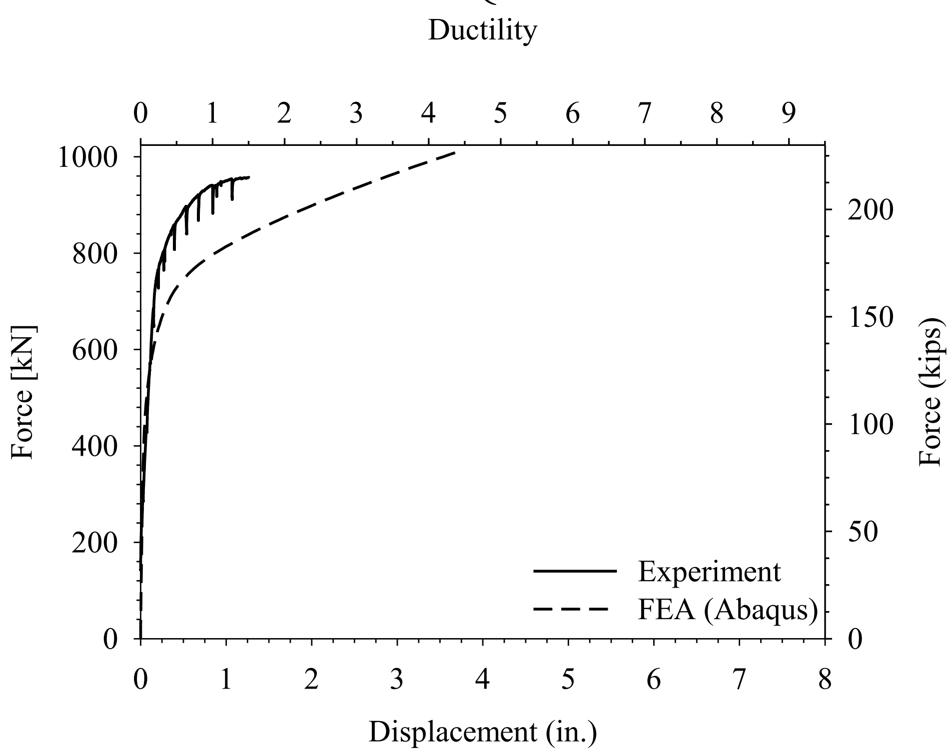

Figure 5.9 M20M shear force-displacement behavior comparison between experiment and ABAQUS.

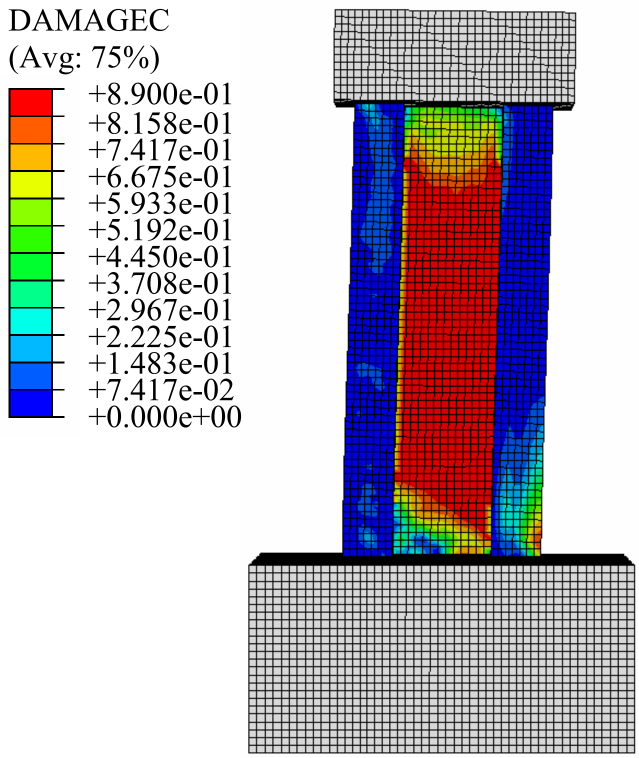

Figure 5.10 M05M contour plot: Compressive damage variable (DAMAGEC)

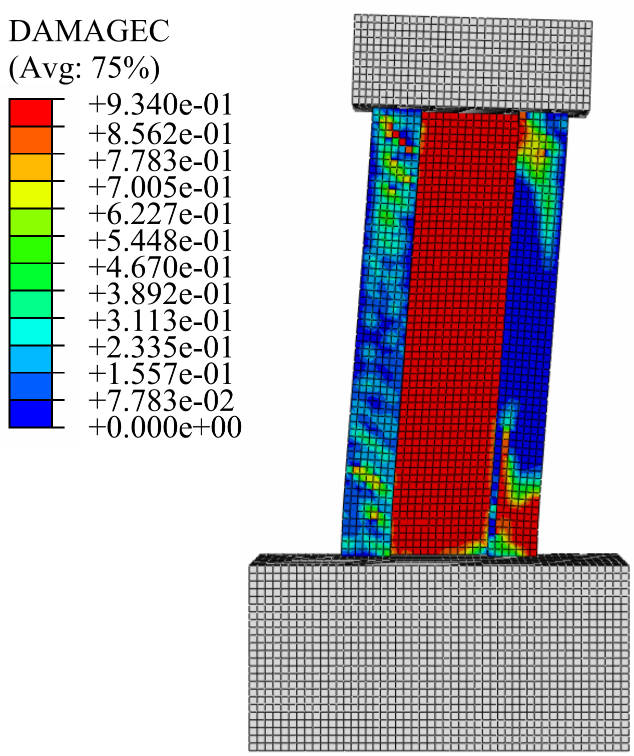

Figure 5.11 M20M contour plot: Compressive damage variable (DAMAGEC)

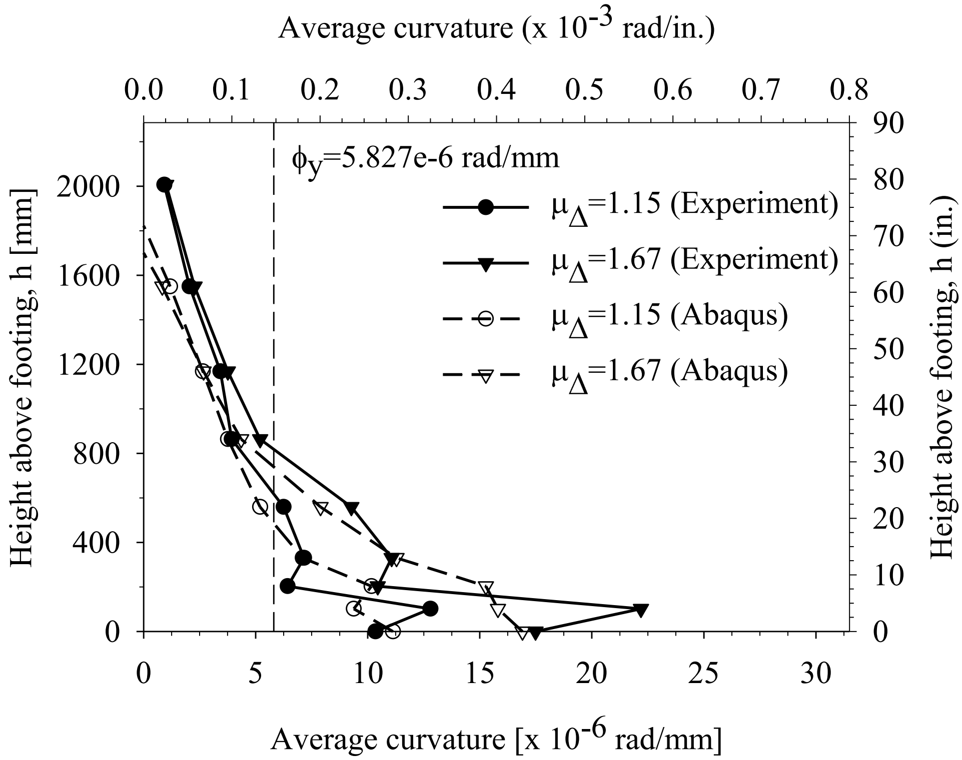

Figure 5.12 M05M curvature profile comparison between experiment and ABAQUS.

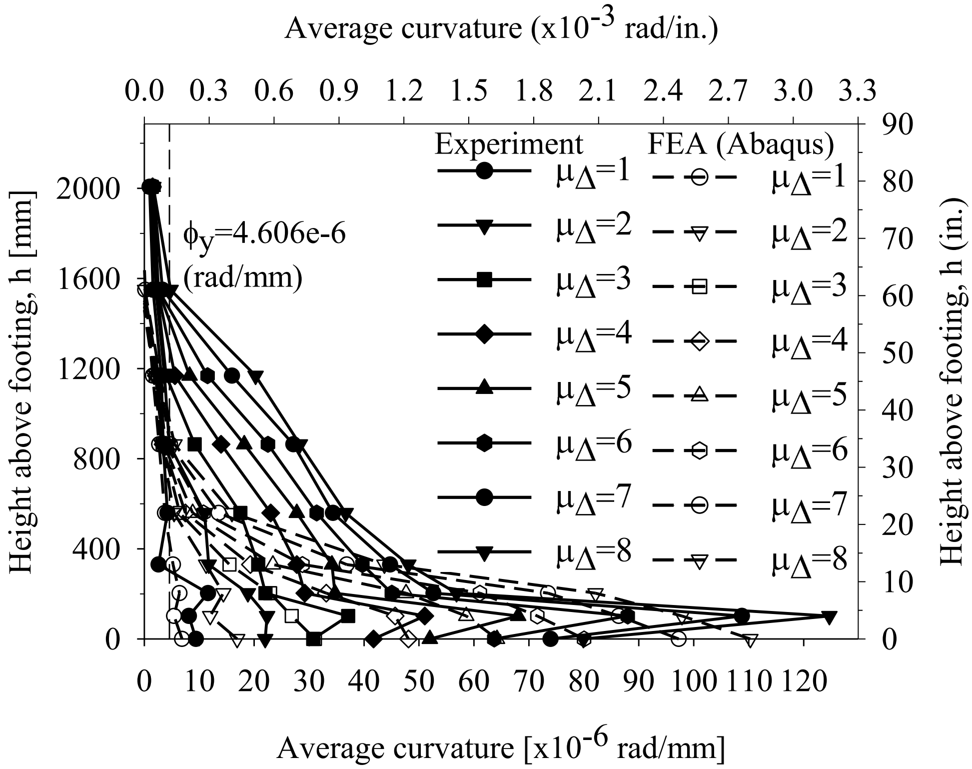

Figure 5.13 M20M curvature profile comparison between experiment and ABAQUS.

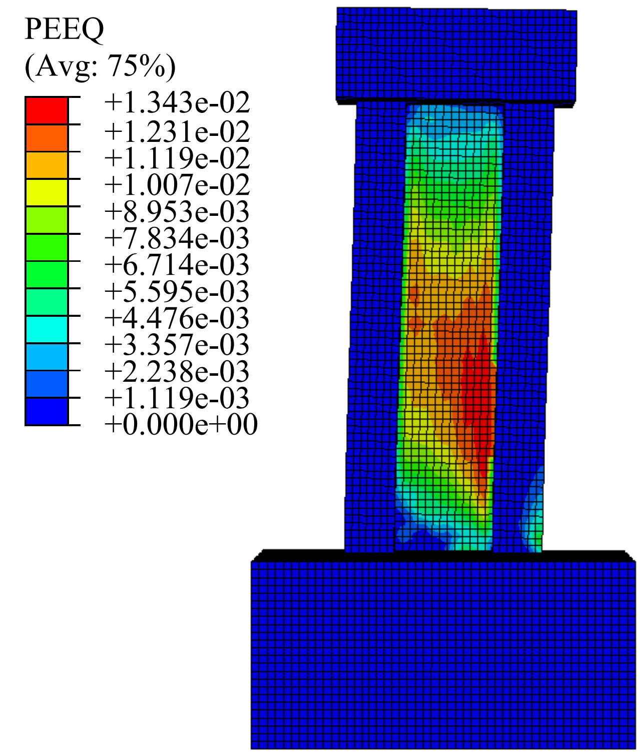

Figure 5.14 M05M contour plot: Compressive equivalent plastic strain (PEEQ).

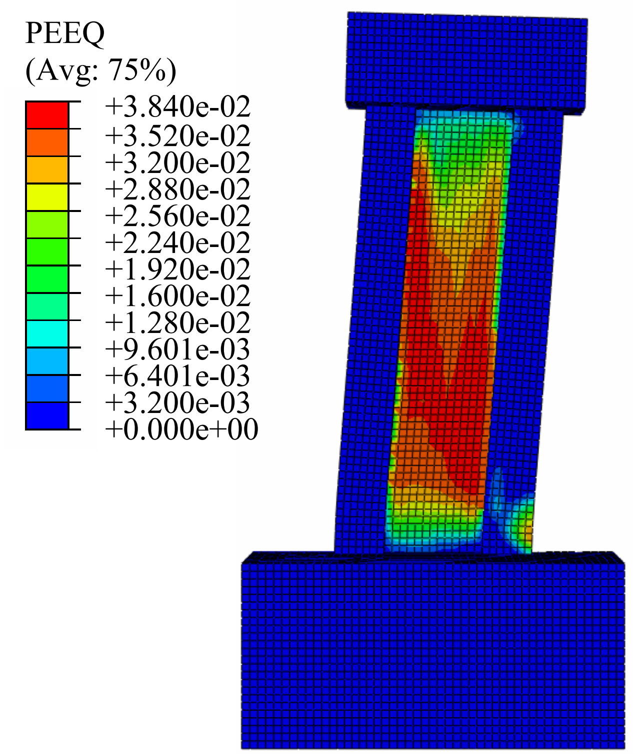

Figure 5.15 M20M contour plot: Compressive equivalent plastic strain (PEEQ).

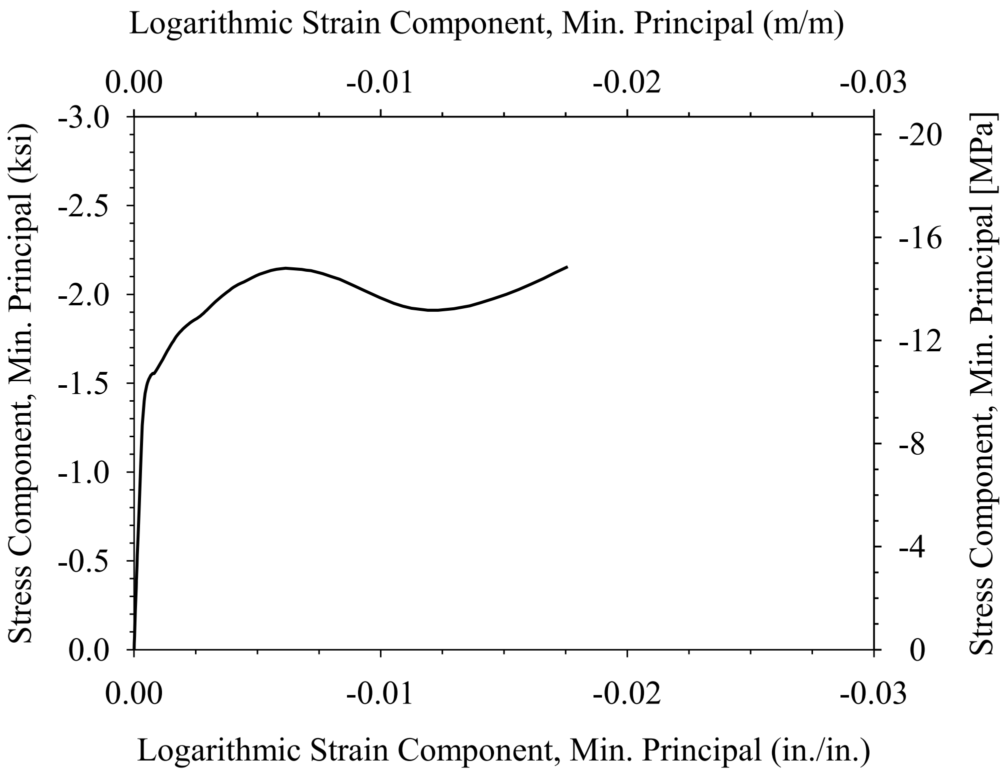

Figure 5.16 M05M: The min. principal stress-log. strain curve of a crushed element.

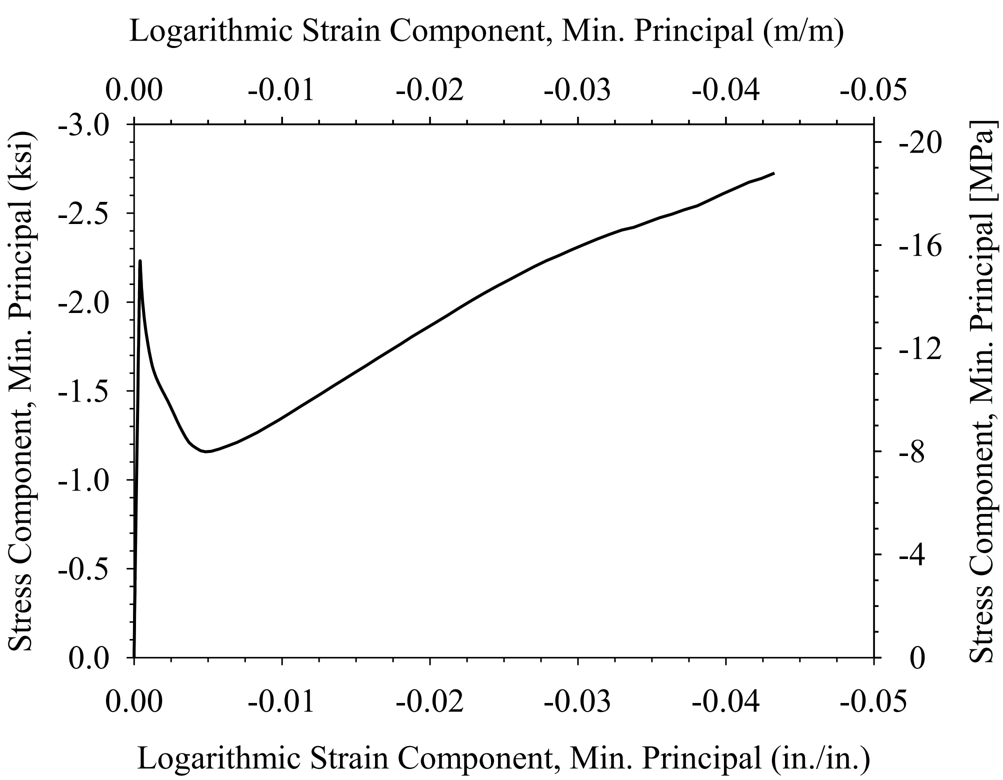

Figure 5.17 M20M: The min. principal stress-log. strain curve of a crushed element.

5.4 VecTor2 Analysis of Single Walls under Monotonic Loading

5.4.1 Geometrical Modeling

The single wall finite element models were created with Formworks, the pre-processing software include in the VecTor2 Bundle v2.80 (Full Version) [39]. A single finite element mesh is defined for all the analyses, as shown in Figure 5.18. The element size is approximately 51 mm x 51 mm (2" x 2"). Five RC regions were defined: one region for the footing, two regions for the boundary elements, one region for the web and one region for the loading block. The regions are shown in different colors in Figure 5.18. The steel reinforcement is smeared uniformly in the concrete regions and is not shown.

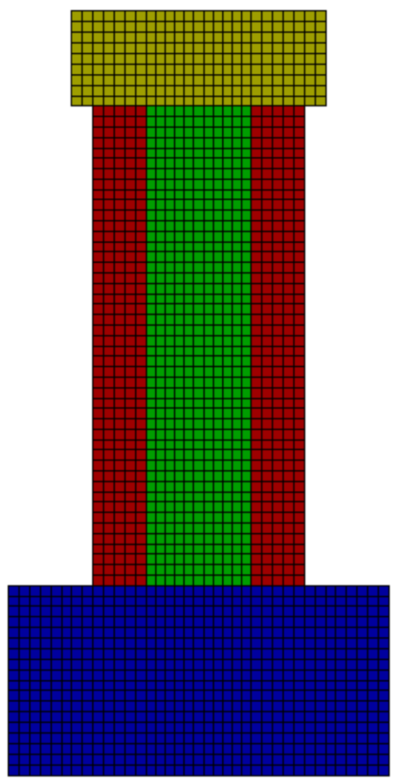

Figure 5.18 VecTor2 finite element mesh for single walls

5.4.2 Material properties

The smeared reinforcement properties were defined together with the definition of concrete properties for each concrete type. There were four concrete types in total, one for the footing, one for the boundary elements, one for the web and one for the loading block. The material properties were defined based on the experimental data for each wall unit. For the footing and loading block, a large value for the elastic modulus was defined to simulate the footing and loading block as rigid regions.

Table 5-6 Summary of the material behavior models in VecTor2.

Convergence criteria	Displacements - weighted
Compression base curve	Popovics (NSC/HSC)
Compression post-peak	Popovics /Mander
Compression softening	Vecchio 1992-A
Tension stiffening	Modified Bentz
Tension softening	Linear
Tension splitting	DeRoo 1995
Confinement strength	Kupfer/Richart
Concrete dilatation	Variable - Kupfer
Cracking criterion	Mohr-Coulomb (Stress)
Crack shear check	Not considered
Crack width check	Crack limit (agg/5)
Concrete bond	Eligehausen model
Concrete creep/relax	Not Considered
Concrete hysteresis	NL w/decay (Palermo)
Steel hysteresis	Seckin model
Rebar dowel action	Tassios (crack slip)
Rebar buckling	Not considered
Previous load history	Considered
Slip distortion	Vecchio-Lai
Strain rate effects	Not considered
Geometric nonlinearity	Not considered
Crack allocation	Variable (Sato)

As previously mentioned, VecTor2 has a large library of phenomenological constitutive models that permit realistic simulation of complex aspects in the response of reinforced concrete structures. A summary of the models defined for the concrete regions, the reinforcement and other behavioral models are shown in Table 5-6. For the compression base curve, the M05M concrete was modeled with the Popovics normal strength concrete (NSC) model, while the models for all other walls used the Popovics high-strength-concrete (HSC) model.

5.4.3 Solution Controls

The applied boundary conditions are described here. The nodes at the bottom of the footing block were constrained in their translational degrees of freedom. Two load cases were defined to represent the axial and horizontal loading. Axial load was applied on top of the load block, evenly distributed on the six nodes at the center of the block. The horizontal load was applied in displacement control at the node on the left edge of the loading bock, 203 mm (8") away from the top. Figure 5.19 shows the finite element mesh with the two load cases shown as arrows and the constraints at the bottom shown as dark blocks.

5.4.4 Results

Figure 5.20 to Figure 5.23 show the comparisons of global force-displacement curves between the experiment data and the results from the VecTor2 analyses for test units M05M, M10M, M15M and M20M [54]. The M05M model is predicted by VecTor2 to fail earlier than what took place in the real experiment. The early failure prediction from the analysis may be due to the over-prediction of the initial stiffness. This is possibly because the tension stiffening effect was over-predicted. With the increase of concrete compressive strength, the effect was reduced and the global behavior was adequately simulated. The capacity of wall M15M was over-predicted, probably due to the fact that the property of the #8 rebar in this test unit was not defined appropriately due to the lack of the available test data.

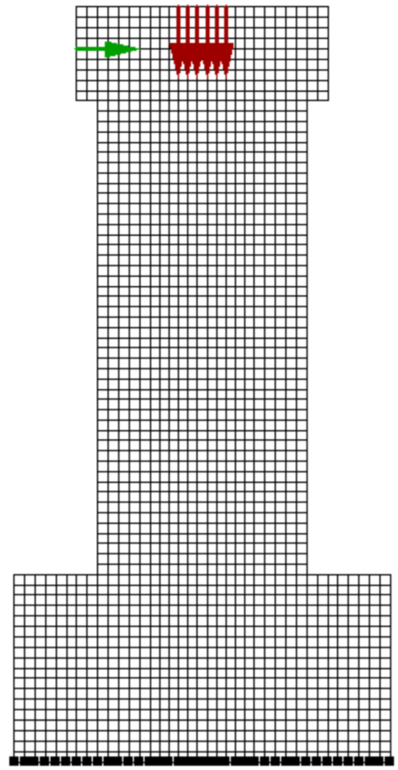

Figure 5.19 Finite element model with load cases for single walls in VecTor2.

Another feature of the VecTor2 analyses on the single walls under monotonic loading, which can be seen in Figure 5.20 through Figure 5.23, is that web crushing failure was predicted appropriately by a drop of the load-carrying capacity. Figure 5.24 and Figure 5.25 show the numerically predicted deformed shape for walls M05M and M20M at web crushing failure. For wall M05M, web crushing occurred next to the compression boundary element along the height of the web, while for M20M, web crushing took place within the plastic hinge region. It can be seen from the deformed shapes of the FE models that the highly distorted (crushed) elements that the failure is mainly due to the shear deformation induced on the elements. The high difference in stiffness between the boundary elements and the web causes a tendency of vertical slip at the interface, where web crushing happens.

However, this effect is clearly more pronounced during elastic web crushing (M05M) than in inelastic web crushing (M15M), in which the largest shear deformations (including those at the interface between wall and boundary element) are concentrated within the plastic hinge region Figure 5.26 and Figure 5.27 show the direction of the principal compressive strain at failure. The parallel lines in Figure 5.26 indicate the elastic crack pattern in the web. In Figure 5.27, crack realignment was observed in the web crushing region and the compression zone of the boundary element is under high stress demand. This later behavior is consistent with the observed fanning cracking mechanism observed in for the walls failing by inelastic web crushing. The region of the web next to the tension boundary element is still highly stressed possibly due to the localized deformation introduced by the tension boundary element onto the web.

It is of interest to evaluate the stress state of the elements in the web crushing region to investigate the degradation of concrete strength for elements under such a complicated stress state. Figure 5.28 and Figure 5.29 show traces of the principal compressive stress versus the principal compressive strain for walls M05M and M20M. It can be seen that minor concrete strength degradation is predicted for the M05M wall element, which reached a maximum compressions stress of approximately 4.6 ksi. By comparison, the HSC concrete element in wall M20M experienced an appreciable amount of strength degradation and only around 30% of its uniaxial strength is utilized. It should be noted that the residual stress of the crushed elements at failure is only between 1 to 2 ksi. It also can be seen that for the HSC model (wall M20M), the stress-strain curves of the crushed element displays unloading and reloading behavior even though the global model loading was monotonic.

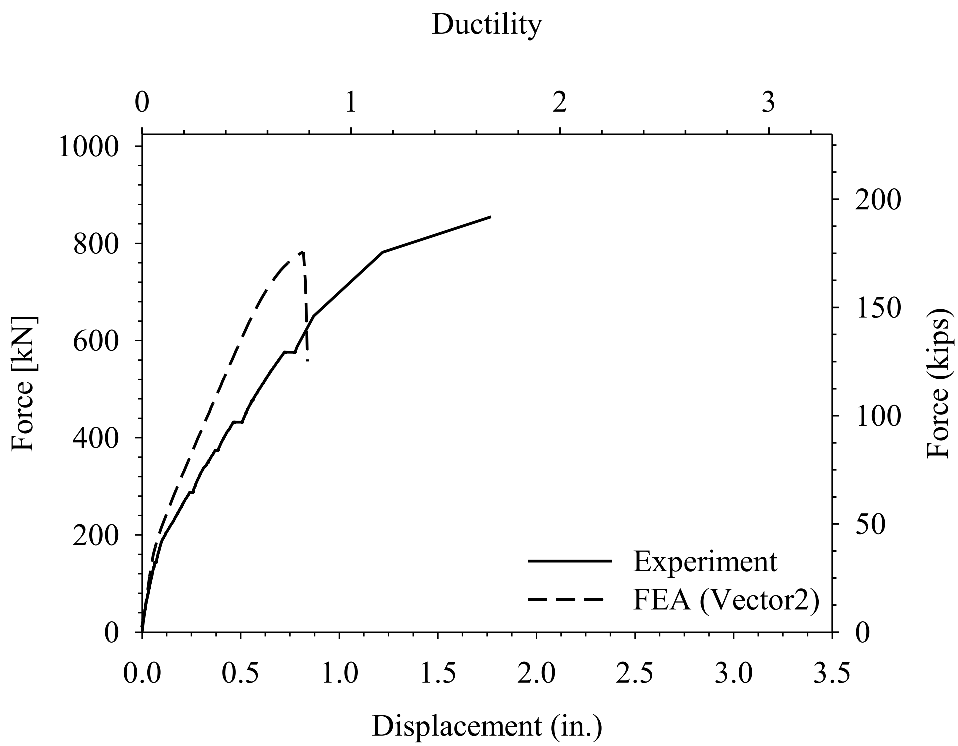

Figure 5.20 M05M global force-displacement behavior comparison between experiment and VecTor2.

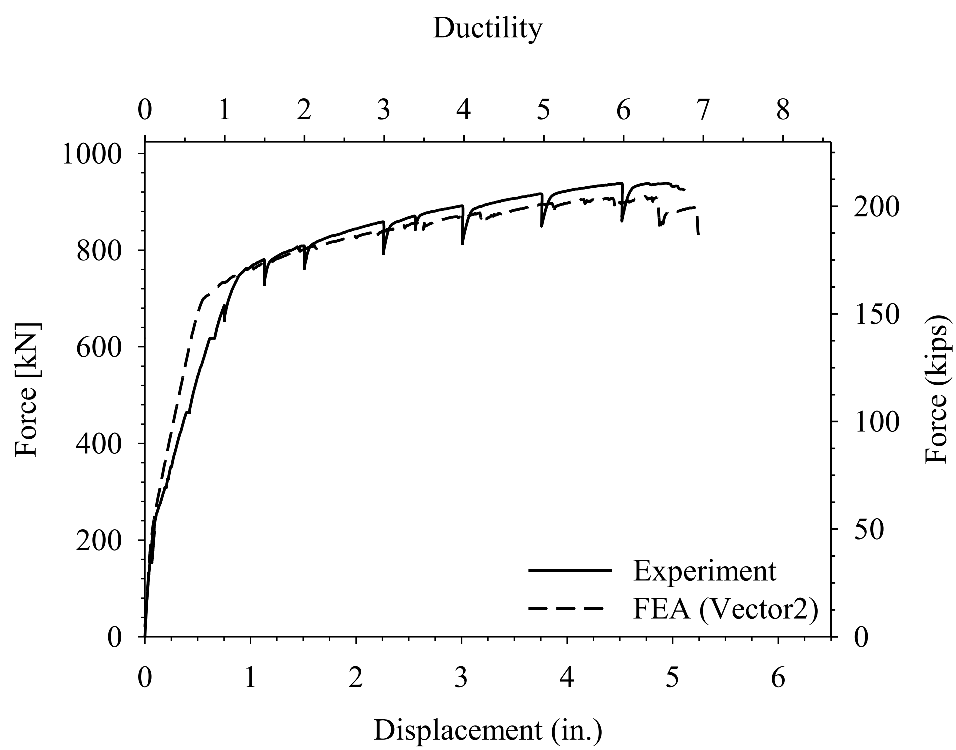

Figure 5.21 M10M global force-displacement behavior comparison between experiment and VecTor2.

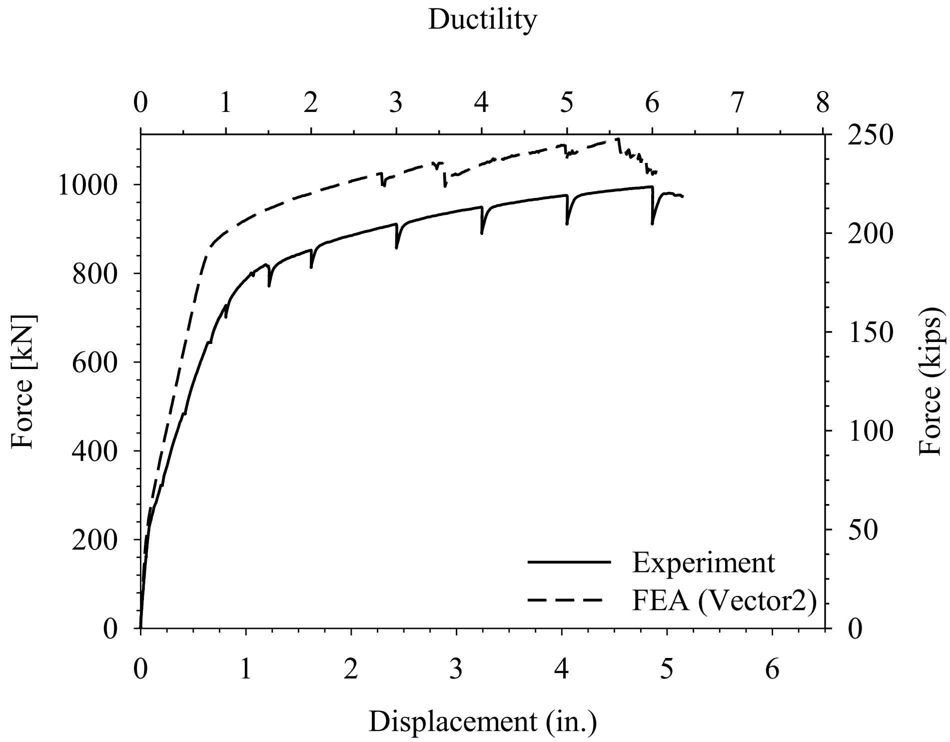

Figure 5.22 M15M global force-displacement behavior comparison between experiment and VecTor2.

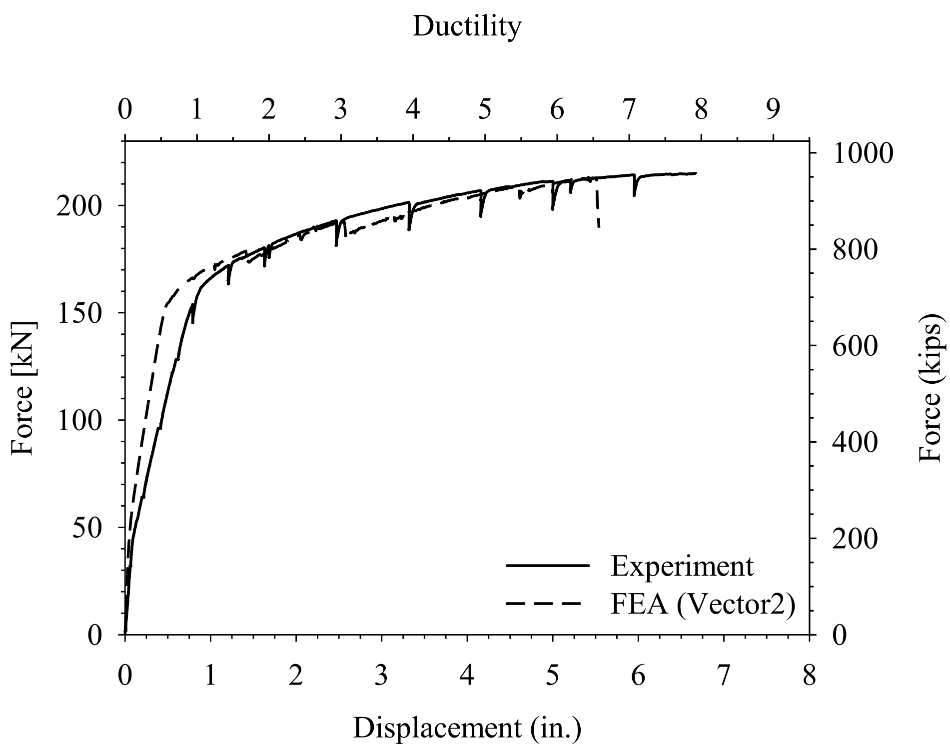

Figure 5.23 M20M global force-displacement behavior comparison between experiment and VecTor2.

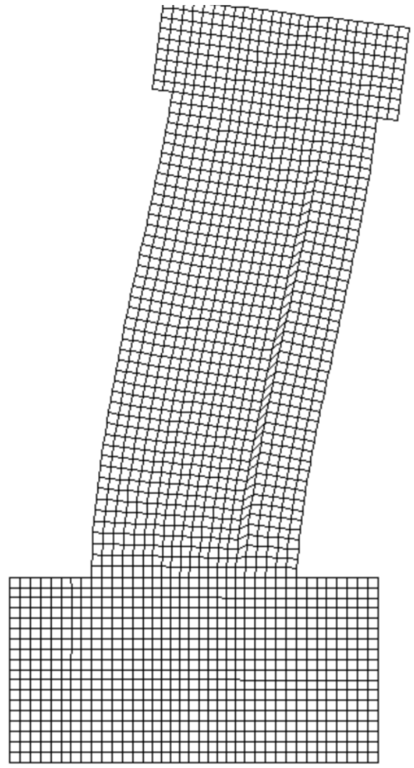

Figure 5.24 M05M deformed model at web crushing failure.

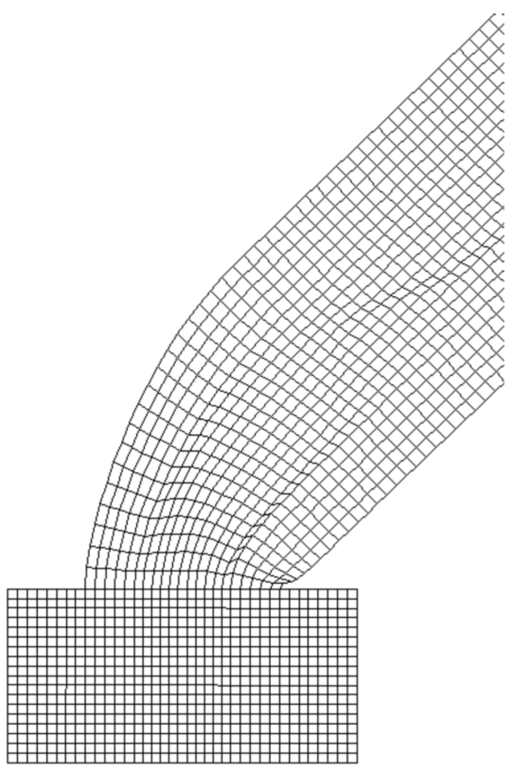

Figure 5.25 M15M deformed model at web crushing failure.

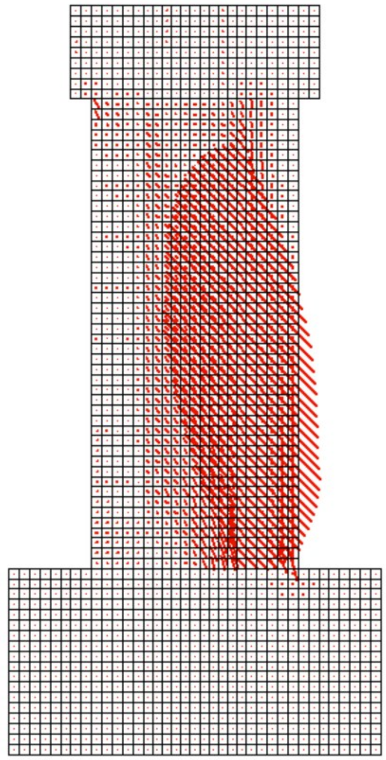

Figure 5.26 M05M direction of principal compressive strain (ε_2) at failure.

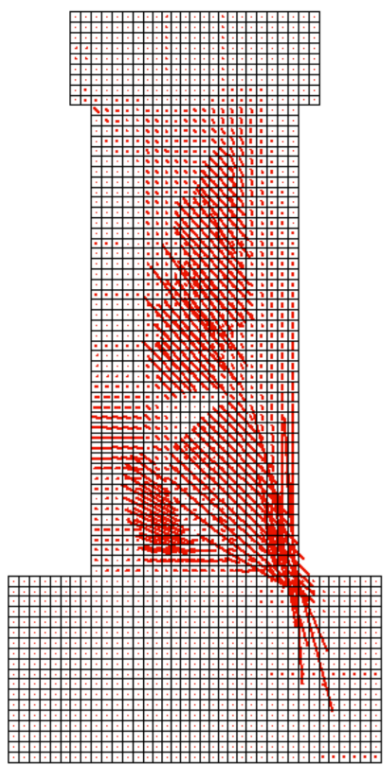

Figure 5.27 M15M direction of principal compressive strain (ε_2) at failure.

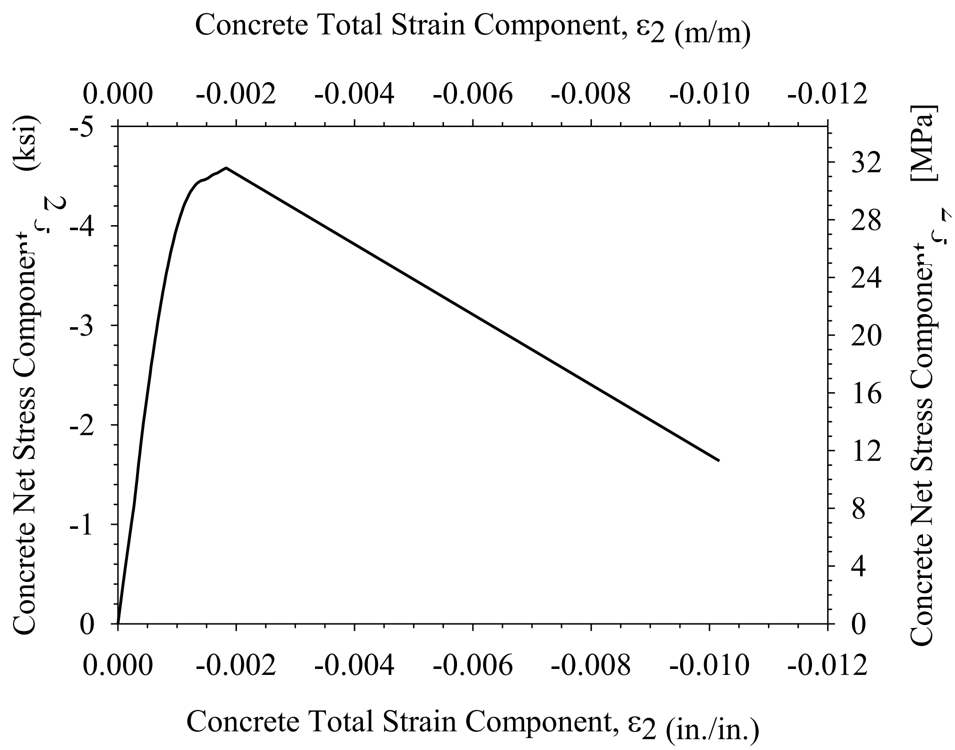

Figure 5.28 M05M: The principal compressive stress-strain curve of a crushed element.

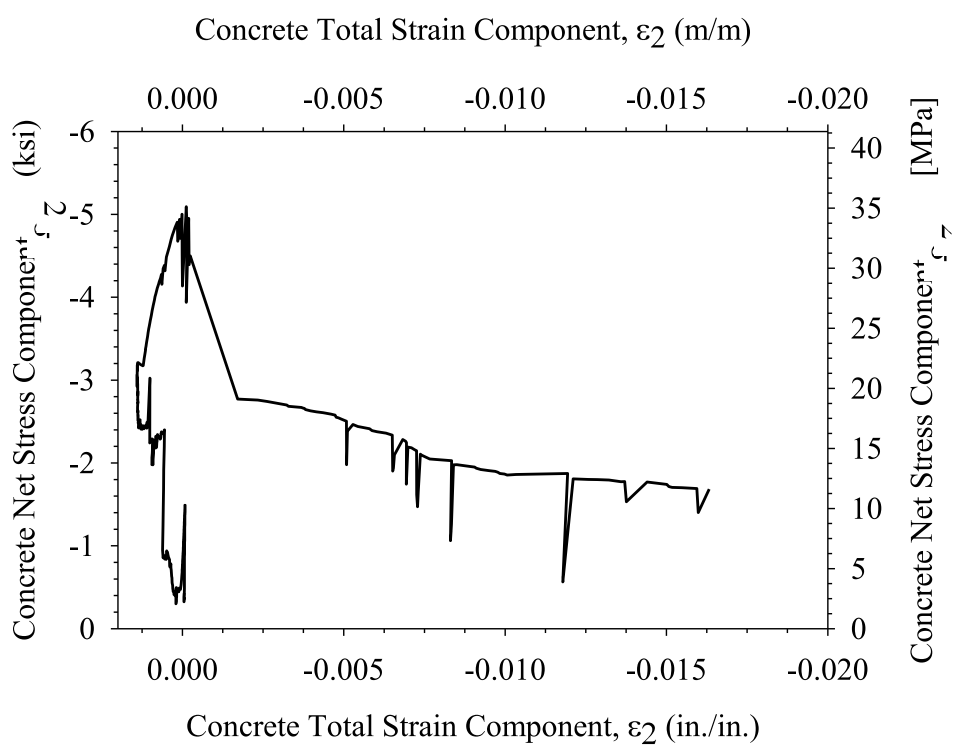

Figure 5.29 M20M: The principal compressive stress-strain curve of a crushed element.

5.5 ABAQUS Analysis of Single Walls under Cyclic Loading

The analysis of the single walls under cyclic loading was attempted with ABAQUS. However, the concrete damaged plasticity (CDP) model was unable to capture the unloading and reloading behavior of the wall under cyclic loading, which is explained in [54] in detail.

5.6 VecTor2 Analysis of Single Walls under Cyclic Loading

5.6.1 General description

With respect to geometrical modeling, the same model as described in Section 5.4.1 was used for analyzing the walls under cyclic loading. Regarding material properties, the same set of the concrete and steel material models as given in Table 5-6 were used for the analysis here. The only differences were on the definition of the compression base curve. Wall M05C was modeled with the Popovics normal strength concrete (NSC) model, while all the other walls used the Popovics high-strength-concrete (HSC) model. The general description of solution controls in Section 5.4.3 still applies to the cyclic analyses. The only difference from the monotonic analyses is in the horizontal loading pattern. The definition of the horizontal loading followed the loading protocol applied during test. First, four cycles in force control were applied, followed by displacement-controlled cycles.

5.6.2 Results

Figure 5.30 to Figure 5.33 show comparisons of the global force-displacement curves between experiment and VecTor2 analyses for test units M05C, M10C, M15C and M20C [54]. The simulated M05C model failed on the first excursion to μ_Δ = -1, while the test specimen failed on the first excursion to μ_Δ = 2 as is shown in Figure 5.30. It can be seen that the load-carrying capacity of the wall at μ_Δ = 1 is over predicted, which may be due to two reasons. First, the initial stiffness of the model from VecTor2 is higher than the test unit. Second, the definition of the steel properties for the #8 longitudinal rebar may have not been appropriate due to the lack of experimental data. The simulated M10C model failed on the second excursion to μ_Δ = 1.5 as is shown in Figure 5.31. The test specimen failed on the first excursion to μ_Δ = 2. It is shown that the simulation captured the behavior of the specimen even though the initial stiffness of the model was not well predicted and the unloading stiffness of the model is a bit higher. For wall M15C, the test specimen failed on the second excursion to μ_Δ = 4, but the simulated model has no indications of web crushing failure at the end of μ_Δ = 4, as is shown in Figure 5.32. Wall M20C failed experimentally upon reaching the first peak to μ_Δ = 6, but the simulated model showed no indication of web crushing failure at the end of μ_Δ = 4, as is shown in Figure 5.33.

Overall, the global hysteretic behavior of the structural walls under cyclic loading was well captured by the VecTor2 models. Web crushing failure of the NSC walls, like M05C and M10C was predicted. Figure 5.34 shows the numerically predicted deformed shape the M10C model at web crushing. Features of an elastic shear failure are observed. Figure 5.35 shows the numerical deformed shape for wall M20C at μ_Δ = 4 x 2. No indication of web crushing is observed throughout the applied cycles for the HSC wall modelss, which will be discussed in Section 5.7.

Figure 5.36 and Figure 5.37 show curves for the principal compressive stress versus the principal compressive strain of the crushed/critical elements in the models for walls M05C and M20C. Since no web crushing was observed in the simulation of wall M20C until the end of μ_Δ = 4, Figure 5.37 shows the stress-strain curve of a critical element. That is, a highly stressed or distorted element in the wall web adjacent to the compression boundary element and within the plastic hinge region. The figures look different due to the distinct difference in the strain range. The maximum compression stress reached by the walls under cyclic loading was approximately 5 ksi, which is similar to the stress level reached by the wall models under monotonic loading. Thus, the simulation shows no appreciable further concrete strength degradation under cyclic loading based on the output of the stress-strain curves.

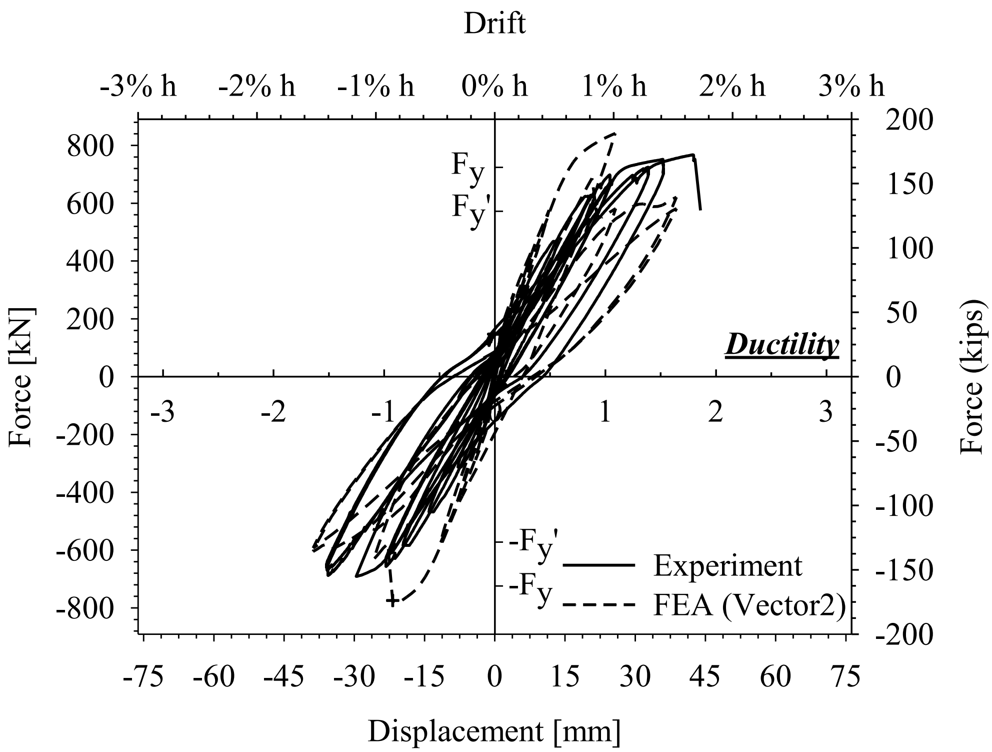

Figure 5.30 M05C global force-displacement behavior comparison between experiment and VecTor2.

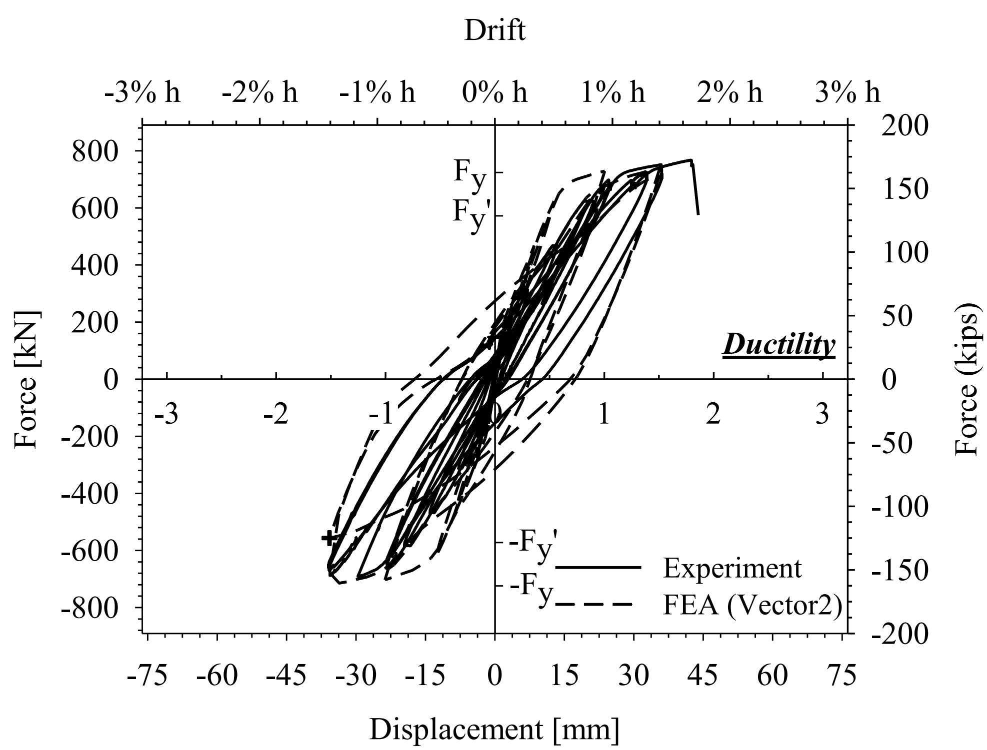

Figure 5.31 M10C global force-displacement behavior comparison between experiment and VecTor2.

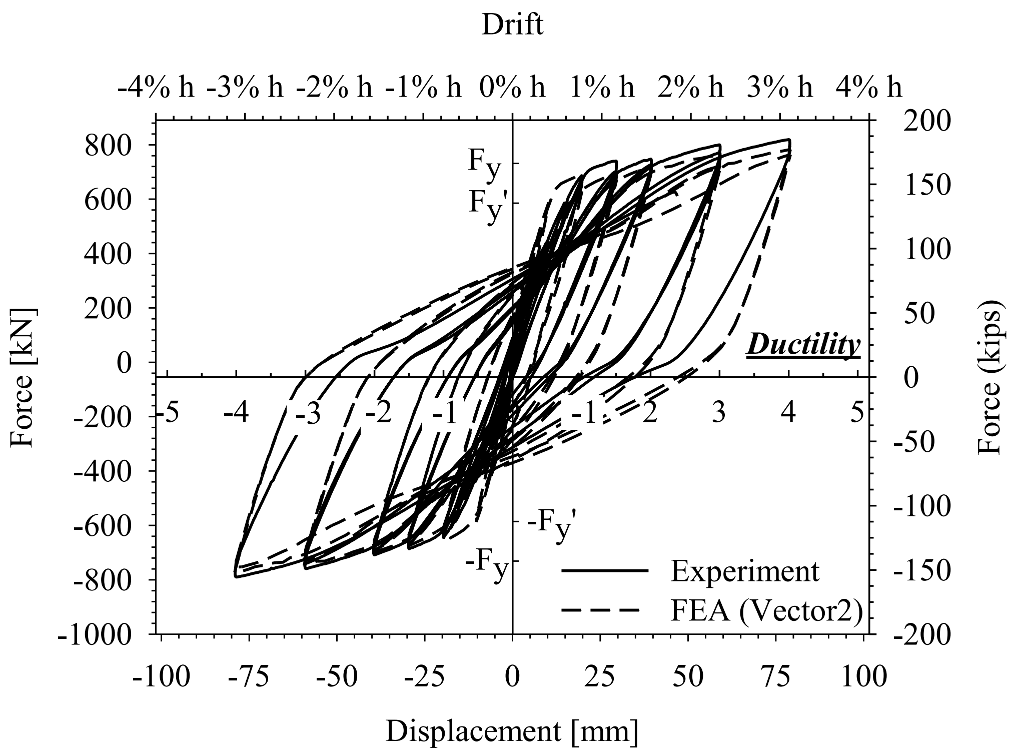

Figure 5.32 M15C global force-displacement behavior comparison between experiment and VecTor2.

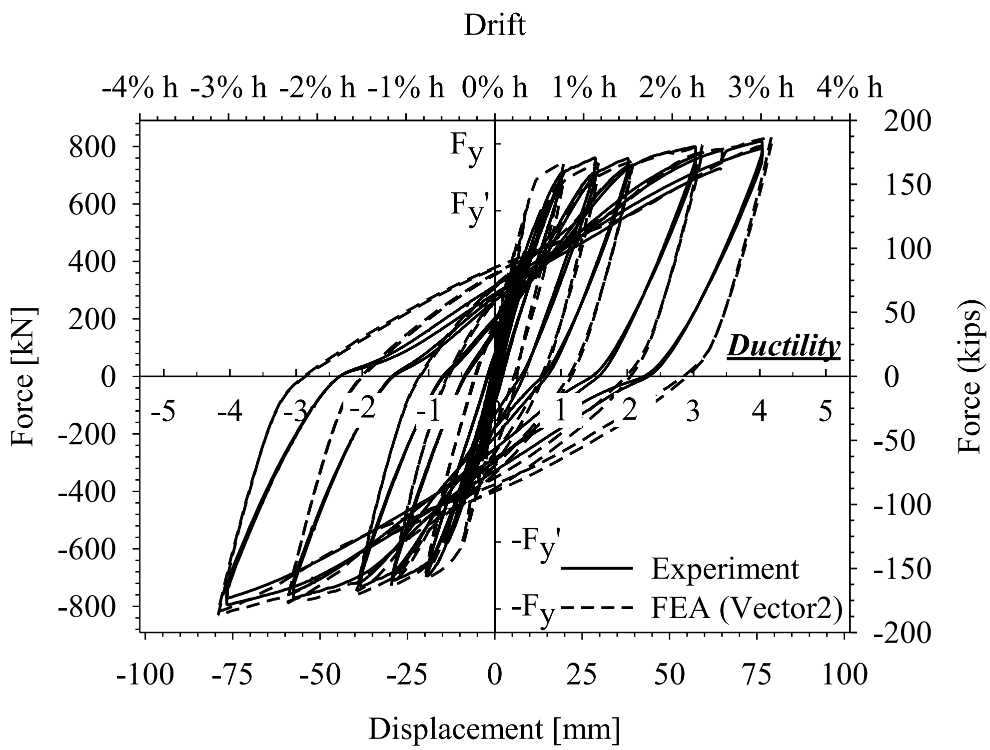

Figure 5.33 M20C global force-displacement behavior comparison between experiment and VecTor2.

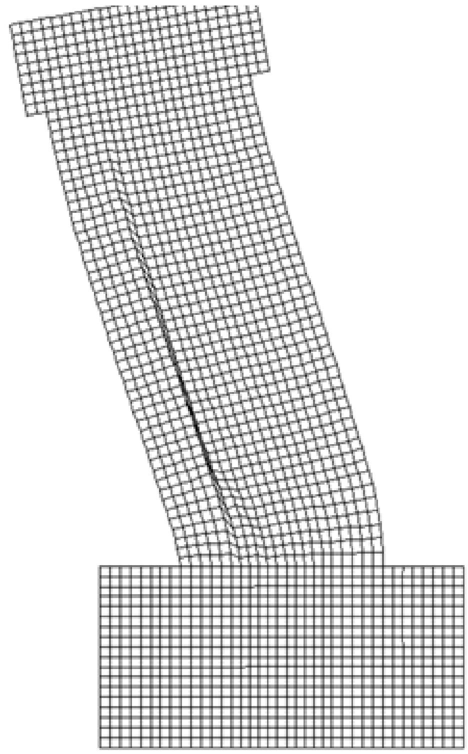

Figure 5.34 M10C deformed model at web crushing failure.

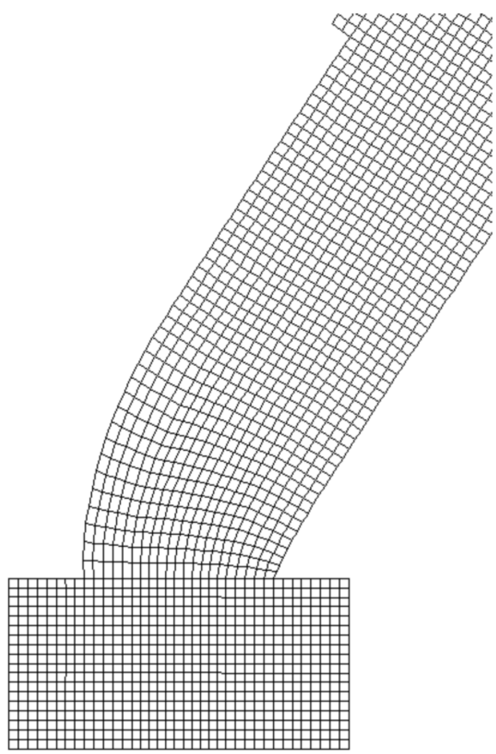

Figure 5.35 M20C model with magnified deformation at μ_{Δ} =4 x 2.

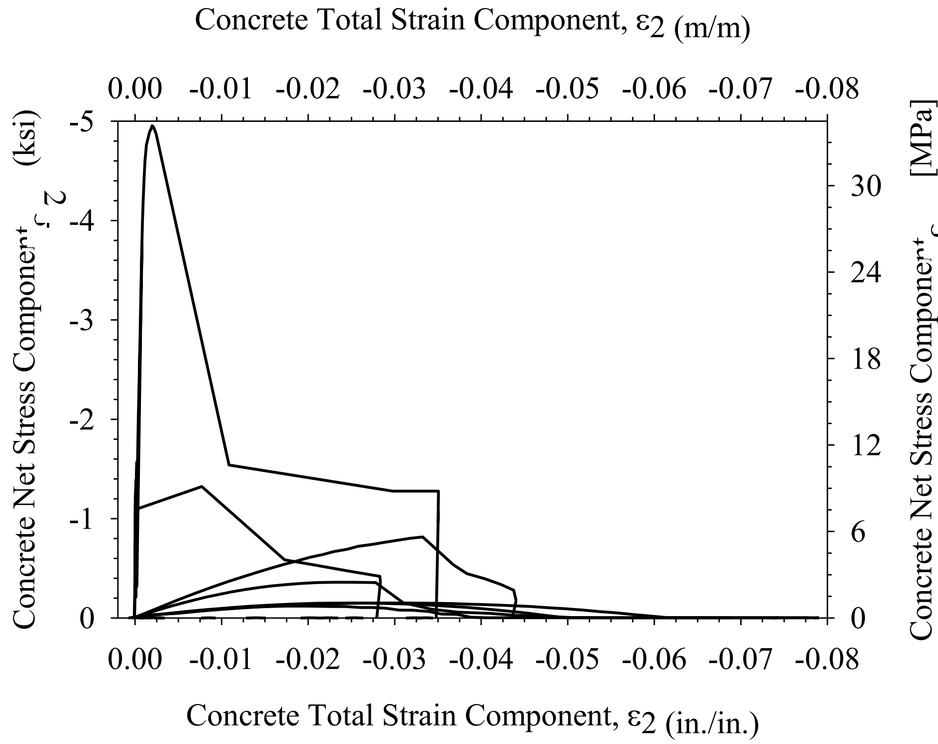

Figure 5.36 M05C: The principal compressive stress-strain curve of a crushed element.

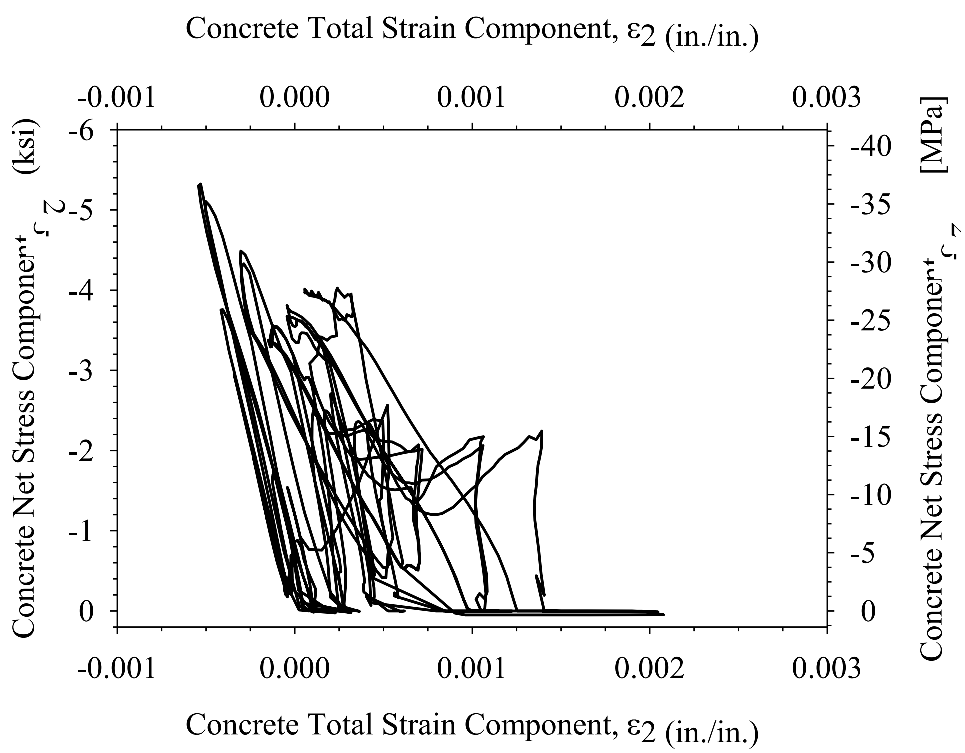

Figure 5.37 M20C: The principal compressive stress-strain curve of a critical element.

5.7 Discussion

A data reduction process was conducted on the VecTor2 analytical results for the M20C wall model. The displacement history of the nodes corresponding to the location of displacement transducers on the test unit were extracted and post-processed in the same procedure as for the experimental data. Separate flexure and shear behavior could then be compared between the experiment and the VecTor2 results as shown in Figure 5.38 and Figure 5.39. Good agreement was achieved between the experimental and numerically simulated flexural and shear response of wall M20C. To investigate the difference in inelastic shear behavior within the plastic hinge region and the elastic shear behavior in the region above the plastic hinge, the force-shear displacement curves for the 'numerically equivalent' bottom and top shear deformation panels for the FE simulation are shown in Figure 5.40. It can be noted that the simulated response in the bottom panel exhibits inelastic shear behavior while the numerical results for the top panel shows the elastic shear behavior. This is consistent with the previously presented experimental data and attests to the adequate simulation capabilities of VecTor2. Concrete degradation in the plastic hinge region due to flexure effects is the main reason for inelastic shear behavior. The term 'flexure-shear interaction' is referred to describe this phenomenon herein.

To evaluate the ability of to capture the web crushing failure of wall M20C in VecTor2, additional displacement-controlled cycles were applied. Web crushing was predicted to happen on the second cycle of μ_Δ = 8, see Figure 5.41. Another analysis was done on the same M20C model with pure monotonic displacement-controlled loading. A comparison of the hysteretic curves under cyclic and monotonic loading is shown in Figure 5.41. It can be seen that failure is predicted at the same ductility level for both models. Thus, it can be seen that while stiffness degradation was adequately captured, degradation due to localized damage due cyclic loading could not be captured by the VecTor2 analysis.

5.8 Conclusions

Modeling of single wall test units with 3D continuum plasticity-based models (ABAQUS) and 2D plane stress phenomenologically-based models (VecTor2) was conducted. The results were compared with the experimental data used to provide further insight into web crushing behavior. Findings based on the analyses are as follows.

First, both ABAQUS and VecTor2 analyses were able to adequately capture the global monotonic response of the single wall units. VecTor2 especially showed good performance in modeling the cyclic and inelastic behavior of the HSC walls. The use of ABAQUS and its CDP model on the analysis of single walls under cyclic loading was unsuccessful. The CDP model needs to be modified to be able to capture degradation from unloading and reloading stiffness under cyclic loading. Moreover, the issue of the visco-plasticity regularization needs to be clarified.

Second, the plasticity-based analyses cannot predict the web crushing failure. Conversely, the phenomenological models built into VecTor2 were able to predict failure under monotonic loading but not under cyclic loading. Further investigation is needed regarding the modeling of web crushing capacity of structural walls under cyclic loading.

Lastly, the analytical results confirm that web crushing in the form of the inelastic shear failure is caused by the flexure-shear interaction effects induced in the web of the structural walls. The absolute values of minimum principal stress reached at the onset of failure are predicted to be much lower than the nominal concrete compressive strengths, usually around or below 5 ksi for the eight tested single wall units.

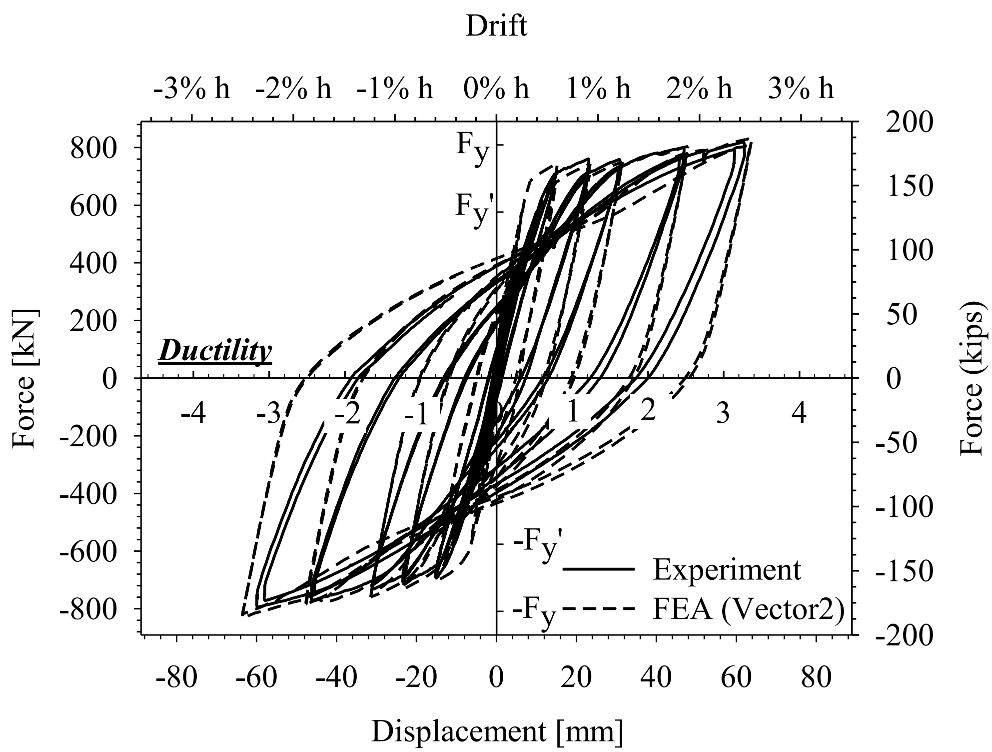

Figure 5.38 M20C flexural force-displacement curves from experiment and VecTor2.

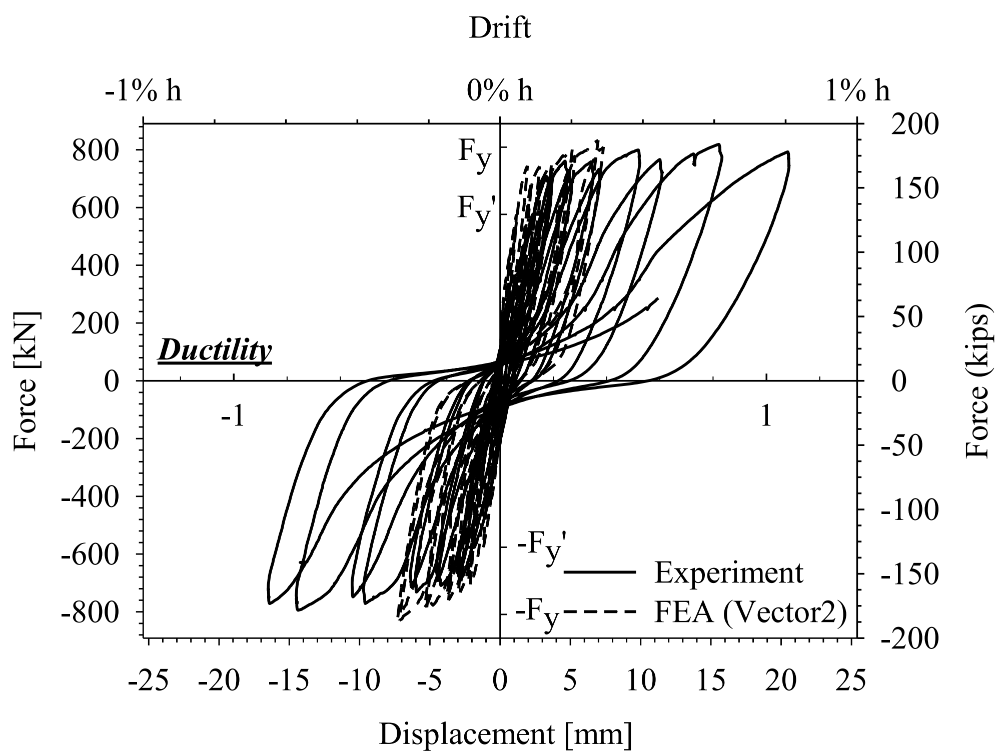

Figure 5.39 M20C shear force-displacement curves from experiment and VecTor2.

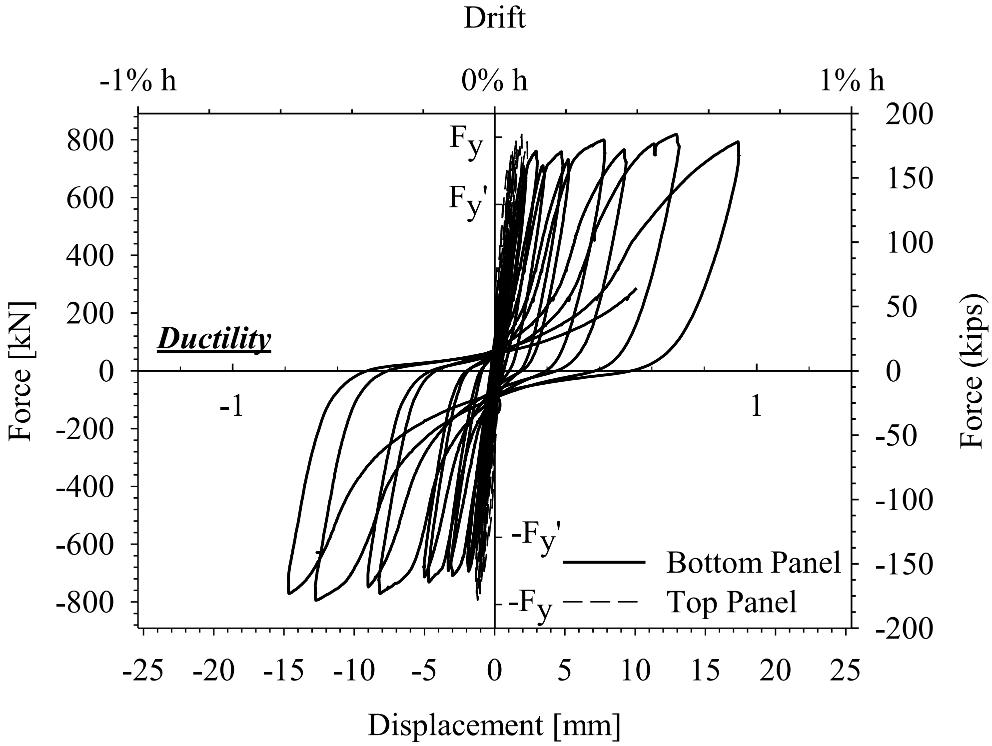

Figure 5.40 M20C VecTor2 analysis: comparison of the shear deformation between the bottom and top panel.

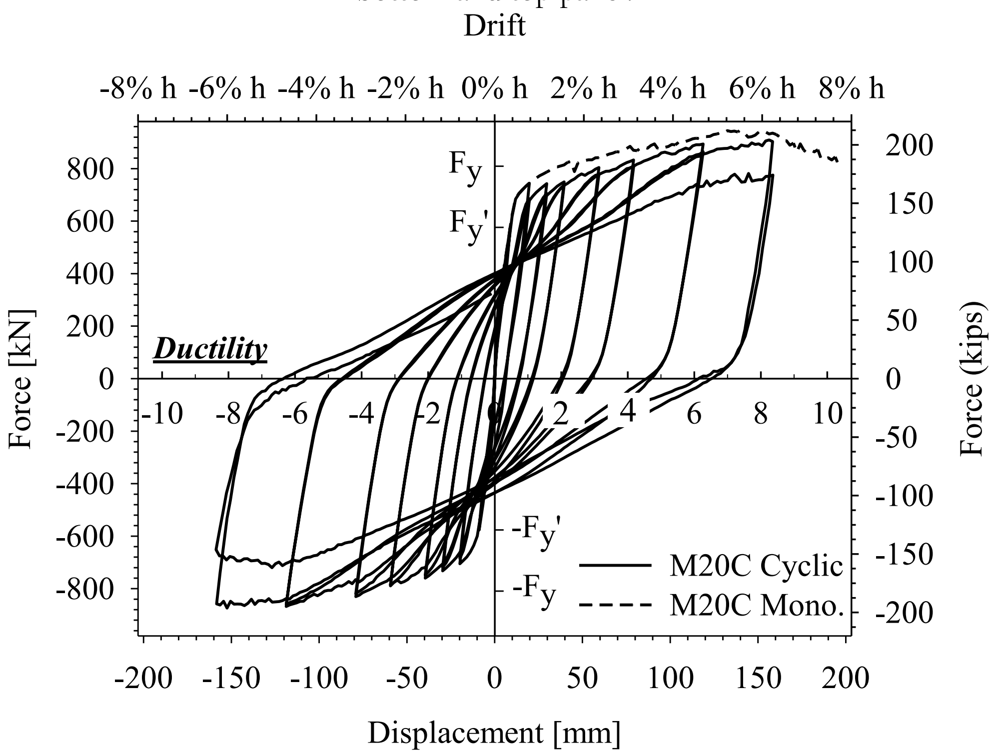

Figure 5.41 M20C global force-displacement behavior comparison under cyclic and monotonic loading with VecTor2.

Chapter 6. **Simplified Analytical Method on HSC Structural Walls**

6.1 Summary

This chapter presents the modification and use of a simplified inelastic analytical model for determining the web crushing capacity of HSC structural walls. The strut-and-tie web crushing model by Hines and Seible [16] is modified by the introduction of a new calculation method for its concrete softening parameter. The analytical results show that the modified Hines and Seible model can predict web crushing capacity of HSC structural walls well. It has been shown that concrete degrades much faster in the HSC walls compared to the NSC units . However, the modified approach to calculate the concrete softening parameter was not able to capture further concrete strength degradation on wall M20C compared to wall M15C, which caused the web crushing capacity of wall M20C to be over-estimated. Nonetheless, the proposed modifications provide a more rational mechanism to evaluate web crushing strength for HSC walls.

6.2 Concrete softening parameter

As is included in the compression field theory (CFT) and modified compression field theory (MCFT), concrete compressive strength degrades with the coexistence of tensile strains in the orthogonal direction. The equation for calculating the concrete softening parameter κ in the MCFT (1986) is:

$$\kappa = \frac{1}{0.8+170\varepsilon_1} \tag{6-1}$$

In the model by Hines and Seible [16], ε_1 is calculated with the first strain invariant quantity, which by means of Mohr's circle can be related to principal and transverse strains by:

$$\varepsilon_1 + \varepsilon_2 = \varepsilon_l + \varepsilon_t \tag{6-2}$$

where ε_1 is the concrete principal tensile strain; ε_2 is the concrete principal compressive strain; ε_l is the longitudinal strain; ε_t is the transverse strain. Since Hines' model [16] is essentially a truss model, no shear transfer at the crack interface is considered. Thus, ε_1 is in the direction perpendicular to the strut and ε_2 is in the direction of the strut. Equation (6-2) is further simplified by leaving ε_2 out of the equation when $\varepsilon_2 \ll \varepsilon_1$ is assumed, as is done in the development by Hines.

Hines proposes that the transverse strain, ε_t can be obtained by using the UCSD three component model [55] to calculate the stress in the transverse steel across the crack at each force and displacement level in an averaged sense:

$$f_v = \frac{V - V_c - V_p}{jd\frac{A_v}{s}cot30°} \tag{6-3}$$

The transverse strain can then be calculated by assuming that the strain has not reach yield:

$$\varepsilon_t = \frac{f_v}{E_t} \tag{6-4}$$

In the Hines and Seible model ε_l is calculated as a constant quantity with an empirical equation calibrated based on available test data. It is realized by Hines that the level of transverse and longitudinal steel plays a significant role in the strength of the web crushing region. Longitudinal and transverse reinforcement can help to reduce the crack width and the principal tensile strain ε_1. Thus, the equation for calculating ε_l is inversely proportional to the sum of the transverse and longitudinal reinforcement ratio in the web, that is:

$$\varepsilon_l = \frac{\varepsilon_y}{100(\rho_n + \rho_h)} \tag{6-5}$$

where ρ_n is the longitudinal reinforcement ratio in the wall and, ρ_t is the transverse reinforcement ratio in the wall, and ε_y is the yield strain of the longitudinal reinforcement.

Evidence that highlights the shortcomings to the approach by Hines in calculating concrete softening parameter, and which motivate the modifications in this study follow. First, it is reasonable to estimate the strains ε_l and ε_t at each force and displacement level, analogous to the approach for calculating ε_t based on the UCSD three-component model. Howver, in the model by Hines and Seible ε_l is computed based on the empirical Equation (6-5) and kept constant, which does not comply with the requirement that the strain should increase with the shift of the neutral axis under increased moment demand. Moreover, since no test data on HSC structural walls was available for calibrating Equation (6-5), it may not be appropriate to extend its applicability for the current study.

On the other hand, it seems reasonable to relate ε_l to a moment curvature analysis, which is at the core of the capacity model by Hines and Seible, and where ε_l is a basic output variable. In this way, the effect of HSC can be included since HSC walls have larger rotating capacity by the reduction of the compression zone at higher moment demands.

Second, the strain of the transverse steel ε_t in the model by Hines is calculated using the UCSD three-component model on an averaged sense. The stress level of the steel is directly related to the horizontal length of the crack, which is reflected in Equation (6-3) as jd. For structural walls with highly reinforced boundary elements, the resultant tension and compression forces are always located in the boundary elements, which will make jd much larger than the sectional depth of the web. However, boundary elements play an important role in resisting tension and compression under moment and will mainly experience flexural cracking. The cracking is mainly oriented in the horizontal direction as was observed in the experiments in this study. It is also difficult for the diagonal shear cracking to penetrate and crack the compression boundary element. It thus seems reasonable to limit the horizontal length of the crack to the web depth only.

This evidence is assumed to be general and could be applied on any structural type with heavily reinforced boundary elements or flanges. However, there is has no physical meaning to say that the boundary elements do not resist shear demand and that the effective cross sectional area can only be the web. The contributions of the boundary elements in V_c and V_p in the UCSD-three component are still admissible.

Third, the neglect of ε_2 in Equation (6-2) could be problematic for two reasons. For one thing, neglecting ε_2 will result in an under-estimated value of ε_1 since the principal compressive strain ε_2 is negative. Based on the first order strain invariant or Mohr's circle, ε_1 should be equal to the sum of the absolute values of ε_2, ε_l and ε_t. Additionally, the assumption that $\varepsilon_2 \ll \varepsilon_1$ is appropriate when tension stiffening effects are considered, as is the case in finite element modeling. However, in a simplified truss model, the tension stiffening effect is not considered. Also, since ε_2 is the concrete principal compressive strain at failure, a comparable value of ε_2 to ε_1 could be possible.

Based on the preceding evidence, a modification is proposed to the model by Hines and Seible in the approach to calculate the concrete softening parameter, as described below.

As a first modification, the distance between the resultant tension and compression forces jd in Equation (6-3) should be replaced with the cross sectional depth of the web D_w. Equation (6-3) thus becomes

$$f_v = \frac{V - V_c - V_p}{D_w \frac{A_v}{s} \cot 30°} \tag{6-6}$$

This change is motivated by, and consistent with, the observed cracking pattern in the tested walls in this study.

As a second change it is proposed that ε_l be estimated based on the strain output of the corresponding fiber from the moment-curvature analysis. Based on the geometry of the strut in the inelastic shear cracking region, web crushing is expected to occur in the zone next to the compression boundary element, which complies with the test observations of NSC structural walls. For HSC walls, however, the web crushing region could be at a different location. Since web concrete in the plastic hinge region is severely damaged, the concept of a strut more of a theoretical assumption than the real test observation. Thus, output the strain of the fiber at the interface of the web and compression boundary element is believed to be reasonable.

It can be noticed that for compression struts that end at the compression boundary element, the tip of the strut is above the base of the wall. Hence, the moment demand base con which the strut demand is calculated should be scaled in proportion. The critical height of the tip to the failing inelastic flexure/shear strut (h_{tip}) is calculated as

$$h_{tip} = L_{pr} - D_W cot\theta_{fs} \tag{6-7}$$

The longitudinal strain of the fiber at the interface between the web and the compression boundary element can be obtained from the moment-curvature analysis at the a moment value scaled by $(L - h_{tip})/L$, where L is the height of the wall.

The third step in the modification is to determine the principal tensile strain ε_1 consistently with the relationships from Mohr's circle,

$$\varepsilon_1 = \frac{1}{2}(\varepsilon_l + \varepsilon_t) + \frac{1}{2}\sqrt{(\varepsilon_l - \varepsilon_t)^2 + \gamma_{lt}^2} \tag{6-8}$$

where γ_{lt} is the concrete shear strain of the strut in the plastic hinge region. The shear strain, γ_{lt} may be considered to be averaged over the wall and calculated as

$$\gamma_{lt} = \frac{\Delta_S}{L} \tag{6-9}$$

where Δ_S is the shear deformation at the top of the wall, and L is the total height of the wall.

It should be noted shear strain γ_{lt} is the net strain of the concrete in the strut, which does not include the shear deformation of the member due to the crack shear slip. Thus, the estimate based on Equation (6-8) may be considered appropriate in an averaged sense.

6.3 Results

The web crushing capacity of the single walls tested under cyclic loading was calculated based on the model by Hines and Seible [16] with the modifications on the concrete softening parameter as described in Section 6.2. Figure 6.1 to Figure 6.4 show the hysteretic behavior of the single walls under cyclic loading with the failure predictions. Table 6-1 shows a comparison of the inelastic web-crushing capacities of single walls under cyclic loading with the Modified Hines-Seible model. The prediction quality of the Modified Hines-Seible model for HSC structural walls improved dramatically, compared to the original model. The experimental investigation showed that M20C was not able to attain additional deformation capacity compared to M15C. Thus, it a good prediction of the experimental response with the presented model is not possible since the model inherently considers that that web crushing capacity is linearly related to concrete compressive strength.

The shear capacity curves based on Equation (2-10) of ACI 318-08 [25], Equation (2-15a) by Oesterle et al. [4], Equation (2-16) by Paulay and Priestley [7] and the UCSD three-component model [55] are also shown in Figure 6.1 to Figure 6.4. It should be noted that for all the models, except for that from ACI 318-08, a maximum shear stress of $0.3f_c'$

was used to avoid unreasonably high values at: (i) small interstory drift ratios for Oesterle's model, (ii) small displacement ductility for Paulay and Priestley's model, and (iii) small cracking angle and concrete softening values in Hines' model. The ACI 318-08 and the UCSD three-component model are diagonal tension capacity models, which are shown along the web crushing capacity models for comparison. Further, it should be noted that shear strength plotted for the ACI 318-08 model is merely proportional to $\sqrt{f_c'}$ without the limit of $f_c' < 10{,}000$ psi.

It is observed that the limit of $0.3f_c'$ does not control web crushing capacity of the walls for concrete compressive strength above 6 ksi. However, it controls the prediction for elastic web crushing failures, as was the case for the M05C wall. The noted limit thus represents an upper bound and thus considered quite reasonable.

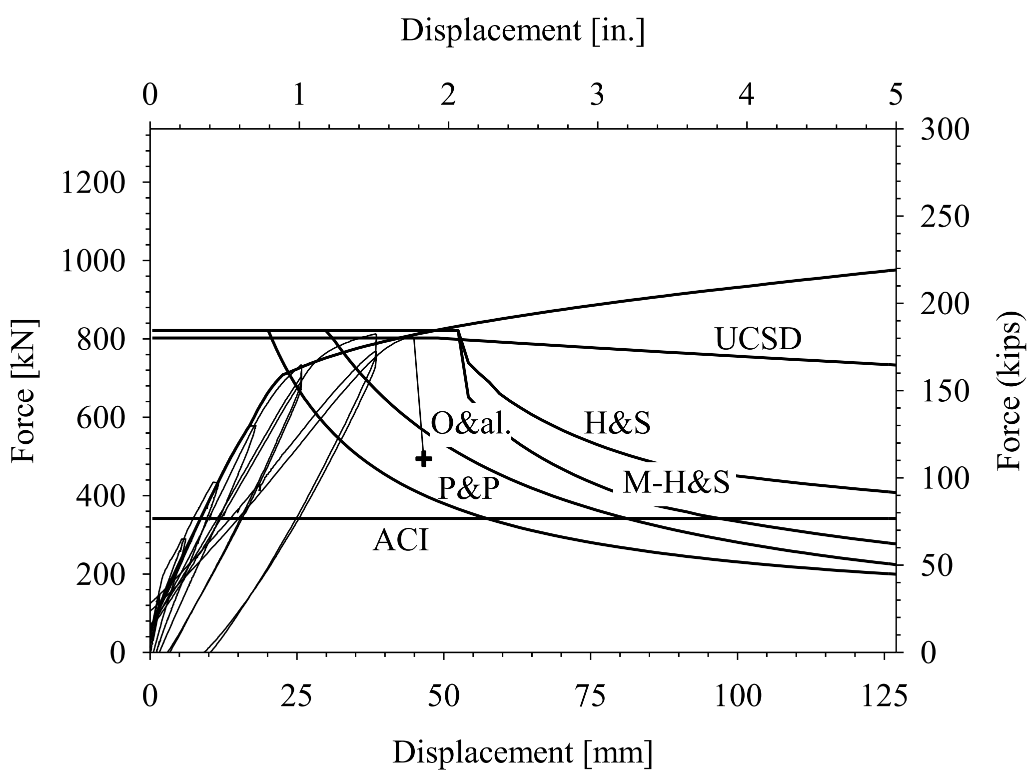

Figure 6.1 M05C hysteretic behavior with failure predictions.

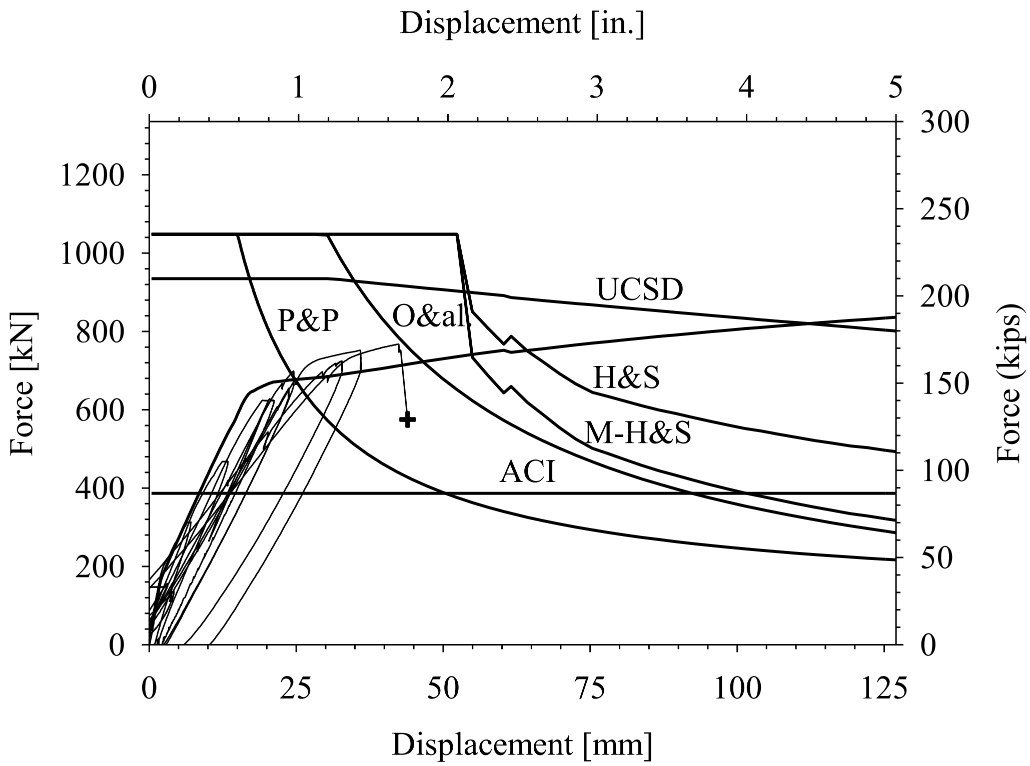

Figure 6.2 M10C hysteretic behavior with failure predictions.

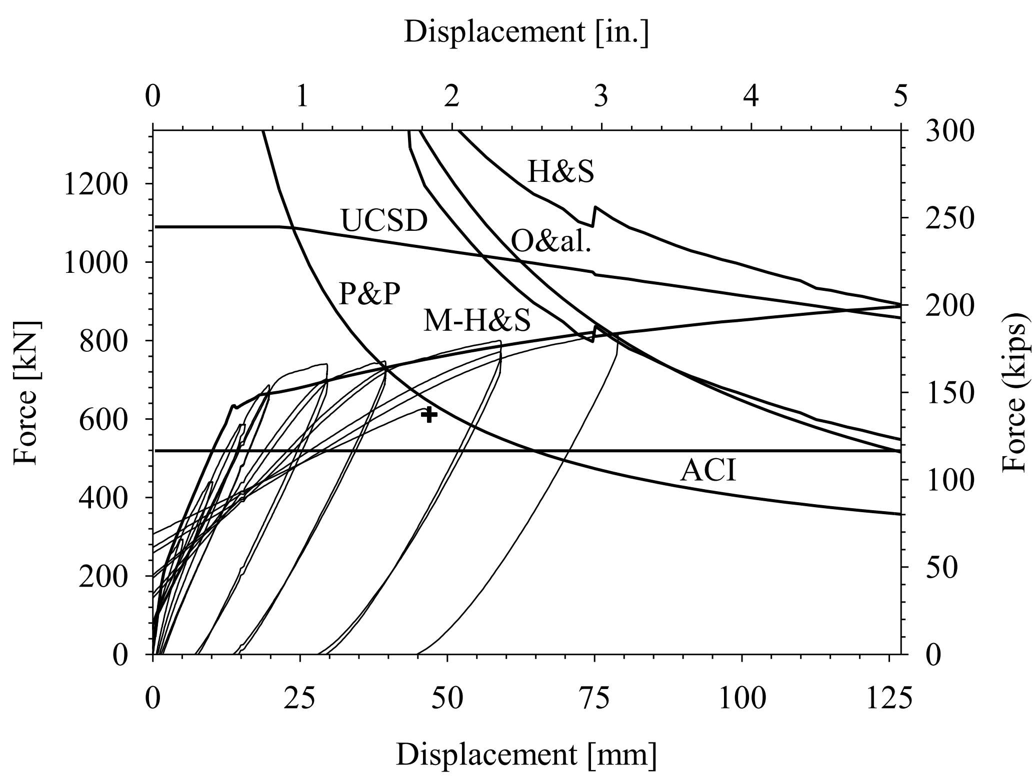

Figure 6.3 M15C hysteretic behavior with failure predictions.

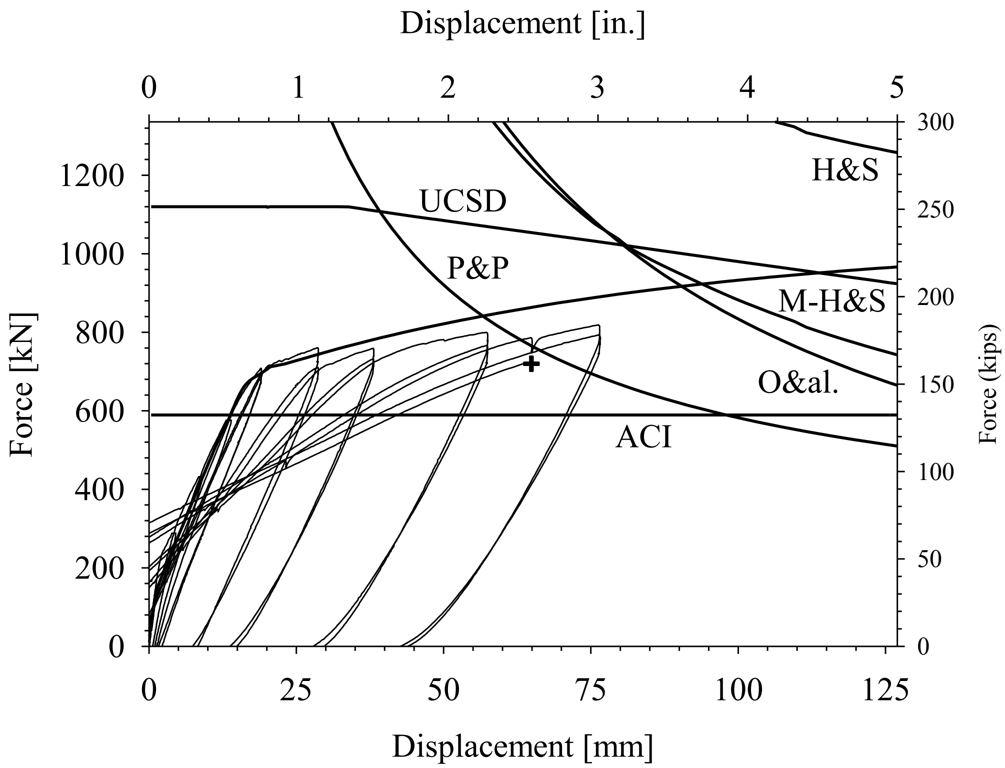

Figure 6.4 M20C hysteretic behavior with failure predictions.

Table 6-1 Comparison of inelastic web-crushing capacities of single walls under cyclic loading with Modified Hines-Seible model.

Test Unit	Experiment		Modified Hines-Seible Model		
	Δ_u (mm)	F_u (kN)	Δ_u (mm)	F_u (kN)	Diff. (%)
M05C	45.0	803	48.5	821	8
M10C	42.7	751	54.9	740	29
M15C	78.7	819	77.2	814	2
M20C	76.5	815	93.9	922	23

Note: 1 in. = 25.4 mm; 1 kip = 4.45 kN.

6.4 Discussion

An expanded discussion based on the results presented in Figure 6.1 to Figure 6.4 and the analytical data is provided below.

Figure 6.5 shows the concrete compression softening parameter at web crushing failure calculated for the single walls under cyclic loading based on the original Hines-Seible model and the Modified Hines-Seible model. The symbols in the figure represent the calculated values of the parameter at failure, while the line trance is the analytical relation for the modified approach. It can be seen in Figure 6.5(a) that the original Hines-Seible model estimates for the softening parameter do not vary much for the different walls. The softening parameter was thus insensitive to compressive strength and the degradation of HSC under cyclic loading is not considered appropriately. In contrast, Figure 6.5(b) shows that smaller values for the softening parameter were obtained for HSC walls compared to the values for NSC walls. However, the values of the parameter are much larger than what was obtained from the NLFEM modeling in Chapter 5, where the concrete under cyclic loading reached maximum compression stress of only approximately 5 ksi based on the VecTor2 analyses. It is believed that the difference resides in the geometry of the studied objects. In the Modified Hines-Seible model, the free body diagram of the strut in the inelastic shear cracking region was studied as the free body diagram, while in the NLFEM study the stress values are obtained form an element, which represents very local behavior.

From Equation (6-1), it can be seen that the concrete compression softening parameter is only a function of the principal tensile strain ε_1, the effect of HSC is not considered explicitly. Since the equation is calibrated based on the membrane tests on NSC, the equation may not be appropriate for evaluating the strain of HSC. A calibration of the equation is needed for better compliance with HSC members.

The shear strength limit of $10\sqrt{f_c'}$ in ACI 318-08 uniformly under-estimated the web crushing capacity of structural walls in this study. Moreover, the equation cannot give any valid information on the displacement ductility of the structural walls, which is an essential index for the seismic design of the structural walls or bridge piers.

While Oesterle's model under-estimated web crushing capacity for wall M05C it gave a good prediction on the other walls, which is not surprising after considering the model is based on test results of similar structural walls failing in web crushing up to displacement ductility 4. The prediction is not conservative for wall M20C since the model is linearly related to the concrete compressive strength and no enhancement in ductility was observed with concrete strengths over 15 ksi. On the other hand, the model by Paulay and Priestley under-estimates the web crushing capacity for all walls, which shows that the model is conservative enough for design. It should be noted that the predictions noted (and plotted) for Oesterle's and Paulay-Priestley's models were modified from their original proposed values as previously discussed. Thus, their performance, as discussed above, essentially applies to a modified version of the models.

It must be realized that the Modified Hines-Seible model as well as the other shear capacity modes were developed to predict web crushing capacity of structural walls under cyclic loading only. There was no intent in predicting web crushing capacity for walls tested under monotonic loading for the following reasons. The monotonic wall tests were conducted for the purpose of serving as a reference to investigate the effect of cyclic loading on concrete degradation. Moreover, the HSC walls under monotonic loading sustained large inelastic deformations before web crushing, which was mainly due to the superior shear transfer mechanism along cracks with the loading in one direction. The behavior of the monotonically tested walls is thus valuable only for research purposes and is not deemed to be realistic for design practice.

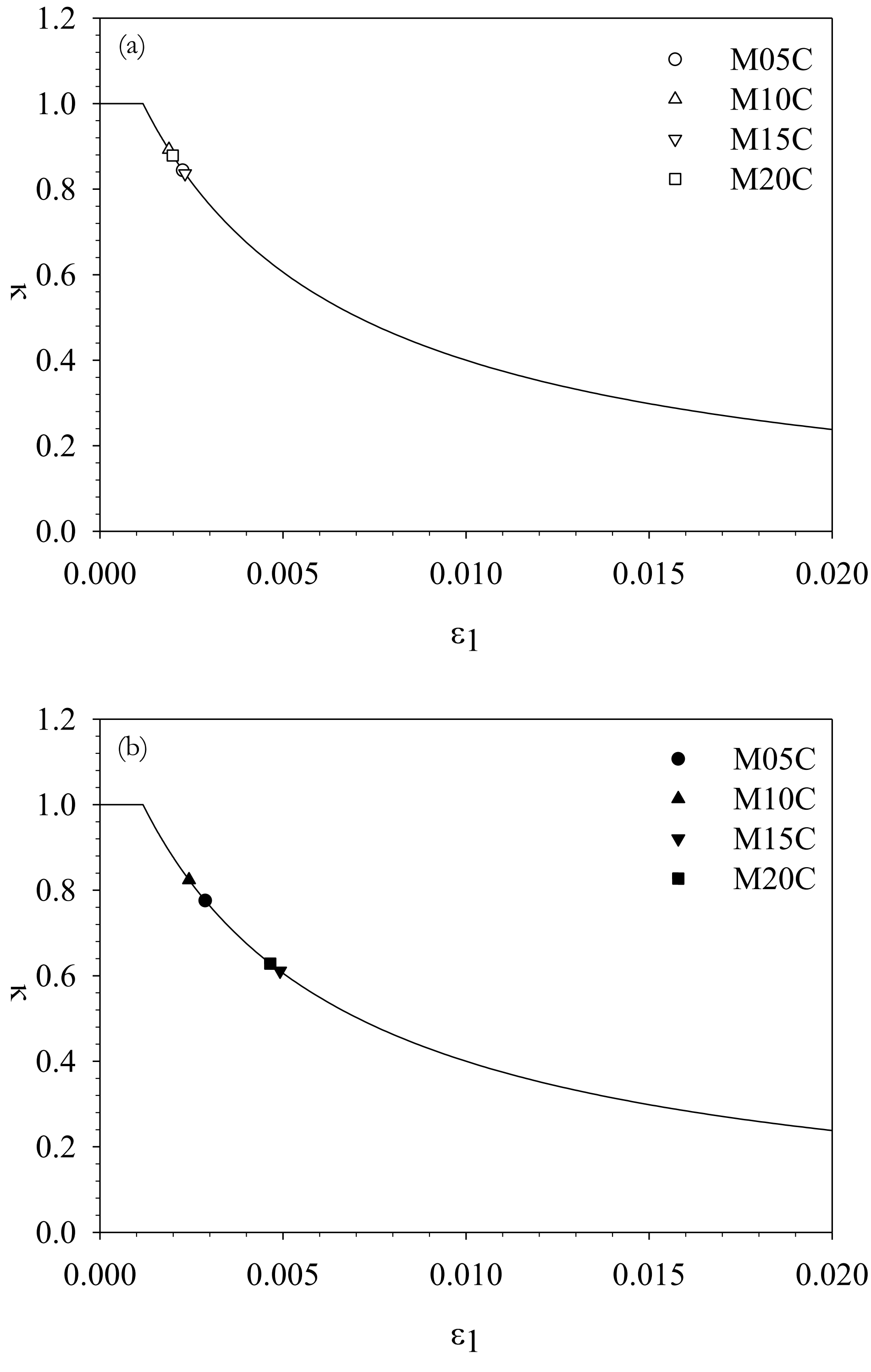

Figure 6.5 Concrete compression softening parameter at web crushing failure for single walls under cyclic loading: (a) Original Hines-Seible model; (b) Modified Hines-Seible model.

6.5 Conclusions

In this study, a simplified analytical method was conducted to predict the web crushing capacity of HSC walls. Modifications to the Hines-Seible model were proposed and shown to dramatically improve the quality of web crushing predictions. The original method for calculating concrete softening parameter was discussed and modifications were proposed based on well-founded arguments. The main findings are described in the following.

First, the Modified Hines-Seible model is still based on the assumption that web crushing capacity is linearly proportional to concrete compressive strength. This assumption was verified in this study up to concrete compressive strengths of 15 ksi. However, test result for wall M20C indicated that there is no appreciable improvement in ductility with concrete strength of 20 ksi. The reason is attributed to the fact that the increased brittleness of concrete with increased compressive strength makes it more susceptible to degradation under cyclic loading. This effect is not captured in the original or modified model. Therefore, the web crushing capacity of M20C wall was over-predicted.

Second, the Modified Hines-Seible mode is essentially a truss model. Different from a NLFEM analysis, the complicated shear stress-distortion relationship at the crack interface and the corresponding structural behavior are neglected. Concrete softening is thus still in an averaged sense and it is different from what was obtained from the NLFEM analyses, which represents a very local behavior.

Chapter 7. **Modeling and Analysis of HSC Hollow Bridge Piers**

7.1 Summary

This chapter presents nonlinear finite element modeling and simplified analysis of the Diagonal Pier Test (DPT) unit subjected to monotonic to study the three-dimensional behavior of wall assemblies and to propose an approach to assess crushing behavior . Nonlinear finite element analyses were conducted using 3D continuum plasticity-based models in the program ABAQUS. The web crushing capacity of the HSC hollow bridge piers was assessed with a simplified analytical method. In the simplified method, an equivalent single wall loaded under in-plane demands in the diagonal direction of the cross section is idealized. The web crushing capacity of the equivalent wall was analyzed with the Modified Hines-Seible model. Analytical results show that diagonal web crushing capacity of the DPT can be well represented by the equivalent single wall concept. However, the web crushing capacity of the BPT unit is over estimated when using this modeling approach due to the failure to consider the damage on concrete from multi-directional loading effects.

7.2 Diagonal Web Crushing Capacity

The web crushing capacity of wall assemblies, or piers as the ones tested in this study, along their principal directions can be studied in the same way as single walls since the wall assembly can be simplified as dual single walls with the flexural contribution of the two webs in the orthogonal direction to loading being neglected. However, the web crushing capacity of wall assemblies or hollow piers along non-principal directions requires different considerations. Further, depending on the geometry of the walls in the assembly, the web crushing capacity of the assembly (or pier) in non-principal directions may control the capacity of the assembly for the following reasons. The aspect ratio of the individual walls in the assembly about the diagonal direction is smaller than that in the principal directions. For the hollow bridge piers test units in this study, the aspect ratio in diagonal direction is 1.94 compared to the aspect ratio of 2.5 in the principal directions. Figure 7.1 shows the analytical force-displacement behavior curves of the Biaxial Pier Test (BPT) unit in the principal and diagonal directions. It can be seen that the capacity of the pier about a diagonal flexural axis is much higher load capacity but a reduced deformation capacity. It is thus anticipated that web crushing will happen earlier in the diagonal direction than in the principal direction. In this study, the diagonal web crushing capacity the hollow pier tested in the diagonal direction (DPT) was investigated to characterize the three-dimensional web crushing capacity of the of wall assemblies.

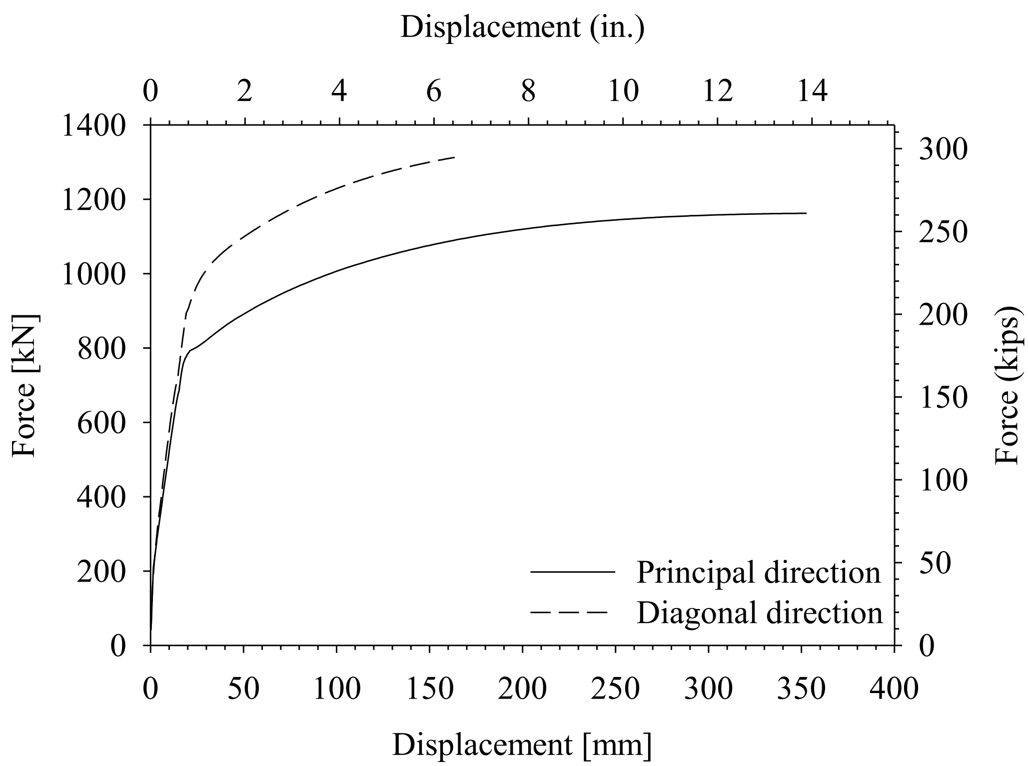

Figure 7.1 The analytical force-displacement responses in principal and diagonal directions.

7.3 NLFEM of the Diagonal Pier Test Unit

The nonlinear finite element modeling (NLFEM) of the diagonal pier test (DPT) unit was conducted with the general purpose finite element program ABAQUS. Since the aim of the analysis was to study the diagonal web crushing behavior of the model and the modeling capabilities in ABAQUS cannot adequately capture the desired cyclic degradation, a monotonic ramp load was applied in the diagonal direction of the DPT unit. The overview of the model is shown in Figure 7.2(a). Figure 7.2(b) shows the discrete reinforcement defined for the model. The footing block was modeled as elastic concrete material and no reinforcement was explicitly modeled in this region. The blocks of the column and the footing are meshed separately with a tie constraint at the interface to connect them together. The mesh for the concrete parts is shown in Figure 7.2(c).An embedment constraint was applied between the reinforcement and the concrete blocks. The concrete damaged plasticity (CDP) material model in ABAQUS was used for the concrete in the column body. Three-dimensional eight-noded continuum-type solid elements with reduced integration (C3D8R) were used for all concrete parts and three-dimensional two-noded truss elements with full integration (T3D2) were used to model the steel reinforcement.

The material properties were defined based on test data from the DPT unit. Details on the steps required to define the CDP model are given in Section 5.3.2. A summary of the material parameters for the material models for DPT simulation is shown in Table 7-1.

To apply a monotonic ramp load on the DPT unit in the diagonal direction, two force components (in x and y directions) were applied on the model. The horizontal force components and the axial load are shown in Figure 7.2(a).

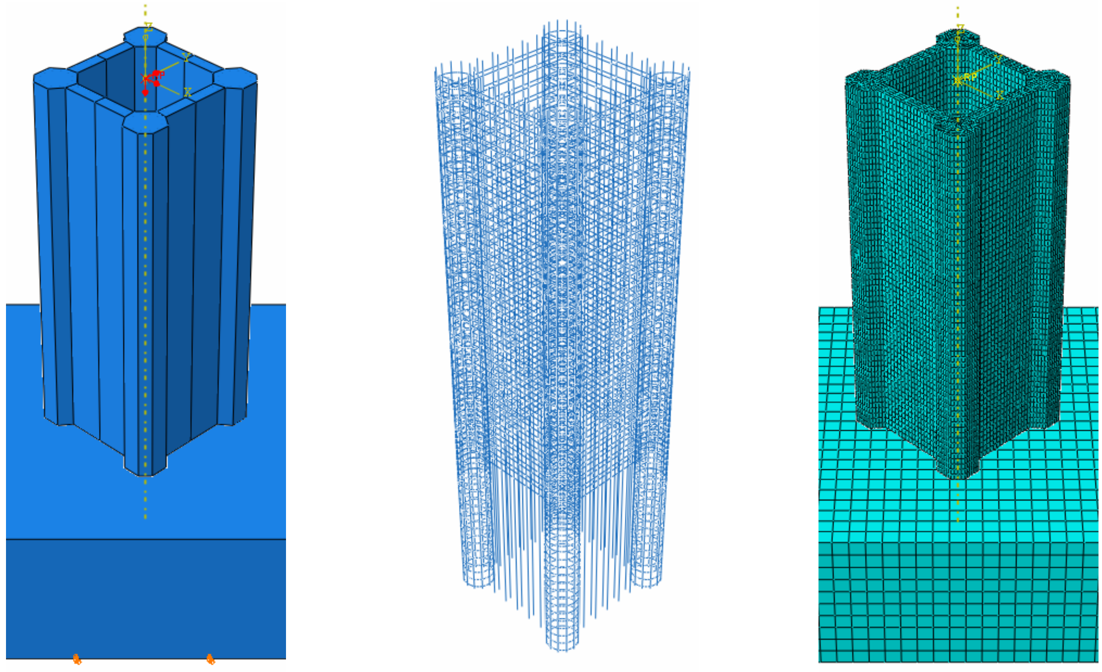

Figure 7.2 Nonlinear finite element model of diagonal pier test (DPT) unit: (a) Model overview; (b) Reinforcement; (c) Mesh of concrete parts

Figure 7.3 shows a comparison of the global force-displacement behavior between the experiment and the FE simulation. It can be seen that the global force-displacement behavior of the DPT unit was predicted well. However, no failure (i.e., drop on the load-carrying capacity) was captured, which indicates that the web crushing capacity of the test unit is unable to be predicted through presented nonlinear finite element modeling approach. Moreover, the effect of the visco-plasticity parameter for controlling the convergence and the accuracy of the results need to be further investigated.

Table 7-1 The concrete and steel material parameters for DPT Unit.

DPT		The parameters of CDP model	
		ψ	27°
		ϵ	0.1
Concrete elasticity		σ_{b0}/σ_{c0}	1.16
E(ksi)	4578	K_c	0.667
ν	0.2	μ	0.0075
Concrete compression hardening		Concrete compression damage	
Stress (ksi)	Crushing strain	DamageC	Crushing strain
5.81	0	0	0
7.24	0.00017	0.07	0.00017
8.00	0.00058	0.21	0.00058
5.26	0.00185	0.52	0.00185
1.71	0.00363	0.79	0.00363
0.57	0.00487	0.89	0.00487
0.28	0.00569	0.92	0.00569
0.15	0.00647	0.95	0.00647
Concrete tension stiffening		Concrete tension damage	
Stress (ksi)	Cracking strain	DamageT	Cracking strain
0.90	0	0	0
0.66	0.00029	0.27	0.00029
0.45	0.00065	0.50	0.00065
0.26	0.00116	0.71	0.00116
0.16	0.00157	0.81	0.00157
0.08	0.00219	0.90	0.00219
0.03	0.00300	0.96	0.00300

Reinforcing Steel Properties					
#6 Steel		#3 Steel			
E(ksi)	29000	E(ksi)	29000		
ν	0.3	ν	0.3		
Stress (ksi)	Plastic strain	Stress (ksi)	Plastic strain		
64.86	0	63.64	0		
65.10	0.00374	63.77	0.00204		
70.36	0.00752	71.07	0.00750		
81.54	0.01699	81.82	0.01698		
90.25	0.02645	90.36	0.02644		
96.84	0.03588	96.95	0.03588		
101.67	0.04528	101.91	0.04528		
105.11	0.05464	105.50	0.05463		
107.49	0.06395	108.04	0.06393		
109.14	0.07320	109.80	0.07317		
110.35	0.08237	111.07	0.08235		
111.39	0.09147	112.13	0.09144		

Figure 7.4 and Figure 7.5 show contour plots of PEEQ and PEEQT at a displacement level of ductility of 4. It is shown that the diagonal truss mechanism in the webs next to the compression boundary element is not well established to transfer the forces from the boundary elements in tension to the compression boundary element. It seems that the cross section of the model is mainly under flexural demands, which will result in tension and compression forces only. The effect of shear demand seems to be isolated from the flexural demand effects. It follows that the inability of the modeling approach to capture the flexure-shear effects does not allow the model to display the diagonal truss mechanism in the webs. Further investigation is needed in this regard.

Figure 7.6 and Figure 7.7 show contour plots for the shear stresses S13 and S23 on the concrete parts of the model. Observation of the contour plots indicates that the webs next to the compression boundary element carry more shear stresses compared to the webs between the extreme tension boundary elements and the middle boundary elements. This verifies that the shear carrying-capacity is reduced due to the occurrence of flexure cracking in the tension walls, even though dowel action and shear transfer across cracks are still able to resist shear. At the same time, the compression zone of the cross section, as well as the region under less tension forces, can resist more shear stresses. This phenomenon exists on coupled shear walls as well as other types of wall assemblies.

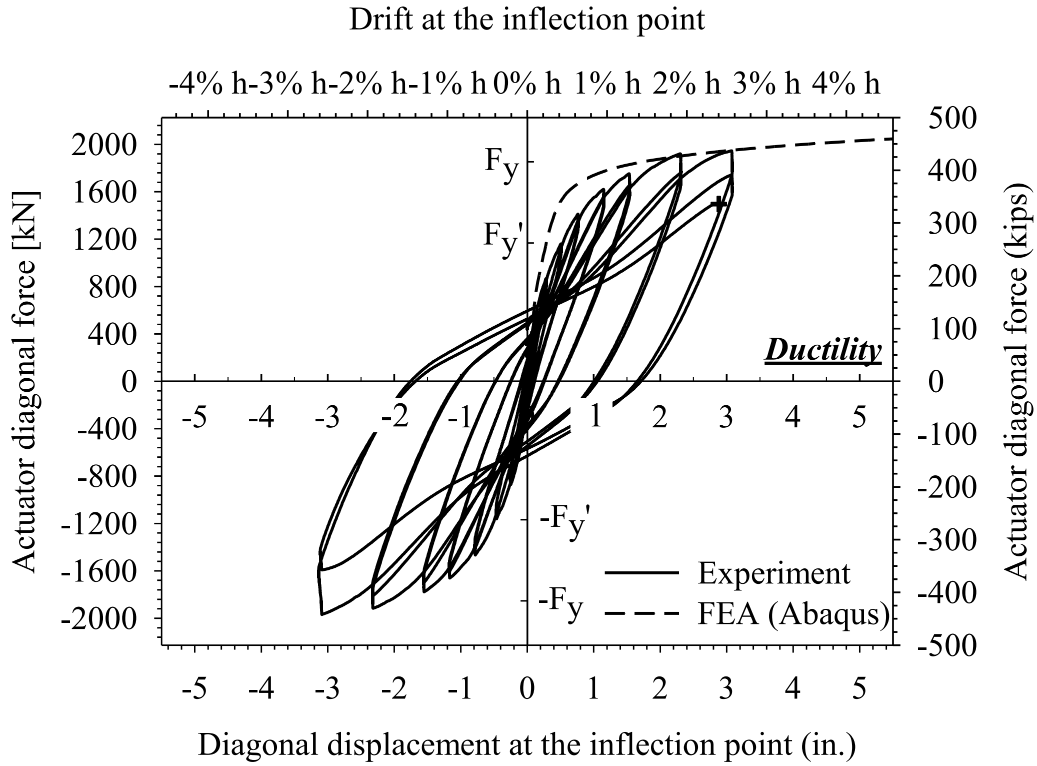

Figure 7.3 DPT: global force-displacement behavior comparison between experiment and ABAQUS.

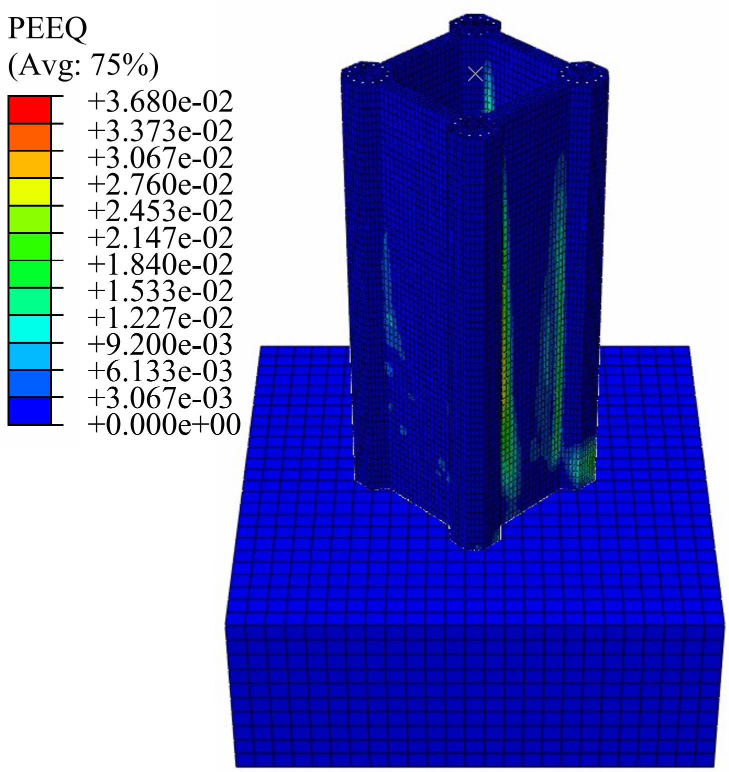

Figure 7.4 DPT Unit contour plot: Compressive equivalent plastic strain (PEEQ).

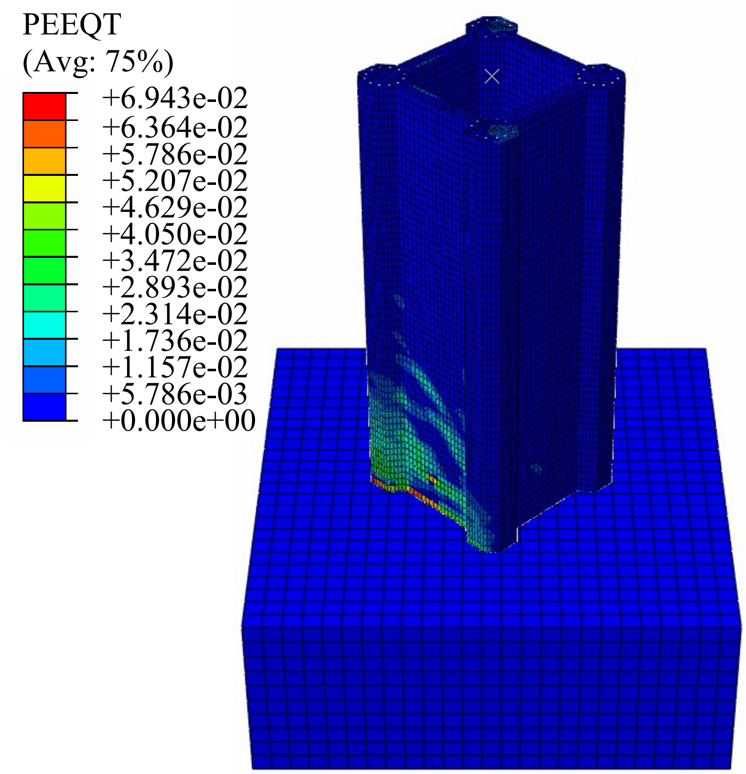

Figure 7.5 DPT Unit contour plot: Tensile equivalent plastic strain (PEEQT).

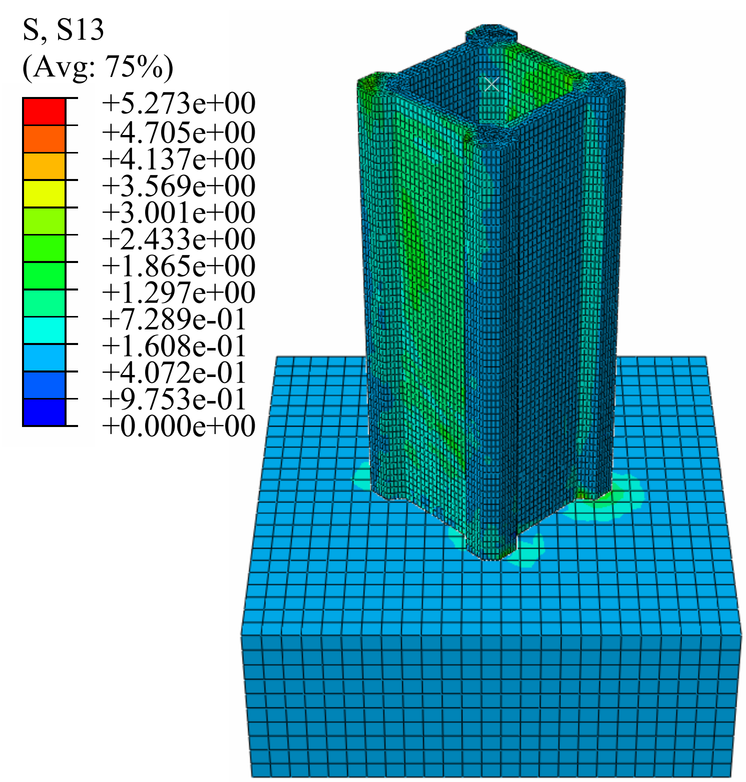

Figure 7.6 DPT Unit contour plot: shear stress component in horizontal plane (S, S13).

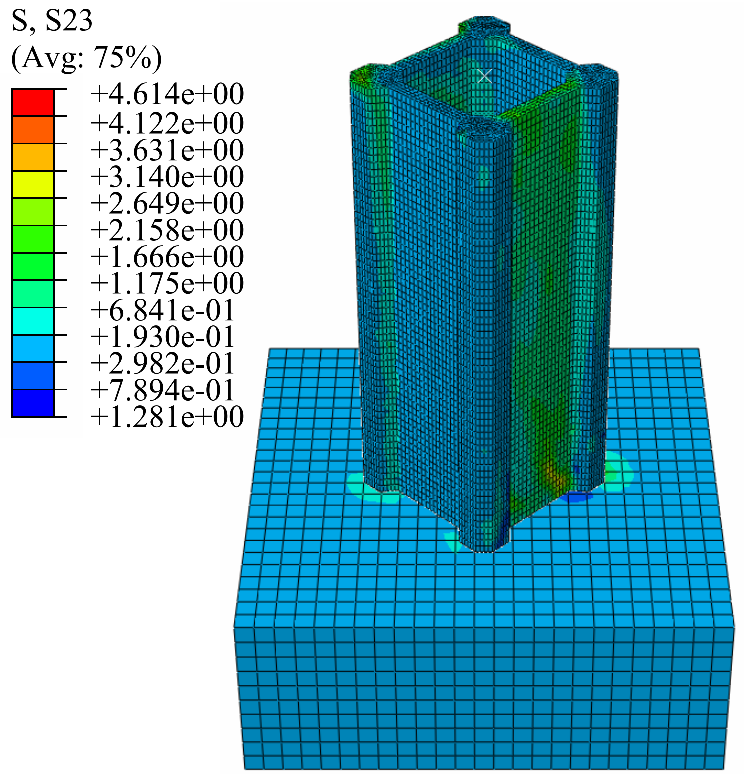

Figure 7.7 DPT Unit contour plot: shear stress component in horizontal plane (S, S23).

7.4 Equivalent Single Wall Unit Analysis

Without considering the multi-directional loading effects, the response of both the Diagonal Pier Test (DPT) and Biaxial Pier Test (BPT) units could be simplified as an equivalent system under in-plane demands. This, rather large, assumption makes it possible to analyze the diagonal web crushing behavior with an equivalent single wall. Figure 7.8 illustrates the elevation of such an equivalent single wall as a projection of the cross section of the hollow pier test units. The performance of the Modified Hines-Seible model in assessing the web crushing capacity of the pier units by means of a simplified equivalent wall was assessed and described next.

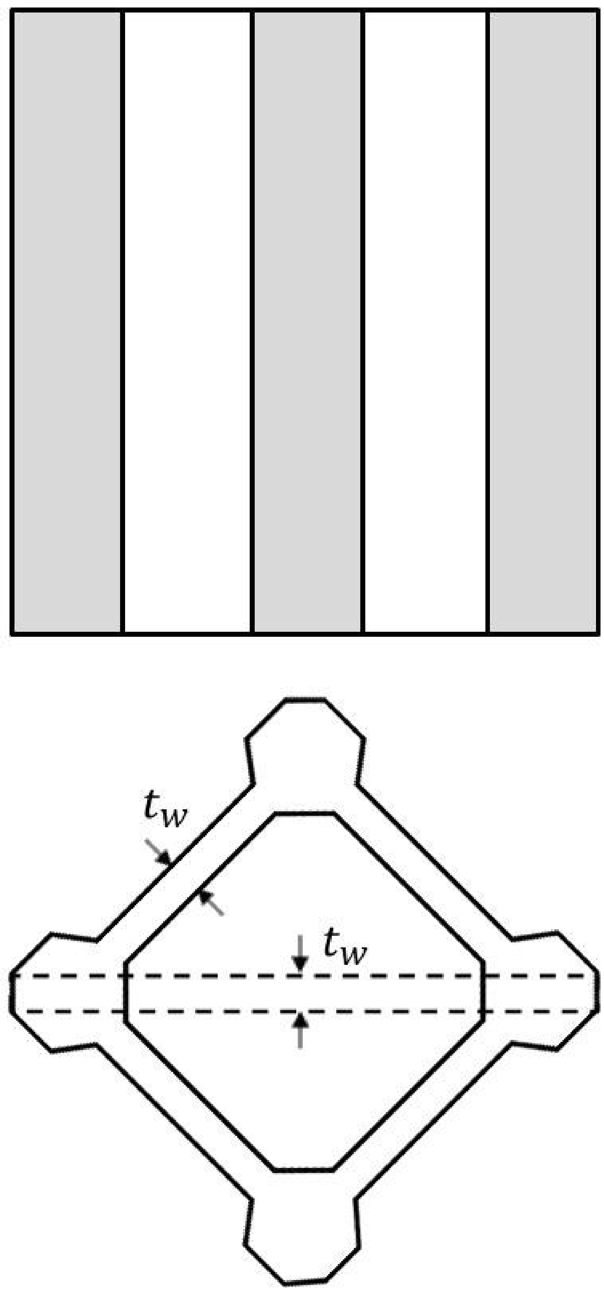

Figure 7.8 Equivalent single wall concept for the capacity analysis of hollow piers.

The boundary elements, which are mainly designed to resist moment demands with concentrated tension or compression forces, are not affected by being located spatially away from the diagonal axis of bending. Thus, they can be assumed to be on the diagonal axis of in-plane with the same dimensions. Unlike the web of a single cantilevered wall under in-plane demands, the concept of an equivalent single wall for the pier wall assembly is such that the web of the equivalent single wall is separated into two segments due to the existence of the boundary elements in the middle. The effect of the two middle boundary elements is described as follows.

First, separation of the middle boundary elements from the one in the far tension side changes the location of the resultant tension force, which will be in the wall and move towards the middle boundary elements with an increase in moment demand. Second, the boundary elements divide the wall into two halves and disturb the cracking pattern. The cracking pattern on each wall will be different in terms of cracking angles and shear demand. Finally, the depth of the web for each segment is determined by the diagonal distance between the adjacent boundary elements. The width of the equivalent wall was assumed to be the width of each wall in the piers. This geometric modification can be obtained through simple calculations based on the premise that the shear strength of the concrete must be the same.

The web crushing capacity of the equivalent single wall was evaluated with the different capacity models presented in Chapter 6. The Modified Hines-Seible model with the concrete softening parameter as described in Section 6.2 was also used. There is a slight difference on the depth of the web D_w in Equation (6.6) for estimating the stress of the transverse steel. Due to the presence of boundary in the middle of the cross section of the equivalent wall, the wall is separated and the depth is assumed to be reduced. This follows from the fact that it is appropriate to assume there is only horizontal cracking in the middle boundary elements due to the moment demand, the dimension of which should not be included in D_W. The net depth of the web for the equivalent single wall for the pier test units was approximately 734 mm (28.9"). With respect to the determination of ε_l, the longitudinal strain of the fiber next to the compression boundary element for the Modified Hines-Seible model, it was noticed that the neutral axis is located in the web of the equivalent wall up to web crushing failure. Therefore, the values of ε_l were negative.

Figure 7.9 and Figure 7.10 show the hysteretic behavior for the DPT and BPT units together with web-crushing capacity curves from different models applied to the just described equivalent single wall. It can be seen that the web crushing capacity of the DPT unit is well predicted by the Modified Hines- Seible model. However, the model is unable to assess (over-predicts) the web crushing capacity of the BPT unit, whose capacity was severely curtailed due to the multi-directional loading. The values of concrete softening parameter κ using the modifications presented in Section 6.2 were 0.77 for the DPT unit and 0.70 for the BPT unit. The reason that the Modified Hine-Seible model can not predict the web crushing capacity of the BPT unit is that concrete damage due to the multi-directional loading failed to be considered. It can be reasonably expected that the BPT pier test unit would have been able to sustain a larger level of displacement ductility if the same loading protocol of the DPT unit had been applied.

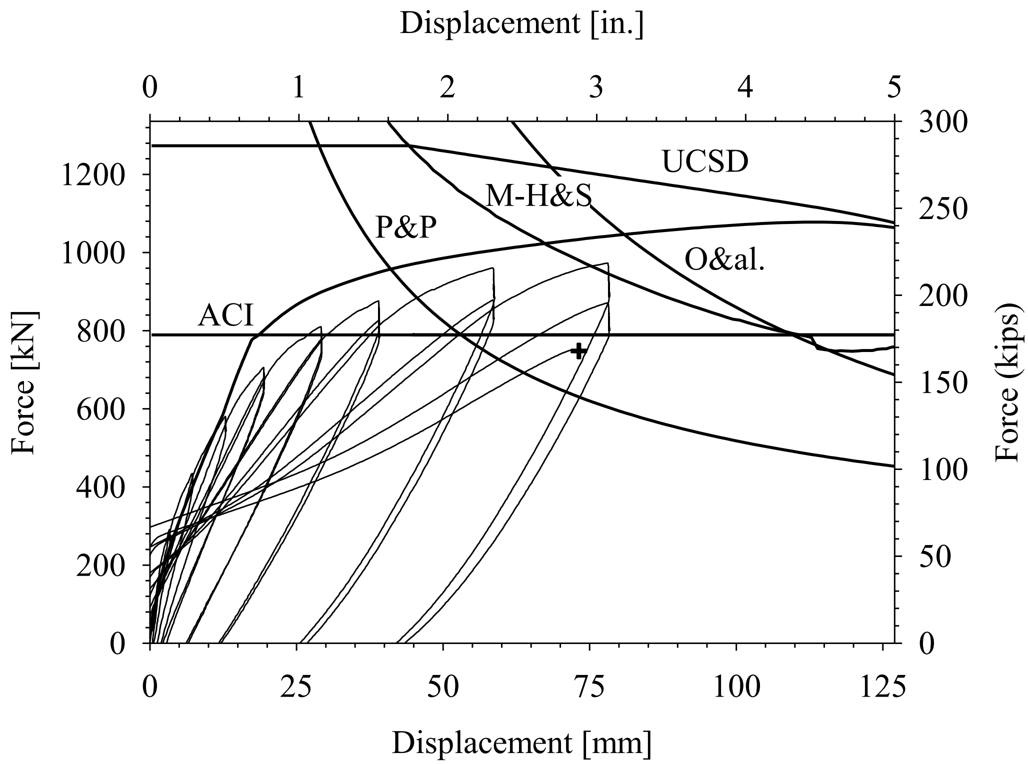

Figure 7.9 DPT Unit hysteretic behavior with failure predictions.

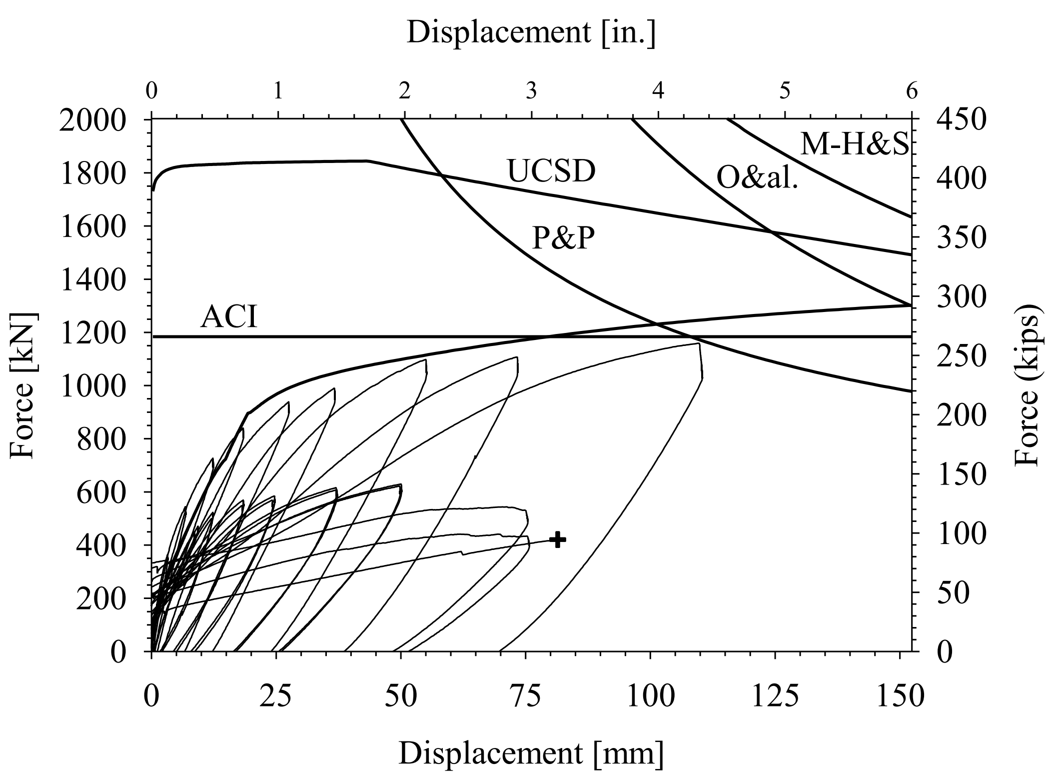

Figure 7.10 BPT Unit hysteretic behavior with failure predictions.

7.5 Conclusions

Nonlinear finite element simulations were conducted on the DPT unit with a monotonic loading along the diagonal direction of the cross section. The modeling approach was able to predict the global force-displacement behavior of the unit quite well. However, the flexure-shear interaction behavior and the truss mechanism in the webs could not be captured with the modeling approach followed in this work. Observations on the distribution of the shear stresses indicate that the webs in the compression side carried more shear stresses than the webs between the tension boundary elements. …

The diagonal web crushing capacity of the DPT and BPT units was also analyzed in this chapter through an equivalent single wall concept. It was found that the Modified Hines-Seible model presented in Section 6.2 predicted the capacity of the DPT pier well, but over-predicted the capacity of the BPT unit. The reason behind over-predicting the web crushing capacity of the BPT pier unit is attributed to the deficiency of considering concrete damage due to the multi-directional loading effects. A parameter reflecting the loading protocol effect is recommended to be included in calculating the reduced concrete compressive strength.

Chapter 8. **Summary and Conclusions**

8.1 Summary

High-strength-concrete (HSC) offers the potential of optimizing structural design and reducing material costs. However, the using of HSC in seismic regions is not well studied and corresponding design guidelines are deficient. Web crushing failure has long been regarded as a brittle failure mode. The current design codes in the US avoid it by limiting the maximum allowable stress provided by the reinforcement. Under such circumstances, this dissertation has evaluated the web crushing performance limits of HSC structural walls and wall assemblies. The hypothesis that HSC can lead to ductile shear failures in reinforced concrete structural walls by delaying (i.e., increasing) web crushing capacity was verified through a comprehensive experimental program and supported by numerical and analytical investigations.

A single wall test program was conducted to verify the effect of concrete compressive strength and cyclic loading on web crushing capacity. Eight 1/5-scale single walls were tested with design concrete compressive strengths of 34, 69, 103, and 138 MPa (5, 10, 15 and 20 ksi) under cyclic and monotonic loading protocols. The experimental results revealed that high-strength-concrete can effectively delay web-crushing failures and increase the displacement ductility levels of structural walls. Contrary to the traditional opinion of shear failures having rapid strength and stiffness degradation and less energy-dissipating mechanism, "ductile shear failures" were identified on HSC structural walls. This behavior is deemed to happen on structural walls with boundary elements or flanges where flexure-shear interaction can take place in well-constrained thin-webbed elements. The flexure effect was introduced in the wall webs by extension of the horizontal cracking in the tension-resisting boundary element, which results in a fanning crack pattern in the wall web. On one hand, the flexural-shear effect improves the deformation capability of the web before web crushing. Yet, this mechanism causes strength and stiffness degradation of the concrete in the web due to excessive cracking, which is the reason of web crushing, particularly from cyclic loading. For high-strength-concrete with compressive strengths over 15 ksi, the further improvement in ductility could be compromised by the rapid strength degradation under cyclic loading.

A wall-assembly test program was conducted within the context of hollow bridge piers to investigate the effect of three-dimensional demands on the web crushing capacity of wall assemblies loaded in non-principal directions and under severe multi-directional loading paths. Two 1/4-scale hollow rectangular bridge pier test units featuring highly-reinforced boundary elements at the four corners and thin connecting webs, were subjected to diagonal and multi-directional cyclic loading with design concrete strengths of 34 and 138 MPa (5 and 20 ksi), respectively. Experimental results showed that both test units exhibited stable ductile behavior until web crushing at moderate ductility levels. The achieved comparable ductility levels of the two pier test units indicated the advantageous effect of HSC in increasing web crushing capacity is compromised by concrete damage and strength degradation under multi-directional loading. Evaluation of the diagonal web crushing behavior is complicated due to the occurrence of middle boundary elements. Different cracking patterns were observed on the diagonally load pier test unit (DPT) between the 'compression' and 'tension' walls, which also indicates the effect of non-principal, or three-dimensional, demands on shear stress distribution. However, for the biaxially loaded pier (BPT) the difference in cracking pattern was minor due to the severity and dominance from the multi-directional loading effects.

Nonlinear finite element modeling (NLFEM) of web crushing capacity of high-strength-concrete structural walls was conducted with 3D continuum plasticity-based finite element models (ABAQUS) and 2D plane stress phenomenologically-based finite element models (VecTor2). Capabilities and limitations of both modeling approaches in evaluating the web crushing failure mechanism and capacity of reinforced concrete walls were investigated. Continuum-based FE analyses with concrete damaged plasticity modeling were able to adequately simulate global behavior of the single walls under monotonic loading. However, issues related to the numerical technique of viscoplastic regularization and the simulation of stiff structural walls under cyclic loading were not clarified. Modifications to the concrete damaged plasticity model in ABAQUS are deemed necessary. The phenomenlolgically-based FE analyses were able to successfully model the behavior of structural walls under both monotonic and cyclic loading. The models were even able to capture the inelastic shear behavior in the plastic hinge region. However, concrete strength degradation under cyclic loading and the web crushing capacity is not considered in the formulation of the analytical model and the web crushing capacity of walls under cyclic loading could not be predicted. Both simulation methods revealed that the concrete stress at web crushing was only a small portion of the cylinder compressive strength, which is attributed to the complex stress state of the concrete in the web crushing region. The simulation results confirm that web crushing in the form of inelastic shear failure is caused by the flexure-shear interaction effects induced in the web of the structural walls.

To evaluate web crushing capacity with simplified analytical methods, the inelastic web crushing capacity model by Hines and Seible was used with modifications to the calculation of the concrete softening parameter. The modifications were verified to be appropriate to predict the capacity of HSC walls. It was noted through the analysis of the single walls in this study that the HSC walls displayed more rapid concrete softening compared with the NSC walls. To apply the simplified method to the pier test units, an equivalent single wall concept about the non-principal loading direction of the cross section was proposed. The modified Hines-Seible model was shown to accurately predict the web crushing capacity of the DPT pier. However, the web crushing capacity of the BPT unit was over estimated by this simplified analysis approach due to the failure to consider concrete degradation from the effects of multi-directional loading.

8.2 Original Contribution

Contrary to current practice, which strictly avoids web crushing failures by prescriptive requirements, this study has fundamentally addressed the issue. Instead of simply being considered a brittle failure, web crushing in a structural wall can be designed to occur after significant and reliable ductile performance is achieved by the use of high-strength-concrete. This counter-intuitive and non-traditional concept was verified through an extensive and original experimental investigation on single in-plane loaded walls and wall multi-directionally loaded hollow piers. Both experimental phases demonstrated that ductile shear failure behavior with the application of high-strength-concrete can be designed for and reliably predicted. The findings from this study can be extended to conclude that ductile shear failure can happen on thin-webbed elements constrained by well-confined boundary elements where flexure-shear interaction is introduced. The findings from this work provide further evidence that the common design-code notion that web crushing is proportional to the tensile strength of concrete and not dependent of the elements inelastic deformation is not only incorrect but leads to over conservative estimate of behavior.

8.3 Future Research Needs

High-strength-concrete shows great potential for slender structural design by increasing the web crushing capacity of structural walls. However, the brittle nature of HSC can result in excessive cracking, which may not satisfy the functional requirements even if safety is not the issue. The structural walls tested in this study shared the same geometry and reinforcement ratios. A parametric study needs to be conducted in order to optimize the structural design approach that best takes advantage of the resistance mechanisms highlighted in this study to achieve the maximum benefits in terms of material resistance and displacement ductility capacity.

Most of the current nonlinear finite element approaches cannot predict the failure of the reinforced concrete structures. The main reason is that the modeling is based on the continuum assumption where cracking is not modeled explicitly. Rather, a failure criteria are implemented in order to capture failure. There is still a long way for general three-dimensional modeling to get reasonable results on stiff reinforced concrete structures with brittle failure modes due to numerical problems along with the difficulties associated with capturing and modeling concrete cracking and crushing. Such challenges indicate that phenomenologically-based models may be a better alternative to continuum and plasticity-based finite element approaches for simulating the behavior of stiff and brittle reinforced concrete structures.

Concrete damage on structural walls in simplified capacity assessment models was evaluated with a concrete softening parameter. However, concrete damage due to multi-directional loading failed to be considered. Another parameter that accounts for such loading effects needs to be included.

8.4 Research Impact

This study highlighted the application of high-strength-concrete in seismic regions and the investigation of the web crushing capacity and failure mechanisms. It has been demonstrated that HSC can enhance the ductility of structural walls by increasing web crushing capacity. A new ductile failure concept, namely that of "ductile shear failures" was proposed and demonstrated to manifest itself with the use of HSC in thin webbed elements constrained by well confined boundary elements that subject the web to flexure/shear effects. Such a failure mode, which was demonstrated to be reliably designed for and predicted for compressive strengths of up to 103 MPa (15 ksi) can be a viable ductile failure mode for seismic design according to a capacity based design philosophy.

The shear design provisions in current design codes were verified to be over conservative. This study provides valuable information on the extension of the current codes to high-strength-concrete. The simplified analytical method proposed in this study can be used to evaluate the web crushing capacity of high-strength-concrete structural walls and wall assemblies.

REFERENCES

REFERENCES

[1]. Hines, E. M., Dazio, A., and Seible, F., "Structural Testing of the New East Bay Skyway Piers," ACI Structural Journal, 103(1):1-10, January-February, 2006.

[2]. Hines, E. M., Dazio, A., and Seible, F., "Structural Testing of the San-Francisco-Oakland Bay Bridge East Span Skyway Piers," Structural Systems Research Project 2002/01, University of California, San Diego, California, 2002.

[3]. Hines, E. M., "Seismic Performance of Hollow Rectangular Reinforced Concrete Bridge Piers with Confined Corner Elements," Dissertation, University of California, San Diego, California, 2002.

[4]. Oesterle, R. G., Aristizabal-Ochoa, J. D., Shiu, K. N., and Corley, W. G., "Web Crushing of Reinforced Concrete Structural Walls," ACI Journal, 81(3):231-241, May-June 1984.

[5]. Oesterle, R. G., Ariztizabal-Ochoa, J. D., Fiorato, A. E., Russell, H. G., and Corley, W. G., "Earthquake Resistant Structural walls – Tests of Isolated Walls, Phase II," NSF Report ENV77-15333, Portland Cement Association, Skokie, IL, 1979.

[6]. Vallenas, J. M., Bertero, V. V., Popov, E. P., "Hysteretic Behavior of Reinforced Concrete Structural Walls," University of California, Report No. UCB/EERC-79/20, Berkeley, California, 1979.

[7]. Paulay, T., and Priestley, M. J. N., "Seismic Design of Reinforced Concrete and Masonry Buildings," Wiley Interscience, New York, 1992.

[8]. Liu, X., Burgueño, R., Egleston, E., and Hines, E. M., 2009a. Inelastic Web Crushing Performance Limits of High-Strength-Concrete Structural Wall – Single wall Test Program, Report No. CEE-RR – 2009/03, Michigan State University, 2009, 281 pp.

[9]. Brueggen, B. L., and French, C. W., "Simplified Modeling of Non-Rectangular RC Structural Walls," 9th US National and 10th Canadian Conference on Earthquake Engineering, Proceedings DVD-ROM, Toronto, Canada, Paper No. 1713, July 2010.

[10]. Waugh, J. D., and Sritharan, S., "Nonlinear Analysis of T-Shaped Concrete Walls Subjected to Multi-directional Loading," 9th US National and 10th Canadian Conference on Earthquake Engineering, Proceedings DVD-ROM, Toronto, Canada, Paper No. 1506, July 2010.

[11]. Maria, H. S., Wood, S. L., and Breen, J. E., 2006. Behavior of Hollow, Rectangular Reinforced Concrete Piers Subjected to Biaxial Loading, ACI Structural Journal, 103 (3), pp. 390-398.

[12]. Mo, Y. L., Wong, D. C., and Maekawa, K., 2003. Seismic Performance of Hollow Bridge Columns, ACI Structural Journal, 100 (3), pp. 337-348.

[13]. Takizawa, H. and Aoyama, H., 1976. Biaxial Effects in Modelling Earthquake Response of R/C Structures, Earthquake Engineering and Structural Dynamics, Vol. 4 (6), pp. 523-552.

[14]. Bousias, S. N., Verzeletti, G., Fardis, M. N., and Guitierrez, E., 1995. Load-Path Effects in Column Biaxial Bending and Axial Force, Journal of Engineering Mechanics, 125 (5), pp. 596-605.

[15]. Wong, Y., Paulay, T., and Priestley, M. J., 1993. Response of Circular Reinforced Concrete Columns to Multi-Directional Seismic Attack, 90 (2), pp. 180-191.

[16]. Hines, E. M. and Seible, F., 2004. Web Crushing Capacity of Hollow Rectangular Bridge Piers, ACI Structural Journal, 101 (4), 569-579.

[17]. Hines, E. M., Dazio, A., and Seible, F., 2001. Seismic Performance of Hollow Rectangular Reinforced Concrete Piers with Highly-Confined Corner Elements – Phase III: Web Crushing Tests, Structural Systems Research Project 2001/27, University of California, San Diego, Calif., 2001, 239 pp.

[18]. Park, R., and Paulay, T., "Reinforced Concrete Structures," Wiley, New York, 1975.

[19]. Hines, E.M., Restrepo, J.I. and Seible, F., "Force-Displacement Characterization of Well-Confined Bridge Piers," ACI Structural Journal, Vol. 101, No. 4, 2004, pp. 537-548.

[20]. Ritter, W., "Die Bauweise Hennebique (Construction Techniques of Hennebique)," Schweizerische Bauzeitung, Zurich, February 1899.

[21]. Mörsch, E., "Der Eisenbetonbau−seine Theorie und Anwendung (Reinforced Concrete Construction−Theory and Application)," 5th Ed., Witter, Stuggart, Germany, Vol. 1, Part 1, 1920.

[22]. Mörsch, E., "Der Eisenbetonbau−seine Theorie und Anwendung (Reinforced Concrete Construction−Theory and Application)," 5th Ed., Witter, Stuggart, Germany, Vol. 1, Part 2, 1922.

[23]. Withey, M. O., "Tests of Plain and Reinforced Concrete Series of 1906," Bull. University of Wisconsin, Engineering Series, 4(1):1-66, 1907.

[24]. Sozen, M. A., and Hawkins, N. M., "Discussion of report of ACI-ASCE Committee 326, Shear and Diagonal Tension," ACI Structural Journal, 59(9):1341-1347, September 1962.

[25]. ACI Committee 318, "Building Code Requirements for Structural Concrete and Commentary (318-08)," American Concrete Institute, Farmington Hills, Michigan.

[26]. Mitchell, D., and Collins, M. P., "Diagonal Compression Field Theory−A Rational Model for Structural Concrete in Pure Torsion," ACI Journal, Proceedings, 71(8):396-408, April 1978.

[27]. Collins, M. P., "Towards a Rational Theory for RC Members in Shear," ASCE Proceedings, Vol. 104(ST4):649-666, April 1978.

[28]. Vecchio, J. V. and Collins, M. P., "The Modified Compression Field Theory for Reinforced Concrete Elements Subjected to Shear," ACI Structural Journal, 83(2):219-231, March-April 1986.

[29]. Belarbi, A., and Hsu, T. T. C., "Constitutive Laws of Concrete in Tension and Reinforcing Bars Stiffened by Concrete," ACI Structural Journal, 91(4):465-474, July-August 1994.

[30]. Belarbi, A., and Hsu, T. T. C., "Constitutive Laws of Softened Concrete in Biaxial Tension-Compression," ACI Structural Journal, 92(5):562-573, September-October 1995.

[31]. Pang, X.-B., D., and Hsu, T. T. C., "Fixed-Angle Softened-Truss Model for Reinforced Concrete," ACI Structural Journal, 93(2):197-207, March-April 1996.

[32]. AASHTO, Standard Specifications for Highway Bridges. 16th edition, Washington, DC (1996), pp. 722.

[33]. AASHTO, AASHTO LRFD Bridge Design Specifications, 3rd Edition, Washington, DC (2004), pp. 1450.

[34]. CSA Committee A23.3, "Design of Concrete Structures," CSA A23.3-04, Rexdale, Ontario, Canada, 2004, pp. 240.

[35]. ABAQUS 6.9 User's Manual, Dassault Systemes S.A., Providence, RI.

[36]. Lubliner, J., Oliver, J., Oller, S., and Onate, E., "A plastic-damage model for concrete," International Journal of Solids and Structures, 25(3):299-326, 1989.

[37]. Lee, J. and Fenves, G. L., "Plastic-Damage Model for Cyclic Loading of Concrete Structures", Journal of Engineering Mechanics, V. 124, No. 8, August 1998, pp. 892-900.

[38]. Lee, J., "Theory and Implementation of Plastic-Damage Model for concrete Structures under Cyclic and Dynamic Loading", Doctoral Dissertation, Civil and Environmental Engineering, University of California, Berkeley, 1996, pp. 151.

[39]. Wong P.S., Vecchio F.J., VecTor2 & Formwork User's Manual. Department of Civil Engineering, University of Toronto; 2002. 214 pp.

[40]. Bentz, E. C., "Sectional Analysis of Reinforced Concrete Members," Doctoral Dissertation, Department of Civil Engineering, University of Toronto, 2000, 310 pp.

[41]. Sittipunt, C., Wood, S. L., Lukkunaprasit, P., and Pattararattanakul, P., "Cyclic Behavior of Reinforced Concrete Structural Walls with Diagonal Web Reinforcement," ACI Structural Journal, 98(4):554-562, July-August 2001.

[42]. Mander, J. B., "Seismic Design of Bridge Piers", Ph.D. Dissertation, University of Canterbury, Christchurch, New Zealand, 1984.

[43]. Fillippou, F. C., Popov, E. P., Bertero, V. V., "Effects of Bond Deterioration on Hysteretic Behavior of Reinforced Concrete Joints", Report EERC 83-19, Earthquake Engineering Research Center, University of California, Berkeley, 1983.

[44]. Park Y. J. and Ang A. H. S., "Mechanistic seismic damage analysis of reinforced concrete," Journal of Structural Engineering, 111(4):722–739, 1985.

[45]. Liu, X., Burgueño, R., Egleston, E., and Hines, E. M., 2009b. Inelastic Web Crushing Performance Limits of High-Strength-Concrete Structural Wall – Wall-Assembly Test Program, Report No. CEE-RR – 2009/06, Michigan State University, 2009, 219 pp.

[46]. Scordelis, A.C., Nilson, A.H. and Gerstle, K., "Finite Element Analysis of Reinforced Concrete", ASCE State-of-the Art Report, New York, 1982.

[47]. Rots, J.G., Computational modeling of concrete fracture, Doctoral Dissertation, Delft University of Technology, 1988, pp. 132.

[48]. Chen, W.F. and Han, D.J., "Plasticity for Structural Engineers," Springer-Verlag, New York, 1988.

[49]. Open System for Earthquake Engineering Simulation (OpenSees), University of California, Berkeley, http://opensees.berkeley.edu.

[50]. Collins, M. P., Mitchell, D. and MacGregor, J. G., "Structural Design Considerations for High-Strength Concrete", Concrete International: Design and Construction, V. 15, No. 5, May 1993, pp. 27-24.

[51]. Barros, M. H. F. M., Martins, R. A. F., and Ferreira, C. C., "Tension Stiffening Model with Increasing Damage for Reinforced Concrete", Engineering Computations, V. 18, No. 5/6, 2001, pp. 759-785.

[52]. CEB-FIP Model Code 1990. Comité Euro-International du Béton.

[53]. Cervera, M., Oliver, J. and Manzoli, O., "A Rate-Dependent Isotropic Damage Model for the Seismic Analysis of Concrete Dams", Earthquake Engineering and Structural Dynamics, V. 25, 1996, pp. 987-1010.

[54]. Liu, X., Burgueño, R., "Inelastic Web Crushing Performance Limits of High-Strength-Concrete Structural Walls and Wall-Assemblies: Modeling and Analysis," Report No. CEE-RR – 2010/10, Michigan State University, East Lansing, MI, 2010.

[55]. Priestley, M. J. N., and Calvi, G. M., "Seismic Design and Retrofit of Bridges", Wiley, New York, 1996.